Enhancing Photoluminescence in Perovskite Nanostructures with Metal Nanoparticles and Nanocavities

Qingyu Wang
Mansfield College
University of Oxford

A thesis submitted for the degree of
Doctor of Philosophy
Michaelmas 2025

Acknowledgements

This thesis would not have been possible without the help and support of many people. I will try to acknowledge as many as I can, even while knowing I cannot name everyone who has contributed along the way.

First and foremost, I am deeply grateful to my supervisor, Professor Robert Taylor. It has been a privilege to work with him over these four years. Beyond his exceptional knowledge and long-standing expertise in optical measurements, he has always been generous, warm, and unfailingly helpful. Whether the question was large or small, he always found time to provide thoughtful, thorough, and efficient guidance. Robert gave us the freedom to explore our projects while offering unwavering support when needed, making my research both enjoyable and rewarding. His passion for science, for work, and for life has influenced and inspired me, shaping both my present and my future. I am profoundly thankful for his mentorship, which has benefited my career and much more. I also wish him a long, healthy, and deeply fulfilling retirement.

I would also like to thank all members of Robert's group with whom I have shared this journey. When I arrived in Oxford immediately after the pandemic, the first DPhil student I met here was Mutibah Alanazi, who kindly introduced me to many aspects of Oxford life and invited me into her project, teaching me how to run experiments. Vitaly Osokin, then a near-complete DPhil student, offered many practical and insightful suggestions. I am especially indebted to Tintu Kuriakose, the PDRA with whom I carried out the plasmonic nanoparticle work that forms a core part of this thesis; her diligence, reliability, and care drove the project forward, and her support for my development and well-being meant a great deal to me. I thank Tristan Farrow for mentoring me when I was new to the lab and for inspiring experimental ideas that deepened my understanding of perovskites. I am grateful to Youngsin Park, a regular visitor, for his steady interest in my progress and for perspective that sharpened my interpretation of experiments and results. I also thank long-term visitor Sanghyuk Park and PDRA Sunny Tiwari for repeatedly helping me resolve experimental and instrumentation issues. Beyond research, many conversations and outings with the group are among my happiest memories of the DPhil.

I gratefully acknowledge our collaborators for their invaluable contributions. Professor Shengfu Yang and his PhD student Hao Sha (University of Leicester) provided the perovskite materials and Ag particles used in Chapter 3 via their mature synthesis methods and liquid He droplet setup. Professor Emilie Ringe and her student Christina Boukouvala (University of Cambridge) supplied high-quality Mg nanoparticles studied in Chapter 4 and offered insightful advice grounded in their deep understanding of plasmonic materials. From the Department of Chemistry, Professor Robert Hoye and Dr Junzhi Ye provided perovskite nanoplatelets and were consistently helpful in discussing and analyzing results related to these samples, and it has been a pleasure to work with them.

Beyond research, I am thankful for the friends I met in Oxford, with whom I shared many good times. I am especially grateful to my housemate, Qianqian Song, a fellow DPhil student and an enthusiast in the kitchen, whose culinary skill provided me with many memorable meals and, even more, countless moments of warmth and joy; her friendship is something I deeply treasure.

Lastly, and certainly not least, I thank my family. Throughout my life, my parents have given me steady and unwavering support, allowing me the freedom to make choices, even risky ones, assured by their constant love. My father's open encouragement made me brave. My mother, though she passed away during my DPhil years, continues to light my life with her love. Their love is my greatest wealth.

There are many others I cannot fully list: Paul Pattinson and colleagues in the Department of Materials who taught me to use cleanroom facilities; Dr Shiling Dong from Robert Hoye's group for repeated XRD measurements; Henry Coop and many former master's students who worked alongside me; previous DPhil students and visitors who developed and refined the facilities and software we use; and the University of Oxford for its many kindnesses and conveniences. To everyone who helped me over these four years in Oxford, I extend my heartfelt thanks.

Writing this Acknowledgements section is the final step in completing my thesis, but it does not feel like an ending. I carry forward the learning and joy behind this work as I look excitedly to the future.

Abstract

Enhancing photoluminescence (PL) is central to advancing optoelectronic and quantum photonic technologies. Low-dimensional $CsPbX_3$ perovskite nanomaterials have emerged as outstanding emitters due to their large exciton binding energies, high oscillator strength, and the ability to sustain excitons at room temperature. Strategies such as cavity-induced Purcell enhancement and plasmonic local-field amplification offer powerful means to modulate their optical response, markedly boosting PL intensity. This thesis investigates the coupling between metal nanoparticles (NPs), optical nanocavities, and lead-halide perovskite nanostructures to actively control and enhance emission, establishing both mechanisms and design principles for hybrid light–matter architectures.

Pronounced plasmon-enhanced emission was demonstrated in Ag/$CsPbBr_3$ nanowire hybrids. A two-step process combining superfluid helium droplet deposition with wet-chemical growth enables precise NP sizing and tunable plasmon resonances, while minimizing damping from chemical residues. Within a tailored four-layer geometry, this approach yields an 8.5-fold PL intensity increase at 4 K, with time-resolved measurements confirming accelerated recombination from plasmon–exciton coupling.

Magnesium is further introduced as an alternative plasmonic material to conventional noble metals. Benefiting from earth abundance and low cost, Mg supports competitive plasmonic resonances and is readily synthesized via colloidal routes into spheroidal Mg/MgO core–shell NPs. Near-field coupling between their dipolar modes and $CsPbBr_3$ nanowire emission delivers PL enhancement factors of 1.7× and 4.1× for different sub-100 nm particles at room temperature. Although weaker than Ag in analogous designs, Mg's self-limiting oxide shell provides improved ambient stability, highlighting a sustainable pathway for plasmonic integration.

Finally, micro-PL studies on $CsPbI_3$ nanoplatelets reveal pronounced quantum confinement, with excitonic energies and recombination dynamics tuned by thickness. Cavity-assisted measurements show brighter and more symmetric emission spectra relative to off-cavity references, though without significant lifetime shortening. These results indicate that excitation/collection efficiency and spectral filtering dominate the observed enhancements, while Purcell acceleration remains weak under the current cavity design.

Collectively, this work establishes new routes to control and amplify light emission in perovskite nanostructures through plasmonic and cavity coupling, providing insights for the rational design of scalable hybrid architectures for optoelectronics and quantum photonics.

Contents

List of Figures **ix**

List of Abbreviations **xviii**

List of Publications **xx**

1 Introduction **1**

1.1 Scope and Organization 1
1.2 $CsPbX_3$ Metal Halide Perovskite Materials 2
1.2.1 Structure 3
1.3 PL of Low-Dimensional Perovskite Nanostructures 8
1.3.1 Low-Dimensional Perovskite and Quantum Confinement . . 8
1.3.2 Formation of Excitons 10
1.3.3 Excitonic Recombination 13
1.3.4 Recombination Dynamics 16
1.4 Plasmon-enhanced PL Emission 17
1.4.1 Localized Surface Plasmonic Resonance 17
1.4.2 LSPR-enhanced PL 19
1.4.3 Metals as Plasmonic Materials 21

2 Experimental Techniques **24**

2.1 Introduction 24
2.2 μPL spectroscopy 25
2.2.1 Laser Sources 26
2.2.2 Optical Layout and Microscopy Setup 31
2.2.3 Temperature Control 34
2.2.4 Detection System 35
2.3 μPL Mapping 39
2.4 Time-Resolved μPL 43
2.4.1 TRPL Layout 44
2.4.2 Data Acquisition 44
2.4.3 Instrument Response Function 45

2.5 Superfluid He Droplet Growth 46
2.5.1 Overview 46
2.5.2 Sample Growth Using He Droplet 47

3 Ag NPs–Enhanced PL in Perovskite Nanowires 51
3.1 Chapter Introduction 51
3.2 Ag Plasmonic Effects on Photonic Nanowires 52
3.3 Sample Fabrication 59
3.4 Setup 66
3.5 µPL Characterization and Device Design 66
3.5.1 μPL Investigation of Nanowires 66
3.5.2 μPL Investigation on Nanowires with Ag Nanoparticles . . . 81
3.5.3 Parameter optimization 89
3.6 Ag NPs Enhanced PL Emission in Perovskite Nanowires 93
3.6.1 Discussion on Plasmon–photon Coupling Mechanism 96
3.7 Conclusion and Discussion 100

4 Plasmonic Mg NPs for PL Enhancement in Perovskite Nanostructures 102
4.1 Chapter Introduction 102
4.2 Plasmonic Mg Nanoparticles 103
4.2.1 Proposed Mg–Perovskite Hybrid Structure with Simulation . 105
4.3 Sample Fabrication and Modification 107
4.3.1 Size-Controlled Faceted Spheroidal Mg Nanoparticles 107
4.3.2 Modification on $CsPbBr_3$ NWs via Electric Field 110
4.3.3 Hybrid Mg–Perovskite Nanostructures 114
4.4 Setup 115
4.5 μPL Characterization on Hybrid Mg–$CsPbBr_3$ Nanostructures . . . 116
4.5.1 μPL Characterization at RT for Uncoated Mg NPs 116
4.5.2 μPL Characterization at 4 K for Uncoated Mg NPs 119
4.6 Plamonic Core-Shell Mg NPs Enhanced Perovskite NW PL at RT . 123
4.6.1 Motivation for spacer design 123
4.6.2 Comparison with Ag NPs Based Plasmonic Enhancement . . 126
4.6.3 Determining the Enhancement factor 127
4.7 Conclusion and Discussion 128

5 PL of Perovskite Nanoplatelets Integrated with Optical Nanocavity 130
5.1 Chapter Introduction . . . 130
5.2 Optical Cavity Coupled PL . . . 131
5.3 Samples . . . 132
5.3.1 $CsPbI_3$ Nanoplatelets . . . 132
5.3.2 Optical Nanocavity . . . 137
5.4 μPL Investigation on Nanoplatelets with Different Layer Numbers . 139
5.5 μPL Investigation on Nanoplatelets Coupled to Optical Nanocavities 144
5.6 Conclusion and Discussion . . . 148

6 Conclusion and Outlook 150

Appendices

A Derivation of LSPR resonance conditions 154

B Reflection of Nanocavities 156

References 158

List of Figures

1.1 **Crystal structure of cubic perovskite $\mathrm{CsPbX_3}$ (space group $Pm\bar{3}m$).** (a) Corner-sharing $\mathrm{BX_6}$ octahedral network. (b) Schematic representation of the unit cell, where A-site cations (green) occupy the cube corners, B-site cations (blue) are located at the body centre, and halide anions (orange) reside at the face centres. 3

1.2 **Electronic band structure and halide-dependent band alignment of all-inorganic $\mathrm{CsPbX_3}$.** (a) Diagram illustration of orbital hybridization in Pb-based perovskites, where the conduction band (CB) is mainly derived from Pb(6p) orbitals, and the valence band (VB) originates from the antibonding interaction between Pb(6s) and X(np). (b) Tuning of band gap energy by varying the halide composition (X = Cl, Br, I), showing the systematic shift of conduction and valence band edges. Adapted from [32] with permission. 6

1.3 **Schematic density of states (DOS) in 3D, 2D, 1D, and 0D systems.** 9

1.4 **Schematic of the Wannier–Mott exciton with optical excitation.** 13

1.5 **Illustration of electron cloud oscillation in a metallic small particle under incident light LSPR.** 17

1.6 **Schematic illustration of PL excitation and decay pathways in (a) free-space condition and (b) LSPR-coupled system.** In free space, carriers are excited from the ground state (S_0) to the excited state S_1 by an external optical field E, followed by either radiative recombination with rate Γ_r or nonradiative recombination with rate Γ_nr. When coupled to plasmonic nanostructures, the excitation can be enhanced by the nearby LSPR E_LSPR, while additional decay channels appear with respect to the boosted LDOS. The short horizontal line below S_1 is to indicate the branching of relaxation pathways, with the black arrow representing the transition from the excited state into these decay channels. 19

1.7 **Dielectric functions of representative plasmonic metals: (a) real part, (b) imaginary part, and the derived figures of merit (c) Q_1 and (d) Q_2.** Reprinted from Ref. [92] under CC BY 4.0 license. 22

1.8 **Comparison of typical plasmonic spectral ranges for various metals and nanostructure geometries.** Adapted from [94] with permission. 23

2.1 **A schematic diagram of the confocal μPL setup shows a frequency-doubled femtosecond laser emitting light at 400 nm, focused onto a sample using a 100× microscope objective. L: Lens. B: Beam Splitter. LPF: Long-pass Filter.** The excitation source is a Ti:Sapphire pulsed laser. The sample is mounted inside a cryostat on an XY stage, which can be positioned manually. The objective lens is mounted on a piezoelectric XYZ stage allowing precise positioning of the laser spot under software control. The spectrometer output can be directed either to a CCD camera for spectral acquisition or to an APD connected to a photon counter for time-resolved measurements, selected via a built-in slit. 27

2.2 **A photograph of the μPL system.** 1: The 400 nm fs pulsed laser as the excitation source. 2: The optical components, including the path of the LED and the optics for the $4f$ system for accurate imaging, and the manual xy stage on which the cryostat with the sample lies. 3: The spectrometer with CCD aligned to an output slit. 4: The temperature control module, connected to the temperature sensor in the cryostat. 28

2.3 **A schematic diagram of a $4f$ system.** 33

2.4 **A diagram of diffraction by a plane grating.** 37

2.5 **Simulated focal-plane intensity distribution under high-NA focusing, based on scalar Debye approximation.** 41

2.6 **A 2D mapping where the sample surface is out of focus.** The color at each pixel presents the integral of the PL at this spot. This is a 50 μm by 50 μm scan with a step of 1 μm in both axes. The sample used here was perovskite NWs. 42

2.7 **Diagram showing the TRPL aqcuisition process.** The sync signal could be chased either by the pulsed electrical output from PicoQuant driver directly when connected to TCSPC card, or by introducing a diode detector to record the Ti:Sapphare laser pulses. 44

2.8 **Measured instrument response function of the APD.** The IRF signal was measured in experiments using the sample surface reflection of second harmonic laser pulses. A Gaussian fitting was applied to the IRF, yielding a FWHM of 61.4 ± 1.1 ps. 46

2.9 **Schematic illustration of Ag NP formation within superfluid He droplets.** (a) *xyz* manipulator. (b) nozzle. (c) skimmer. (d) pick up region including a alumina oven with silver inside. (e) deposition station. This work was conducted by the group of Prof. Shengfu Yang at the University of Leicester. 48

2.10 **AFM image of a sample with He droplet synthesized CdS NPs projected to a silicon substrate. The image was collected by the group of Prof. Shengfu Yang at the University of Leicester.** 49

3.1 **Proposed Ag NP–perovskite NW hybrid nanostructure.** (a) Artistic view of the hybrid nanostructure. (b) Left: Simplified 2D model for the four-layer structure. Right: Three panels showing the corresponding spatial distribution for E_z, E_y and $|E_{\mathrm{tot}}|^2$ for the hybridised plasmonic eigenmode at 520 nm. (c,d) Electric intensity $|E_{\mathrm{tot}}|^2$ along the vertical y-axis without and with the PMMA interlayer, respectively. This simulation was conducted by Dr. Xavier Romain. 58

3.2 **TEM images of $CsPbBr_3$ NWs with different reaction time and different centrifugation time.** (a–d) TEM images of NW with reaction time of (a) 15 min; (b) 30 min; (c) 45 min; (d) 60 min. (e–g) TEM images of NWs with different centrifugation times. The TEM images presented here were collected by the group of Prof. Shengfu Yang at the University of Leicester. 61

3.3 **RT absorption and PL of** $CsPbBr_3$ **Nanowires.** The PL was measured from a drop-cast thin film, whereas the absorption spectrum was acquired in solution at a relatively high concentration. 62

3.4 **Characterization of He droplet synthesized Ag NPs.** (a) TEM image of the Ag NPs dropcasted on the TEM grid. (b) The size distribution of the Ag NPs on Si substrate. The red curve refers to a normal distribution fitted to the histogram and shows an average of 6.97 nm. (c) UV–Vis absorption spectrum of the Ag NPs on Si substrate. The data presented in this figure were collected by Hao Sha from the group of Prof. Shengfu Yang at the University of Leicester. 63

3.5 **Characterization of wet chemically synthesized Ag NPs.** (a) TEM image of the Ag NPs deposited on the TEM grid. (b) The size distribution of the Ag NPs on Si substrate. The red curve refers to a normal distribution fitted to the histogram and shows an average of 7.95 nm. The data presented in this figure were collected by Hao Sha from the group of Prof. Shengfu Yang at the University of Leicester. 63

3.6 **AFM measurements of PMMA layer thickness obtained from solutions with different concentrations.** Different PMMA solutions were spin-coated onto silicon substrates, with scratches introduced to enable thickness determination. The data presented in this figure were collected by Hao Sha from the group of Prof. Shengfu Yang at the University of Leicester. 65

3.7 **Power dependence of PL spectra of $CsPbBr_3$ NWs at 4 K under pulsed excitation (400 nm), comparing two sample configurations** (a) NWs spin-coated directly on bare Si. (b) NWs spin-coated on a PMMA-covered Si substrate. In the NWs/PMMA/Si sample, two emission features are partially resolved, with a main peak at ∼529 nm and a weaker shoulder at ∼532 nm. The NWs/Si sample exhibits a single broader and asymmetric peak, suggesting a superposition of the same emission components without spectral resolution. 68

3.8 **RT PL of $CsPbBr_3$ NWs.** The samples were the same as in Figure 3.7. The peak centre were at 520 nm for both samples, with the fitted FWHM of ∼19 nm for the sample without PMMA and 20 nm for the one with PMMA, indicating a similar peak profile that is barely influenced by the PMMA layer at RT. 70

3.9 **Log–log plot of integrated PL intensity as a function of excitation power at 4 K, from the NWs/PMMA/Si structure.** The near-linear dependence (slope = 0.79, R^2 = 0.996) indicates localized-excitonic recombination dominates the emission process, with minimal contribution from free-carrier processes. 73

3.10 **Diagram showing DOS versus energy in this model.** Excitons can be excited to the free exciton state (purple area), or localized in the discrete localized states (black bars in green area). Different pathways including radiative recombination are indicated. As illustrated in this diagram, spatial and energetic disorder leads to a distribution of localized exciton states, resulting in inhomogeneous broadening and variations in the PL peak position across the sample. This figure is adapted from Ref. [191] with modifications and used with permission. 75

3.11 **TRPL of NWs under 4 K.** Different time regions highlighted in the figure referring to different dynamics. Yellow: localized excitons. Blue: traps. The lifetime for the single exponential region was fitted to 59.8 ps with IRF deconvoluted. 77

3.12 **PL and TRPL of NW/Si, NW/Ag/Si and NW/PMMA/Ag/Si structures at 4 K.** PL and TRPL at different positions showcased the enhancement from Ag NPs. More positions were investigated and estimated enhancement factor was ~ 4 for only introducing Ag NPs and ~ 29 for the full structure. 84

3.13 **Room-temperature PL spectra and their temporal evolution.** (a–c) Position-dependent PL spectra of NW/Si, NW/Ag/Si, and NW/PMMA/Ag/Si, respectively. Each spectrum exhibits a Gaussian profile; fitted curves and extracted parameters are labeled accordingly. For NW/PMMA/Ag/Si, a power-dependent measurement was performed, while for NW/Si and NW/Ag/Si the excitation power was fixed at 4 μW. (d–f) PL time series measurements for the corresponding samples. The excitation power was measured 400 μW. Note: ND filters were applied during the time series acquisition; as a result, the absolute PL intensities differ from the counts shown in the spectra. All experiments were conducted in air, rather than under vacuum. 87

3.14 **AFM image of Ag NPs coated Si substrate.** The bright dots refer to the Ag NPs. The image was collected by the group of Prof. Shengfu Yang at the University of Leicester. 90

3.15 **Optimizing parameters by investigating multiple configurations under larger excitation area.** (a–c) Power-dependent μPL spectra taken at three different positions on the hybrid device. At position 3, the individual emission lines form several single NWs that can be resolved in the spectra. (d) Position-dependent PL peak intensity as a function of excitation fluence on the hybrid device. (e,f) Optimization of device parameters by varying the Ag NP size and PMMA layer thickness. 92

3.16 **Enhanced PL for optimized parameters.** (a,b) μPL spectra from bare NW sample and the optimized device configuration under 4 K. Multiple PL emission spectra were presented to show the highly position dependence. (c,d) 2D mapping on bare NWs and hybrid metal-perovskite NWs respectively. 94

3.17 **Comparison of TRPL for various device configurations.** . . 96

4.1 **Crystal structures of HCP, BCC, and FCC lattices.** Schematic representations of the conventional unit cells of hexagonal close-packed HCP, body-centered cubic BCC, and face-centered cubic FCC structures. The line frames represent unit cells. The lattice parameters are taken from Mg (HCP), K (BCC), and Au (FCC), respectively. 104

4.2 **Finite-element simulations of plasmonic enhancement in a Mg–$\mathbf{CsPbBr_3}$ NW hybrid structure.** (a) Schematic and cross-sectional field distribution showing strong localized field distribution at the NW–NP interface. (b) Wavelength-dependent enhancement factor of $|E_z|^2$. The simulations were conducted by Dr. Xavier Romain. 106

4.3 **Colloidal Mg NPs synthesized in different sizes.** (a–e) SEM images demonstrating progressive size increase. (f) STEM image of an individual hexagonal platelet synthesized under similar conditions, exhibiting a $\sim$10 nm self-limiting oxide shell [224]. The data presented in this figure were collected by Christina Boukouvala from the group of Prof. Emilie Ringe at the University of Cambridge. 108

4.4 **Size-dependent optical absorption of colloidal Mg NPs.** (a) Normalized UV-vis absorption spectra of the series used in the chapter. (b) Corresponding mean diameters and size distributions. The data presented in this figure were collected by Christina Boukouvala from the group of Prof. Emilie Ringe at the University of Cambridge. . . 110

4.5 **Comparison of emission from NWs grown with and without AC electric field.** (a) μPL spectra on both samples (w and w/o electric field) with three different positions at the same excitation condition, corresponding peak intensity in counts labelled. (b) Corresponding TRPL of the PL peaks in the low excitation regime. 112

4.6 **2D mapping of the EF and reference samples.** (a–b) 2D PL mappings over a $50 \times 50\,\mu\text{m}^2$ area of (a) the EF sample and (b) the reference sample. The colour scale represents the integrated PL intensity in the range of 500–550 nm. (c) Integrated PL intensity over the entire mapped area. The repetitive fluctuations originate from the relatively low signal-to-noise ratio of this setup. All mappings were performed using a 450 nm CW diode laser with a power density of 1.27 W/cm^2. 115

4.7 **RT measurements of the Mg–NW hybrid structure with Mg NPs AT81–104.** (a) μPL investigation on the hybrid structure. Blue dots: PL peak intensities as a function of Mg NP size; red dots: spectral peak centres for varying NP size. Both PL enhancement and peak shift are simultaneously observed in sample AT81–83. (b) PL lifetimes of the corresponding samples obtained from bi-exponential fitting. Green triangles: weighted average lifetime [234]; purple diamonds: fast-component lifetime. (c) TRPL decay curves for all seven samples, including the NW-only reference sample. 117

4.8 **Comparison of spectral profiles at RT and 4 K, with and without Mg NPs.** (a–b) RT PL spectra of (a) the bare NW sample and the (b) Mg–NW hybrid structure, shown here for AT84 Mg NPs with a mean diameter of 98 nm as an example. (c–d) 4 K PL spectra of the corresponding samples. Note that the labels '1, 2, 3' mark different excitation spots within the same panel; thus, AT84 1 at RT and at 4 K do not necessarily represent the identical spatial position. 120

4.9 **4 K measurements of the Mg–NW hybrid structure with Mg NPs AT81–104.** (a) μPL results on the hybrid structure. Blue dots: PL peak intensities as a function of Mg NP size; red dots: spectral peak shifts with varying NP size. An overall red-shifting compared to RT emissions was observed, indicating the transition in PL mechanism. (b) TRPL decay curves at 4 K for all seven samples, including the NW-only reference sample. The long lifetime component is significantly stronger at 4 K 122

4.10 **PL measurements on SiO_2 coated Mg NPs at RT.** (a) UV-Vis absorption spectra of SiO_2 coated AT83 (mean diameter 90 nm) and AT84 (mean diameter 98 nm) Mg NPs. The green shade area indicates the emission from NWs. (b–d) μPL spectra at RT from (b) the reference and (c–d) coated Mg NPs AT83 (blue) and AT84 (red), respectively. Different color brightness in each plot represent different positions. (e) TRPL at RT. The excitation was 7.6 MHz, with a fluence of 16.8 $\mu J/cm^2$. 124

4.11 **Comparison of PL enhancement by SiO_2-coated Mg and Ag NPs.** (a) PL spectra of hybrid structures with SiO_2-coated Mg NPs AT83 (90 nm) and AT84 (98 nm), and Ag NPs (80 nm). (b) UV–Vis absorption spectra of the corresponding metal NPs. (c) TRPL decay curves at RT. The excitation repetition rate was 7.6 MHz with a fluence of 16.8 $\mu J/cm^2$. 127

4.12 **2D mapping of hybrid structures with statistical analysis.** Spatial PL mapping and the corresponding histograms of extracted bright pixels with peak intensity for (a) NW-only, (b) NW with SiO_2-coated AT83 (mean diameter 90 nm) Mg NP, and (c) NW with SiO_2-coated AT84 (mean diameter 98 nm) Mg NP samples. 128

5.1 **Summary of PL peak ranges for $CsPbI_3$ NPLs with n = 3–6 MLs.** PL peak positions are inferred from Ref. [257]. A schematic illustration of NPLs with different number of MLs is shown below. . 133

5.2 **Normalized PL spectra of $CsPbI_3$ NPLs synthesized at (a) 0 °C, (b) 23 °C, (c) 40 °C, and (d) 60 °C, with the corresponding Cs(oleate) injection volumes indicated.** 134

5.3 **TEM images of NPL with different layer numbers.** The images were collected by the group of Prof. Robert Hoye at the University of Oxford. 136

5.4 **Design and fabrication of periodically arranged Si pillar nanocavities.** (a) Layout of the nanocavity array, with each block consisting of a periodic arrangement of Si pillars. The inset shows an enlarged view of block B1. The three sets of arrays are defined as C1–5, B1–5, and A1–5, corresponding to pillar diameters of 190 nm, 180 nm, and 170 nm, respectively. (b) Schematic illustration of a single Si pillar nanocavity. (c) Optical microscope image of the patterned arrays at 5× magnification. (d) Optical microscope image at 100× magnification, resolving the periodic pillar arrangement within an individual block (C5). 138

5.5 **Spin-coated NPLs on nanocavity arrays for μPL measurements.** Inset: white-light microscope image from the μPL setup, showing the measurement region (C5) with nanopillars of 190 nm diameter. 139

5.6 **Normalized PL spectra of $CsPbI_3$ NPLs.** The μPL measurements were performed under 400 nm excitation at a fluence of $0.17\,\mathrm{mJ\,cm^{-2}}$. 140

5.7 **Normalized UV–Vis absorption spectra of $CsPbI_3$ NPLs with different thicknesses.** (a) $n = 2$, (b) $n = 3$, (c) $n = 4$, and (d) $n = 6$. Pronounced excitonic absorption peaks are observed for thin NPLs, which gradually weaken and broaden with increasing thickness. The $n = 5$ data are missing, due to the high level of impurities in the corresponding NPLs. 141

5.8 **XRD patterns of $CsPbI_3$ NPLs with different thicknesses.** (a–d) XRD patterns of n =3, 4, 5, and 6, respectively. The reflections marked with black * correspond to the black-phase perovskite peaks at 14.1° ((100) plane) and 28.2° ((200) plane). Additional features marked with orange * in panels (a) and (b) suggest the presence of a secondary phase. The XRD data were collected by Charlie Nicholls from the group of Prof. Robert Hoye at the University of Oxford. . 143

5.9 **TRPL decays of $CsPbI_3$ NPLs with different thicknesses.** (a–d) TRPL traces of n = 3–6 NPLs measured under excitation fluences of 0.17, 0.34, 0.67, and 1.68 mJ/cm^2, respectively. 144

5.10 **PL spectra of $CsPbI_3$ NPLs with and without the nanocavity.** 145

5.11 **Cavity-induced PL spectral shaping and spatial loading of $CsPbI_3$ NPL.** (a) Normalized PL of $CsPbI_3$ NPLs measured on nanocavity regions of different pillar diameters and on reference regions. (b) Simulated optical response of nanocavities with varying pillar diameters. (c) Optical microscope images of on-cavity and off-cavity regions; the excitation (laser) spot is indicated. The simulations shown in panel (b) were conducted by Dr. Mengyun Wang 146

5.12 **TRPL of $CsPbI_3$ NPLs on- and off-cavity.** Excitation at 400 nm with a fluence of 0.34 mJ/cm^2. 147

B.1 **Reflection spectra of Si pillar nanocavities.** Arrays with different pillar diameters are shown for the A, B, and C series (A3–5: 170 nm; B3–5: 180 nm; C3–5: 190 nm), in comparison with a bare Si substrate, a platinum-coated reference (Pt_ref), and the dark background signal. These modulations arise from guided-mode resonances induced by the lateral index modulation, and spectrally overlap with the emission band of $CsPbI_3$ NPLs, confirming that the designed nanocavity arrays can provide optical feedback near the perovskite PL wavelength. The data presented in this figure were collected by Dr. Mengyun Wang 157

List of Abbreviations

0D, 1D, 2D, 3D	Zero, one, two or three-dimensional, referring in this thesis to spatial dimensions of the nanostructure.
AC	Alternating current
APD	Avalanche photodiode
BBO	Beta-barium borate
BCC	Body-centered cubic
CB	Conduction band
CBM	Conduction band minimum
COM	Centre-of-mass
DOS	Density of states
FCC	Face-centered cubic
FWHM	Full width at half maximum
HCP	Hexagonal close-packed
hBN	Hexagonal boron nitride
IR	Infrared
IRF	Instrument response function
LDOS	Local density of optical states
LO	Longitudinal optical (phonon)
ML	Monolayer
NA	Numerical aperture
NC	Nanocrystal
NP	Nanoparticle
NPL	Nanoplatelet
NSET	Nanometal surface energy transfer
NW	Nanowire

OA	Oleic acid
OAm	Oleylamine
ODE	Octadecene
OLA	Oleylamine
PL	Photoluminescence
PLQY	Photoluminescence quantum yield
PMMA	Poly(methyl methacrylate)
PMT	Photomultiplier tube
RT	Room temperature
SET	Surface energy transfer
SERS	Surface-enhanced Raman scattering
SHG	Second-harmonic generation
SRH	Shockley–Read–Hall
STE	Self-trapped exciton
TCSPC	Time-correlated single-photon counting
TEM	Transmission electron microscopy
TMD	Transition metal dichalcogenide
TRPL	Time-resolved photoluminescence
UV	Ultraviolet
UV–Vis	Ultraviolet–visible
VB	Valence band
VBM	Valence band maximum
XRD	X-ray diffraction
μ**PL**	Micro-photoluminescence

List of Publications

- Kuriakose, Tintu, Hao Sha, Qingyu Wang, Gokhan Topcu, Xavier Romain, Shengfu Yang, and Robert A. Taylor. Plasmon-Enhanced Photo-Luminescence Emission in Hybrid Metal–Perovskite Nanowires. Nanomaterials, **15**(8), 608, 2025.
- Junzhi Ye, Charles Nicholls, Kieran De-Ville, Rui Xu, Zongming Ni, Qingyu Wang, Jielin Tan, Eilidh L. Quinn, Maxime Atkinson, Wei Zhang, Haitao Zhao, Robert A. Taylor, Yunwei Zhang, Robert L. Z. Hoye. Stronger Lewis Base Antisolvents Improve Perovskite Nanocrystal Stability. (Submitted)
- Qingyu Wang, Christina Boukouvala, Tintu Kuriakose, Xavier Romain, Emilie Ringe, Robert A Taylor. Enhanced Photoluminescence in Perovskite Nanowires using Plasmonic Mg Nanoparticles at Room Temperature. (Submitted)

1

Introduction

Contents

1.1 Scope and Organization 1
1.2 CsPbX$_3$ Metal Halide Perovskite Materials 2
  1.2.1 Structure 3
1.3 PL of Low-Dimensional Perovskite Nanostructures . . 8
  1.3.1 Low-Dimensional Perovskite and Quantum Confinement 8
  1.3.2 Formation of Excitons 10
  1.3.3 Excitonic Recombination 13
  1.3.4 Recombination Dynamics 16
1.4 Plasmon-enhanced PL Emission 17
  1.4.1 Localized Surface Plasmonic Resonance 17
  1.4.2 LSPR-enhanced PL 19
  1.4.3 Metals as Plasmonic Materials 21

1.1 Scope and Organization

This thesis focuses on understanding and tailoring exciton dynamics in lead halide perovskite nanostructures through their interaction with plasmonic and photonic resonances. The scope covers both fundamental aspects of light–matter coupling and practical strategies to enhance photoluminescence (PL) efficiency, by employing the localized surface plasmon resonances (LSPRs) of metal nanoparticles (NPs) as well as dielectric nanocavities. Special emphasis is placed on how different resonances affect excitonic recombination pathways and spectral characteristics in different environments.

The thesis is organized as follows. Chapter 1 describes the crystal and energy structure of perovskite materials and their optical properties. It continues with a discussion of plasmonics and the interaction of light with metals. Chapter 2 introduces the experimental techniques used throughout this work, including sample preparation, optical characterization, and low-temperature spectroscopy methods. The subsequent three chapters present the main experimental studies. Chapter 3 investigates Ag NP enhanced PL of $CsPbBr_3$ nanowires (NWs) at cryogenic temperature (4 K), where excitonic features can be spectrally resolved. Chapter 4 extends the study to Mg NPs, demonstrating room temperature (RT) PL enhancement of $CsPbBr_3$ NWs and assessing Mg as a low-cost alternative plasmonic material. Chapter 5 shifts the focus from plasmonic enhancement to photonic confinement, employing a two-dimensional (2D) nanocavity to couple with the emission of $CsPbI_3$ nanoplatelets (NPLs). This transition provides a direct comparison between plasmonic and cavity-based strategies, highlighting the general principles of resonant control in perovskite nanostructures.

Together, these studies establish a comprehensive framework for understanding how plasmonic and photonic resonances can manipulate excitonic emission in perovskite nanomaterials, offering both fundamental insights and practical guidelines for future optoelectronic applications.

1.2 $CsPbX_3$ Metal Halide Perovskite Materials

All-inorganic perovskite nanocrystals (NCs), such as $CsPbX_3$ (X = Cl, Br, I), have attracted sustained attention owing to their exceptional optoelectronic properties. Their band structures can be precisely tuned, enabling absorption and emission across the ultraviolet (UV) to the near-infrared (IR) region [1]; a high degree of defect tolerance suppresses non-radiative recombination and underpins their remarkable optical stability [2, 3]. In addition, all-inorganic perovskite NCs exhibit high charge-carrier mobilities and long diffusion lengths, which are favourable for efficient charge transport in optoelectronic devices [4–7]. Their exceptionally high photoluminescence quantum yield (PLQY), often approaching unity, further enables highly efficient photonic energy transfer [8–10]. Collectively, these properties establish all-inorganic perovskite NCs as promising materials for a wide range of applications, including light-emitting diodes, lasers, and photovoltaics.

This thesis mainly focuses on low-dimensional all-inorganic perovskite NCs, typically $CsPbI_3$ and $CsPbBr_3$, and presents a general background on the crystal structure of perovskites, their phase stability, and the unique optoelectronic properties that make them attractive for fundamental studies and practical applications.

1.2.1 Structure

Crystal structure

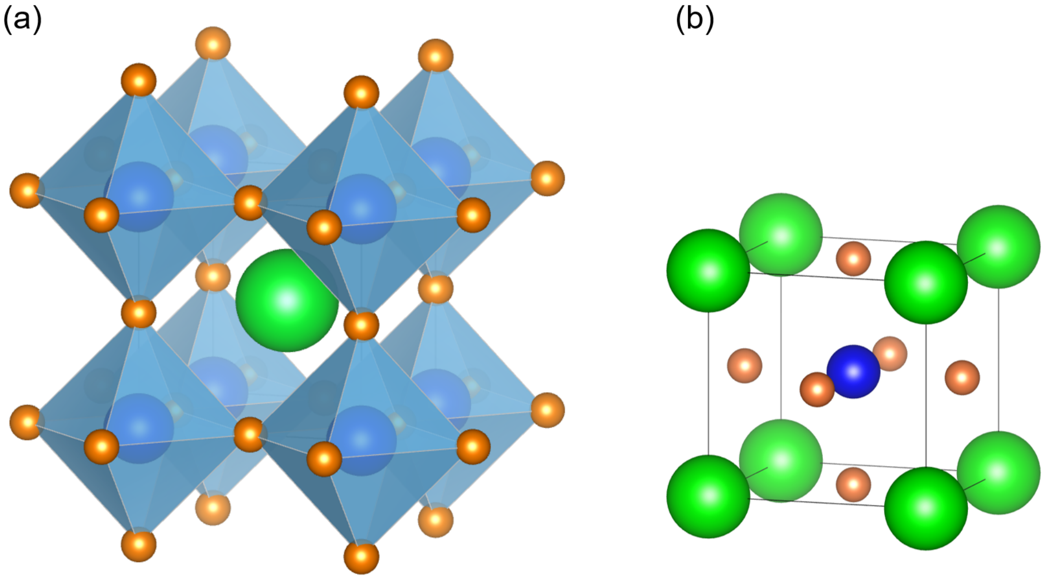

Figure 1.1: Crystal structure of cubic perovskite $CsPbX_3$ (space group $Pm\bar{3}m$). (a) Corner-sharing BX_6 octahedral network. (b) Schematic representation of the unit cell, where A-site cations (green) occupy the cube corners, B-site cations (blue) are located at the body centre, and halide anions (orange) reside at the face centres.

Perovskite refers to a class of materials originally named after $CaTiO_3$, and is generally described by the chemical formula ABX_3. In lead halide perovskites, the A-site and B-site cations typically carry charges of +1 and +2, respectively, while X represents an anion with a -1 charge. The crystal structure can be exemplified by Pb-based halide perovskites as presented in Figure 1.1: the B-site cation resides at the body centre of the cubic cell, coordinated by six X-site anions at the face centres to form a BX_6 octahedron, while the A-site cations occupy the eight cube corners. This highly symmetric framework serves as the parent structure from which a wide range of structural variations and property tunability arise, making halide perovskites particularly versatile for optoelectronic applications.

In real materials, however, deviations from this ideal stoichiometry are common. Vacancies at the A-, B-, or X-sites, as well as interstitials or antisite defects, can occur during synthesis or under external stimuli [11, 12]. These point defects not only modify the local coordination environment but can also influence the overall structural stability, electronic band structure, and carrier dynamics [12, 13]. The remarkable defect tolerance of halide perovskites allows them to maintain high optical quality despite the presence of such imperfections.

Unit cell and symmetry

The unit cell of an ideal perovskite adopts a highly symmetric cubic geometry, described by the space group $Pm\bar{3}m$ (often referred to as the α-phase), as shown in Figure 1.1.

The lattice constant a for cubic perovskite phase ($Pm\bar{3}m$) is set by $a \approx 2(r_\mathrm{B}+r_\mathrm{X})$ while the A-site cation must fit into the cuboctahedral cavity at the cube corner with $r_\mathrm{A} \approx \sqrt{2}\,a/2 - r_\mathrm{X}$. r_A, r_B, and r_X are the ionic radii of the A-site cation, B-site cation, and X-site anion, respectively.

The strong ionic bonding favours the formation of a cubic symmetry. Lower-symmetry perovskite polymorphs, such as tetragonal or orthorhombic phases, can arise from octahedral tilting and distortion. Under certain environmental conditions, more severe distortions may further drive phase transitions into non-perovskite structures or even lead to structural decomposition. A detailed discussion of the phase transitions in $CsPbBr_3$ and $CsPbI_3$ will be presented later. The electronic properties of perovskites are primarily governed by the B–X interactions, while the A-site cation, although not directly contributing to the band structure, plays a crucial role in charge balance and in stabilizing the framework through electrostatic interactions with the surrounding BX_6 octahedra [14]. The tuning of the A-site sizes also influences the tilting and distortion of the corner-sharing BX_6 octahedra, and thus modifies the lattice constant and the B–X–B bond angle, thereby enabling indirect band gap engineering and adjustment of the optical properties [15, 16].

Not all ternary metal halides can form stable perovskite structures, since the size of the A-site cation plays a decisive role in maintaining the ABX_3 stability. This effect was first introduced by Goldschmidt through the tolerance factor (t) [17], and was later complemented by the octahedral factor (μ) [18, 19]. These factors are defined as follows:

$$t = \frac{r_\mathrm{A} + r_\mathrm{X}}{\sqrt{2}(r_\mathrm{B} + r_\mathrm{X})},$$

$$\mu = \frac{r_\mathrm{B}}{r_\mathrm{X}}$$

Empirically, stable three-dimensional (3D) perovskite phases are most often formed when $0.8 \lesssim t \lesssim 1.0$ and $0.44 \lesssim \mu \lesssim 0.90$ [20]. If the A-site cation is too small or too large, the lattice tends to distort or collapse, leading instead to lower-dimensional or non-perovskite structures.

The tolerance factors reported for $CsPbCl_3$, $CsPbBr_3$ and $CsPbI_3$ are 0.87, 0.86, and 0.81 respectively, denoting the specific low ambient phase stability for $CsPbI_3$ at cubic phase [21, 22].

In practice, only three A-site cations have been found to individually sustain stable 3D lead halide perovskites: caesium (Cs^+), methylammonium (MA^+), and formamidinium (FA^+) [23, 24]. Other cations can occasionally be incorporated, typically in mixed compositions or under special structural constraints. For example, partial substitution with rubidium (Rb^+) or potassium (K^+) has been shown to improve stability in mixed-cation perovskites [25–27], while bulky organic cations (e.g., butylammonium) are well known to stabilize low-dimensional Ruddlesden–Popper phases rather than true 3D frameworks [28, 29]. Ruddlesden–Popper phases are layered, perovskite-derived structures consisting of finite slabs of corner-sharing BX_6 octahedra separated by additional rock-salt–type AX layers, as first described by Ruddlesden and Popper [30, 31]. These observations highlight the delicate balance between ionic size and structural stability, as governed by the tolerance factor, in determining whether a ternary halide forms a stable perovskite lattice.

Band edge energies

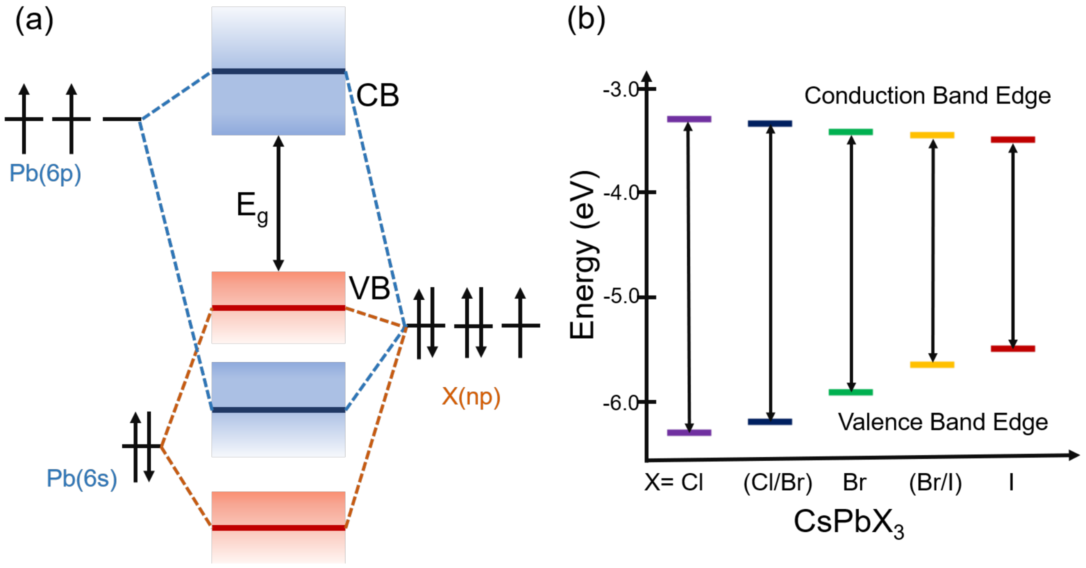

Figure 1.2: Electronic band structure and halide-dependent band alignment of all-inorganic $CsPbX_3$. (a) Diagram illustration of orbital hybridization in Pb-based perovskites, where the conduction band (CB) is mainly derived from Pb(6p) orbitals, and the valence band (VB) originates from the antibonding interaction between Pb(6s) and X(np). (b) Tuning of band gap energy by varying the halide composition (X = Cl, Br, I), showing the systematic shift of conduction and valence band edges. Adapted from [32] with permission.

The electronic band structure of all-inorganic halide perovskites is generally determined by the B-site metal cation and the halide anion. The conduction band minimum (CBM) is typically derived from the metal cation np orbitals (e.g., Pb 6p, Sn 5p, Ge 4p), while the valence band maximum (VBM) arises from the antibonding interaction between the cation states and the halide np orbitals [33, 34]. In the widely studied class of Pb-based $CsPbX_3$ (X = Cl, Br, I), for example, the CBM originates mainly from Pb(6p) orbitals, and the VBM is formed by hybridization between Pb(6s) and X(np) states, as illustrated in Figure 1.2(a).

Most Cs-based perovskite NCs exhibit a direct band gap, which facilitates efficient radiative recombination and accounts for their strong absorption and remarkably high PLQY [1]. Nevertheless, a weak indirect character has been reported in distorted phases, arising from symmetry breaking and slight shifts of the band extrema induced by the Rashba effect [35, 36]. This minor energetic offset can be thermally overcome, and $CsPbX_3$ thus generally retains the optical characteristics of a direct band gap semiconductor.

The band gap energy can be tuned through halide substitution, with the CBM and VBM shifting systematically depending on the halide ionic radius, as shown in Figure 1.2(b). The degree of antibonding mixing of the anion orbital in the VBM will decrease from Cl to Br to I because the anion p levels move upward, which explains the decreasing trend of the gaps from Cl to I. Experimentally, the optical band gap is reported to be approximately 3.0 eV for $CsPbCl_3$ (~ 410 nm), 2.3 eV for $CsPbBr_3$ (~ 540 nm), and 1.7 eV for $CsPbI_3$ (~ 730 nm) [1, 9]. This wide tunability across the visible spectrum makes all-inorganic halide perovskites highly attractive for optoelectronic applications ranging from light-emitting diodes to solar cells.

Phase transition

Beyond the ideal cubic lattice, halide perovskites adopt a variety of lower-symmetry phases, driven primarily by collective tilting of the BX_6 octahedra. These transitions govern not only symmetry lowering but also the stability window of the perovskite phase.

Three photoactive phases, namely cubic (α, $Pm\bar{3}m$), tetragonal (β, $P4/mbm$) and orthorhombic (γ, $Pbnm$) exhibit corner sharing octahedra framework, and are collectively referred to as the black phases. In contrast, the non-photoactive phase δ-phase, which is referred as non-perovskite structure, could still retain orthorhombic or trigonal symmetry with edge sharing octahedra [37–39]. Although the α-phase exhibits the highest symmetry and is most desirable for optoelectronic applications, it readily transforms into the thermodynamically stable δ-phase at RT [40]. The instability of the perovskite phase in the bulk at RT is primarily intrinsic, arising from factors such as lattice strain and ionic size mismatch, which increase the free energy and destabilize the phase. Efforts have been made to stabilize the α-phase, including surface passivation strategies [41] and exploiting the high surface-to-volume ratio of NCs [42]. Surface passivation employs surface ligands to externally stabilize the crystal structure, even when the perovskite lattice cannot intrinsically sustain the preferred high-symmetry phase. A higher surface-to-volume ratio, corresponding to an increased fraction of surface atoms, allows lattice strain accumulated in the bulk to be partially relieved at the surface, thereby lowering the total strain energy and enabling the perovskite phase to persist.

Table 1.1: Reported phase transitions of $CsPbBr_3$ single crystals with corresponding temperature ranges and stable polymorphs [43, 44].

Temperature Range (K)	**Stable Phase**	**Bandgap (eV)**
< 380	Orthorhombic (γ)	2.32–2.36
$\sim$380 – $\sim$403	Tetragonal (β))	$\sim$2.37
> 403	Cubic (α)	$\sim$2.38

Table 1.2: Reported phase transitions of $CsPbI_3$ with corresponding temperature ranges and stable polymorphs [38].

Temperature Range (K)	**Stable Phase**	**Bandgap (eV)**
< 610 (heating)	Non-perovskite (δ)	
> 610 (heating), > 550 (cooling)	Cubic (α)	1.73
450–550 (cooling)	Tetragonal (β)	
< 450 (cooling)	Orthorhombic (γ)	

Table 1.1 and 1.2 present the summarized transition temperature and the corresponding phase for $CsPbBr_3$ and $CsPbI_3$ respectively.

1.3 PL of Low-Dimensional Perovskite Nanostructures

1.3.1 Low-Dimensional Perovskite and Quantum Confinement

The reduction in dimensionality makes a substantial difference to the optical properties of halide perovskites. Even though bulk 3D perovskites already exhibit favourable PL characteristics, their low-dimensional counterparts, such as zero-dimensional (0D) quantum dots (QDs), one-dimensional (1D) NWs and 2D thin films have attracted particular attention in recent years [45–50]. In this thesis, the focus is placed on the PL of perovskite NWs and NPLs, with typical sizes on the order of tens of nm. At this size scale, although the inherent emission properties remain nearly unchanged relative to the basic ABX_3 composition [51, 52], their emission properties deviate significantly from those of classical bulk semiconductors due to the pronounced influence of quantum confinement.

In low-dimensional perovskites, strong quantum and dielectric confinement yield large exciton binding energies, typically tens of meV, so PL is dominated by excitonic recombination even at RT [53], unlike the case in bulk 3D perovskites where the exciton binding energy is only a few meV, and excitons are thermally ionized at RT with the thermal energy $k_{\mathrm{B}}T \approx 26\,\mathrm{meV}$, thus PL governed by free carrier recombination.

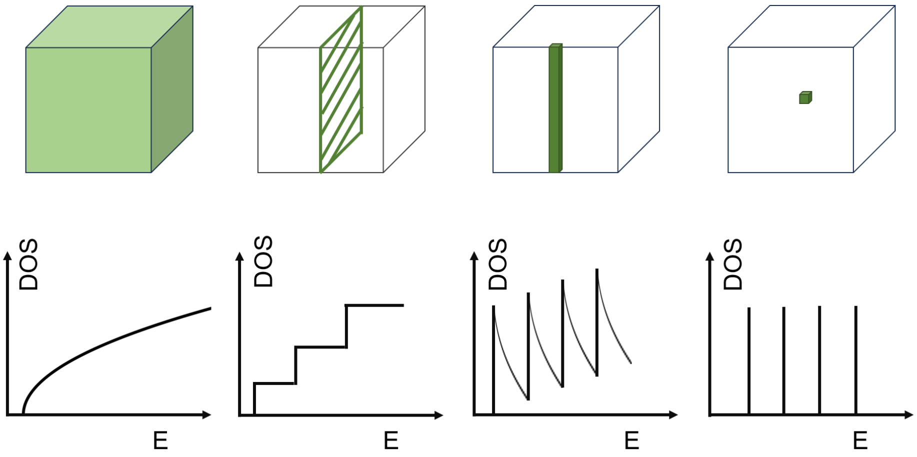

Figure 1.3: Schematic density of states (DOS) in 3D, 2D, 1D, and 0D systems.

Within the free-electron approximation, the density of states (DOS) takes distinct forms in different dimensions. As illustrated in Figure 1.3, $\mathrm{DOS}_{\mathrm{3D}}(E) \propto \sqrt{E}$ increases smoothly with energy; $\mathrm{DOS}_{\mathrm{2D}}(E)$ is constant within each sub-band and exhibits a stepwise increase; $\mathrm{DOS}_{\mathrm{1D}}(E) \propto 1/\sqrt{E - E_n}$ shows singularities at the sub-band edges; $\mathrm{DOS}_{\mathrm{0D}}(E)$ collapses into a set of discrete δ-functions. These DOS characteristics directly affect the strength of Coulomb interactions and thus the exciton binding energies. Thus, the progressive evolution of DOS from 3D to 0D provides the fundamental basis for the enhancement of exciton binding energies in low-dimensional semiconductors.

The following sections will discuss in detail how quantum confinement modifies the electronic band structure of perovskites, resulting in the enhancement of exciton binding energies and the characteristic excitonic emission features observed in low-dimensional perovskite systems.

1.3.2 Formation of Excitons

When the low-dimensional perovskite is excited by incident light at an energy above the bandgap, electrons are promoted from the valence band to the conduction band, leaving corresponding holes in the valence band. Since the spatial limit restricts the free movement of the electron and holes, the strong overlap of both wavefunctions facilitates the bonding of the electron–hole pair, or, the formation of excitons. Empirically the strength of confinement can be evaluated by the Bohr radius of the exciton and the size of the nanostructure.

Excitons are Coulomb-bound electron–hole pairs formed in semiconductors upon optical excitation. Their properties can be described within the effective-mass hydrogenic model, in which the electron and hole interact via a Coulomb potential screened by the material's dielectric constant. The exciton Hamiltonian reads

$$H = -\frac{\hbar^2}{2\mu}\nabla^2 - \frac{e^2}{4\pi\varepsilon_0\varepsilon_\mathrm{r} r}, \tag{1.1}$$

where $\mu = m_\mathrm{e}^* m_\mathrm{h}^*/(m_\mathrm{e}^* + m_\mathrm{h}^*)$ is the reduced mass, ε_r the relative dielectric constant, and r the electron–hole separation. This analogy to the hydrogen atom leads to discrete exciton states with well-defined binding energies and radii.

The characteristic spatial extent of the bound electron–hole pair is the excitonic Bohr radius,

$$a_\mathrm{B}^* = \frac{4\pi\varepsilon_0\varepsilon_\mathrm{r}\hbar^2}{\mu e^2}, \tag{1.2}$$

which scales linearly with the dielectric screening and inversely with the reduced mass. In GaAs, $a_\mathrm{B}^* \sim 10\,\mathrm{nm}$, while in lead-halide perovskites $a_\mathrm{B}^* \sim 5$–$10\,\mathrm{nm}$, reflecting their stronger Coulomb binding due to reduced dielectric screening [1, 54].

Quantum confinement is expected whenever the physical dimension of the nanostructure L approaches or falls below a_B^*. For example, the 1D NWs in Chapter 3 feature one dimension of tens of μm and ∼20 nm for the other two dimensions, which means that the quantum confinement is in two dimensions and along the NWs there is no confinement. The NPLs in Chapter 5 feature a thickness of ∼5–10 nm, indicating a strong confinement in one dimension and a 2D model for such a system.

In close analogy to the hydrogen atom, the exciton binding energies form a Rydberg series.

$$E_n = -\frac{\mu e^4}{2(4\pi\varepsilon_0\varepsilon_\mathrm{r})^2\hbar^2}\cdot\frac{1}{n^2} = -\frac{e^2}{8\pi\varepsilon_0\varepsilon_\mathrm{r}a_\mathrm{B}^*}\cdot\frac{1}{n^2}, = -\frac{R_y^*}{n^2} \tag{1.3}$$

where

$$R_y^* = \frac{\mu e^4}{2(4\pi\varepsilon_0\varepsilon_\mathrm{r})^2\hbar^2} = \frac{\mu}{m_\mathrm{e}}\frac{1}{\varepsilon_\mathrm{r}^2}R_y \tag{1.4}$$

is the effective Rydberg constant, analogous to the hydrogen atom Rydberg constant $R_y = 13.6\,\mathrm{eV}$. The corresponding average electron–hole separation scales as

$$R_n \sim n^2 a_\mathrm{B}^*, \tag{1.5}$$

This leads to the simple scaling relation

$$E_n \sim -\frac{1}{R_n}, \tag{1.6}$$

The ground-state exciton binding energy in bulk semiconductors is therefore

$$E_\mathrm{b}^\mathrm{3D} = R_y^* = \frac{\mu}{m_\mathrm{e}}\frac{1}{\varepsilon_\mathrm{r}^2}R_y = \frac{e^2}{8\pi\varepsilon_0\varepsilon_\mathrm{r}a_\mathrm{B}^*} = -E_1, \tag{1.7}$$

with the radius $R_1 = a_\mathrm{B}^*$. The reduction of the exciton binding energy compared to hydrogen is primarily due to two factors: (i) the smaller effective mass of the exciton in a semiconductor compared to the free electron mass m_e; and (ii) the dielectric screening of the Coulomb interaction by the relative permittivity ε_r.

Furthermore, the formula for E_b varies in reduced dimensions, where the exciton binding energy is significantly enhanced due to stronger Coulomb interactions and weaker dielectric screening.

In strictly 2D systems such as quantum wells or thin films, the exciton spectrum becomes [54]

$$E_n^\mathrm{2D} = -\frac{R_y^*}{(n-\frac{1}{2})^2}, \qquad n = 1, 2, \ldots, \tag{1.8}$$

with the ground-state binding energy $E_\mathrm{b}^{\mathrm{2D}} = 4R_y^*$, i.e., four times larger than in 3D.

In 1D systems such as quantum wires, the Coulomb potential $V(x) \sim -e^2/|x|$ leads to a divergence in the idealized model. Therefore, there is no such universal formula for binding energy under 1D quantum confinement. However, an even higher binding energy of $E_\mathrm{b}^{\mathrm{2D}}$ over $8R_y^*$ has been reported in traditional semiconductor NW [55], implying an increase of confinement due to the reduction of dimensions.

In 0D QDs, the electron and hole are fully confined, and the exciton binding energy is governed by the dot size R. By solving the Schrödinger equation with the boundary conditions and for extremely small R, we have [56]

$$E_\mathrm{b}^{0D} \sim \frac{\pi \hbar^2}{2\mu R^2}. \tag{1.9}$$

Thus, when the dot radius becomes comparable to or smaller than a_B^*, the exciton binding energy can reach hundreds of meV, much larger than in the bulk [57].

Besides the relative motion of the electron–hole pair that gives rise to discrete exciton binding energies, an exciton can also move as a whole quasiparticle within the crystal. This centre-of-mass (COM) motion is characterized by a parabolic dispersion with respect to the exciton wave vector $\mathbf{K}$,

$$E_n(\mathbf{K}) = E_\mathrm{g} - E_\mathrm{X}(n) + \frac{\hbar^2 \mathbf{K}^2}{2M}, \tag{1.10}$$

where E_g is the band gap energy, $E_\mathrm{X}(n)$ the binding energy of the n-th exciton state, and $M = m_\mathrm{e}^* + m_\mathrm{h}^*$ the total exciton mass. Needless to say, the energy levels above the ground state are negligible in perovskites due to the line broadening by electron–phonon coupling, dynamic disorder or and structural inhomogeneities [58, 59].

For the ground state ($n = 1$), this reduces to

$$E_1(\mathbf{K}) = E_\mathrm{g} - E_\mathrm{b} + \frac{\hbar^2 \mathbf{K}^2}{2M}. \tag{1.11}$$

and the equation is nothing but the dispersion relation of a free exciton.

In lead halide perovskites, excitons are of the Wannier–Mott type, with Bohr radii (∼10 nm) much larger than the lattice constant (∼0.1 nm). This extended character allows the exciton to be regarded as a mobile quasiparticle that can propagate through the lattice, in close analogy to a free particle with effective mass M.

1.3.3 Excitonic Recombination

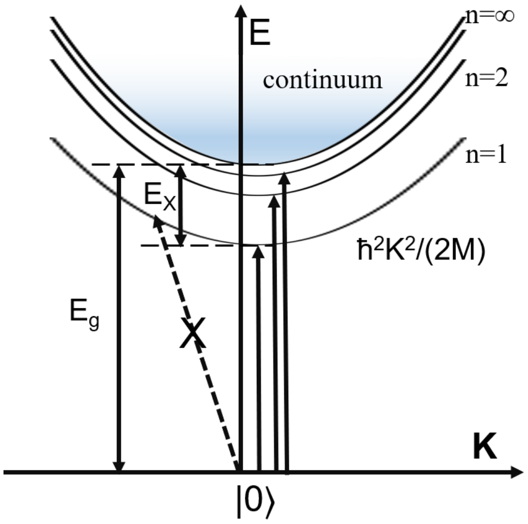

Figure 1.4: Schematic of the Wannier–Mott exciton with optical excitation.

Exciton absorption and emission can be regarded as inverse processes. In absorption, as noted with the arrows in Figure 1.4, because the photon momentum is several orders of magnitude smaller than the Brillouin zone dimensions, optical absorption can only create excitons with COM momentum $\mathbf{K} \approx 0$. Direct excitation of finite-$\mathbf{K}$ excitons is forbidden in the dipole approximation, as indicated by the crossed arrow.

In the PL process, excitons created at higher states or in the continuum relax non-radiatively into the ground state, and only those at $\mathbf{K} \approx 0$ can recombine radiatively, producing the dominant PL peak. It should be noted that optical excitation above the band gap also promotes electron–hole pairs directly into the continuum. These free carriers relax rapidly via phonon scattering, and part of them can be captured by Coulomb interaction to form bound excitons. Therefore, even under above-band-gap excitation, the PL spectrum is often dominated by the recombination of the ground-state exciton. In cases where exciton binding is weak or nonradiative channels dominate, continuum carriers may instead recombine directly across the band gap, producing a broad emission background.

Quantum confinement modifies this picture by compressing the exciton in real space, which, according to the uncertainty principle, broadens its distribution in momentum space. This relaxes the strict **K**-selection to some extent, and increases the interaction with a wider range of momentum states, especially in low-dimensional perovskites such as NPLs or NWs.

Furthermore, excitons in reduced dimensions such as small QDs and thin NPLs can undergo fine structure splitting due to a combination of exchange interactions, spin–orbit coupling, and lattice symmetry breaking, lifting the degeneracy of excitonic states, resulting in distinct energy levels corresponding to bright and dark excitons [60–62]. The bright exciton states are optically allowed and dominate radiative recombination, while dark excitons are spin-forbidden and exhibit different recombination characteristics [63]. This phenomenon further reveals the power of quantum confinement on the excitonic emissions.

Exciton–phonon interaction

In semiconductors, acoustic phonons play an important role in momentum transfer and allow excitons to scatter between finite-**K** states and relax toward the radiative zone near $\mathbf{K} \approx 0$, which is also demonstrated in perovskites [64]. In polar semiconductors like lead-halide perovskites, excitons could couple strongly to longitudinal optical phonons (LO phonons) [65]. Since LO phonons can carry substantial momentum, they provide the missing momentum required for optical transitions into or out of finite-**K** exciton states [66]. As a result, both absorption and PL may show phonon-assisted features, such as linewidth broadening and sidebands shifted by the LO phonon energy [44, 59, 67–69]. Additionally, strong exciton–phonon coupling can lead to the formation of self-trapped excitons (STEs), where the exciton wave function becomes localized in real space due to local lattice distortions, common in perovskites. Such localization implies a broader distribution in momentum space, allowing recombination across a wide **K** range and giving rise to broadband PL emission [70, 71].

However, trap states introduce sub-bandgap energy levels that can capture photoexcited carriers, facilitate non-radiative recombination via the Shockley–Read–Hall (SRH) mechanism [72, 73]. In this process, electrons and holes recombine through a localized defect state, releasing energy in the form of phonons rather than photons. This mechanism, unlike spectral reshaping processes, reduces the overall PL efficiency and typically manifests as shorter lifetimes of PL from excitonic recombinations.

Multi-exciton states and Auger recombination

Multi-excitonic behaviour such as biexciton emission and Auger recombination are significant in low-dimensional perovskites.

Under high excitation densities, multiple electron–hole pairs can occupy a single nanostructure, and the most general case is of two-exciton interaction. The emission line is shifted and broadened relative to the single exciton emission due to repulsive interaction, as was demonstrated in $CsPbBr_3$ NCs [74]. The biexciton binding (or anti-binding) energy can reach ∼100 meV in lead-halide perovskite NCs given the strong Coulomb interaction under confinement [75].

The presence of multiple excitons also activates strong non-radiative Auger recombination. In this process, one electron–hole pair recombines, with its energy transferred to a third carrier instead of emitting a photon. This leads to ultrafast decay of multi-exciton populations, manifested experimentally as fast decay components in lifetime traces [76]. Due to enhanced carrier overlap, Auger recombination is particularly efficient in perovskite QDs and NPLs, especially representing a major loss channel at high excitation powers [77, 78], although much of the work presented in this thesis involves carrier and excitonic densities that are too low to invoke any major Auger effects.

1.3.4 Recombination Dynamics

Carrier/Exciton dynamics in the ABC model. Under excitation, the carrier density $n(t)$ follows the fomula as ABC model [79]

$$\frac{\mathrm{d}n}{\mathrm{d}t} = G(t) - An - Bn^2 - Cn^3, \tag{1.12}$$

where A denotes monomolecular (trap-assisted, SRH) recombination, B denotes bimolecular radiative recombination, and C denotes Auger (three-particle) recombination. G represents the carrier generation rate. For pulsed excitation, $G(t)$ is finite only within the duration of the excitation pulse and is zero at all other times.

Excitonic vs. free-carrier picture. When $E_\mathrm{b} \gg k_B T$ (strongly bound Wannier–Mott excitons), the photoexcited electrons are mostly bonded to a corresponding hole, in which case one may treat n as the exciton density; then the radiative channel is effectively monomolecular, while non-radiative traps add to A, and multi-exciton Auger retains the cubic loss:

$$\frac{\mathrm{d}n_\mathrm{X}}{\mathrm{d}t} = G_\mathrm{X} - (A_\mathrm{X} + A_\mathrm{nr})n_\mathrm{X} - C_\mathrm{X} n_\mathrm{X}^3, \qquad I_\mathrm{PL} \propto n_\mathrm{X}. \tag{1.13}$$

Low-dimensional perovskites. Quantum confinement reshapes the recombination coefficients. (i) Trap states at surfaces or interfaces can strongly increase the monomolecular coefficient A, unless adequately passivated; (ii) enhanced carrier wavefunction overlap boosts the radiative recombination term; (iii) the same spatial overlap also strengthens Auger interactions, thereby increasing the coefficient C. These trends explain both the sublinear power dependence of PL at high pump fluences and the pronounced sensitivity to sample morphology. Experimentally, PL transients in perovskites frequently display multi-exponential decays, reflecting the coexistence of trap-assisted recombination, occasional Auger processes, and excitonic contributions. Therefore, disentangling the relative weights of these channels requires careful consideration of carrier density, trap density, morphology, and dimensionality of the system. It should also be noted that the applicability of the simple ABC formalism to lead–halide perovskites has been debated. Recent studies indicate that the ABC model may fail to fully capture recombination dynamics under relatively intense excitation, implying that the excitation power regime plays a crucial role in correctly revealing the underlying processes [80, 81].

1.4 Plasmon-enhanced PL Emission

1.4.1 Localized Surface Plasmonic Resonance

When electromagnetic waves strike a metal surface, the free electrons in the metal collectively oscillate with the oscillation of the incident wave. At a specific frequency, the amplitude of this collective oscillation reaches its maximum, forming plasmon resonance, leading to absorption and scattering of light in specific wavelength regions [82]. For bulk materials, whose sizes in all dimensions far exceed the wavelength of light, plasmons vibrate at the so-called plasma frequency, whose energy is determined by [83]

$$E_p = \hbar\sqrt{\frac{Ne^2}{m\epsilon_0}}$$

where ϵ_0 represents the permittivity of free space, N denotes the electron density, e is the electron charge, and m is the electron mass.

Unlike the collective oscillations of electrons in bulk materials, the surfaces of metal micro- and nanostructures can support another important type of free electron collective oscillation, namely surface plasmon oscillation. Surface plasmon oscillation occurs at the interface between metal and dielectric and can propagate along the interface or be localized within the metal nanostructure, the latter being referred to as LSPR.

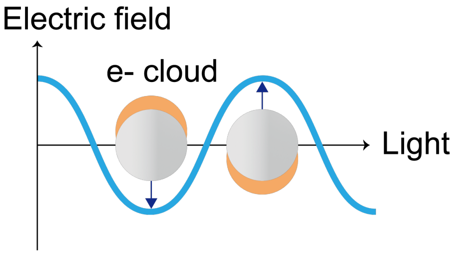

Figure 1.5: Illustration of electron cloud oscillation in a metallic small particle under incident light LSPR.

The scattering from metallic nanostructure surfaces of incident light fields gives them a wide distribution of wave vectors, allowing localized surface plasmons to be directly excited by incident light. When the particle's geometric parameters are much smaller than the wavelength of the surrounding light, the interaction between the NP and incident light can be described using a quasi-static approximation. In this case, the electric field can be regarded as spatially uniform across the NP, allowing the particle to oscillate coherently with the incident field, and the problem reduces to an interaction with an electrostatic field. The complete description of scattering and absorption by spherical NPs is provided by Mie theory, which solves Maxwell's equations without the size restriction. In the small-particle limit ($a \ll \lambda$), Mie theory reduces to the quasi-static dipole solution, thereby linking the Drude dielectric function with the experimentally observed absorption and scattering features of metallic NPs below ∼100 nm in the visible regime [84].

For spherical metallic NPs in the quasi-static limit, the LSPR occurs when the real part of the dielectric function satisfies

$$\mathrm{Re}\{\varepsilon(\omega)\} = -2\varepsilon_{\mathrm{m}}, \tag{1.14}$$

with ε_{m} the dielectric constant of the surrounding medium. In terms of wavelength, the resonance peak is approximately given by

$$\lambda_{\mathrm{max}} = \frac{\lambda_p}{\sqrt{2n_{\mathrm{m}}^2 + 1}}, \tag{1.15}$$

where λ_p is the plasma wavelength of the bulk metal and n_{m} is the refractive index of the medium.

Beyond spherical symmetry, the plasmon resonance is modified by the particle morphology. The Gans extension of Mie theory shows that for ellipsoidal NPs, the polarizability along a given axis i can be expressed as [85]

$$\alpha_i \propto \frac{\varepsilon - \varepsilon_{\mathrm{m}}}{\varepsilon_{\mathrm{m}} + (\varepsilon - \varepsilon_{\mathrm{m}})P_i}, \tag{1.16}$$

where P_i is the depolarization factor determined by the aspect ratio. This predicts distinct longitudinal and transverse modes, with the longitudinal mode red-shifting as the particle elongates. These results highlight that the LSPR peak is strongly governed not only by the dielectric environment but also by NP size and shape.

1.4.2 LSPR-enhanced PL

LSPR can substantially enhance the PL of nearby emitters by modifying both the excitation and emission processes.

The strong confinement of the electromagnetic field within the regions below the diffraction limit near metallic nanostructures leads to significant local field enhancement and increases the excitation rate of emitters placed within the plasmonic near-field [86]. In semiconductor systems such as lead halide perovskites, where excitons dominate the optical response, this local field amplification directly enhances exciton generation rates.

In addition to modifying excitation, plasmonic resonances can act like optical cavities, strongly influencing the emission pathway [87]. Coupling between excitonic dipoles and plasmonic modes alters the local density of optical states (LDOS), resulting in an increased radiative recombination rate through the Purcell effect. Such an accelerated radiative channel competes with non-radiative recombination processes, leading to enhanced external quantum efficiency.

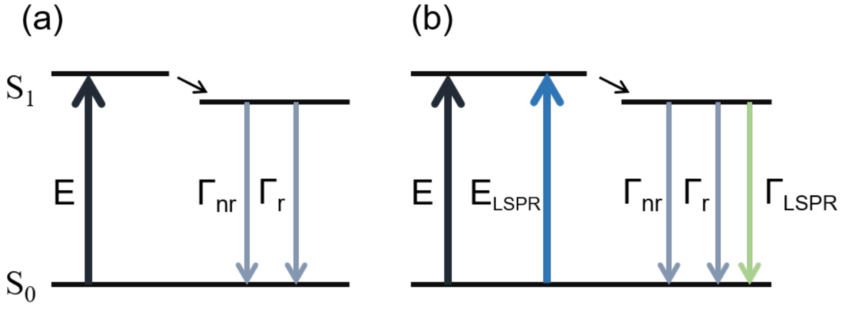

Figure 1.6: Schematic illustration of PL excitation and decay pathways in (a) free-space condition and (b) LSPR-coupled system. In free space, carriers are excited from the ground state (S_0) to the excited state S_1 by an external optical field E, followed by either radiative recombination with rate Γ_r or nonradiative recombination with rate Γ_nr. When coupled to plasmonic nanostructures, the excitation can be enhanced by the nearby LSPR E_LSPR, while additional decay channels appear with respect to the boosted LDOS. The short horizontal line below S_1 is to indicate the branching of relaxation pathways, with the black arrow representing the transition from the excited state into these decay channels.

The interaction between an emitter and a resonant mode can be further quantified by the coupling strength g as shown below. For an two-level emitter with transition dipole moment $\vec{\mu}_{eg}$ interacting with the cavity electric field $\vec{E}$, the coupling strength can be expressed as [88]

$$g = \vec{\mu}_{eg} \cdot \vec{E} = \vec{\mu}_{eg} \cdot \sqrt{\frac{\hbar\omega_{\mathrm{c}}}{2\varepsilon_0\varepsilon_{\mathrm{r}}V_{\mathrm{eff}}}}, \tag{1.17}$$

where ω_{c} is the cavity resonance frequency, ε_0 is the permittivity of free space, ε_{r} is the relative permittivity of the cavity medium, and V_{eff} is the effective mode volume. In the weak-coupling regime, the effect of g is manifested through the Purcell enhancement of spontaneous emission, with typically reduced lifetimes, whereas the strong-coupling regime gives rise to hybrid exciton–photon (or exciton–plasmon) polaritonic states with characteristic mode splitting [89].

It is clear that a smaller mode volume and stronger dipole moment lead to larger coupling strengths, and therefore plasmons are favoured due to their ability of localized confinement. In such a scenario, plasmonic coupling could be regarded as a special cavity that confines the E field to a sub-wavelength nanoscale volume [90]. Considering the formula for both the coupling strength and Purcell factor (shown below), the extremely low volume leads to high enhancement factors [87].

The framework of the Purcell effect generally describes how resonant nanostructures modify spontaneous emission rates. The enhanced radiative recombination rate Γ_{rad} of an emitter is related to the intrinsic rate Γ_0 through the Purcell factor F_{P}, which is defined with respect to a resonant mode characterized by a quality factor Q and an effective mode volume V as [88]

$$F_{\mathrm{P}} = \frac{\Gamma_{\mathrm{rad}}}{\Gamma_0}. \tag{1.18}$$

$$F_{\mathrm{P}} = \frac{3}{4\pi^2}\left(\frac{\lambda}{n}\right)^3 \frac{Q}{V}, \tag{1.19}$$

where λ is the emission wavelength and n is the refractive index of the medium. This expression reveals that radiative enhancement is maximized when emitters are spectrally and spatially coupled to high-Q/low-V resonances. As discussed above, plasmonic nanostructures provide extremely small mode volume V, but the Q factor in practical with metal NPs may strongly limit the overall performance due to

Ohmic losses. Since the Purcell effect serves as a unifying principle underlying both plasmon-enhanced and cavity-enhanced emission, the following chapters also study classic nanocavities with defined Q to evaluate the modification of PL.

1.4.3 Metals as Plasmonic Materials

According to the resonance condition (Eq. 1.14), for a metallic NP embedded in a dielectric medium with complex permittivity $\varepsilon(\omega) = \varepsilon_1 + i\varepsilon_2$, the resonance occurs when the real part satisfies $\varepsilon_1 \approx -2\varepsilon_{\mathrm{m}}$. Therefore, metals with a negative ε_1 of suitable magnitude across the visible or near-IR regime are preferred for sustaining LSPR. In practice, however, the imaginary part ε_2 represents the damping of free electron oscillations and accounts for Ohmic losses. A large ε_2 indicates that instead of coherently oscillating with the incident light to form LSPR, the electron motion dissipates energy as heat, thereby limiting the strength and quality of the resonance.

Therefore, a quality factor as the rate of resonance and damping is defined to evaluate the ability of metals to generate LSPRs,

$$Q_1 = -\frac{\epsilon_1}{\epsilon_2} \tag{1.20}$$

Moreover, the resonance behaviour of LSPR can be directly compared to that of a damped harmonic oscillator, where a quality factor characterizes the balance between energy storage and dissipation. By definition, Q is the ratio of the resonance frequency to the linewidth. In the plasmonic case, a similar Q factor is governed by the complex dielectric function of the metal, such that in the small-particle limit it can be expressed as [91]

$$Q_2 = \left| \frac{\omega\,(\mathrm{d}\varepsilon_1/\mathrm{d}\omega)}{2\varepsilon_2} \right|, \tag{1.21}$$

This expression highlights the dual role of the dielectric response: the slope of ε_1 determines how strongly the electrons respond to the driving field, while ε_2 accounts for Ohmic losses that dampen the oscillation.

Figure 1.7 summarizes the dielectric functions and Q-factors for different metals in the UV to IR range, directly showing the advantageous materials for a range of applications.

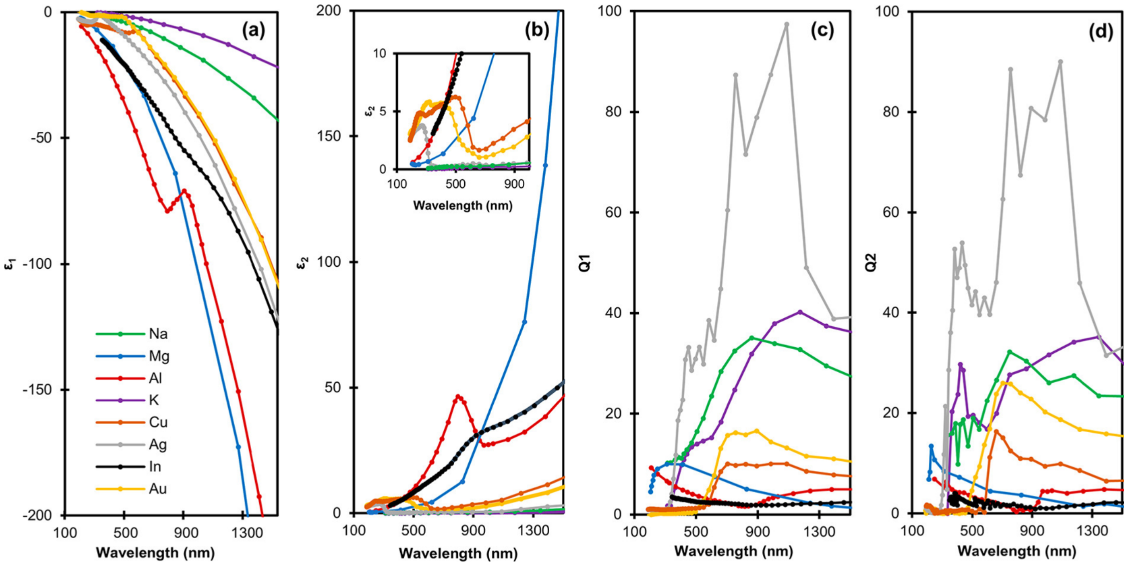

Figure 1.7: Dielectric functions of representative plasmonic metals: (a) real part, (b) imaginary part, and the derived figures of merit (c) Q_1 and (d) Q_2. Reprinted from Ref. [92] under CC BY 4.0 license.

Specifically, the resonance condition in air ($\varepsilon_\mathrm{d} \approx 1$) requires $\mathrm{Re}\{\varepsilon(\omega)\} \approx -2$. The real part shown in panel (a) remains negative across the UV to near-IR spectral range for all metals, which is a prerequisite for sustaining plasmon oscillations. The suitability differs by spectral region: Ag and Au exhibit appropriate values of ε_1 in the visible, accounting for their widespread use as conventional plasmonic materials; Mg and Al decrease more rapidly, making them suitable for plasmonics in the near UV range; while Cu also maintains $\varepsilon_1 \sim -2$ within the visible range with better matching than Ag, the high ϵ_2 limits its effectiveness, resulting in low Q_1. Among noble metals, Ag shows the lowest ε_2 across the visible, yielding superior performance; Au remains effective in the red but exhibits stronger damping toward the blue. Mg, as a relatively new plasmonic candidate discussed in this thesis, also maintains a low ε_2 across the visible, highlighting its promise as a low-cost alternative plasmonic metal, especially in the blue and UV.

Panels (c) and (d) quantify the plasmonic quality factors Q_1 and Q_2. Ag consistently exhibits the highest Q values in the visible region, confirming its superior performance, while Mg reaches Q values comparable to or even exceeding those of Ag in the UV–blue regime, underscoring its emerging potential as an alternative plasmonic material. These comparisons highlight the continued dominance of Ag in the visible and the promising role of Mg, providing the motivation for the following chapters to explore their LSPR characteristics in the context of PL enhancement from perovskite nanostructures.

Furthermore, the morphology imposes additional limitations on plasmonic performance, where the size, shape, and intrinsic material properties collectively influence the strength of the LSPR and its spectral characteristics [82, 93]. Figure 1.8 summarizes recently reported experimental plasmonic spectral ranges for different metals and geometries, further illustrating how morphology-dependent effects determine the accessible wavelength regime and resonance quality.

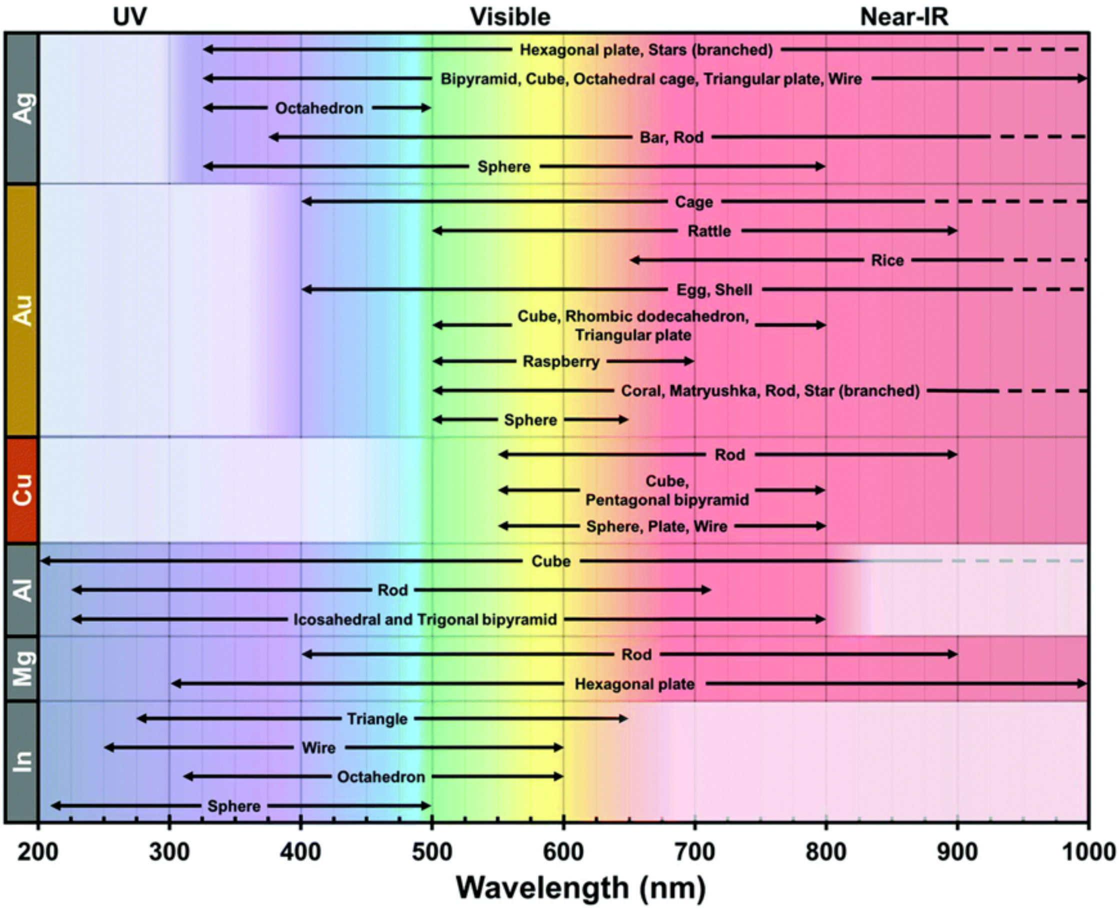

Figure 1.8: Comparison of typical plasmonic spectral ranges for various metals and nanostructure geometries. Adapted from [94] with permission.

2

Experimental Techniques

Contents

2.1 Introduction 24
2.2 μPL spectroscopy 25
  2.2.1 Laser Sources 26
  2.2.2 Optical Layout and Microscopy Setup 31
  2.2.3 Temperature Control 34
  2.2.4 Detection System 35
2.3 μPL Mapping 39
2.4 Time-Resolved μPL 43
  2.4.1 TRPL Layout 44
  2.4.2 Data Acquisition 44
  2.4.3 Instrument Response Function 45
2.5 Superfluid He Droplet Growth 46
  2.5.1 Overview 46
  2.5.2 Sample Growth Using He Droplet 47

2.1 Introduction

In this chapter, an overview of the experimental techniques involved in the following chapters is provided.

The PL characterisation in this work was primarily performed using a micro-PL (μPL) setup equipped for both RT and cryogenic measurements combined with a pulsed laser to excite the samples optically. Spatially resolved PL spectra were acquired by focusing the excitation laser onto individual nanostructures, enabling investigation of sample heterogeneity. Time-resolved PL (TRPL) measurements were carried out using a time-correlated single-photon counting (TCSPC) system to study carrier dynamics with sub-nanosecond resolution. In addition, PL mapping across selected areas was conducted to correlate spectral features with spatial morphology, offering insight into microscale variations in optical response.

In the thesis, different plasmonic metal NPs and perovskite NCs were employed for the PL investigations. The synthesis of all perovskite NW samples discussed in Chapter 3 and Chapter 4, as well as the fabrication of size-controlled Ag NPs described in Chapter 3, was carried out by the group of Prof. Shengfu Yang at the University of Leicester. The synthesis of plasmonic Mg NPs, with and without silica coating, was conducted by the group of Prof. Emilie Ringe at the University of Cambridge. The fabrication of perovskite NPLs with varying layer numbers was performed by the collaborative group led by Prof. Robert Hoye in the Department of Chemistry, University of Oxford.

2.2 μPL spectroscopy

The μPL spectroscopy technique is capable of recording spatially-resolved PL spectra, with a resolution of the order of micrometers. The realization of such resolution comes from confocal spectroscopy that aligns the illumination and the collection paths through the same high numerical aperture (NA) objective. By focusing both excitation and collection to the same diffraction-limited spot and rejecting out-of-focus light, μPL enables the investigation of local optical properties within single nanostructures or heterogeneous regions of the sample, and when the excitation or collection spots are scanned across the surface of the sample 2D hyperspectral maps can be recorded with spectral and spatial information available at each recorded point.

This technique is particularly useful for studying perovskite NWs, NPLs, and other micro-/nano-scale materials, where spatial inhomogeneities [48, 95] and local field effects [96] play a significant role in the observed PL behaviour. When combined with temperature control or time-resolved capabilities, μPL becomes a powerful tool for probing carrier dynamics under variable conditions.

A typical μPL spectroscopy system consists of three parts: excitation source, microscope, and signal detection. Depending on the characteristics of the samples and the specific research objectives, different experimental setups were employed in the study.

Figure 2.1 shows an example of the optical characterization setup used in this thesis, configured for time-resolved measurements with a 405 nm, 76 MHz pulsed laser excitation source, which is suitable for probing short carrier lifetimes in the sub-nanosecond to few-nanosecond regime. The system includes a high-resolution microscope objective lens, typically 50 or 100× magnification, for focusing and collection, a cryostat for temperature control, a piezo stage for position control and a TCSPC module for lifetime acquisition. This configuration allows for high spatial and temporal resolution in the study of perovskite nanostructures and is the most commonly used one. A telecentric $4f$ system is integrated into the excitation path, enabling precise relay imaging of the beam profile between optical planes, which will be explained further later. Moreover, an LED white light source with a commercial camera connected to a computer is also aligned to the microscopy optics so that the real-time image of the sample surfaces can be viewed and recorded, allowing a more precise and more straightforward control for the investigations.

In practice, to further achieve objectives such as controlling incident light power and temperature, additional modules—such as a temperature controller connected to the cryostat with a temperature sensor, and a tunable ND filter—are also integrated into the setup. Figure 2.2 shows a photograph of the setup, where the optical design maximizes performance, convenience, and safety for experimental use.

Using this setup as an overview, the following sections will provide a step-by-step discussion of the system, beginning with the laser source.

2.2.1 Laser Sources

In this work, a Ti:Sapphire femtosecond laser was used as the main excitation source, playing a central role in the most significant PL and TRPL measurements on perovskite samples. In addition, taking into account the relatively short lifetime

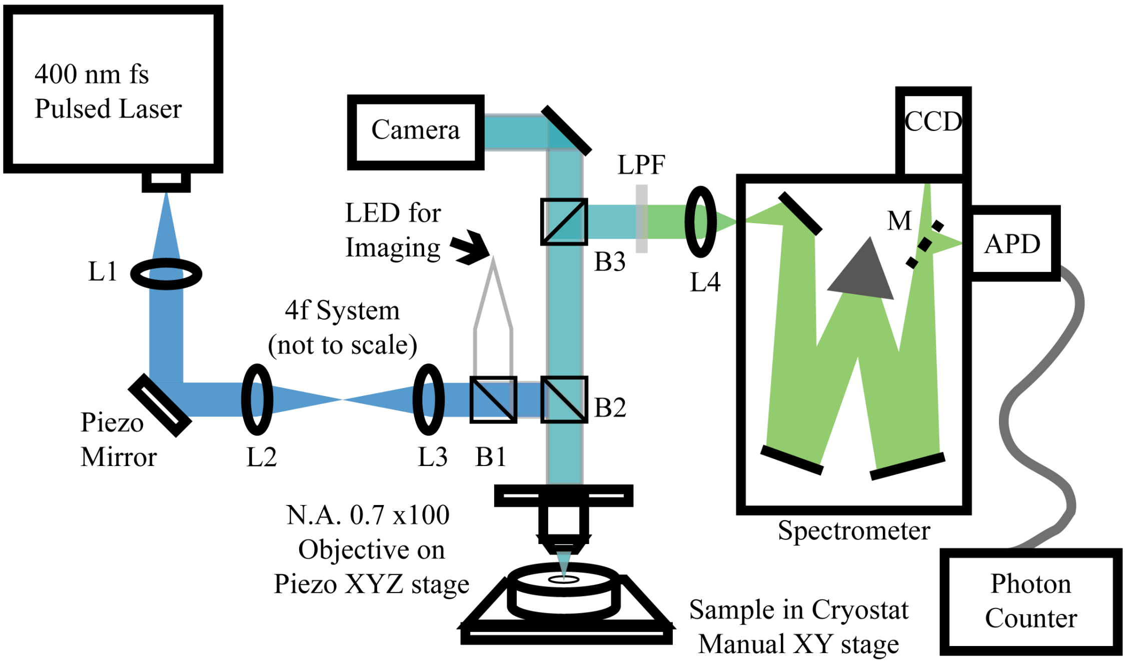

Figure 2.1: A schematic diagram of the confocal μPL setup shows a frequency-doubled femtosecond laser emitting light at 400 nm, focused onto a sample using a 100× microscope objective. L: Lens. B: Beam Splitter. LPF: Long-pass Filter. The excitation source is a Ti:Sapphire pulsed laser. The sample is mounted inside a cryostat on an XY stage, which can be positioned manually. The objective lens is mounted on a piezoelectric XYZ stage allowing precise positioning of the laser spot under software control. The spectrometer output can be directed either to a CCD camera for spectral acquisition or to an APD connected to a photon counter for time-resolved measurements, selected via a built-in slit.

of carriers in perovskites, a 405 nm diode pulsed laser was also used in a separate set of PL mapping experiments to study the spatial distribution of the emission. Several CW lasers, primarily blue diode lasers with central wavelengths in the range of 400–450 nm and typical output powers on the order of a few milliwatts, were also occasionally used. As the most critical results were obtained using pulsed laser sources, their specifications are provided below for reference.

400 nm fs Pulsed laser

An ultrafast laser system was used to deliver fs pulses at 400 nm for PL measurements especially high-resolution decay curves. The complete setup comprises the following modules:

Coherent Verdi V8 pump laser

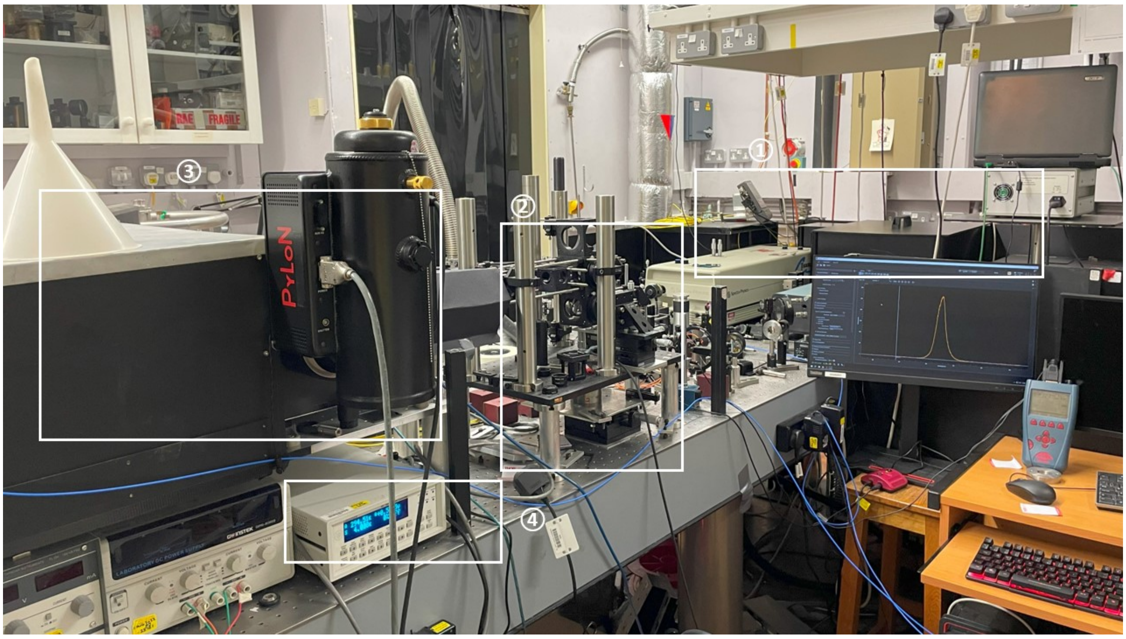

Figure 2.2: A photograph of the μPL system. 1: The 400 nm fs pulsed laser as the excitation source. 2: The optical components, including the path of the LED and the optics for the $4f$ system for accurate imaging, and the manual xy stage on which the cryostat with the sample lies. 3: The spectrometer with CCD aligned to an output slit. 4: The temperature control module, connected to the temperature sensor in the cryostat.

The Nd:YVO_4 CW laser employed in this system functions as the pump to the 400 nm laser output. It operates at a wavelength of 532 nm with a maximum output power of approximately 8 W. This green beam delivers a high-quality $TEM_{0\,0}$ spatial mode and exhibits exceptionally low relative intensity noise (<0.02% rms) [97], making it particularly well-suited for applications requiring high stability and beam coherence [98].

Coherent Mira 900 Ti:Sapphire fs oscillator

The 532 nm output from Verdi V8 then enters the Mira 900 oscillator as a pump, generating 800 nm pulses with a repetition rate at 76 MHz and pulse durations typically at 100 fs. Mode-locking in Coherent Mira 900 is achieved by the Kerr-lens mode-locking mechanism.

The Kerr-lens mode-locking technique is widely employed in Ti:Sapphire oscillators to generate ultrashort pulses with high peak powers [99]. Generally speaking, this so-called self-focusing effect is a nonlinear optical phenomenon arising from the intensity-dependent refractive index of the gain medium (in this case the Al_2O_3

crystal doped with Ti ions) [100, 101]. The relation between the beam intensity and the refraction index of the medium can be expressed by

$$n_I = n_0 + n_2 I$$

where n_0 is the linear refractive index, n_2 is the nonlinear refraction index and I is the intensity of the laser. It is reported that the n_2 for Ti:Sapphire is around 3×10^{-16} cm^2/W [102], which is relatively low compared to the n_0 of the order of 1. Therefore, under high-intensity fs pulsed conditions, this phenomenon dominates and acts as an intensity-dependent lens within the laser cavity, favouring the formation and amplification of short pulses over CW operation. Additionally, dispersion compensation elements are incorporated within the cavity to maintain pulse duration and spectral bandwidth [103, 104].

Pulse Switch

A pulse picker and cavity dumping system is employed to reduce the effective repetition rate from approximately 76 MHz to lower frequencies by adjusting the divider on the control panel, thereby maintaining the per-pulse energy. The ability to flexibly adjust the repetition rate is critical for experiments, as it helps maintain sample integrity by avoiding multiple excitations within the carrier decay time and preserves the benefits of high-intensity output. The pulse picker employs an acousto-optic modulator driven by a powerful radio frequency pulse to diffract pulses out of the main beam with an efficiency of $\sim$ 50%.

The maximum output power of the 800 nm pulsed laser, measured immediately after the pulse picker, was approximately 40 mW with highly stable readings. In most experiments, the pulse picker was operated with a divider setting of 10, resulting in an effective repetition rate of 7.6 MHz. Using the relation

$$E_{\text{pulsed}} = \frac{P}{f},$$

the energy per pulse was estimated to be approximately 5.26 nJ. Assuming a Gaussian temporal profile for each pulse and a pulse duration of ~100 fs, the corresponding peak power was calculated to be on the order of 50 kW.

Ultrafast Harmonic Generation System

To obtain the desired 400 nm output for excitation experiments, an Inrad Model 5-050 harmonic generation system was employed to perform second-harmonic generation (SHG) of the fundamental infrared (IR) pulses. Within the module, a beta-barium borate (BBO) nonlinear crystal is used to frequency-double the incoming 800 nm fs pulses, generating blue pulses centred at 400 nm. Owing to the ultrafast nonlinear response and minimal group velocity dispersion of thin BBO crystals, the pulse duration of the second-harmonic output remains comparable to that of the fundamental, yielding $\sim$ 100 fs pulses [105]. This output is particularly well suited for above-bandgap excitation in perovskite PL experiments, especially for probing the ultrafast carrier dynamics during the initial decay phase.

405 nm PicoQuant Pulsed laser

In the PL mapping setup, the excitation source consists of a LDH-P-C-405 pulsed diode laser head with an output at 405 nm, driven by a PicoQuant PDL 800-B driver [106, 107]. This compact and stable laser module enables efficient excitation of perovskites, and is well-suited for spatially resolved PL measurements. Unlike the mode-locking mechanism used in Ti:Sapphire lasers, the generation of optical pulses in the diode laser system is directly controlled by the external driver. The PDL 800-B driver produces short, well-defined electrical pulses that drive the laser diode for a brief duration above its lasing threshold, resulting in ps optical pulses of width < 70 ps [107]. The base trigger frequency is 40 MHz,and the integrated pulse generator includes selectable repetition rate dividers (1, 2, 4, 8, 16, 32), allowing flexible adjustment of the output pulse frequency to suit different experimental requirements [107]. This tunable repetition rate is particularly useful for optimizing the excitation fluence and avoiding cumulative heating effects or photobleaching during long-duration spatial mapping, which is crucial for delicate semiconductors such as perovskites [108, 109].

The precise electrical pulse output from the PicoQuant driver also serves as the synchronization reference for the excitation laser, ensuring accurate timing for lifetime measurements, which will be discussed in detail in section 2.4.

2.2.2 Optical Layout and Microscopy Setup

Refering to Figure 2.1, all the optical layouts share a standard configuration. After emission from the laser source, the excitation beam first passes through a set of reflective mirrors and a electrically-controlled shutter, which serves to enable or block the beam as required. The beam then propagates through a $4f$ system equipped with a pinhole at the Fourier plane, serving as a spatial filter to clean the beam profile and enhance focus quality.

Following the $4f$ system, the laser is coupled into the objective lens to excite the sample. The resulting excitation spot can be focused down to approximately $1\,\mu$m in diameter when the 100× 0.7 N.A. Mitutoyo long working distance objective is used. The PL signal emitted from the sample is collected by the same optical path in an epi-illumination configuration. Along this return path, appropriate optical filters are placed in the beam path to suppress residual laser light, thereby ensuring a high signal-to-noise ratio for the spectroscopic measurements.

The sample is mounted on a manually adjustable stage with micrometer screws for both the x and y axes, enabling precise lateral positioning. A confocal detection geometry is employed in the collection path, in which only the signal from the focal plane is directed into the spectrometer, thereby improving spatial resolution and suppressing out-of-focus background.

Additionally, a white LED illumination path is integrated into the system via beam splitters. This allows real-time imaging of the sample surface using a Thorlabs camera, enabling convenient alignment, focus adjustment, and continuous monitoring during measurement. The LED and laser paths are spatially combined and carefully aligned, to ensure that the resulting beam remains within the optical window of the microscope.

It should be noted that due to multiple reflections and beam-shaping elements, substantial power losses occur along the excitation path. While the total transmission efficiency from the laser source to the sample surface was not directly measured, power readings taken between the shutter and the microscope input consistently showed losses of at least 50%, underscoring the importance of careful alignment and optical throughput optimization.

A significant portion of the beam path is constructed using the Thorlabs cage system, which offer excellent mechanical stability and modular alignment capabilities. Optical components are primarily arranged at 45° or 90°, making the system easy to align and reducing sensitivity to external disturbances, improving the reliability, safety, and operational efficiency of the setup.

$4f$ System

The $4f$ system in our optical path consists of two identical lenses spaced by the sum of their focal lengths, as shown in figure 2.3. It is arranged such that the first lens focuses the incoming beam to an intermediate focus and the second lens re-collimates the beam allowing it to fall on the input of the microscope objective lens. The input focal plane corresponds to the reflection path from the upstream mirrors, while the output focal plane is aligned to the back aperture of the objective lens.

Additionally, a mirror located at the input focal plane is piezo-controlled, allowing the precise adjustment of the beam's incident angle on the objective, which in the small angle approximation allows the laser spot to be scanned across the sample surface as $x = f\theta$. When coupled with the piezo scanner into which the objective is mounted, this system allows for the excitation of the sample at one position and collection of light from another.

Confocal Signal Collection

In this setup, confocal detection is realized through the combined functionality of the microscope optics and the entrance slit of the spectrometer. The excitation beam is tightly focused onto the sample (order of $1\,\mu$m) via the high NA objective, while PL emission is collected by the same objective and focused onto the incident

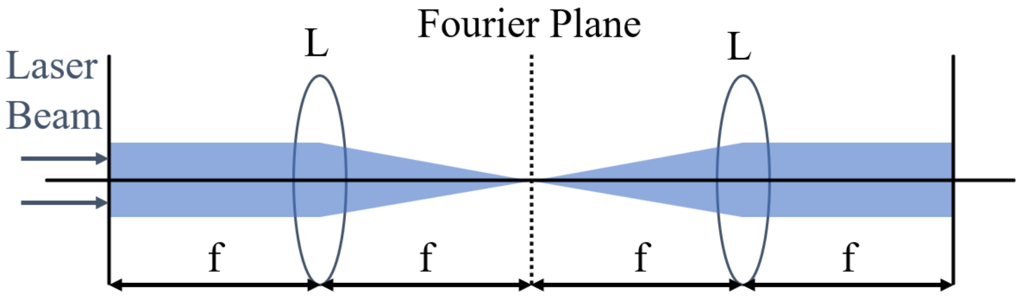

Figure 2.3: A schematic diagram of a $4f$ system.

slit of the spectrometer through the optical system. A long-pass filter is inserted in the collection path to effectively suppress residual excitation light. A lens focuses the collected PL onto the spectrometer slit, which is placed at the confocal plane. The spectrometer slit's width is adjustable, allowing a balance between spatial resolution and signal intensity. Emission from regions outside the focal plane is not well focused at the slit and will be effectively suppressed, enhancing the spatial selectivity and background rejection of the detection.

Most of the results were obtained using a Mitutoyo objective lens (100×, NA = 0.7), providing a focused laser spot size of approximately 1 μm. In some cases, a 10× objective lens was employed instead, allowing excitation over a larger area while preserving the high signal-to-noise optical configuration. This enabled the observation of collective PL emission across extended regions of the sample surface (100 μm^2 as opposed to 1 μm^2).

White Light Illumination and Imaging System

To enable real-time imaging and precise alignment of the sample, a fibre-coupled white light LED source is integrated into the optical path via a beam splitter.

A Thorlabs Quantalux sCMOS camera is used to capture bright-field images of the sample or to visualize the PL signal when the excitation laser is on. This camera, connected to the acquisition computer via USB and operated using Thorlabs ThorCam software, offers high sensitivity and spatial resolution for visualizing the sample in real time. The beam splitter in the collection path controls the collection path: when inserted, it diverts the signal to the camera, enabling real-time imaging; when removed, the full signal continues toward the spectrometer for spectral acquisition.

2.2.3 Temperature Control

Given that the PL properties of perovskite materials exhibit strong temperature dependence, temperature-resolved measurements are essential for a comprehensive understanding of their emission behaviour. For example, the behaviour of excitons, carrier recombination pathways, and defect-state dynamics can vary significantly between cryogenic and room temperatures. At RT, thermal activation can facilitate carrier trapping into deep defect states, which may lead to longer carrier lifetimes and lower radiative efficiency. In contrast, at low temperatures, non-radiative recombination is typically suppressed, leading to enhanced PL intensity and narrower spectral features due to reduced phonon interactions. In addition to changes in the PL spectrum, the narrower and enhanced emission peak at low temperatures offers improved spatial resolution, making it easier to distinguish individual nanostructures, as carrier diffusion is strongly limited. Therefore, while the primary goal of this work is to investigate PL enhancement induced by plasmonic nanostructures or optical cavities under RT conditions, low-temperature experiments are also valuable for understanding the emission processes of the hybrid structures of interest.

The Janis microscope cryostat used to house the samples features a cylindrical vacuum chamber and a copper sample stage in direct thermal contact with the cryogenic cold stage. Samples were mounted onto the copper base using a thin layer of vacuum grease to ensure good thermal contact while maintaining mechanical stability at low temperatures. An integrated temperature sensor and a heater are located beneath the sample platform, enabling precise temperature monitoring and regulation. The cryostat is connected to a Lakeshore 311 temperature controller, which provides closed-loop feedback control with fast response and high stability. Prior to cooling, the system was evacuated overnight via a dedicated vacuum valve connected to the helium (He) return line, ensuring a high-vacuum environment for thermal insulation and preventing condensation. Liquid He is introduced into the system through a dedicated transfer arm, while a separate return line allows He vapour to exit. Controlled He flow through the flow meter enables continuous cooling, while the integrated thermal sensor and heater module enabled stable temperature regulation from $5\,\mathrm{K} \pm 1\,\mathrm{K}$ to RT ($\sim 300\,\mathrm{K}$), with minimal thermal drift throughout the measurement range.

2.2.4 Detection System

The collected PL signal passes through the input slit of the spectrometer, where it is subsequently dispersed by a diffraction grating to separate the different wavelengths for detection.

Spectrometer Overview

The PL spectra were acquired using two different spectrometers tailored to different experimental needs: a Princeton Instruments HRS-300MS, coupled to the Ti:Sipphare laser, and an Andor Shamrock 303i mainly used for mappings.

The Princeton Instruments SpectraPro HRS-300 spectrometer adopts a Czerny–Turner optical design with a focal length of 300 mm. It covers a broad spectral range from the UV to the near-IR, accommodating diverse experimental needs. The system supports interchangeable diffraction gratings with groove densities ranging from 50 to 3600 grooves/mm, enabling flexible tuning of spectral resolution. The typical spectral resolution could reach below 0.10 nm with a standard entrance slit of $10\,\mu\mathrm{m}$, though in practice it depends on both the slit width and the selected grating. The spectrometer provides two exit ports that can be configured with different detectors, such as a CCD array or an avalanche photodiode (APD), depending on the measurement requirements. The spectrometer is controlled using Princeton Instruments' LightField software, allowing precise adjustment of grating position, integration time, slit width, and other acquisition settings.

The Andor Shamrock 303i spectrometer shares the Czerny–Turner configuration, with a focal length of 303 mm. It also accommodates interchangeable gratings for a range of spectral resolutions and is compatible with various Andor CCD detectors for high-sensitivity detection across the visible to near-infrared range. System control is managed via Andor Solis software, which offers full access to acquisition parameters including exposure time and output slit selection. In this thesis, the Shamrock 303i was primarily employed for PL mapping measurements, providing stable performance and sufficient spectral resolution for spatially resolved studies.

Gratings

Diffraction gratings are key optical components in the spectrometer, responsible for dispersing incident light into its constituent wavelengths. A grating typically consists of a reflective surface patterned with a large number of closely spaced grooves. When light encounters this periodic structure, it is diffracted according to the principle of constructive interference, resulting in the angular separation of different wavelengths.

Referring to figure 2.4, the diffraction condition follows the equation [110]:

$$m\lambda = d(\sin\theta_i + \sin\theta_d) \tag{2.1}$$

where m is the diffraction order, λ is the wavelength of light, d is the groove spacing (inverse of groove density), θ_i is the incident angle, and θ_d is the diffraction angle. The sign convention depends on the specific geometry of the system. By selecting appropriate groove densities, the grating allows the spectrometer to resolve spectral features over the desired wavelength range.

Among these, 0-order diffraction ($m = 0$) corresponds to the condition where the diffracted angle equals the specular reflection angle and the grating behaves like a flat mirror without dispersion occurring. In practice, the first-order diffraction ($m = \pm 1$) is designed to carry the highest intensity due to optimized blaze angles that maximize efficiency at specific wavelengths. Higher orders ($m \geq 2$) generally suffer from lower efficiency and increased overlap and can introduce spectral ambiguities. To suppress

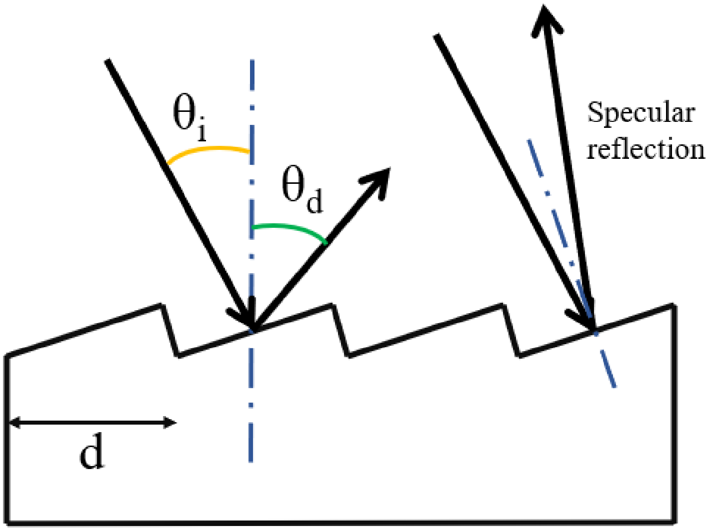

Figure 2.4: A diagram of diffraction by a plane grating.

the undesired reflection or overlap, gratings are often designed with anti-reflective coatings and angular configurations that redirect and eliminate the specular beam.

The spectral resolution is determined by several factors, including the groove density, the focal length of the spectrometer, the entrance slit width, and the detector pixel size. In general, higher groove densities and narrower slits improve spectral resolution, with a lower of signal intensity. Both spectrometers were equipped with three switchable gratings mounted on the turret. The grating parameters used in this work to match the peak profile of perovskite materials are as follows:

- 300 g/mm, blaze wavelength 500 nm
- 600 g/mm, blaze wavelength 750 nm
- 1200 g/mm, blaze wavelength 500 nm

All three gratings were loaded on the SpectraPro HRS-300 spectrometer, and the first and the third grating was utilized on the Andor Shamrock 303i spectrometer.

CCD

The spectroscopic measurements were recorded using two cooled CCD detectors.

The PyLoN 256E CCD (Princeton Instruments), used in the Ti:Sapphire setup, is a liquid-nitrogen-cooled detector set to -80 °C to minimize dark noise. The full sensor array consists of 1024×256 pixels with a pixel size of $26\,\mu\text{m}\times26\,\mu\text{m}$, although spectra were read out in binned mode along the vertical direction, yielding a 1024×1 profile.

For the mapping experiments, an Andor Newton silicon CCD is integrated to the Shamrock 303i spectrometer, which features thermoelectric cooling down to $-40\,°\text{C}$ while operating. The sensor array consists of 1600×200 pixels with a pixel size of $16\,\mu\text{m} \times 16\,\mu\text{m}$, and is also read out as a linear array.

Regarding the spectral resolution, a higher groove density increases the angular dispersion, improving wavelength separation. Narrower entrance slits enhance resolution by limiting the input beam width but reduce signal intensity. The focal length affects the spatial scale of the spectrum on the detector, with longer focal lengths providing finer spectral detail. Finally, the CCD pixel size sets the fundamental limit on how the dispersed spectrum can be sampled. Taking all these factors into account, they jointly determine the spectral resolution achievable in measurement.

To estimate the CCD pixel resolution, which describes how the detected wavelength varies with pixel position, we consider the linear dispersion of the system, defined as $D = \frac{d\lambda}{dx}$, which quantifies the rate of wavelength change across the detector plane. Starting from the grating equation (Eq. 2.1) and assuming a fixed incident angle, the wavelength variation is determined by the changes in diffraction angle. Differentiating both sides with respect to the position x, and using the relationship that $x = f\theta_d$ when θ_d is a small value, we obtain

$$D = \frac{d}{m\ f} = \frac{1}{m\,n\,f}$$

where n is the groove density of the grating, f is the focal length of the spectrometer and m is the diffraction order. Since first-order diffraction (m=1) is typically used, this simplifies to

$$D = \frac{1}{nf} \tag{2.2}$$

Thus, the pixel resolution can be expressed as $\Delta\lambda_{\text{pixel}} = D \cdot (\text{pixel size})$.

The estimated pixel resolutions for each grating and CCD are summarized in Table 2.1:

Table 2.1: Estimated CCD pixel resolutions for each grating configuration.

Grating	Groove Density (g/mm)	PyLoN 256E	Andor Newton
300 g/mm	300	0.289 nm/pixel	0.176 nm/pixel
600 g/mm	600	0.144 nm/pixel	–
1200 g/mm	1200	0.072 nm/pixel	0.044 nm/pixel

In practice, the measured pixel resolutions for the 300 g/mm grating were approximately 0.2765 nm/pixel for the PyLoN 256E CCD and 0.1685 nm/pixel for the Andor Newton CCD. The slight deviations from the theoretical estimates likely originate from approximations made in the derivation, such as the small-angle assumption, as well as practical factors including the actual beam divergence, the slit width and the optical alignment. Nevertheless, the close agreement between estimated and experimental values confirms the high spectral resolving power of the μPL system.

2.3 μPL Mapping

While the μPL setup used in this work enables excitation with a tightly focused laser spot down to 1 μm, offering high spatial resolution, the system relies on a manually operated sample stage for positioning. This stage, equipped with micrometer screw-driven knobs, allows fine adjustments in the X and Y directions. However, manual operation inevitably introduces limitations when working with samples at the nanoscale. Not only can subtle hand movements affect the optical alignment—often highly sensitive in μPL systems—but spatial inhomogeneity in sample distribution may also lead to biased or unrepresentative PL spectra if data are collected from only a few selected locations.

To address these challenges and minimize user-induced bias, a program-controlled 2D mapping μPL system was employed. This automated setup enables spatially resolved PL measurements over a defined area with certain step lengths. By scanning across the sample in a controlled manner, it becomes possible to construct detailed PL intensity and spectral maps, allowing for more objective and comprehensive characterization of samples, especially the sample in this study where the distribution of the materials strongly influences the strength of coupling and the localized measurements are highly sensitive.

To enable high-resolution spatial mapping of PL, the Andor μPL system is integrated with a piezoelectric xy scanning stage where the objective lenses are mounted, controlled by a PI E727 digital piezo controller. This setup allows for precise and repeatable movement across the sample surface with sub-micron accuracy. The scanning process is automated through a custom LabVIEW-based control program, enabling programmable scans over areas up to 100 μm×100 μm.

During scanning, the system records a full PL spectrum at each position. In this thesis, the step size is typically set to 1 μm for most mappings, which matches the optical excitation spot size to ensure spatially independent measurements. In cases where finer resolution is required, 0.5 μm steps may be used. The exposure time per pixel is generally set to 1 s, but this parameter can be adjusted depending on the emission intensity of the sample to balance signal quality and total acquisition time.

After data collection, hyperspectral maps are analysed using a dedicated software package developed by former group member Dr. Luke Nuttall. This program allows post-processing operations such as spectral integration over selected wavelength ranges, pixel-wise intensity mapping, and extraction of spectra from user-defined spatial regions. Such a detailed analysis is critical for evaluating the spatial uniformity of sample distribution. Importantly, it also avoids user-induced selection bias associated with manual point measurements, ensuring that data analysis reflects the true optical behaviour of the entire scanned region rather than isolated features.

In high-resolution optical measurements such as μPL mapping by a high NA objective lens, the optical system exhibits diffraction-limited behaviour, resulting

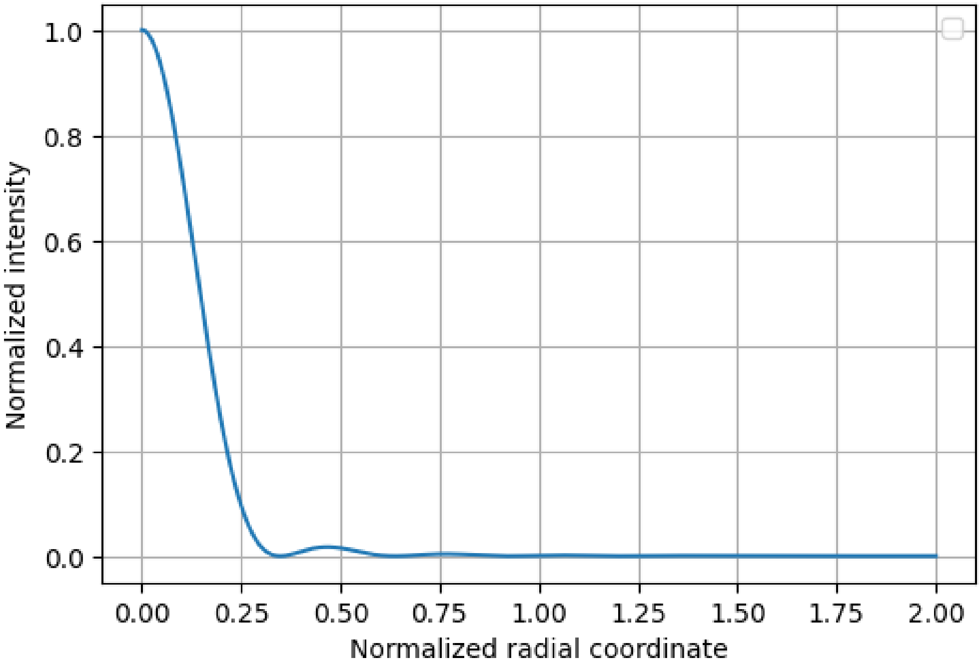

Figure 2.5: Simulated focal-plane intensity distribution under high-NA focusing, based on scalar Debye approximation.

in a characteristic intensity distribution near the focal plane.

$$I(r) \sim |\frac{J_1(x)}{x}|^2, x = kr\sin(\theta)$$

where J_1 is the first order Bessel function, θ is the convergence angle determined by the objective's NA value, $k = \frac{2\pi}{\lambda}$ is the wave number. This intensity distribution arises from circular aperture diffraction and follows the square of a first-order Bessel function, resulting in a bright central peak surrounded by rings of diminishing intensity, described by the scalar Debye approximation [110, 111]. One thing to note is that for focal-plane intensity, any far-field approximation can no longer be applied, but the structure of the square of J_1, or of the Airy pattern, remains valid for focal-plane intensity [112].

Figure 2.5 shows qualitatively how the intensity distribution follows a Bessel function form, producing a bright central spot surrounded by less bright rings. This diffraction structure is intrinsic to focused light in high-resolution optical systems and is normally confined to a small area, which becomes negligible under a 1 μm scan step. However, it may contribute to apparent PL features in μPL mapping, particularly when slight defocus occurs.

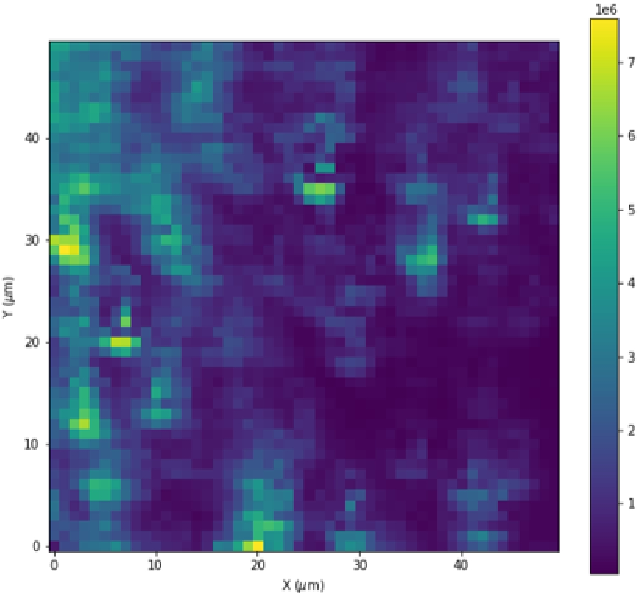

Figure 2.6: A 2D mapping where the sample surface is out of focus. The color at each pixel presents the integral of the PL at this spot. This is a 50 μm by 50 μm scan with a step of 1 μm in both axes. The sample used here was perovskite NWs.

In mapping experiments, the scan is executed automatically using the LabVIEW-controlled piezo stage with fixed acquisition parameters: excitation power, step size, exposure time, and focal setting. However, sample unevenness or surface roughness may lead to subtle defocusing across the mapped region. Because the system uses a fixed focal plane, parts of or even the whole scan area may not be perfectly in focus due to non-ideal initialization, in which case some ring-like features often appear in PL intensity maps, as demonstrated in figure 2.6. These features are not intrinsic to the material but result from diffraction: The excitation beam's outer rings can still interact with the sample and generate PL, which is collected even if the spot is off centre. Although the system is designed in a confocal configuration, minor defocusing across the scanned area effectively breaks the confocal condition locally. As a result, PL excited by the regions of the laser's 'Airy pattern' that are normally rejected by the pinhole may still be partially collected, giving rise to ring-like PL features in the final mapping data. Since μPL mapping scans the excitation beam while keeping detection fixed, these diffraction-induced signals contribute to the final map.

Despite efforts to maintain optimal alignment, completely eliminating this effect in practice is challenging, especially for hybrid structures like the ones used in this study, where surface roughness or structural inhomogeneity can lead to unavoidable local defocus. Nevertheless, as previously discussed, when the defocus remains within a limited range, the contribution of diffraction-induced excitation outside the spot centre is minimal and consistent. Provided that all measurements are acquired under comparable conditions, especially focal setting and alignment, integrating or averaging the PL signal over the entire mapped region effectively restricts such local variations, making the data reliable. However, such ring artifacts highlight the importance of uniform focusing and caution in spatial interpretation.

2.4 Time-Resolved μPL

TRPL is used to study how fast photo-excited carriers recombine in a material. In this technique, the sample is excited by a pulsed laser, and the time it takes for the emitted PL to decay is measured.

The most common method to do this is TCSPC. In TCSPC, the system records the time delay between the laser pulse (as a trigger) and the arrival of a single emitted photon. This process is repeated many times to build up a histogram of photon arrival times. This histogram gives the PL decay curve, which reflects how the excited states in the material relax over time. It is essential to keep the total count rate at least a factor of 1000 below the repetition rate to ensure that the probability of detecting 2 photons is negligible and to avoid any saturation of the detectors. In our case, the intensity was adjusted to ensure that the maximum count rate was below 5×10^4 counts per second.

By fitting this decay curve to exponential functions, carrier lifetimes can be extracted, which gives direct information about recombination dynamics, such as radiative vs. non-radiative processes or defect-related traps.

2.4.1 TRPL Layout

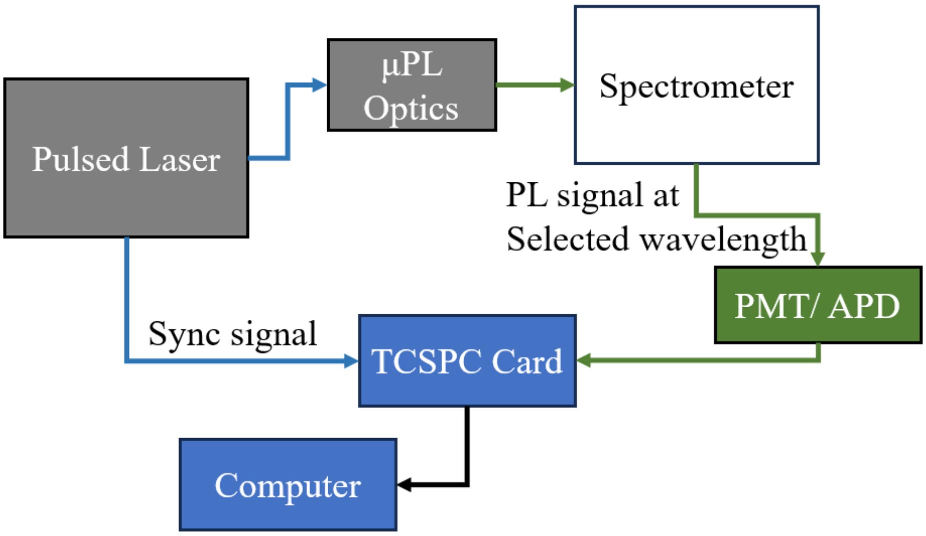

Figure 2.7: Diagram showing the TRPL aqcuisition process. The sync signal could be chased either by the pulsed electrical output from PicoQuant driver directly when connected to TCSPC card, or by introducing a diode detector to record the Ti:Sapphare laser pulses.

The process of acquiring TRPL data, as illustrated in Figure 2.7, can be described as follows. Laser pulses generated at a selected repetition rate also provide a synchronous signal to the TCSPC card, which is recorded as the trigger (or start) for photon timing. On the other hand, the PL signal, instead of being collected by the CCD, is redirected by a built-in mirror in the spectrometer to pass through a narrow slit, allowing only a selected wavelength range (usually 1–3 nm) to reach the detector (in this figure an APD). The electrical signal from the detector is sent to the TCSPC card as the stop input. The card records the arrival/delay times of individual photons into time bins, building a histogram that reflects the PL decay curve, which is then displayed and analysed on the computer.

2.4.2 Data Acquisition

In the experiment, two TCSPC cards were available: a PicoQuant PicoHarp 300 box with a minimum bin width of 4 ps, and another PicoQuant Timeharp card with 25 ps bin width. A Ti:Sapphire laser system was primarily used for TRPL measurements. The repetition rate was typically set to 7.6 MHz, allowing a full decay cycle of 131 ns, which is suitable for most PL lifetimes in perovskite materials with similar structures, commonly ranging from a few to several tens of nanoseconds [46, 47, 113].

However, as discussed in the previous chapter, the introduction of metal nanostructures is expected to shorten the PL lifetime. Therefore, to resolve the rapid decay components associated with plasmonic effects, high temporal resolution in the initial decay range is crucial. To achieve sufficient sensitivity for this time window, the APD was primarily used and aligned in the TRPL setup.

Both the photomultiplier tube (PMT) and APD are available in this lab to operate in single-photon counting mode in this setup, but their signal generation mechanisms differ. The PMT produces a fast, high-gain electrical pulse through a cascade of dynodes in vacuum, which amplifies the photoelectron signal with excellent timing precision and low dark noise [110, 114]. In contrast, the APD generates its signal via an internal avalanche multiplication process in a semiconductor junction [114]. While APDs typically have higher photon detection efficiency (especially in the visible range) and are more compact, they may show slightly higher dark counts compared to high-end PMTs. In both cases, the output electrical pulses are processed by the TCSPC card to register the precise arrival time of each photon.

2.4.3 Instrument Response Function

In TRPL measurements, the measured decay is always influenced by the instrument response function (IRF), which reflects the combined timing characteristics of the laser pulse width, detector response time and timing bias caused by the TCSPC electronics. In addition, the optical path including mirrors, lenses, filters, and other elements can introduce temporal dispersion and delay, which may further broaden the IRF. To accurately fit and interpret the decay curves, the IRF contribution must be properly accounted for and deconvoluted from the measured signal.

The IRF in the experiment was measured using the reflected signal from the sample surface under excitation by the second harmonic of the Ti:Sapphire laser,

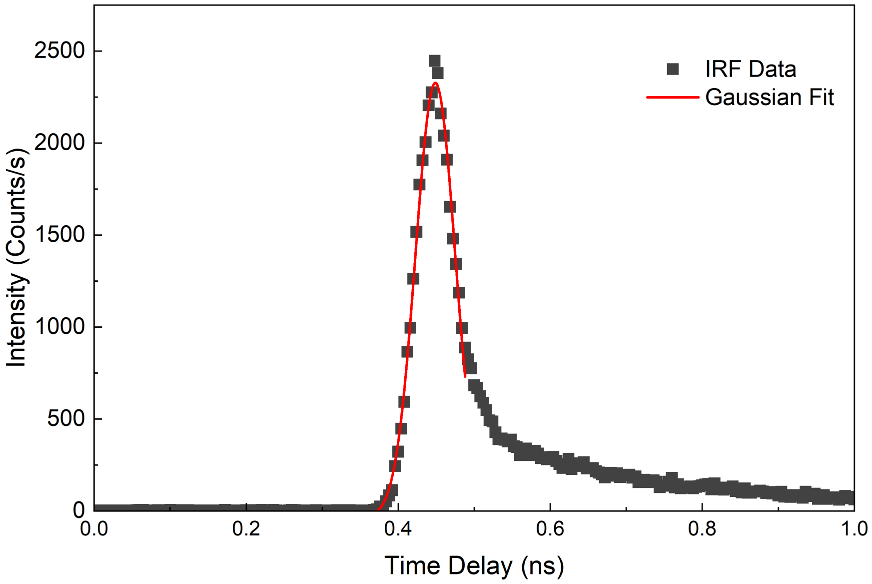

Figure 2.8: Measured instrument response function of the APD. The IRF signal was measured in experiments using the sample surface reflection of second harmonic laser pulses. A Gaussian fitting was applied to the IRF, yielding a FWHM of 61.4 ± 1.1 ps.

at 800 nm. An example IRF trace with a Gaussian fit is shown in Figure 2.8. The full width at half maximum (FWHM) of the fitted IRF peak is 61.4 ps, which is comparable to the fast decay components observed in samples enhanced by plasmonic nanostructures. In this context, proper treatment of the IRF during fitting is essential to accurately extract the true decay dynamics, particularly in the case discussed in Section 3.6, where lifetime is evaluated as one of the key criteria for plasmonic enhancement.

2.5 Superfluid He Droplet Growth

2.5.1 Overview

In Chapter 3, Ag NPs were prepared not by conventional routes, such as solution-based methods, gas-phase methods, template-based methods, etc [115–118], but instead through a non-traditional synthesis approach based on superfluid He droplet assisted deposition.

Unlike conventional synthesis approaches, this technique enables the growth of ligand-free NPs directly on solid substrates under cryogenic and ultra-clean conditions [119]. The absence of surface contaminants makes it suitable for plasmonic applications, especially where direct contact with the structure is required. Any surface contamination or ligand residue could significantly influence the effective gap and thus suppress the enhancement [93].

In addition, achieving precise control over reaction conditions in the traditional method is challenging, leading to inconsistent particle sizes [120]. The size and morphology of the resulting NPs using He droplet are more uniform and controllable [119], facilitating the design of well-defined plasmonic structures.

Furthermore, NPs may undergo aggregation during synthesis, leading to reduced dispersion quality and diminished functional performance [121]. The superfluid He droplet method also allows for soft-landing of the particles onto the substrate [122], which further improves the spatial distribution and surface coverage of the metal NPs.

These characteristics make the method especially advantageous for constructing perovskite–plasmonic hybrid systems, where nanoscale precision, clean interfaces, and strong local field enhancement are critical to device performance.

2.5.2 Sample Growth Using He Droplet

In this method, He droplets are formed by forcing precooled, high-pressure He gas (typically 20 bar) through a narrow nozzle under supersonic expansion. Once produced, these droplets enter a pickup region where they serve as ultra-cold nanoreactors, capturing vapour-phase atoms or molecules on contact. The captured species are immediately cooled and aggregate inside the droplet through stepwise atomic addition, leading to NP formation.

The experimental setup used for Ag NP synthesis via He droplet deposition is schematically shown in Figure 2.9. It primarily consists of a continuous He droplet source, metal evaporation ovens, and a deposition chamber. In this setup, high-purity He gas is first precooled using a closed-cycle cryo-compressor and then undergoes supersonic expansion through a 5 mm nozzle into a high-vacuum chamber,

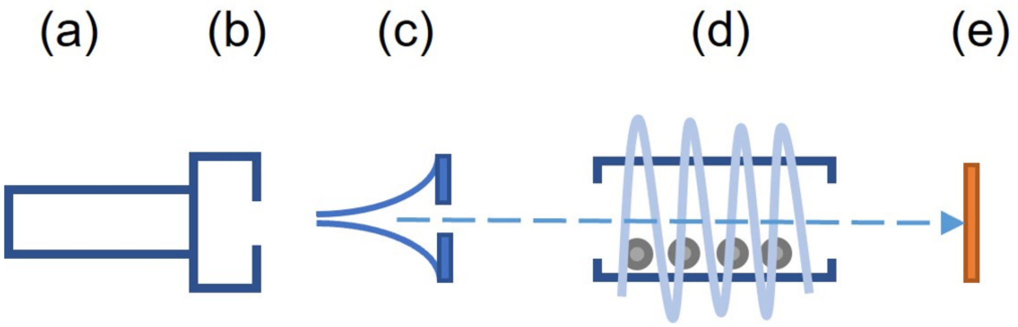

Figure 2.9: Schematic illustration of Ag NP formation within superfluid He droplets. (a) *xyz* manipulator. (b) nozzle. (c) skimmer. (d) pick up region including a alumina oven with silver inside. (e) deposition station. This work was conducted by the group of Prof. Shengfu Yang at the University of Leicester.

forming He droplets. The stagnation pressure is maintained around 15 bar, and the nozzle temperature is stabilized near 7.5 K. The nozzle itself is mounted on an *xyz* translation stage for fine positional control relative to the downstream skimmer.

As the droplets enter the pickup region, they encounter silver vapour emitted from an alumina crucible heated in a resistive oven. The oven temperature is carefully adjusted to tune the local Ag vapour pressure, which in turn controls the average number of Ag atoms embedded in each droplet. These atoms are sequentially captured and nucleate inside the droplets, forming Ag NPs. The doped droplets then continue toward the substrate stage, where they undergo soft landing. Upon contact, the He rapidly evaporates, leaving behind well-dispersed Ag NPs directly deposited onto the surface.

An example AFM image of a nanostructured sample fabricated via the He droplet technique is shown in Figure 2.10. Although this particular sample is not based on Ag, it provides a representative demonstration of the NP deposition behaviour enabled by this method.

The scan covers a 2 μm × 2 μm area, within which a dense population of nanoscale bright features is clearly visible. These features correspond to individual NPs, with their lateral dimensions roughly estimated to lie in the range of 5–12

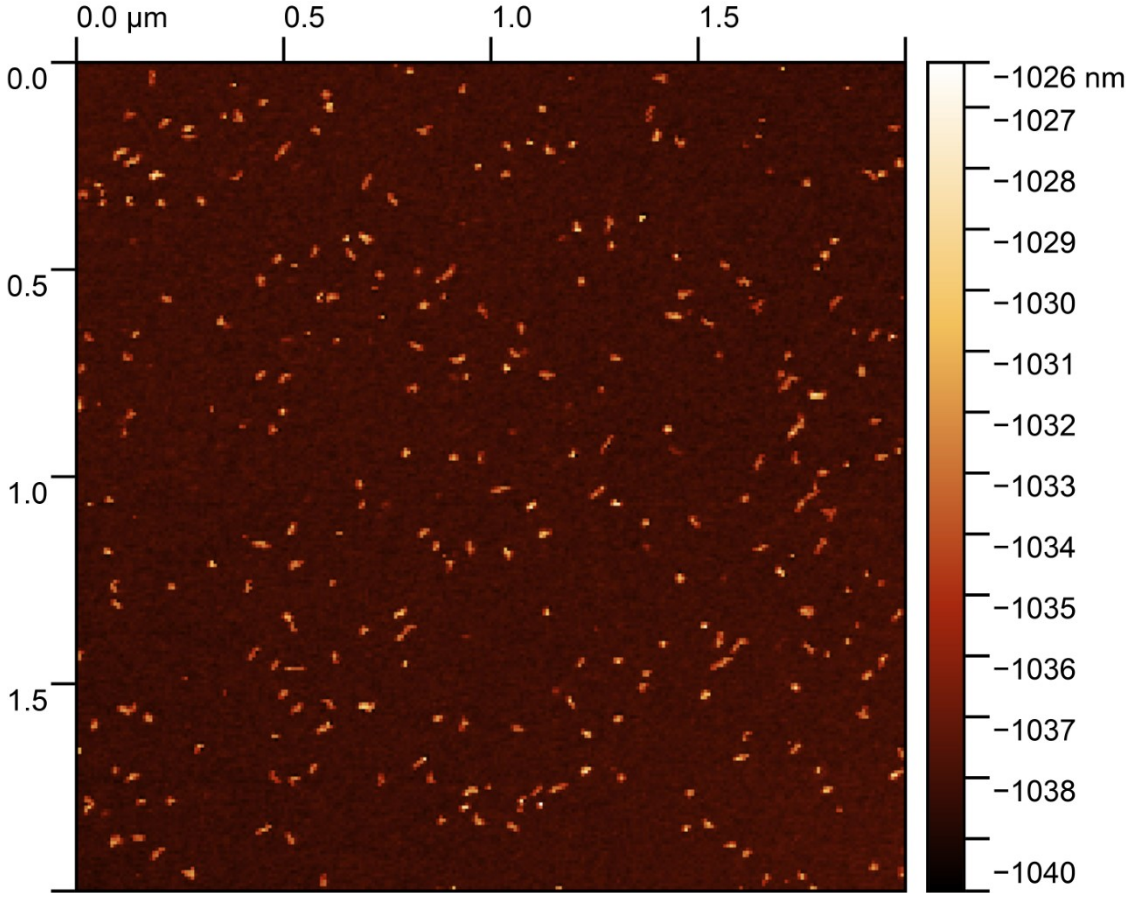

Figure 2.10: AFM image of a sample with He droplet synthesized CdS NPs projected to a silicon substrate. The image was collected by the group of Prof. Shengfu Yang at the University of Leicester.

nm. This size estimate is consistent with expectations from He droplet assisted aggregation under controlled pickup and deposition conditions.

The brightness variation in the image remains relatively uniform, suggesting that the particle height (and thus the volume) distribution is fairly narrow, even though complete uniformity is not achieved. Importantly, the lateral distribution of NPs is not perfectly homogeneous—clusters or local density fluctuations are observable throughout the scanned region. This spatial inhomogeneity likely reflects variations in He droplet flux or pickup statistics during deposition, and it can potentially affect subsequent optical measurements (e.g., local field enhancement or PL uniformity).

Despite this, the overall morphology highlights several strengths of the He droplet method: (1) the NP sizes are consistently controlled; (2) the deposition is ligand-free and substrate-compatible; and (3) the "soft-landing" nature of the process avoids damage on impact, preserving the nanoscale integrity of the particles. These factors make it well-suited for fabricating plasmonic or hybrid nanostructures on delicate optical materials such as perovskites.

3

Ag NPs–Enhanced PL in Perovskite Nanowires

Contents

3.1 Chapter Introduction 51
3.2 Ag Plasmonic Effects on Photonic Nanowires 52
3.3 Sample Fabrication 59
3.4 Setup 66
3.5 µPL Characterization and Device Design 66
  3.5.1 μPL Investigation of Nanowires 66
  3.5.2 μPL Investigation on Nanowires with Ag Nanoparticles 81
  3.5.3 Parameter optimization 89
3.6 Ag NPs Enhanced PL Emission in Perovskite Nanowires 93
  3.6.1 Discussion on Plasmon–photon Coupling Mechanism . . 96
3.7 Conclusion and Discussion 100

3.1 Chapter Introduction

This chapter is structured to progressively establish and validate the plasmon-enhanced PL in Ag–perovskite NW hybrid structures. Section 3.2 provides a detailed analysis of the LSPR mechanisms relevant to Ag-enhanced NW emission, alongside a review of previously reported enhancement effects. Guided by these insights, and supported by simulations, an optimized hybrid nanostructure design is proposed. Section 3.3 describes the synthesis procedures for the designed samples and their structural characterizations. Section 3.5 presents an investigation of the PL properties of the hybrid structures, including the influence of Ag NPs, optimization of design parameters, and the correlation between structural modifications and emission performance. Finally, the chapter concludes with an analysis of the plasmonic coupling mechanisms in these hybrids and a quantitative determination of the PL intensity enhancement factors.

3.2 Ag Plasmonic Effects on Photonic Nanowires

Motivation

Among various strategies for achieving optical output enhancement, noble metal nanostructures have attracted significant attention due to their unique function producing electric fields localized to subwavelength distance scales, known as LSPR. Their superior optical characteristics, low plasmonic damping losses, and high tunability in nanostructure fabrication, makes it highly effective in boosting the emission efficiency of semiconductors, QDs, and perovskites.

Photonic NWs have become essential components for nanoscale light manipulation, enabling light generation, propagation, detection, and amplification [123–125]. Their high aspect ratio and ability to confine and guide light make them promising for waveguides, photodetectors, and light-emitting devices, while synthesis control allows tuning of optical and electronic properties [126]. In optically pumped nanolasers, NWs can act as both gain medium and optical cavity, forming ultra-compact coherent light sources [127], and their large surface-to-volume ratio enables sensitive chemical and biological sensing [128, 129].

Among various NW materials, inorganic lead halide perovskites $CsPbBr_3$ have attracted increasing attention for their strong PL, narrow emission bandwidth, high charge mobility, facile solution synthesis, and compositional tunability across the visible spectrum [47, 50, 130, 131]. Their all-inorganic composition improves stability compared to hybrid perovskites [1], and recent advances in synthesis have enabled precise control over dimensions and morphology [46], marking them as an emerging platform for next-generation nanophotonic and optoelectronic devices.

A key challenge is optimizing optical performance, especially photon conversion efficiency. Combining semiconductor NWs with noble metals can enhance light emission through LSPRs, which confine electromagnetic fields and boost both absorption and emission[132–134]. Silver (Ag), in particular, stands out among noble metals owing to its high plasma frequency, sharp LSPR features, and comparatively low optical losses in the visible range, as indicated by its small imaginary part of the dielectric constant [135]. These characteristics enable stronger near-field confinement and higher quality plasmonic resonances, which improve the spatial and spectral overlap between the plasmonic mode and the perovskite emission, thereby maximizing the Purcell enhancement and minimizing non-radiative damping.

Reported PL enhancement factors for such noble metal coupled emission systems include 40-fold in Au/CdS core-shell NPs [136] and 23-fold in CdSe QDs [137]. An exitonic emission from trap-rich CdTe QDs was reported to be enhanced by 1460-fold using Au nanocones [138]. Metal–semiconductor core-shell NWs have also been predicted to provide high optical gain and potential for electrical injection [139], making them promising for employing Ag NPs to achieve strong enhancement by proper device design.

In this chapter, we investigate a hybrid $CsPbBr_3$ NW device incorporating Ag NPs and a dielectric spacer to enhance light-matter interactions via plasmonic coupling. The four-layer structure is designed to increase photon absorption while suppressing non-radiative losses. Ag NPs are fabricated using superfluid He droplet deposition for precise size control. Low-temperature μPL and time-resolved spectroscopy are used to characterize the optical performance. The results demonstrate the potential of this architecture for quantum information processing and integrated nanophotonic applications.

Competition Between Radiative Enhancement and Quenching

As indicated previously, the introduction of plasmonic Ag NPs brings local field enhancement according to the following two mechanisms:

- **LDOS modified radiative recombination rate**:

  In the case of LSPR, the LDOS is increased by the surrounding plasmonic environment, giving rise to the Purcell effect. An increased LDOS at the emission wavelength enhances the radiative decay rate, thereby shortening the PL lifetime if non-radiative rates remain similar, as more carriers preferentially recombine through radiative channels. This effect is typically observed when radiative processes dominate the recombination dynamics. However, if mode coupling is inefficient, non-radiative processes may instead be enhanced. Such LSPR-induced LDOS tuning in the sub-wavelength regime is highly sensitive to the structural configuration and the quality of the plasmonic resonance.

- **Excitation cross-section enhanced by the confined local field** :

  When the excitation wavelength is resonant with the LSPR of the Ag NPs, the collective oscillation of electrons generates strongly enhanced and spatially confined electromagnetic fields in their near-field region. NW located within these “hot spots” experience a substantially increased local electric field amplitude compared to the incident field, and consequently the effective absorption cross-section is increased, leading to a higher excitation rate. This enhancement is determined not only by the field strength but also by the spatial overlap between the NW and the near-field distribution. This indicates that not only the NP’s size, which tunes the LSPR, but also the spatial configuration is crucial in generating enhancement.

Practically, in emitter–plasmonic NP hybrid systems, particularly when the emitter–metal separation approaches the nanometre scale, the observed PL response results from a delicate balance between radiative enhancement and multiple non-radiative quenching channels. It is also massively affected by quenching due to inefficient plasmon–photon coupling and energy dissipation, and the primary quenching mechanisms relevant to our Ag–NW structures are outlined below.

1. **Nonlocal dielectric response** : Plasmon resonances, rooted in classical electrodynamics, arise from the collective oscillation of conduction electrons in response to an external electromagnetic field. However, at separations ∼10 nm, the free-electron gas in metals exhibits spatially dispersive behaviour, leading to a nonlocal dielectric response [93]. In this regime, the local-field enhancement saturates, preventing the indefinite increase predicted by purely classical models [140]. This intrinsic limitation reduces the coupling efficiency in the immediate vicinity of the metal surface and can be further influenced by factors such as dielectric spacer layers, surface roughness, particle faceting, and imperfect layer conformity [93, 140].

2. **Near-field non-radiative energy transfer** : In the context of plasmon–emitter interactions, plasmonic coupling–induced energy transfer from an excited dipole (e.g., molecule, QD, semiconductor exciton) to a nearby metallic surface via near-field coupling occurs when the free-electron oscillations in the metal, excited by the emitter, dissipate as heat or through other non-radiative channels [141]. This process is known as surface energy transfer (SET). SET is a general phenomenon observed across various geometries, from ideal infinite metal planes to nanostructured metals. Nanometal surface energy transfer (NSET), which specifically refers to energy transfer to metal NPs, has been extensively investigated, showing a $1/d^4$ distance dependence [142]. This mechanism successfully explains the quenching of emitter–metal NP systems for NP sizes of a few nanometres and for emitter–NP separations effective up to ∼20 nm [142–144]. In addition, a Förster resonance energy transfer mechanism has been reported for larger NPs with better spectral overlap with the LSPR, showing a characteristic $1/d^6$ distance dependence that is typically effective over the 1–10 nm range [142]. It is also highlighted that LSPR plays a significant role in the NSET process [142, 144]. While the energy loss as a function of distance provides valuable insight for sensing applications, it also imposes constraints on device design aimed at achieving strong coupling with minimal energy dissipation.

3. **Surface assisted Landau damping** : For Ag NPs smaller than the electron mean free path, conduction electrons experience enhanced inelastic scattering at the metal boundary, thereby increasing the intrinsic damping of LSPR. The decay of LSPR can generate non-thermal high-energy electron–hole pairs (hot carriers) in the metal, which rapidly thermalise through electron–electron or electron–phonon interactions, dissipating energy as heat or injecting into nearby materials, thus bypassing radiative emission from the emitter [145]. Moreover, under direct contact with Ag NPs, plasmon-induced hot electron injection and charge transfer from mode overlap can occur, both of which can be suppressed by introducing a spacer layer [146]. Furthermore, when molecules or ligands are adsorbed on a metal surface, their molecular orbitals may align with or approach the metal's Fermi level. Upon plasmon decay, hot electrons in the metal can be transferred or injected into these molecular orbitals, thereby creating additional non-radiative decay channels [147]. A clean synthesis of Ag NPs via He droplets, as discussed previously, would effectively eliminate such losses. Previous studies have shown that both plasmon-induced hot electron processes and resonant energy transfer, as discussed above, can take place on a timescale of $<$100 fs in metal–perovskite NC complexes [146], which is far shorter than the temporal resolution of our measurement system and therefore cannot be directly resolved in the present measurements.

4. **Interface defect-assisted recombination** : Imperfections or trap states at the dielectric–semiconductor or dielectric–metal interfaces can serve as non-radiative recombination centres [72, 148]. Under strong local fields, not only is the radiative path enhanced due to LSPR, but carrier capture by such traps may also be promoted owing to the increased LDOS [149], further reducing the PLQY. In such scenarios, a combination of improved PL intensity together with lifetime variations not solely attributable to the Purcell effect alone, can be observed.

Therefore, near-field conditions are critical for achieving plasmonic enhancement, as the localized fields associated with LSPR decay rapidly with distance, typically following a high-order power in the regime of tens of nanometres. Nevertheless, the intrinsic plasmonic response of Ag NPs cannot be increased indefinitely due to ohmic losses in the metal and the nonuniform distribution of surface charge density. Moreover, direct contact between metal NPs and perovskite NWs, or separations of only a few nanometres, can introduce additional damping channels, including non-radiative energy transfer and hot-carrier injection. Consequently, incorporating an appropriately designed dielectric spacer is essential to optimize LSPR coupling while suppressing losses. It should also be noted that, when coupling surface plasmon modes to NW emission, ultrafast energy dissipation and competing recombination pathways are inevitable. Given that our aim is to promote efficient coupling between LSPR modes and radiative recombination channels, the above considerations provide guidelines about the relevant materials and structural parameters.

Expected NW/PMMA/Ag NP System with Simulation

Guided by the preceding discussion, we proposed a caesium lead halide perovskite NW-based four-layer structure ($CsPbBr_3$/PMMA/Ag/Si) as illustrated in Figure 3.1(a). Ag NPs, in the defined size and distribution, are the source used to generate plasmonic effects. A thin dielectric poly(methyl methacrylate) (PMMA) layer is deposited by spin-coating between the perovskites and Ag NPs to reduce contact-induced losses and unfavourable energy dissipation whilst ensuring strong coupling. Finite-element method simulations with COMSOL Multiphysics 6.2. were conducted by Dr. Xavier Romain to illustrate the working principle using a simplified 2D geometry depicted on the left in Figure 3.1(b). The $CsPbBr_3$ NW is modelled by a $10\,\text{nm} \times 10\,\text{nm}$ infinitely long wire, while the plasmonic component is designed with a 10 nm thin layer of silver. A 5 nm thin PMMA layer separates the NW and the plasmonic layer and the whole structure is placed on a silicon substrate.

The three additional panels in Figure 3.1(b) present the spatial distributions of the electric field components E_z and E_y, as well as the total field intensity $|E_{\text{tot}}|^2$,

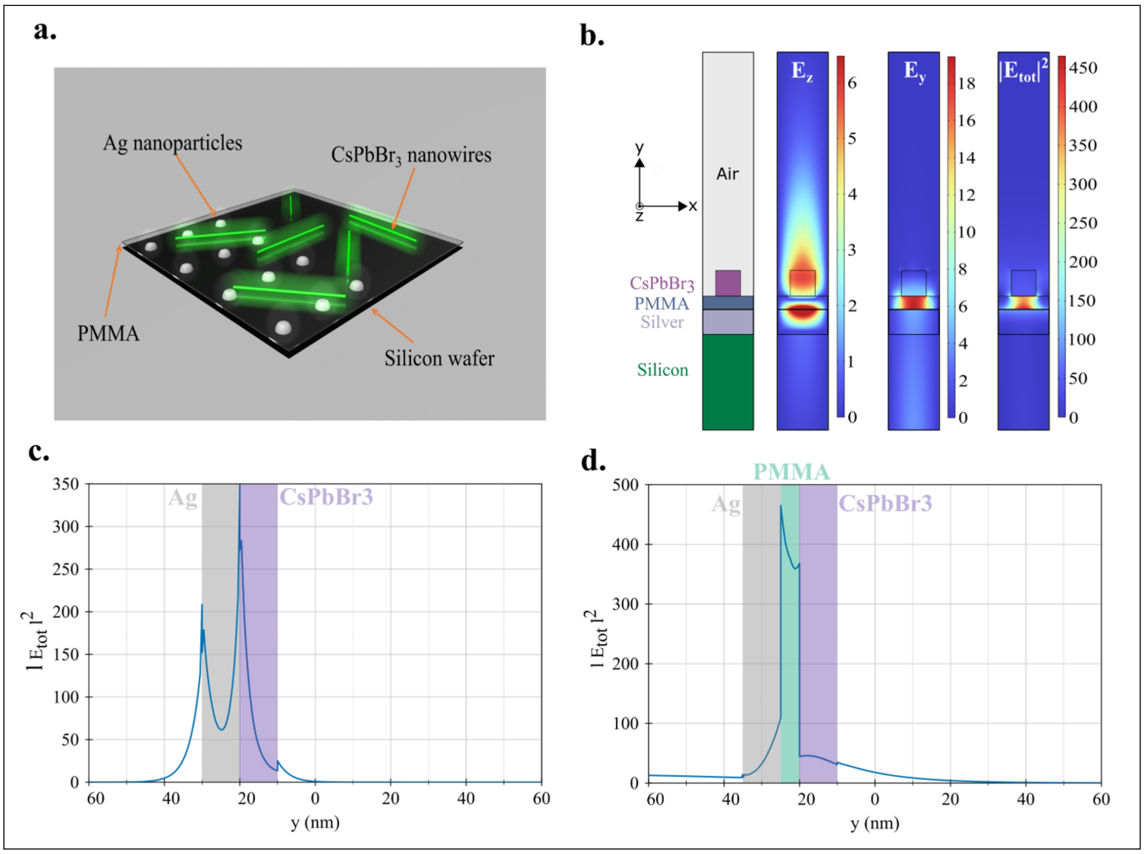

Figure 3.1: Proposed Ag NP–perovskite NW hybrid nanostructure. (a) Artistic view of the hybrid nanostructure. (b) Left: Simplified 2D model for the four-layer structure. Right: Three panels showing the corresponding spatial distribution for E_z, E_y and $|E_{\text{tot}}|^2$ for the hybridised plasmonic eigenmode at 520 nm. (c,d) Electric intensity $|E_{\text{tot}}|^2$ along the vertical y-axis without and with the PMMA interlayer, respectively. This simulation was conducted by Dr. Xavier Romain.

for the hybridized plasmonic eigenmode at around 523 nm. The E_z distribution clearly shows a normal-field enhancement at the Ag surface due to surface charge accumulation, while the E_y distribution indicates hybridization of the plasmonic mode with the perovskite mode in the PMMA interlayer. As a result, $|E_{\text{tot}}|^2$ is strongly confined within the PMMA region, mitigating non-radiative plasmonic quenching that would otherwise reduce PL efficiency.

Figures 3.1(c) and (d) plot the $|E_{\text{tot}}|^2$ profile along the y-axis through the centre of the structure. In Figure 3.1(c), without a PMMA interlayer, the field intensity peaks are located at the Ag–perovskite interfaces and decay rapidly within the perovskite region. The peak positions and widths are consistent with the highly localized near-field coupling characteristic of LSPR modes [150], where the incident light induces a local dipole in the Ag NP and the enhanced field remains concentrated at the contact interface. By contrast, Figure 3.1(d) shows that introducing a PMMA interlayer shifts the main field peak toward the PMMA/perovskite interface, with the peak amplitude slightly exceeding that of the case without PMMA. This indicates that the PMMA layer effectively redistributes the near-field enhancement to better overlap with the perovskite emission region, optimizing photon–plasmon coupling while reducing non-radiative quenching channels.

In the LSPR regime, the induced dipole in the Ag NP creates strong normal (out-of-plane) fields at the metal–dielectric interface due to surface charge accumulation and the discontinuity of the normal field across high-contrast boundaries, whereas the tangential field remains continuous and therefore weaker and more broadly distributed. The PMMA spacer pushes the normal-field hotspot toward the PMMA/perovskite interface and preserves near-field coupling at tens-of-nanometre distances[93, 151], consistent with the observed profiles.

These simulations highlight the PMMA interlayer's role in steering the LSPR-enhanced field toward the perovskite emission region while suppressing non-radiative loss at the metal interface. Guided by these insights, we next fabricated hybrid NW structures with controlled layer configurations and examined their optical response via μPL measurements.

3.3 Sample Fabrication

The sample was fabricated by our collaborator group at the University of Leicester and this section is partially adapted from the supporting information of our previously published article [152].

$CsPbBr_3$ **Perovskite Nanowires**

The $CsPbBr_3$ perovskite NWs were synthesized at Leicester University using a colloidal solution-phase approach. In a typical procedure, 0.1 mmol of caesium carbonate (Cs_2CO_3) and 0.3 mmol of lead bromide ($PbBr_2$) were dissolved in a solvent mixture consisting of 10 ml of 1-octadecene (ODE), 0.5 ml of oleylamine

(OLA), and 0.5 ml of oleic acid (OA). The reaction solution was magnetically stirred and maintained at 125 °C for 60 minutes to promote precursor dissolution and NW nucleation.

After completion of the reaction, the crude mixture was centrifuged at 6000 rpm for 5 minutes to remove unreacted species and excess organic ligands. The resulting NCs were redispersed in 1.5 ml of hexane, forming a colloidal suspension that contained both NWs and a small fraction of nanocubes.

To increase the NW purity, the dispersion underwent a purification step involving centrifugation at 3000 rpm for 5 minutes, followed by redispersion of the sediment in 5 ml of hexane. This purification cycle was repeated several times to obtain a high-purity sample of $CsPbBr_3$ NWs.

Characterization following purification, as shown in transmission electron microscopy (TEM) images (Figure 3.2(e–g)), revealed that the NWs had a uniform diameter of approximately 30 nm and lengths reaching up to 7 μm, indicating a high aspect ratio.

The optical properties of the $CsPbBr_3$ NWs at RT were characterized by UV–vis absorption and PL spectroscopy, as shown in Figure 3.3. The absorption spectrum exhibits a gradual onset around 500 nm, indicating a sharp band edge without significant sub-bandgap features. The PL spectrum shows a prominent emission peak centred at 520 nm, with a FWHM of approximately 18 nm, indicating a fairly narrow size distribution and high optical quality of the NWs. The small Stokes shift between absorption and emission suggests typical near-band-edge emission behaviour.

These characteristics make the NWs suitable for coupling with plasmonic NPs, such as Ag, whose LSPRs can spectrally overlap with the emission band of the NWs. Under such spectral alignment, enhanced light–matter interaction is expected through near-field effects, motivating the integration of Ag NPs with the NW system.

Ag nanoparticles

The technique for the synthesis of Ag NPs, the He droplet method, has been described in Section 2.5.2. Under a stagnation pressure of 15 bar at the nozzle and

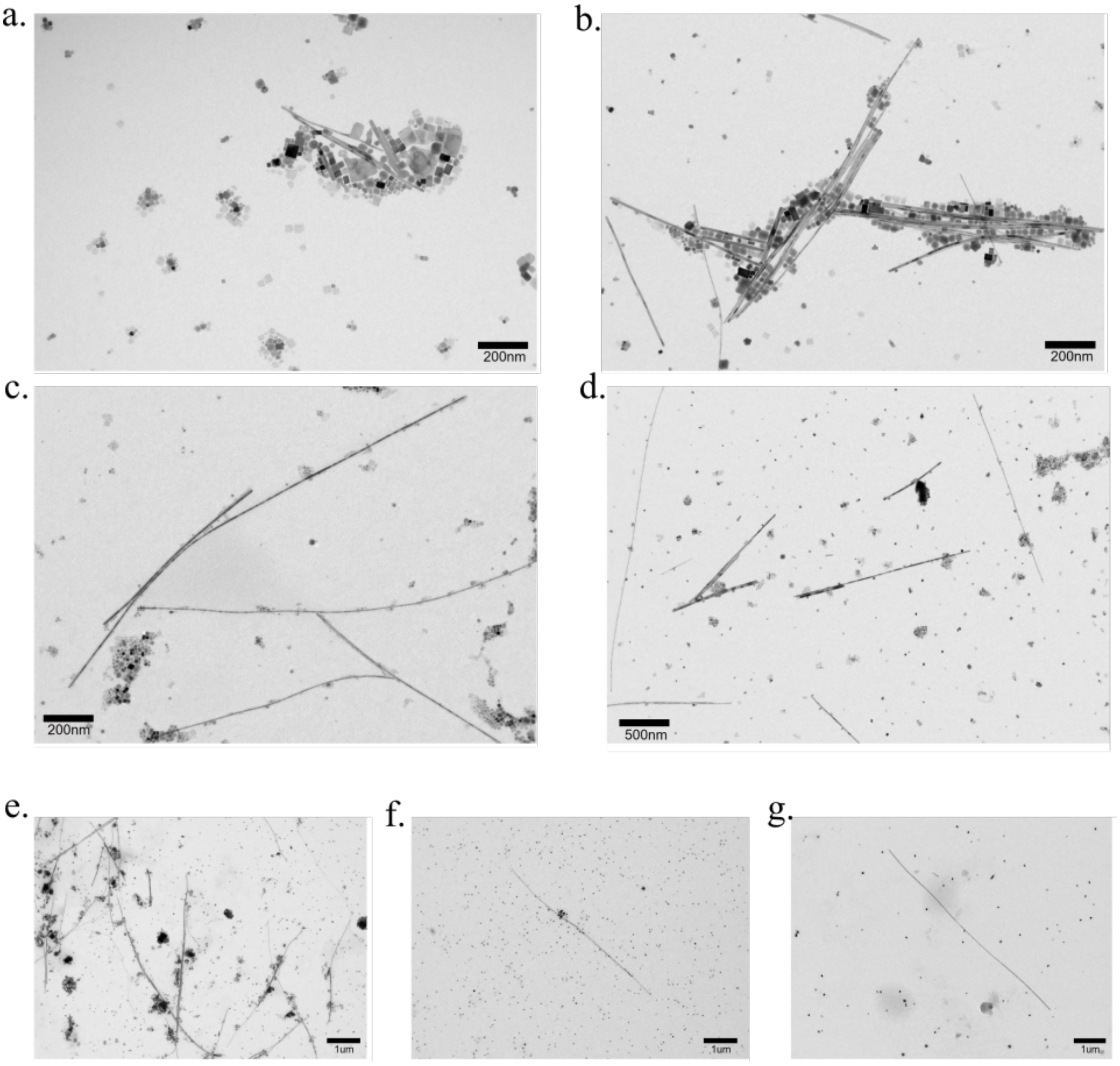

Figure 3.2: TEM images of $CsPbBr_3$ NWs with different reaction time and different centrifugation time. (a–d) TEM images of NW with reaction time of (a) 15 min; (b) 30 min; (c) 45 min; (d) 60 min. (e–g) TEM images of NWs with different centrifugation times. The TEM images presented here were collected by the group of Prof. Shengfu Yang at the University of Leicester.

a temperature of approximately 7.5 K, the resulting Ag NPs exhibit an average diameter of about 7 nm. Figure 3.4(a) presents a TEM image of the Ag NPs directly deposited onto the TEM grid, while Figure 3.4(b) shows the corresponding size distribution of the particles across a defined area. Figure 3.4(c) displays the Ultraviolet–visible (UV–Vis) absorption spectrum measured from Ag NPs with an average size $\sim 7\,\mu$m, deposited on Si substrates. The spectral profile centred at around 410 nm is consistent with previous theoretical and experimental studies [82,

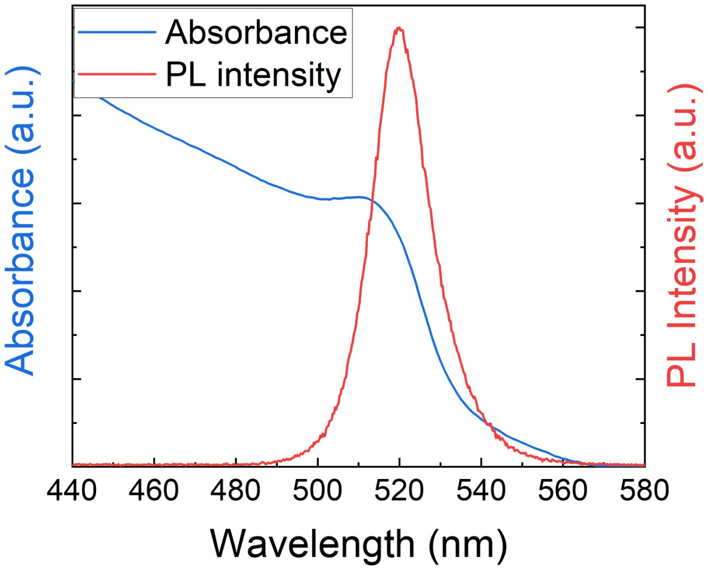

Figure 3.3: RT absorption and PL of $CsPbBr_3$ **Nanowires.** The PL was measured from a drop-cast thin film, whereas the absorption spectrum was acquired in solution at a relatively high concentration.

153]. Although the main UV–Vis absorption peak does not coincide exactly with the emission centre of $CsPbBr_3$ NWs (typically around 520 nm), plasmonic coupling can still occur due to the spectral overlap between the NW emission and the Ag NP absorption band.

Moreover, it is well established that the plasmonic resonance of Ag NPs undergoes a red shift upon introduction of a dielectric environment [82], which is the case in the hybrid structure designed in this chapter. This red shift moves the resonance peak closer to the NW emission, thereby enhancing the spectral overlap and potentially boosting the plasmonic enhancement effect.

For comparison, a separate batch of Ag NPs synthesized via a conventional wet chemical method was characterized using the same procedures. Figure 3.5(a) shows a TEM image of Ag NPs obtained by dropcasting the solution onto a TEM grid. Targeting a similar particle size, this method yielded Ag NPs with an average diameter of approximately 8 nm as indicated in Figure 3.5(b). However, when comparing the size distributions from both synthesis approaches, a broader Gaussian fit was observed for the sample prepared using the He droplet technique.

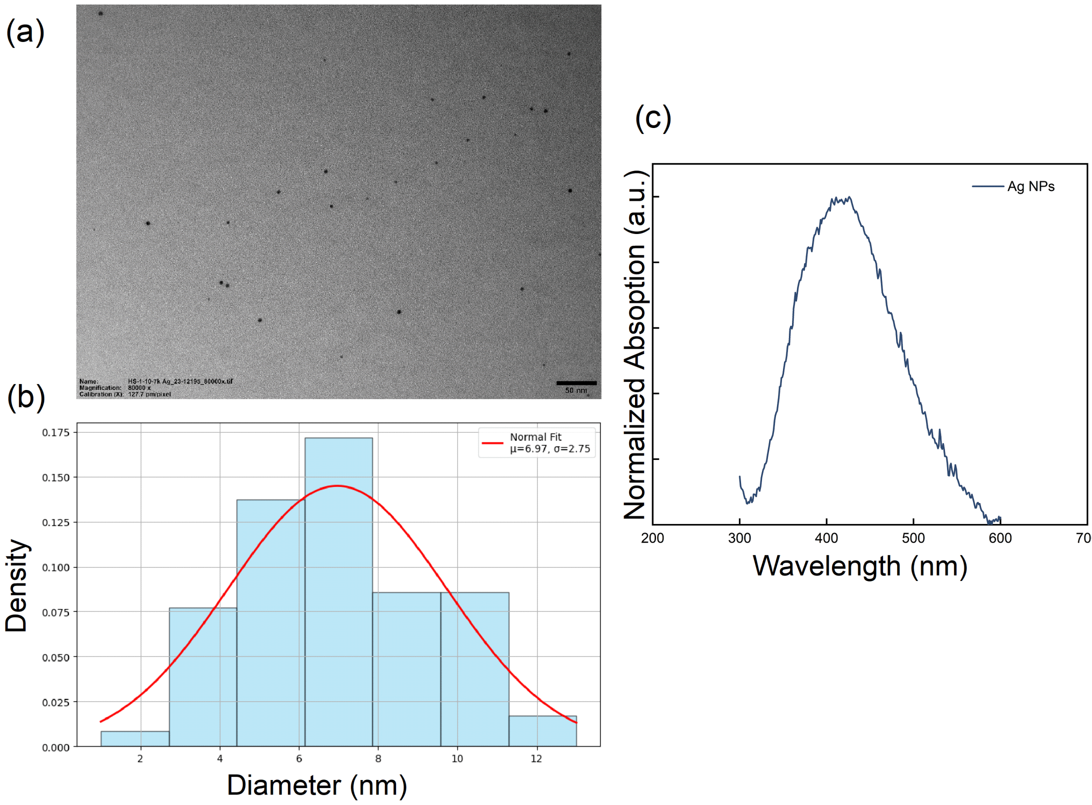

Figure 3.4: Characterization of He droplet synthesized Ag NPs. (a) TEM image of the Ag NPs dropcasted on the TEM grid. (b) The size distribution of the Ag NPs on Si substrate. The red curve refers to a normal distribution fitted to the histogram and shows an average of 6.97 nm. (c) UV–Vis absorption spectrum of the Ag NPs on Si substrate. The data presented in this figure were collected by Hao Sha from the group of Prof. Shengfu Yang at the University of Leicester.

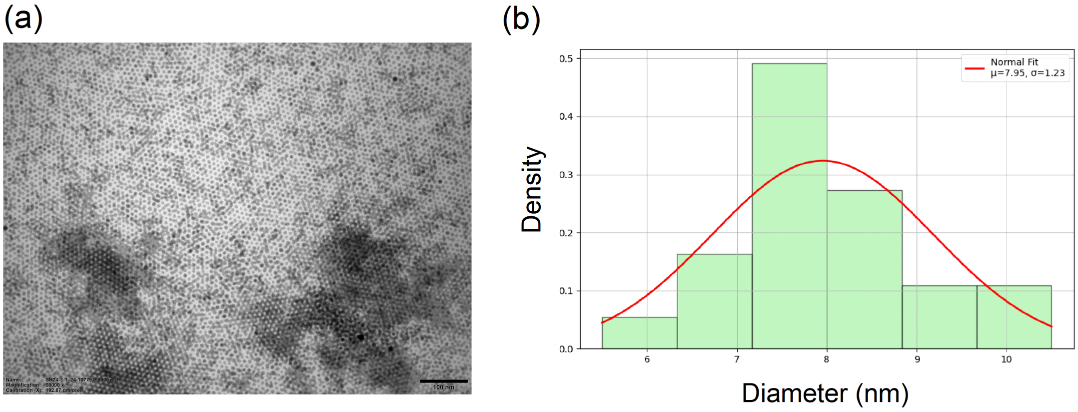

Figure 3.5: Characterization of wet chemically synthesized Ag NPs. (a) TEM image of the Ag NPs deposited on the TEM grid. (b) The size distribution of the Ag NPs on Si substrate. The red curve refers to a normal distribution fitted to the histogram and shows an average of 7.95 nm. The data presented in this figure were collected by Hao Sha from the group of Prof. Shengfu Yang at the University of Leicester.

This broader distribution is probably due to the relatively new and less mature status of the He droplet synthesis apparatus compared to the well-established chemical methods. As a result, the particle size distribution in practice is not as tightly controlled as initially anticipated. Nevertheless, precise tuning of the average particle size remains achievable, as the technique allows for systematic control through adjustment of experimental parameters. This flexibility proves advantageous for our experimental design, particularly in producing Ag NPs with a target mean diameter. Therefore, despite the current limitations, Ag NPs synthesized via the He droplet technique were still chosen as the preferred material for the subsequent experiments.

Hybrid Structure

As discussed in Section 3.2, the dielectric layer plays a critical role in facilitating plasmonic enhancement, where precise control over its thickness is essential. In this experiment, PMMA was employed as the dielectric/buffer layer.

To prepare the PMMA solution, 50 mg of PMMA powder was dissolved in 10 ml of toluene and heated at 60 °C for 30 minutes. The solution can be further diluted to obtain PMMA solutions of varying concentrations. These solutions were subsequently spin-coated onto the substrate to form PMMA thin films with different thicknesses, as illustrated in Figure 3.6.

There are abundant options for dielectric layers, while PMMA features easily tunable thickness, high transparency and stable properties. The thickness of PMMA films can be reliably tuned by adjusting the concentration of the solution and spin-coating parameters such as speed and duration [154], as indicated in Figure 3.6. PMMA is highly transparent across the UV–Vis range, which ensures minimal optical interference with the plasmonic response of the Ag NPs. Also, PMMA is chemically stable, non-reactive with metallic NPs and resistant to environmental degradation under ambient conditions. This chemical inertness ensures that the dielectric layer does not introduce unwanted chemical interactions or artifacts during optical measurements [155].

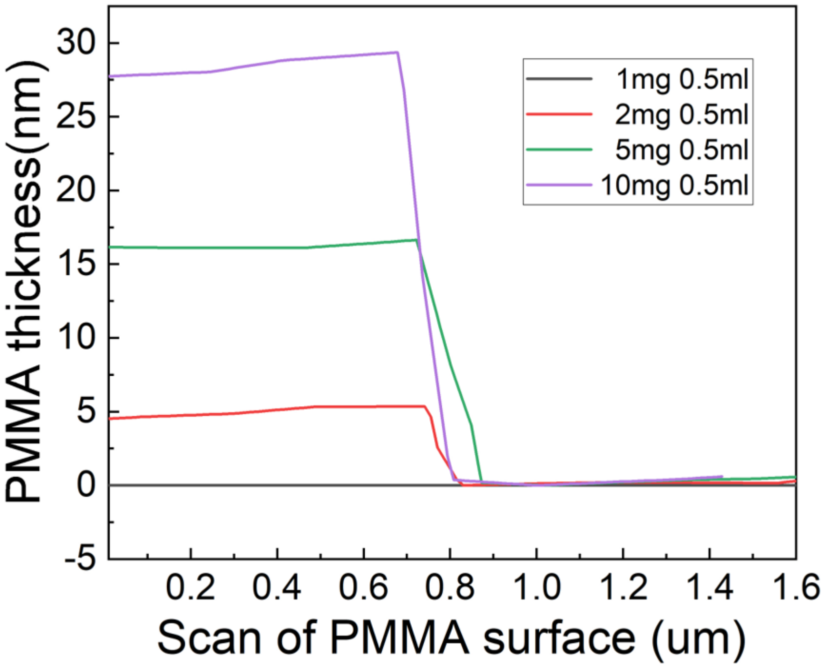

Figure 3.6: AFM measurements of PMMA layer thickness obtained from solutions with different concentrations. Different PMMA solutions were spin-coated onto silicon substrates, with scratches introduced to enable thickness determination. The data presented in this figure were collected by Hao Sha from the group of Prof. Shengfu Yang at the University of Leicester.

In the standard procedure for the hybrid sample preparation, Ag NPs are first deposited directly onto the Si substrate using the He droplet technique. Following this, a PMMA layer is spin-coated onto the substrate to achieve the required film thickness based on the specific experimental design.

Finally, a diluted $CsPbBr_3$ NW solution is spin-coated onto the top layer, using 20 µL per sample at 3000 rpm for 1 minute. After spin-coating, the samples are left to dry and then stored under appropriate vacuum conditions to ensure measurements are performed while the samples remain fresh. This step is critical to prevent PL peak shifts caused by the intrinsic instability of perovskite materials, which are known to degrade easily under ambient conditions [156, 157].

3.4 Setup

In this chapter, the Ti:Sapphire system with an emission wavelength of 400 nm and a tuneable repetition rate was employed for all the μPL data except for the ones achieved in mappings. An APD detector with TCSPC cards featuring 4 ps per bin or 25 ps per was connected to the Princeton spectrometer for TRPL measurements. Liquid He was connected to the cryostat for cryogenic measurements.

3.5 µPL Characterization and Device Design

3.5.1 μPL Investigation of Nanowires

To investigate the plasmonic enhancement effect of Ag NPs on the PL of perovskite NWs, it is essential first to determine the intrinsic emission mechanism of the NWs themselves. As discussed in previous sections, the PL emission of perovskites can originate from either excitonic recombination or free carrier recombination. When the structural dimensionality of the material is reduced from bulk to 2D films, 1D NWs, or even 0D QDs, quantum confinement effects become more pronounced. This increased confinement leads to an enhancement in exciton binding energy, which in turn promotes the formation and stability of excitons as the dominant photoexcited species [158].

Previous studies have confirmed that in low-dimensional perovskite structures, including NWs, PL emission is predominantly governed by excitonic recombination due to strong quantum confinement and enhanced exciton binding energies [159–161]. Specifically, μPL observation on single colloidal mixed-halide $CsPbX_3$ NCs at low temperatures reveals sharp emission peaks and excitonic fine structure, illustrating clearly the signatures of strong exciton confinement in 0D perovskites [159]. Strong exciton–photon coupling has been observed in perovskite NWs, with Rabi splitting reaching up to ~560 meV near the exciton resonance, indicating exciton-dominated behaviour [160]. Additionally, time-resolved and power-dependent PL measurements in low-dimensional perovskite films revealed carrier dynamics consistent with excitonic recombination, supporting the conclusion that excitons dominate the radiative process under typical excitation conditions [161]. Furthermore, perovskite materials typically exhibit exciton binding energies exceeding thermal energy at RT, promoting excitonic behaviour even without cooling [53].

Enhanced quantum confinement and increased exciton binding energy, which favour the formation of stable bound electron–hole pairs even at RT. However, since the emission mechanism can still be influenced by specific factors such as size, temperature, excitation density, and defect density, it is necessary to experimentally verify the excitonic nature in our samples under relevant conditions. To this end, we undertook μPL measurements on NW/Si structures at both RT and 4 K to examine their intrinsic emission behaviour before introducing any plasmonic components.

Measurements on Nanowires

To investigate the intrinsic PL emission mechanism of $CsPbBr_3$ NWs, a power-dependent μPL on bare NW samples was performed. The samples were prepared by spin-coating NWs onto a. PMMA-coated Si substrate and b. bare Si substrate with proper cleaning. In our configuration, PMMA serves mainly as a spacer. Excitation was provided by the Ti:Sapphire pulsed laser with a repetition rate of 76 MHz, focused to a beam diameter of 1 µm, with the excitation power varied from several μW to 1 mW.

Measurements were mainly conducted at ∼4 K to suppress thermal effects, reduce phonon scattering, and enhance the resolution of possible spectral substructures. At 4 K, the PL spectra of $CsPbBr_3$ NWs exhibit distinct differences depending on the underlying substrate, as indicated in Figure 3.7. For NWs deposited on a PMMA-coated Si surface, two relatively well-resolved peaks can be discerned: a dominant peak at 529.5 nm and a weaker shoulder-like feature around 532.5 nm. In contrast, NWs directly deposited onto bare Si surface exhibit a single broad emission peak centred at ∼530 nm, with a characteristically asymmetric sharp increase on the blue side and gradually sloping on the red side. The low excitation power data of NW/Si was excluded from the plot due to relatively low peak intensity and thus low signal-to-noise ratio.

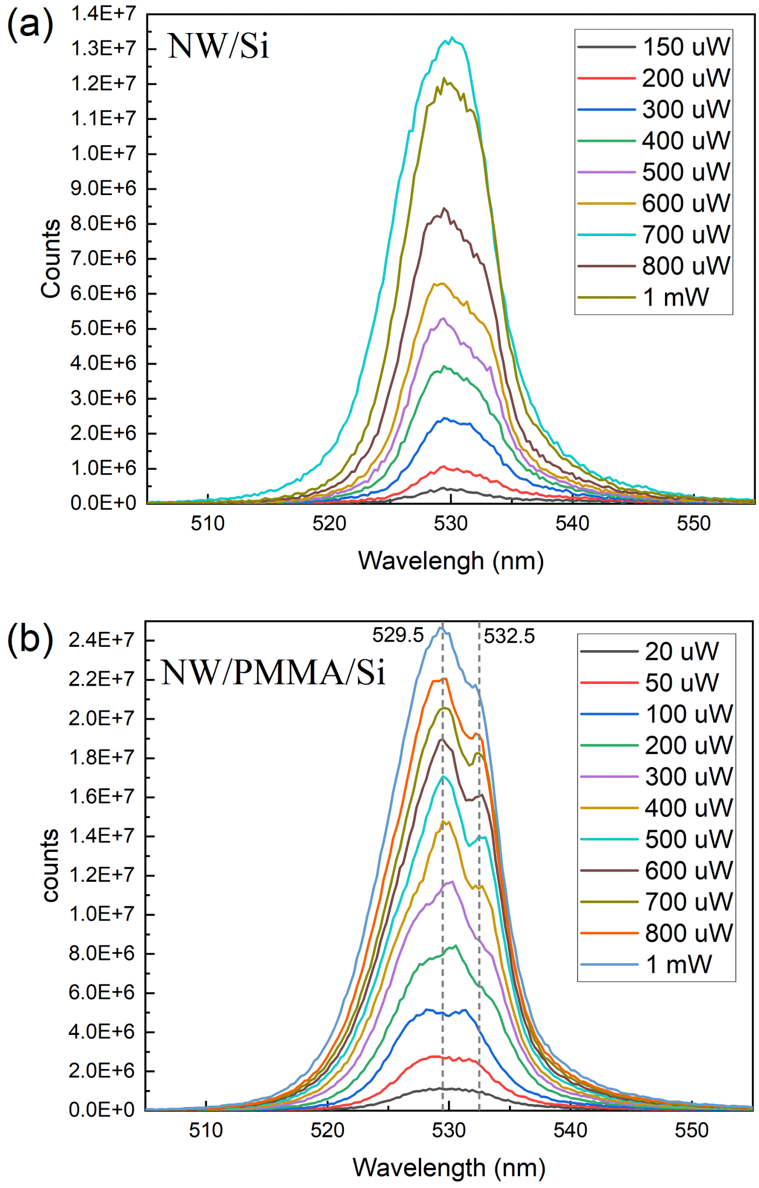

Figure 3.7: Power dependence of PL spectra of $CsPbBr_3$ **NWs at 4 K under pulsed excitation (400 nm), comparing two sample configurations** (a) NWs spin-coated directly on bare Si. (b) NWs spin-coated on a PMMA-covered Si substrate. In the NWs/PMMA/Si sample, two emission features are partially resolved, with a main peak at ∼529 nm and a weaker shoulder at ∼532 nm. The NWs/Si sample exhibits a single broader and asymmetric peak, suggesting a superposition of the same emission components without spectral resolution.

Such asymmetric shapes are commonly observed and do not necessarily imply the presence of complex or multiple emission mechanisms directly. Rather, this slightly trapezoidal profile may be attributed to spectral inhomogeneity arising from NW size and orientation distributions, asymmetric local density of states, or even to residual unresolved fine structure.

Distributional, compositional or lattice inhomogeneity: NWs were not uniformly distributed in terms of size, shape, or spatial positioning. Even with spin-coating, aggregation or clustering of NWs with varying dimensions may occur, resulting in local optical inhomogeneities. Moreover, both the PMMA layer and the NWs were processed using toluene as the solvent; consequently, spin-coating the NWs onto PMMA can partially redissolve the PMMA layer, promoting excessive NW clustering. At cryogenic temperatures, the PL linewidth narrows primarily due to the suppression of phonon-assisted broadening, which enhances spectral resolution and may reveal deviations from an ideal Gaussian lineshape. In such cases, the distribution of NWs itself results in slight peak asymmetry, broadening, or the appearance of side shoulders. While the PL spectra analysed here were selected from regions with relatively narrow and representative peaks, rather than rare spots, they may still be affected by such morphological variations. Therefore, although the data reflect typical spectral behaviours of the sample, the influence of spatial and structural inhomogeneity cannot be entirely ruled out.

Even in uniform $CsPbBr_3$ NWs, small spatial variations in halide composition or lattice strain can lead to slight local bandgap shifts [162]. These appear as low-energy shoulders or broadened tails adjacent to the main exciton peak, especially when the secondary domains are weak or not well resolved.

In the sample with a PMMA layer, the resolution at low temperature was relatively better to make this effect visible as a subtle second peak at 532 nm, clearer at stronger excitations; in the sample without the PMMA, the same feature appears merged with the main peak, manifesting as an extended red tail.

Asymmetric density of states: In low-dimensional perovskite structures, confined excitons often exhibit an asymmetric DOS due to localization introduced by spatial localization induced by lattice strain and structural imperfections, especially for solution-process-based perovskite materials [163]. Interactions between excitons and low-energy lattice vibrations can produce sidebands or red-shifted tails, especially at cryogenic temperatures. As a result, the PL emission line under 4 K may present a sharp high-energy cutoff with an exponential low-energy tail even for pure excitonic recombination due to the exciton localization, where low-temperature conditions suppress thermal hopping between localized states. [164, 165].

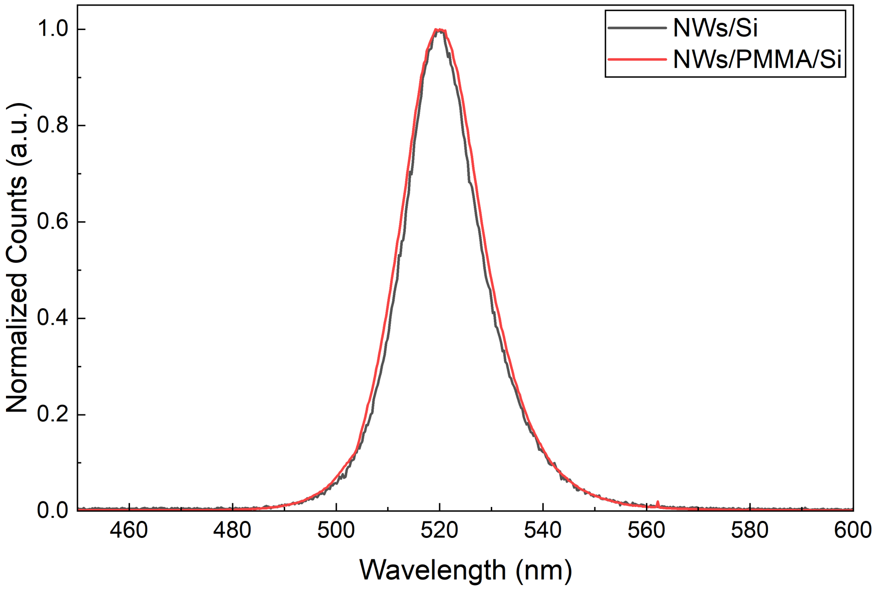

Figure 3.8: RT PL of $CsPbBr_3$ **NWs.** The samples were the same as in Figure 3.7. The peak centre were at 520 nm for both samples, with the fitted FWHM of ∼19 nm for the sample without PMMA and 20 nm for the one with PMMA, indicating a similar peak profile that is barely influenced by the PMMA layer at RT.

However, thermal activation of phonons at RT allows excitons to escape from shallow traps, enhancing spatial averaging and producing a more symmetric and homogeneously broadened spectrum [163, 166]. As in Figure 3.8, the PL spectra featured a broader and more Gaussian-like shape at RT for the same samples. This temperature-dependent phenomenon of the peak shape further supports a scenario where exciton recombination, modulated by localized phonon-assisted transport, is contributing to the radiative process in these NWs.

Residual fine structure: While these minor features such as low-energy shoulders or asymmetric tails may partially originate from compositional or morphological inhomogeneities within the NW ensemble, they are also consistent with the presence of unresolved excitonic fine structure. In strongly confined perovskite nanostructures, quantum confinement enhances excitonic fine-structure splitting, and at cryogenic temperatures excitons preferentially occupy the dark ground state, making its weak emission and associated dynamics experimentally relevant. Previous studies have reported that bright–dark exciton splitting arises typically on the order of a few meV in perovskite nanostructures [167, 168]. Additional splitting can result from shape anisotropy or dielectric confinement effects in NWs [169]. Although the spectral resolution in our measurements does not resolve these components individually, their combined contribution may manifest as a broadened low-energy tail or shoulder near the main peak, particularly at cryogenic temperatures where homogeneous broadening is suppressed [169].

In fact, slight spectral asymmetry of this kind is widely regarded as a natural signature of excitonic PL in many perovskite nanostructures, particularly those synthesized via solution-phase methods [170]. While the presence or absence of PMMA alters the appearance of secondary features, the fundamental nature of the emission remains unchanged. These variations in line shape likely reflect minor structural inhomogeneities and confinement-related optical effects rather than a change in recombination mechanism.

Discussion on PL mechanisms

Although the PL emission spectra at RT feature a symmetric, Gaussian-like profile, indicating classic free exciton behaviour for low-dimensional NCs, a detailed discussion of the dominant recombination process is still significant for understanding the optical properties.

As previously reviewed, excitonic recombination typically governs the PL response in NW structures. In our measurements, no distinct sub-bandgap emission, secondary red-shifted peaks, or power-dependent spectral changes were observed. If the emission were primarily trap-assisted, given the limited density of trap states, spectral broadening or peak shifting due to power-dependent trap filling effects would be expected [171]. Intuitively, the absence of such features suggests that trap states do not dominate cryogenic PL emission [172–174]. This further evidences the quality of the NW samples.

The stability of the PL peak position across a wide range of excitation powers, combined with the absence of high-energy blue-shifts, further supports the interpretation that the emission possibly arises from neutral excitonic recombination rather than free carrier with band-filling effects [175, 176].

However, the high aspect ratio of NW structures could enable further surface defects, leading to a substantial increase in trap state density. In such a scenario, the density of trap sites may be so high that photo-generated excitons are insufficient to saturate them, even under strong excitation conditions. To further evaluate the dynamics in the emission process, we adopt an alternative perspective by analysing the power-dependent PL intensity through a power-law relationship, which offers a more quantitative assessment [177, 178].

It is known that the emission intensity and the excitation power follows the relation [177]

$$I \propto P^{\alpha}$$

where I is the emission intensity and P is the power of the laser. α provides insight into the nature of the radiative recombination mechanism. $\alpha = 1$ indicates an ideal free exciton-generated PL, while $\alpha < 1$ often suggests either free-to-bound or donor–acceptor pair recombination [179], and in the context of perovskites, trap state [178] and localized exciton recombination [67, 180].

Here, a log–log plot is introduced to directly extract the α value. Figure 3.9 presents the integrated PL signal over the range 528–533 nm, covering the full emission peak without including spectral background. The resulting log–log plot of integrated PL intensity versus excitation power reveals a clear sublinear trend, well fitted by a power law $I \propto P^{\alpha}$ with $\alpha = 0.79$.

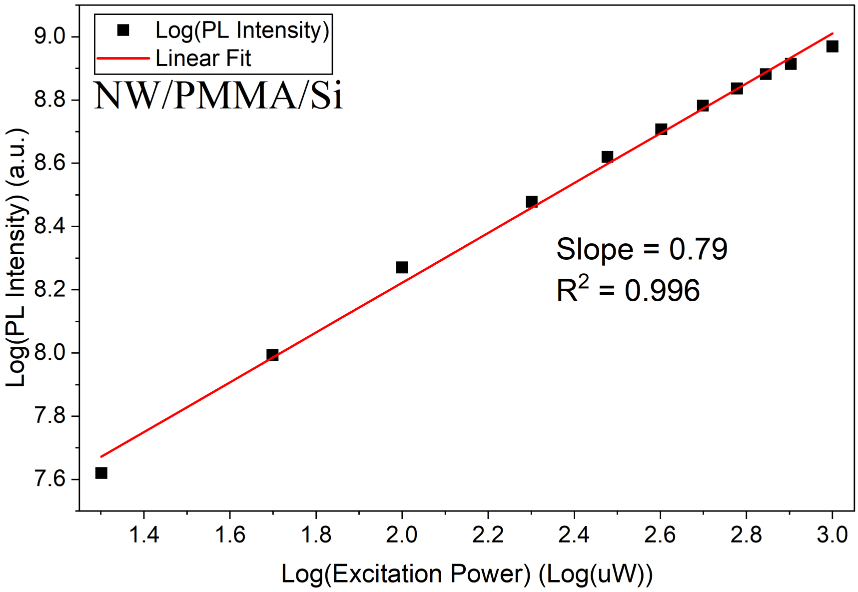

Figure 3.9: Log–log plot of integrated PL intensity as a function of excitation power at 4 K, from the NWs/PMMA/Si structure. The near-linear dependence (slope = 0.79, $R^2 = 0.996$) indicates localized-excitonic recombination dominates the emission process, with minimal contribution from free-carrier processes.

In experiments, typical free exciton-dominated emission normally features α between 1 and 2 [178, 181], while our power-dependent NW PL has a lower α. The observations, on the other hand, resemble the scenario reported by Keisei Shibata et al., where a lower-energy emission band appearing below the free exciton peak at 4 K exhibits a sublinear dependent ($\alpha = 0.74$) and no apparent spectral shift, which was attributed to localized exciton emission in the perovskite single crystal [67]. Another work on $MoSe_2$/CrSBr also presents the same interpretation for a even lower α value [180]. In our case, the low-temperature PL spectrum of the NW sample shows a comparable $\alpha = 0.79$ and a narrow peak spectrally invariant across a wide range of excitation powers, supporting the assignment to shallowly localized excitons rather than free excitons, where the latter case is likely to experience a high excitation density-induced blue-shift [182, 183].

Exciton localization in $CsPbBr_3$ NWs can arise from multiple general mechanisms. Point defects such as halide vacancies intrinsically introduce shallow trap states near the band edges, capturing excitons and causing localized low-energy emission [184];

the high surface-to-volume ratio of NWs magnifies the effect of surface states, where excitons reaching the surface can be trapped, altering recombination pathways and reducing radiative efficiency [184, 185]. Structural strain induces local band-edge fluctuations that form confinement potentials for excitons, well documented in low-dimensional materials [186]. Fluctuations in quantum confinement resulting from diameter inhomogeneity or compositional variation along the NWs create regions of enhanced exciton confinement that can trap carriers preferentially [187, 188].

Moreover, exciton–phonon coupling provides an intrinsic localization mechanism. In $CsPbBr_3$, strong Fröhlich coupling with LO phonons can distort the local lattice and trap excitons into STE states, particularly at low temperatures where thermal activation is insufficient to delocalize them [67]. These states typically emit red-shifted compared to free excitons and can dominate PL at cryogenic temperatures. STE emission is stable even under 4 K, with a much longer lifetime proved than free exciton decays [189].

Together, these mechanisms of defect traps, surface-state traps, strain-induced potentials, quantum confinement fluctuations, and LO phonon-mediated exciton self-trapping create complex, multi-pathway exciton localization in $CsPbBr_3$ NWs under 4 K.

From an exciton DOS perspective, localized excitons occupy spatially confined states, whereas free excitons occupy a broader, continuous DOS (see Figure 3.10). At 4 K, when the localization effect becomes significant, the excitons are predominantly captured by states located slightly below the continuum edge. These localized states are abundant in perovskite materials and play a key role in sustaining bright emission [190]. A portion of them recombined, generating PL without apparent peak shifting, compared to free exciton recombination. However, non-radiative pathways including traps suppressed their contribution to the PL signal, where abundant traps and localized states exist in the NW structure. As a result, even under a strong incident laser, the PL remains sublinear without a clear transition to free exciton-dominated emission.

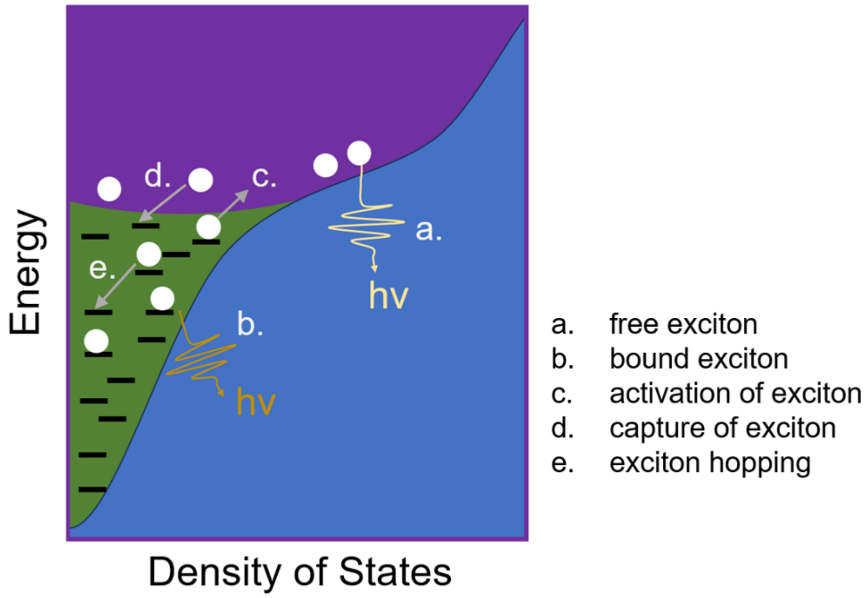

Figure 3.10: Diagram showing DOS versus energy in this model. Excitons can be excited to the free exciton state (purple area), or localized in the discrete localized states (black bars in green area). Different pathways including radiative recombination are indicated. As illustrated in this diagram, spatial and energetic disorder leads to a distribution of localized exciton states, resulting in inhomogeneous broadening and variations in the PL peak position across the sample. This figure is adapted from Ref. [191] with modifications and used with permission.

The PL characteristics shifted toward those expected for free exciton emission as temperature increased, accompanied by line broadening and the appearance of a symmetric peak profile. This behaviour can be interpreted as thermally activated detrapping of localized excitons into higher-energy free exciton states. A delocalizing energy for excitons of 13 meV was reported for 2D perovskite nanosheets [192]. In our NWs, an experimental $\alpha = 1.71$ ($R^2 = 0.998$) was obtained from power-dependent measurements (within the tens of μW range) on the same sample at RT, indicating excitonic recombination and other possible channels such as free carriers, further supporting the assumption above.

The RT environment provides sufficient thermal energy for localized excitons to escape from the potential wells of their localized states, as illustrated in Figure 3.10 c. The phonon energy at RT becomes comparable to the exciton de-localization potential and contributes to the formation of a free exciton ensemble, thereby modifying both the population dynamics and the resulting PL response [180].

Also, as shown in Figure 3.10, localized excitons generally occupy states near the bandgap. Previous work has investigated the DOS of localized excitons, reporting a temperature-induced broadening from a narrow, near-band-edge DOS at cryogenic temperatures to a broadened distribution at RT [193]. However, the reason for the broadened PL emission is consistently investigated and attributed to the interaction with phonons [67, 163, 166]. Although studies show that the energy splitting between localized excitons and free excitons expanded as temperature increased from 4 K to 300 K, with the peak shifting in the opposite direction observed near RT [67], it is often difficult to distinguish between the two peaks solely based on spectral position and profile because of the close energy states and possible exciton transfers [180], which further substantiates the earlier assumption regarding how PL shifts from 4 K to RT. It highlights that, compared to the continuous PL–temperature dependence, the power dependence of PL intensity provides a more reliable indicator for analysing the underlying emission mechanism.

In practice, transmission and coupling losses in the optical setup reduce the actual power reaching the sample surface to less than 50% of the nominal laser output, and the spatial distribution of NWs further weakens the absorption of excitation energies. Incorporating this loss factor into the carrier density estimate and the parameters from the laser setup, the effective peak carrier density per pulse is calculated to the order of $10^{18} \sim 10^{19}$ cm^{-3} in the power range. Despite this high instant carrier density which is comparable to or above the reported Mott threshold for perovskites [194, 195], no clear signs of exciton unbinding were observed, given the linear dependence in the log–log plot lacking the trend of α towards 2, which is typical for free carrier recombination. However, the minor bending at the strong-excitation end may refer to exciton–exciton annihilation. These strongly support the conclusion that recombination remains localized-exciton-dominated, and any high-density effects did not drive a transition of the mechanism in this excitation power regime.

Though clear enough for interpreting exciton behaviours, power-dependent PL alone is insufficient to unambiguously distinguish trap-state involvement, particularly when the trap density is high or when the excitation area is inhomogeneous. Trap-dominated emission also exhibits sublinear power dependence and even a constant spectral profile when states are not fully saturated under experimental conditions. To further clarify the recombination mechanism and distinguish between normal trap-mediated and excitonic emission pathways, we next turned to TRPL measurements, which provide insight into carrier lifetimes and non-radiative recombination dynamics.

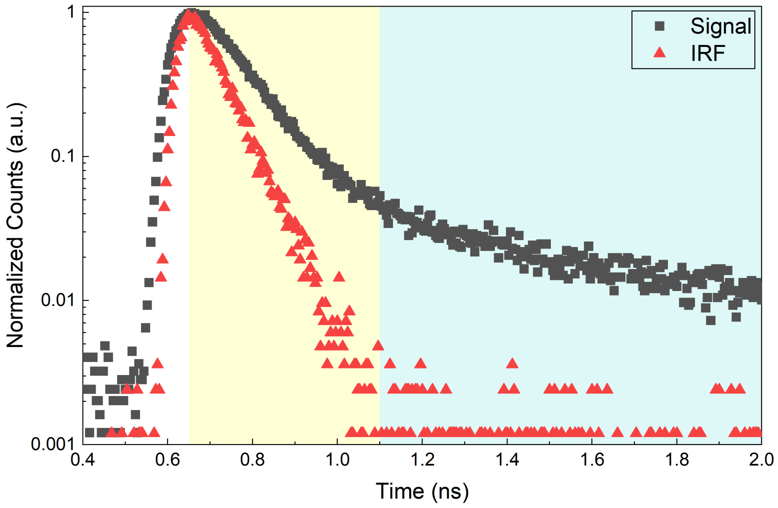

Figure 3.11: TRPL of NWs under 4 K. Different time regions highlighted in the figure referring to different dynamics. Yellow: localized excitons. Blue: traps. The lifetime for the single exponential region was fitted to 59.8 ps with IRF deconvoluted.

Figure 3.11 presents the TRPL data of measured at 4 K, together with the IRF for reference. The decay signal exhibits a clear biexponential shape, which can be segmented into two distinct time regimes based on the visible transition on the log–plot.

The initial fast-decay component (shaded in yellow) at 4 K, following a nearly-parallel increase along the triggering laser pulse, is attributed to the radiative recombination of localized excitons, consistent with the near-band-edge PL peak and its narrow linewidth. The lifetime was fitted as 59.8 ps, which is in agreement with previous reported lifetimes of low-dimensional perovskite NCs on the order of $\sim$ 10–100 ps [45]. Given the low temperature and prompt decay, the relatively sharp and monoexponential decay in this region is consistent with excitons trapped in shallow potential wells, for which the decay lifetime is reported to increase as the degree of localization weakens [45]. As stated previously, STE emission features significantly longer lifetime on the order of $\sim 100\,\text{ns}$ at cryogenic temperatures, which contradicts our observation on the NWs. To clarify, unless otherwise specified, the following discussion on localized excitons refers to those induced by shallow traps or confinement potentials.

In contrast, the later-time region (shaded in blue) displays a much slower and long-lived decay tail, which deviates from a simple monoexponential form. This long tail is likely associated with trap-assisted emission, where carriers are temporarily captured by deep trap states and subsequently recombine over extended time scales. This term, by proper fitting with IRF deconvoluted, was found to be 896 ps, dramatically longer than that of excitonic decay. The transition from the fast decay to the slower tail indicates the coexistence of different recombination pathways at cryogenic temperatures.

To further confirm the small lifetimes, the IRF is also shown in Figure 3.11, clearly demonstrating that both the temporal resolution of the system and the fitting results reliably reflect the intrinsic carrier dynamics, rather than being dominated by the detection system. In the trigger arrival region (shaded in white), the TRPL signal closely follows the rising edge of the IRF, indicating that the recorded photons originate from the excitation event and are not affected by spurious background signals. In the subsequent decay region, the TRPL signal exhibits a significantly slower decline in counts compared to the IRF, confirming that the time resolution of the TCSPC setup is sufficient to resolve the PL dynamics. If the PL decay curve were to exhibit a similar decay slope to the IRF, it would imply that the measured dynamics fall below the resolution limit of the setup, making it unreliable to extract meaningful insights into the emission mechanism.

To evaluate the contributions from localized excitons and the traps, we calculate the contribution of PL from different decay components. Given the biexponential decay fitting form

$$I(t) = A_1 e^{-\frac{t}{\tau_1}} + A_2 e^{-\frac{t}{\tau_2}}$$

where A_i is the amplitude of each component. The photon contribution from recombination process i at an arbitrary time t can be expressed as $A_i e^{-t/\tau_i}$.

The total emission intensity is the integral of $I(t)$ over the full time range:

$$I = \int_0^{+\infty} I(t) = A_1\tau_1 + A_2\tau_2$$

According to van Driel et al., the excited-state density is obtained by time-integrating the emission curve, and different decay components must be weighted by their respective radiative decay rates [196]. Therefore, when comparing contributions from biexponential TRPL fits, $A_i\tau_i$ refers to the total photon output of the corresponding decay, while $1/\tau_i$ serves as a coefficient related to the instantaneous radiative state density. Depending on the aspect of interest, a careful selection of the comparison approach is a must. In our context, we are primarily interested in the overall PL performance and the potential enhancement induced by Ag NPs, and therefore the weight of each recombination component should be evaluated by the term $A_i\tau_i$.

Our fitting yielded amplitudes of $A_1 = 13.14$ for the fast mono-exponential decay and $A_2 = 0.184$ for the long tail. Additionally, the fitting results from EasyTau directly provided the integrated intensities (i.e., total photon counts attributed to each component), showing consistent values of $I_1 = 196.2\,\mathrm{kCounts}$ and $I_2 = 41.1\,\mathrm{kCounts}$, indicating that the contribution from localized excitons was approximately 4.8 times of that from the trap-assisted emission component. These results demonstrate that the PL emission of the NW sample is primarily dominated by localized exciton recombination, accompanied by a non-negligible trap-assisted process.

The lifetime for the main radiative channel varies. The fast decay component observed in our TRPL measurements is attributed to localized excitons, while in fact it is a combined process involving both rapid trap capture and exciton recombination [197, 198]. The recombination rate $\Gamma_1 = 1/\tau_1$ can therefore be expressed as a sum of two parallel channels:

$$\Gamma_1 = \Gamma_{\text{rad}} + \Gamma_{\text{cap}} = \frac{1}{\tau_{\text{rad}}} + \frac{1}{\tau_{\text{cap}}},$$

where the second term represents the non-radiative trap-capture process. Due to the high density of trap states in $CsPbBr_3$ NWs, this effect contributes to a further reduction in the measured lifetime. In such cases, gradual trap filling or the elimination of capture channels may, in contrast, result in a lengthened lifetime for the initial decay range.

Moreover, while the intrinsic radiative rate of excitons is typically constrained by momentum conservation, spatial localization alters the exciton momentum distribution and thus modifies the probability of radiative recombination. Depending on the localization strength, this effect can either enhance or suppress the radiative transition rate [199]. Previous studies have predicted that shallow localization may increase lifetime under certain spatial regimes, while in practice, significantly prolonged lifetimes have been observed for strongly localized states [199, 200].

These factors suggest that in our system, any variation in lifetime must be interpreted with care, particularly under plasmonic coupling, as changes may result not only from modifications in the radiative channel, but also from altered trap capture dynamics and exciton localization behaviours.

Overall, the combined analysis reveals dual contributions from localized exciton and trap-assisted emission processes, which dominate different time regimes in the TRPL profile. However, the localized exciton recombination pathways are primarily associated with defects, shallow traps, and confinement potentials. Therefore, although trap-assisted emission is not the dominant radiative pathway, the presence of significant defect- and surface-related contributions can be inferred in this sample. This conclusion provides an important reference for the subsequent discussion on the mechanism of plasmonic enhancement.

Since localized exciton radiative recombination has been identified as the dominant mechanism, and considering the fast decay dynamics of the NWs as well as the resolution of our TCSPC system, we focus our analysis on the early-stage decay within the first few nanoseconds. Moreover, our primary objective is to investigate the overall PL enhancement induced by plasmonic Ag NPs, which reflects an integrated outcome of multiple recombination processes. Therefore, instead of applying a biexponential fit to deconvolute individual decay components, we consistently employ a monoexponential fitting approach within the dominant decay window to extract representative lifetimes for comparison.

Moreover, despite the use of pulsed excitation and the generation of relatively high instant carrier densities, no signature of stimulated emission or lasing was observed in the measured power range. Specifically, the log–log plot of integrated PL intensity as a function of excitation power (Figure 3.9) did not reveal any threshold-like nonlinearity or abrupt change in slope. The emission spectra remained the same shape and width, with no spectral narrowing or other features typically associated with lasing. The extracted power-law exponents are consistent with spontaneous excitonic recombination under moderate to high excitation conditions. This is likely due to the structural limitations that NWs were not perfectly straight with well-defined facets, which is crucial for Fabry–Pérot modes, along with random orientation and dense arrangement that prevents coherent optical feedback, despite sufficient excitation conditions [50, 194].

The peak profile, on the other hand, provides no prominent signs of saturation or quenching up to excitation powers of 1 mW for NW samples, indicating that the power-dependent response remained reliable and measurable throughout this range. These results confirm that all PL behaviour reported here originates from spontaneous emission processes, further confirming the input power range for the following measurements.

3.5.2 μPL Investigation on Nanowires with Ag Nanoparticles

To understand the impact of introducing Ag NPs on the optical properties of NW systems, we first conducted preliminary measurements on a series of samples prior to parameter optimization. The samples in this section were NW/Si, NW/Ag/Si and NW/PMMA/Ag/Si (top to bottom) structures with a more diluted NW solution spin-coated on the top layer. The thickness of the PMMA layer was about 15 nm and the size of Ag NPs was under 10 nm. At RT, the surface luminescence characteristics of each sample were generally uniform, so we used Gaussian fitting to briefly analyse their PL spectra. In contrast, at low temperatures (4 K), the samples exhibited significant inhomogeneity, so we performed PL and TRPL measurements at multiple locations on each sample to more comprehensively assess their localized emission behaviour. We also performed PL time series measurements to verify the PL stability of the samples under excitation. These results are discussed below.

4 K PL and TRPL

The coupling between LSPR and PL is strongly temperature-dependent. As previously discussed, at 4 K, the PL spectra exhibit minimal phonon-induced broadening, while the overall signal is enhanced due to suppressed non-radiative processes. This leads to improved spatial resolution in μPL measurements. In addition, the emission mechanism of NWs at low temperature has been extensively studied, providing a reliable basis for further investigations. The suppression of phonon activity at 4 K also reduces electron-phonon scattering in metallic structures, resulting in less damping and stronger local field confinement, i.e., enhanced LSPR. Simultaneously, trap states that require thermal activation are effectively deactivated at cryogenic temperatures, allowing a more intrinsic observation of coupling behaviour. Samples are also more stable under low-temperature vacuum conditions, where the lack of surface adsorbates and reduced ion migration minimize photobleaching and spectral shifts. In general, low temperatures offer a clearer physical picture and stronger field–matter coupling. Therefore, low-temperature μPL measurements were chosen as the starting point for investigating the coupling between NWs and plasmonic Ag NPs.

Figure 3.12 presents both μPL and TRPL results measured at 4 K. The excitation power was 2 μW at a repetition rate of 7.6 MHz and wavelength of 400 nm, corresponding to a fluence of approximately 67 μJ/cm^2 per pulse. For each sample, multiple positions were measured; however, representative spectra with relatively strong emission are shown for comparison. Plotting them together facilitates a direct evaluation of relative PL intensities. The variability in PL peak shape and width is attributed to the inhomogeneous distribution of NWs and the collective emission from NW clusters. The peak shifts observed in the figure are not representative of the average peak position for a given sample. In fact, PL profiles varied unpredictably as the sample was scanned across micron-scale regions, confirming significant spatial inhomogeneity. Notably, sharp sub-peaks with FWHM down to ~1 nm were occasionally observed, which are attributed to emission from individual NWs. A clear enhancement in PL intensity is observed upon the introduction of Ag NPs, while the NW/PMMA/Ag/Si full structure yields an even greater increase, with peak intensities differing by orders of magnitude compared to the NW-only configuration.

We measured TRPL at multiple selected spots for three types of samples: NW/Si, NW/Ag/Si, and NW/PMMA/Ag/Si. As explained above, the fitting was conducted to mainly extract the dominant early-stage decay process, which reflects the primary radiative recombination pathway. The recorded lifetimes are presented in table 3.1.

Table 3.1: TRPL lifetimes (in ps) measured at different sample positions for each configuration. Starred points indicate specific positions of interest (see text for discussion).

Sample	**P1**	**P2**	**P3**	**P4**	**P5**	**P6**	**P7**
NW/Si	84	81	102	149**	100	101	120
NW/Ag/Si	68	70	41*	32*	29*	31*	107**
NW/PMMA/Ag/Si	128	121	123	121	121	128	122

* Denotes fast-decay positions with strong LSPR coupling or potential trap-assisted quenching.
** Indicates positions with longer lifetimes, possibly due to weak coupling or different NW density.

For the reference NW/Si group, the lifetimes mostly fall in the range of 80–150 ps, with an average around 100 ps, which is consistent with radiative recombination of shallow localized excitons at low temperature. Since non-radiative losses are suppressed at 4 K, the lifetime mainly reflects the balance between radiative decay and trap capture. The relatively broad distribution could be due to inhomogeneity in trap density or clustering of NWs.

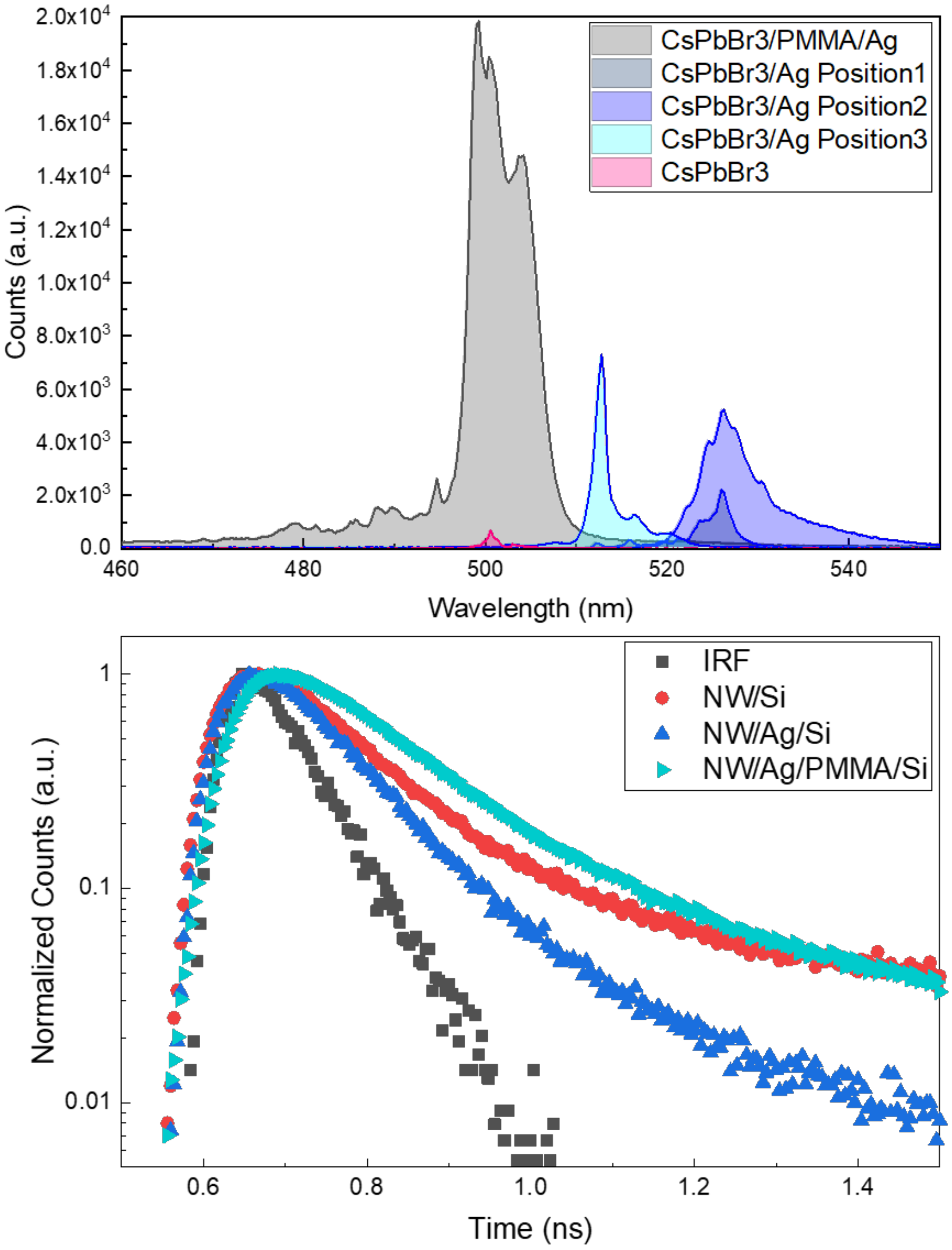

Figure 3.12: PL and TRPL of NW/Si, NW/Ag/Si and NW/PMMA/Ag/Si structures at 4 K. PL and TRPL at different positions showcased the enhancement from Ag NPs. More positions were investigated and estimated enhancement factor was ∼ 4 for only introducing Ag NPs and ∼ 29 for the full structure.

Compared with the reference NW/Si group, the NW/Ag/Si samples show a clear decrease in lifetime, especially in regions where the values drop below 40 ps. This behaviour is generally consistent with enhanced radiative recombination due to LSPR coupling from Ag NPs. For points that show longer lifetime (e.g. 107 ps), it's likely that the NWs at the position were not efficiently coupled to the Ag NPs—either due to physical separation or weak field overlap. However, it is also observed that the TRPL decay curves in NW/Ag/Si deviate more strongly from monoexponential behaviour, suggesting that additional non-radiative or fast relaxation channels may be active. One possibility is that the direct contact between NWs and Ag introduces new interfacial traps or quenching sites, increasing the contribution from ultrafast non-radiative capture processes. These ultrafast components reduce the apparent lifetime and also distort the decay shape, making the overall fitting less clean.

The NW/PMMA/Ag/Si samples show the strongest PL enhancement—up to 30× higher intensity compared to NW/Ag/Si. This suggests that the addition of a PMMA spacer layer not only improves emission efficiency, but also stabilizes the recombination dynamics. In this configuration, the dielectric layer helps suppress quenching effects by physically and electronically isolating the NW surface from the Ag interface. At the same time, the PMMA can still maintain sufficient near-field coupling to support LSPR-induced enhancement of the radiative rate. However, the altered local dielectric environment at the PMMA/perovskite interface can modify the spatial distribution of the excitonic wavefunction through dielectric confinement of the local optical field, which may enhance exciton localization and reshape the LDOS. In a scenario where radiative recombination is dominated by localized excitons associated with shallow trap states, stronger localization can promote carrier capture into radiative traps, thereby increasing the radiative recombination rate and, in principle, shortening the radiative lifetime [199, 201]. As a result, the balance of both mechanism shifts toward a cleaner and more efficient radiative process. In this sense, the modulation of radiative recombination dynamics via a dielectric spacer appears more favourable than direct metal contact, which introduces competing non-radiative effects. Such observation is consistent with previous reports where dielectric layers were employed to ensure sufficient plasmon-photon coupling [160, 202].

Moreover, several TRPL measurements were conducted under different excitation powers. The analysis revealed that, in the excitation regime in our measurement (from tens of nW to a few μW), the decay curves remained nearly unchanged in shape with varying total counts. This indicates the minimal contribution of power-dependent higher-order quenching mechanisms, such as Auger recombination or exciton–exciton annihilation [159]. Therefore, the observed differences in decay dynamics across samples can be more confidently attributed to intrinsic emission properties or plasmonic coupling effects, rather than carrier-density-driven recombination processes.

These observations together, suggest that the PL enhancement mechanism in NW/PMMA/Ag/Si is not solely due to stronger field coupling with LSPR, but also due to the suppression of loss channels. While NW/Ag/Si exhibits stronger local fields in theory, the overall emission efficiency is reduced by faster contact-induced energy dissipation. In contrast, the PMMA-spaced structure achieves a better trade-off between field enhancement and trap suppression, resulting in both higher PL intensity and more regular decay behaviour.

RT PL and Time Series

RT PL measurements were conducted across each sample to assess the spectral uniformity and emission characteristics, and further test the stability of such hybrid structures at ambient RT and air. As shown in Figure 3.13(a–c), all three structures (NW/Si, NW/Ag/Si, and NW/PMMA/Ag/Si) exhibit well-defined emission peaks centred around 520 nm, with FWHM ranging from 10 to 16 nm. The spectra are well-fitted by Gaussian functions, suggesting that the emission arises predominantly from a single radiative recombination channel, likely free exciton recombination. While slight variations in peak position, linewidth, and intensity are observed at different positions on the same sample, these shifts remain within 100 meV, indicating overall spectral uniformity across the sample surfaces. Notably, the introduction of Ag NPs

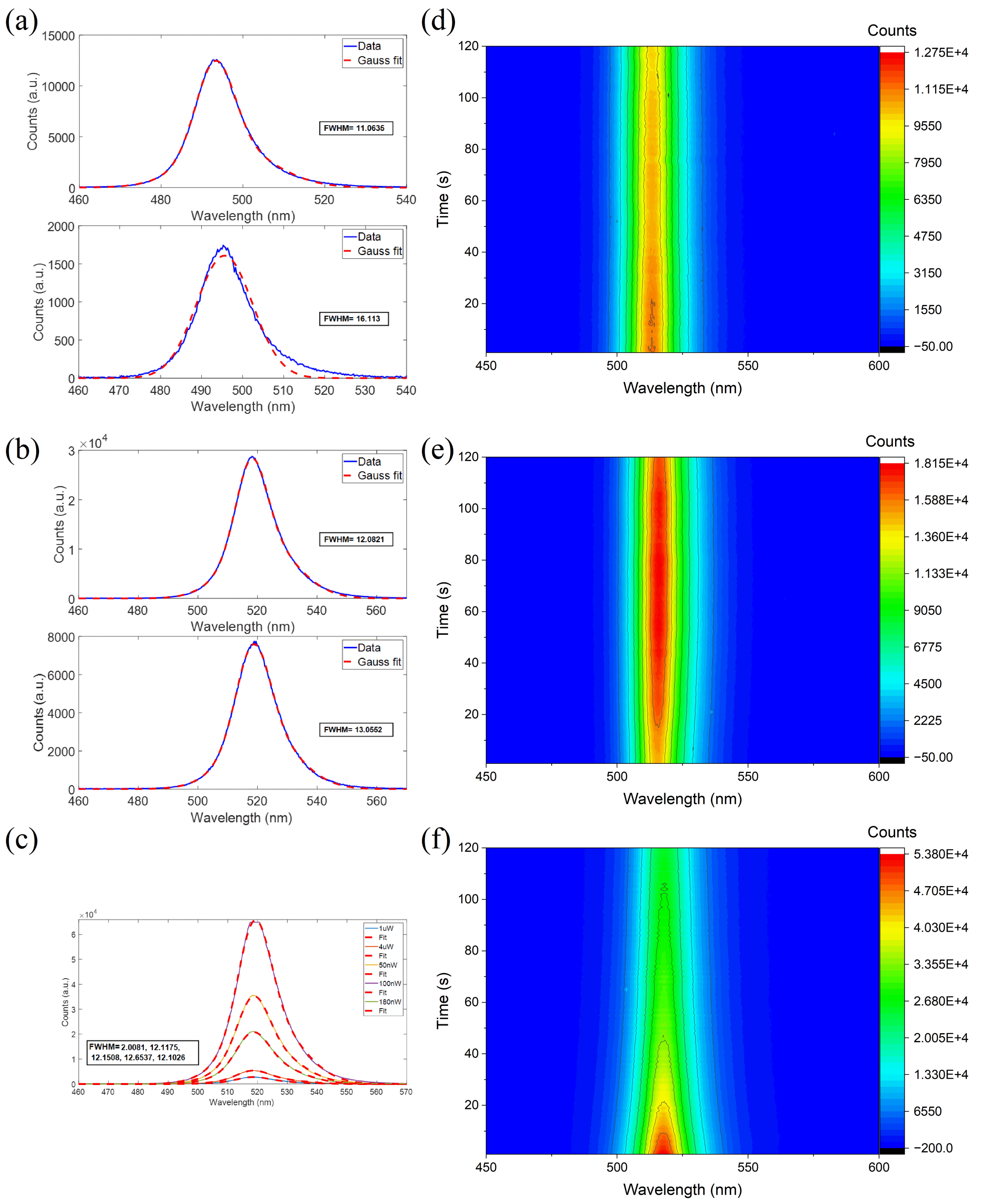

Figure 3.13: Room-temperature PL spectra and their temporal evolution. (a–c) Position-dependent PL spectra of NW/Si, NW/Ag/Si, and NW/PMMA/Ag/Si, respectively. Each spectrum exhibits a Gaussian profile; fitted curves and extracted parameters are labeled accordingly. For NW/PMMA/Ag/Si, a power-dependent measurement was performed, while for NW/Si and NW/Ag/Si the excitation power was fixed at 4 μW. (d–f) PL time series measurements for the corresponding samples. The excitation power was measured 400 μW. Note: ND filters were applied during the time series acquisition; as a result, the absolute PL intensities differ from the counts shown in the spectra. All experiments were conducted in air, rather than under vacuum.

does not induce any consistent redshift or blueshift in the emission peak, suggesting minimal perturbation to the excitonic energy levels. Among the three samples, NW/PMMA/Ag/Si exhibits the highest PL intensity under identical excitation conditions (4 μW). Although this enhancement may be indicative of plasmonic coupling, contributions from local NW aggregation, variations in emitter density, or substrate-induced effects cannot be excluded.

The RT PL time series measurements (Figure 3.13(d–f)) reveal distinct time-series behaviours across the three sample configurations. The NW/PMMA/Ag/Si sample exhibits the highest initial PL intensity, followed by a rapid decay throughout the measurement period. This suggests that while the PMMA spacer, aiming to position the NWs at an optimal distance from the Ag NPs to achieve strong plasmonic enhancement, it also hinders charge dissipation and thermal relaxation, in which case strong local heating and the activation of non-radiative pathways appears, ultimately compromising stability despite the initial strong emission. This could also be attributed to the field distribution of the incident light, where the most intense portion of the electric field from the laser was concentrated in the PMMA layer, leading to strong localized heating that damaged the perovskite NWs. Notably, at the position shown in Figure 3.13(c), we also confirmed that incident powers above 1 μW could damage the sample, likely due to the enhanced localization of both the optical field and thermal energy caused by the presence of the PMMA spacer.

In comparison, the NW/Ag sample displays moderate initial PL intensity but the most stable emission over time. A slight initial increase is observed within the first 20 seconds, followed by a plateau with minimal decay. This suggests that direct Ag contact, while potentially introducing non-radiative losses, may also assist in stabilizing surface states or facilitating charge extraction, thus suppressing minutes-level degradation which happened with PMMA layer introduced.

However, this structure surprisingly features the best stability despite that Ag NPs are prone to oxidation in ambient air, which could be significantly accelerated under laser excitation. Localized photothermal heating and hot-carrier generation during laser irradiation enhance reactivity with oxygen and trace moisture, promoting the formation of silver oxide, which degrades plasmonic performance and hence the PL intensity [203, 204]. This could suggest that under the excitation powers used, oxidation is not severe enough to impact the optical performance within the measurement timescale. Alternatively, the NW–Ag interface may promote efficient carrier extraction or localized field redistribution that stabilizes the emission. It is also possible that partial oxidation of Ag may occur, but it does not immediately affect the plasmonic coupling, especially if a thin native oxide layer forms while not fully quenching the enhancement.

The bare NW sample shows the weakest PL intensity and a gradual monotonic decline over the 2 min measurement. The absence of any plasmonic structure leads to limited radiative efficiency. Among the three samples, it demonstrates relatively high temporal stability, with less abrupt changes than the PMMA/Ag configuration.

Taken together, these results highlight a competition between initial PL enhancement and emission stability, likely influenced by LSPR-induced radiative acceleration, interfacial dynamics and structural design.

Although these interpretations point to intrinsic mechanisms, we note that minor instrumental drift or laser-induced sample repositioning at the early stage of measurement cannot be entirely excluded, especially given the sensitivity of the system.

However, a comparison of RT PL intensities was also conducted between the NW/Si structure and the designed NW/PMMA/Ag/Si hybrid structure. A clear intensity difference was observed with approximately 10 times difference. Also, in these 3 samples, beam broadening/narrowing is not occurring as a function of power, similar to the case under 4 K.

3.5.3 Parameter optimization

To further investigate the optimal conditions for PL enhancement in this hybrid metal–perovskite nanostructure system, we systematically tuned several key experimental parameters, including the thickness of the PMMA spacer and the size of the Ag NPs. In the process of optimization, the surface density of Ag NPs was measured by AFM to be approximately 10 particles per μm^2. A more diluted $CsPbBr_3$ NW solution was used for spin coating to minimize aggregation while maintaining sufficient NW density for interaction with the Ag NPs. This allowed for a denser and more uniform distribution of Ag NPs, enabling stronger near-field plasmonic coupling without sacrificing spatial separation or triggering excessive NW clustering.

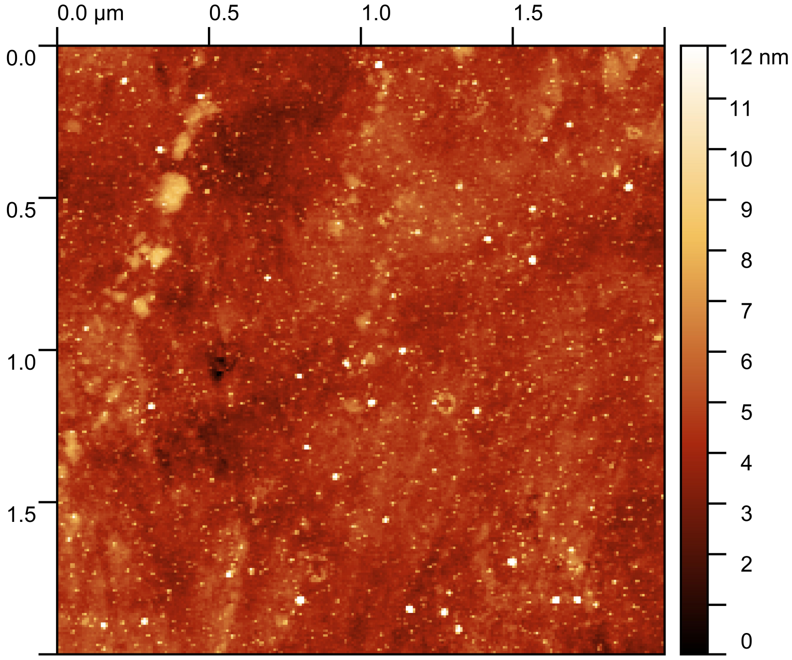

Figure 3.14: AFM image of Ag NPs coated Si substrate. The bright dots refer to the Ag NPs. The image was collected by the group of Prof. Shengfu Yang at the University of Leicester.

Furthermore, unlike the initial measurements conducted using a 100× objective lens (with a laser spot size of $\sim 1\,\mu m$), this set of experiments employed a 10× objective lens. This change increased the laser spot size by a factor of 10, providing approximately 100 times greater area coverage. Such broader illumination helps reduce the strong position dependence previously observed due to NW inhomogeneity and local clustering, and thus yields more spatially averaged and representative PL intensities. Additionally, the lower magnification reduces the per-unit-area laser power density, helping to avoid laser-induced sample damage especially under high local field enhancement.

All measurements in this optimization study were performed at 4 K using the same 400 nm pulsed laser with a repetition rate of 7.6 MHz. Low-temperature conditions were maintained to ensure high spectral resolution for clearer observation of the intrinsic plasmonic enhancement behaviour.

As in Figure 3.15(a-c), we first performed excitation power-dependent μPL measurements at multiple positions across the hybrid metal–perovskite NW samples. The PL peak intensity varied between different positions. This is likely caused by variations in local coupling strength and, inevitably NW distribution. However, the peak shape and spectral position remained mostly consistent across measurements. At such low excitation fluence, emission profiles resembling those of single NWs were well preserved. Despite position-to-position variability, the integration over a consistent spectral range allows the average PL peak intensity to reliably reflect the emission characteristics of the structure under study.

Figure 3.15(d) illustrates a representative approach we adopted to evaluate device performance: by selecting multiple excitation spots within a large illumination area and extracting the average PL peak intensity as a function of fluence, we obtained a more statistically meaningful metric for comparing samples. This strategy helps further minimize the influence of spatial inhomogeneity and local clustering effects that would otherwise obscure the intrinsic enhancement behaviour of different configurations.

To further evaluate the maximum PL enhancement, we investigated samples with varying Ag NP diameters and PMMA spacer thicknesses. A similar averaging method was employed as described above, and only PL spectra exhibiting relatively narrow FWHM and stable peak positions were used in the analysis, corresponding to measurement spots that most likely represent optimal NW–Ag coupling conditions.

The comparison of PL intensity across different configurations is shown in Figure 3.15(e–f). Among all combinations, the structure composed of 7.5 nm Ag NPs and a 15 nm PMMA spacer exhibited the strongest PL response, consistently featuring better PL intensity over other configurations across the full fluence range, followed by the 8 nm Ag NPs and 5 nm PMMA structure. We therefore adopted this as the optimal device configuration for subsequent experiments.

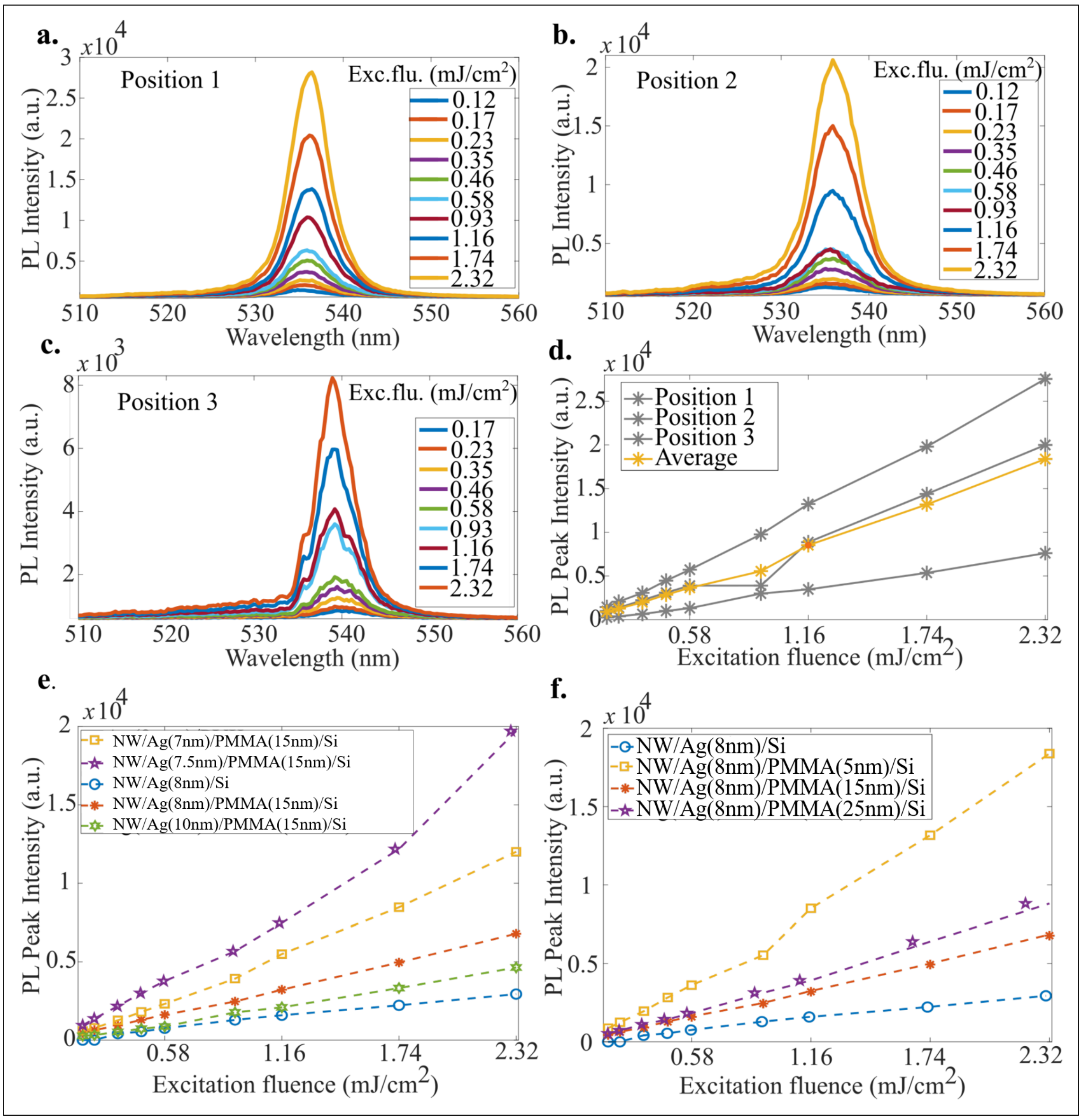

Figure 3.15: Optimizing parameters by investigating multiple configurations under larger excitation area. (a–c) Power-dependent μPL spectra taken at three different positions on the hybrid device. At position 3, the individual emission lines form several single NWs that can be resolved in the spectra. (d) Position-dependent PL peak intensity as a function of excitation fluence on the hybrid device. (e,f) Optimization of device parameters by varying the Ag NP size and PMMA layer thickness.

It is worth noting that the Ag NPs inherently exhibit a size distribution as described in Figure 3.4; however, over 50% of the particles fall within the target size range of 7.5±1 nm. Additionally, to ensure the reliability of the observed enhancement effects, although measurements were repeated over multiple days, all samples were stored either in a dry nitrogen environment or maintained under vacuum within the cryostat throughout this period. No signs of degradation were observed, confirming the stability of the perovskite NWs under the experimental conditions.

The principles as the enhancement are controlled by the competition of radiative enhancement and non-radiative quenching, while both factors have complex dependence on the spacer distance and particle size, even the surrounding material, as indicated in the beginning of this chapter. Although the LSPR features significant decay as the distance increases, a smaller distance may cause unexpected energy dissipation and enhanced non-radiative pathway and thus a reduced PL emission. The size, shape of the Ag NP further limit the LSPR strength which is intrinsic to metal NPs[93]. Therefore, making a balance of all those complicated factors is especially crucial with a hybrid nanostructure in the few nm range. The PL emission, under this condition, was maximized, while the mechanisms of such enhancement was ambiguous. A comprehensive study on the optimized device configuration was conducted, with a comparison to the pure NW emission to further prove the plasmonic behaviour.

3.6 Ag NPs Enhanced PL Emission in Perovskite Nanowires

PL spectra were measured at 4 K for the NWs and the hybrid nanostructure under the determined parameters. The hybrid metal–perovskite NW device exhibited a PL intensity enhancement of approximately tenfold compared to pure perovskite NWs, as shown in Fig. 3.16(a) and (b). This pronounced enhancement is attributed to the incorporation of a dielectric spacer layer, which tailors the electromagnetic field distribution, mitigates excessive absorption of the incident light by the Ag

NPs, and ensures efficient photon–plasmon coupling through optimal matching with the LSPR of the Ag NPs.

However, both the Ag NP distribution and the arrangement of perovskite NWs are intrinsically random, leading to significant local variations in enhancement. Obtaining a representative μPL measure of the collective emission from the hybrid NWs remained challenging due to spatial inhomogeneities. To address this, we performed 2D mapping measurements over selected regions, enabling us to extract an averaged emission signal.

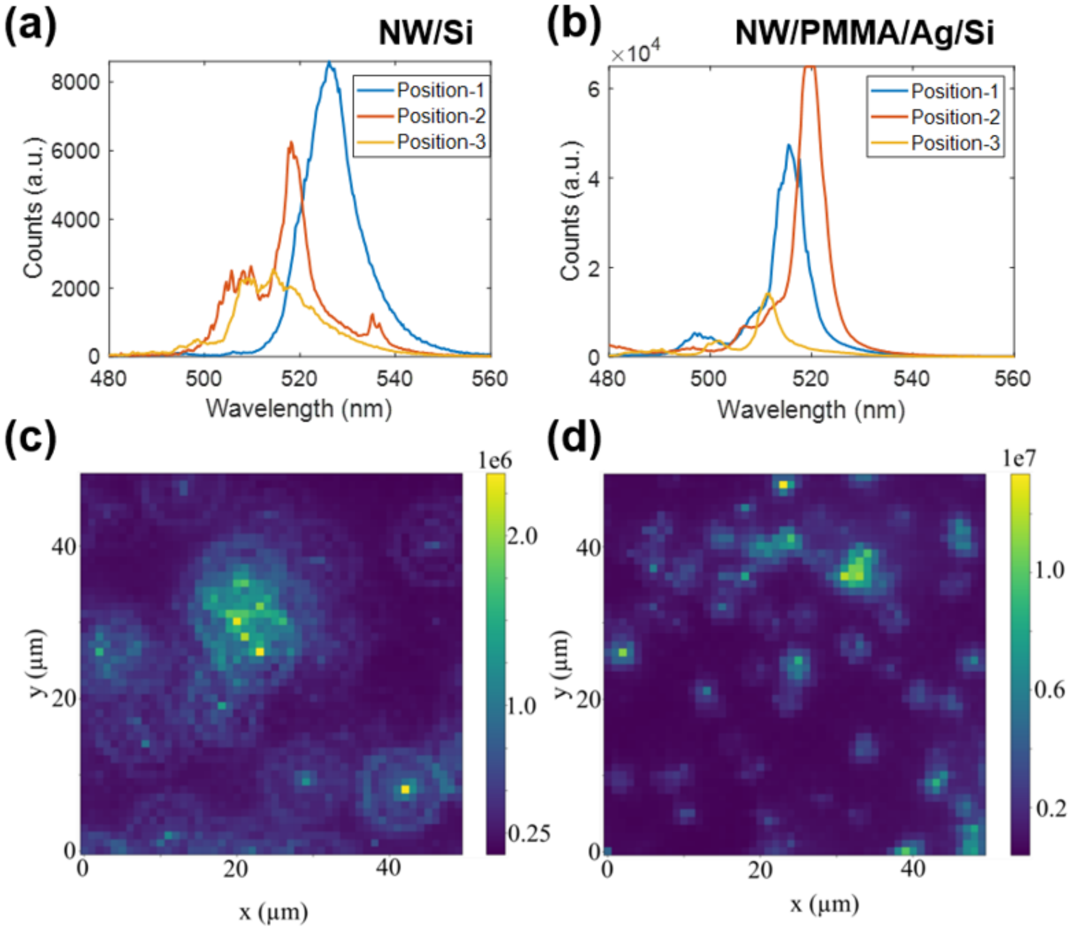

Figure 3.16: Enhanced PL for optimized parameters. (a,b) μPL spectra from bare NW sample and the optimized device configuration under 4 K. Multiple PL emission spectra were presented to show the highly position dependence. (c,d) 2D mapping on bare NWs and hybrid metal-perovskite NWs respectively.

Figures 3.16(c) and (d) present representative PL intensity maps of pure perovskite NWs and hybrid NWs fabricated with optimized parameters. Each scan covered an area of 50 × 50 μm^2, with a pixel resolution of 1 × 1 μm^2. The excitation source was a 405 nm pulsed laser operating at a repetition rate of 10 MHz, with an average power of 800 nW at the sample surface. A 100× objective lens was used, yielding a laser spot size of approximately 1 μm, which matches the pixel size in the scan and ensures that each pixel measurement corresponds to an individual laser spot excitation. Although some minor defocusing occurred during the mapping process, the total contribution to the PL intensity was included in the evaluation. Such 2D scans were repeated at multiple regions across both types of samples to further reduce manual errors. From these measurements, the mean PL intensity enhancement factor for the hybrid NWs was determined to be 8.5 ± 2.4, with the uncertainty representing the standard deviation from different scanned areas. This averaged value is considered more representative of the overall enhancement effect than isolated measurements.

In summary, PL measurements combined with spatial mapping provide an averaged enhancement factor that accounts for the spatial inhomogeneity inherent to the hybrid NW samples. The mapping approach partially resolves the influence of random Ag NP and NW distributions, but certain uncertainties remain. For example, the lateral spacing between individual Ag NPs and NWs cannot be precisely determined; multiple Ag NPs may accompany a given NW with optimal alignment for LSPR coupling, while another bright emission spot may originate from an intrinsically strong-emitting NW or a cluster of NWs with minimal plasmonic interaction. Such scenarios are intrinsic to the system and cannot be entirely eliminated in the measurements. Consequently, the PL intensity, although it can representative of the device performance, it alone cannot differentiate the best plasmon-enhanced emission from the background luminescence. To probe the underlying recombination dynamics more directly and disentangle these contributions, TRPL measurements were performed.

In addition to the extreme brightness observed in the PL mapping which indicates the dominance of radiative processes in these regions, TRPL measurements were performed on the corresponding samples as shown in Figure 3.17, yielding lifetimes

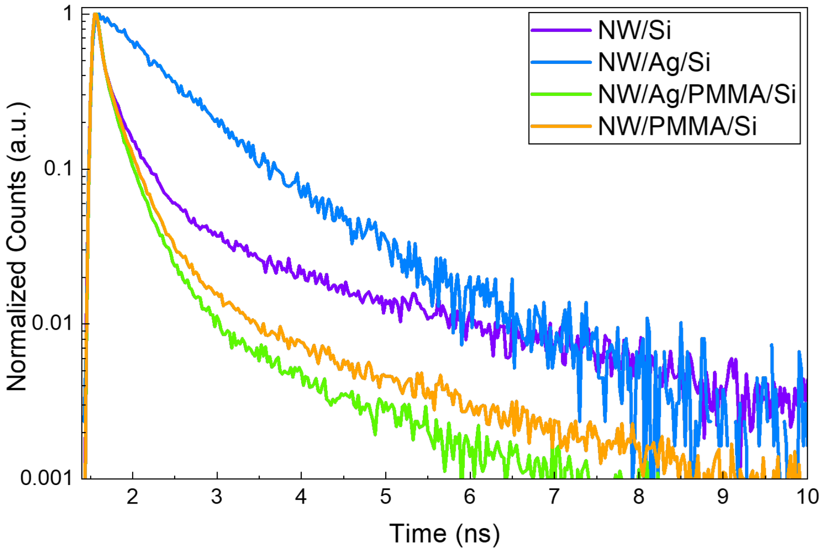

Figure 3.17: Comparison of TRPL for various device configurations.

of 71 ps, 689 ps, 64 ps, and 61 ps for NW/Si, NW/Ag/Si, NW/PMMA/Ag/Si, and NW/PMMA/Si, respectively. The NW/Ag/Si configuration exhibits a markedly longer lifetime than the other structures, whereas the introduction of the PMMA spacer in the hybrid device results in a slight decrease in the lifetime and a clear suppression of the long-lived tail observed in the recombination dynamics of bare perovskite NWs on the Si substrate. The presence of localized surface plasmons can enhance the radiative decay rate, which on its own would be expected to shorten the PL lifetime. Nevertheless, in hybrid NW configurations, if non-radiative recombination centers such as surface states are suppressed, this effect can counterbalance or even outweigh the radiative acceleration, potentially resulting in an unchanged or even prolonged lifetime, consistent with analogous observations in metal-enhanced and perovskite–plasmonic hybrid systems [49, 205, 206]. Although a shortened lifetime was observed for the complete structure, additional, more complex mechanisms may also be involved and remain to be revealed.

3.6.1 Discussion on Plasmon–photon Coupling Mechanism

The TRPL curves exhibit unexpected lifetime variations: the introduction of Ag alone results in a prolonged decay with a more monoexponential profile, whereas the introduction of PMMA alone, without LSPR, leads to a slightly shortened lifetime with a similar decay shape. Nevertheless, we attribute the observed PL improvement to effective plasmon–photon coupling, supported by substantial evidence. The following section discusses the underlying mechanism in detail.

Apparent Purcell Factor Analysis and Limitations

Given the observed variations in PL lifetime, it is instructive to evaluate the degree of radiative rate modification among different configurations. This can be expressed in terms of the Purcell factor F_{P}, which quantifies the change in the radiative decay rate due to modifications in the local photonic environment and is defined as

$$F_{\mathrm{P}} = \frac{\Gamma_{\mathrm{rad}}}{\Gamma^{0}_{\mathrm{rad}}},$$

where Γ_{rad} and $\Gamma^{0}_{\mathrm{rad}}$ are the radiative recombination rates in the modified and reference structures, respectively.

Experimentally, Γ_{rad} can be determined from the measured PL lifetime τ and PLQY via

$$\Gamma_{\mathrm{rad}} = \frac{\mathrm{PLQY}}{\tau}.$$

In the current experiments, the absence of accurate PLQY values prevents a direct separation of radiative and non-radiative channels. As a result, only an apparent Purcell factor

$$F^{\mathrm{app}}_{\mathrm{P}} \approx \frac{\tau_0}{\tau}$$

can be estimated, assuming negligible variation in the non-radiative decay rate. This approximation is, however, strongly affected by the complex recombination dynamics in perovskites and by additional loss channels introduced by metallic components. Consequently, the current estimation likely deviates from the true radiative enhancement, and a more rigorous quantification would require time- and spectrally-resolved lifetime measurements combined with absolute PLQY determination.

These considerations highlight that the observed lifetime variations are not only dictated by radiative acceleration, but are the result of merged plasmonic enhancement and non-radiative loss channels. In the following section, we investigate the underlying plasmonic coupling mechanisms in greater detail to better resolve these contributions.

Discussion the Enhancement Mechanism via Lifetimes

Suppressed Non-radiative Recombination:

The NW/Ag/Si sample (blue curve) exhibits a significant increase in PL intensity, along with a substantially longer average lifetime. This indicates that the excitation process is enhanced via near-field coupling between the Ag NPs and the NWs, LSPR at the pump wavelength. In this system, both the fast and slow decay components originate from localized exciton emission associated with different potential minima. Plasmonic coupling and the modified dielectric environment can suppress certain non-radiative channels, particularly those linked to surface-related dissipation, allowing long-lived localized exciton states to contribute more prominently to the total emission [49, 205, 206]. As a result, the average lifetime increases even though the overall PL intensity is enhanced.

Optimized LSPR with Minimal Energy Dissipation:

The NW/PMMA/Ag/Si sample (purple curve) exhibits the strongest PL enhancement and the shortest lifetime among all configurations. Introducing a ∼15 nm PMMA spacer effectively reduces non-radiative energy transfer to the metal while maintaining near-field coupling. This configuration increases the LDOS at the emission wavelength, leading to faster radiative decay and an improved quantum yield. The reduced contribution of trap-assisted recombination further shortens the overall lifetime. In addition, the dielectric PMMA layer tunes the resonant spectrum to a red shift, providing a better-matched LSPR condition [82]. The chosen PMMA thickness represents a balance between minimizing energy-transfer losses to the metal and preserving sufficient plasmon–emitter coupling. Since the LSPR near-field is non-propagating and decays nearly exponentially with distance (typical decay length on the order of 5–30 nm) [151], the spacer thickness critically determines the coupling strength.

Altered Dielectric Environment and Interface from PMMA:

The NW/PMMA/Si sample (yellow curve) also shows a shorter lifetime compared to NW/Si. In this case, the PMMA layer modifies the dielectric environment at the NW/substrate interface, increasing the LDOS and reducing the influence of substrate-induced non-radiative channels. These effects increase the relative weight of the intrinsic fast decay channel, resulting in a shorter measured lifetime despite the absence of plasmonic structures.

The PMMA coating slightly elevates the NWs and reduces the effective dielectric screening at the perovskite interface, thus strengthening the Coulomb interaction between electrons and holes [199, 201]. This reduced screening can enhance exciton binding and localization, which in turn may increase the contribution of radiative shallow traps, thus accelerating radiative recombination and shortening the overall PL lifetime. In addition, PMMA also changes the local optical field distribution near the perovskite interface by increasing the fraction of the optical field confined within the perovskite layer, and reduces coupling into substrate-guided modes, thereby enhancing the interaction between excitonic dipoles and free-space radiative modes. This redistribution of the local optical field can further promote radiative recombination and contribute to a shorter radiative lifetime [207].

3.7 Conclusion and Discussion

In this chapter, we demonstrate pronounced plasmon-enhanced emission from hybrid nanostructures composed of Ag NPs and $CsPbBr_3$ perovskite NWs. A two-phase fabrication method, combining superfluid He droplet deposition with wet-chemical synthesis, enabled precise control over NP size and plasmon resonance, while avoiding chemical residues that can cause plasmon energy losses. The engineered four-layer architecture of 7.5 nm Ag NPs and a 15 nm PMMA spacer yielded the strongest enhancement, with μPL mapping at 4 K revealing an average 8.5-fold increase in emission intensity compared to bare NWs. Time-resolved spectroscopy confirmed accelerated recombination dynamics arising from tailored plasmon–exciton interactions.

Despite these advances, the hybrid devices exhibit limited stability under ambient conditions, due to the chemical reactivity of Ag and the intrinsic fragility of perovskite emitters. Furthermore, the enhancement is constrained by morphology inhomogeneity, with most measurements reflecting collective PL rather than optimally aligned single NW–Ag coupling. The low-temperature emission is dominated by localized excitons, a regime likely to shift toward free-exciton behaviour at RT due to phonon-induced delocalization. Temperature-dependent spectroscopy could clarify this transition. Plasmonic enhancement here arises from a combination of interface effects, field confinement, LDOS modification, and near-field energy coupling; however, the present temporal resolution limits prevent a full separation of radiative and non-radiative contributions in the fast-decay regime. Higher spatial and temporal resolution TRPL studies under varied conditions would enable a more complete picture of the underlying dynamics.

The outstanding performance of these hybrid nanostructures underscores their potential in applications demanding efficient light–matter interaction at low excitation powers [160, 161]. These measurements lay a strong foundation for advancing lead halide perovskite–based nanophotonic devices, ranging from visible-wavelength nanolasers to practical light-emitting diodes and photodetectors, where plasmonic coupling can selectively enhance light emission or absorption. The precise integration of plasmonic and semiconductor components demonstrated here addresses key engineering challenges in the field and marks a significant step toward scalable, on-chip photonic technologies.

4

Plasmonic Mg NPs for PL Enhancement in Perovskite Nanostructures

Contents

4.1 Chapter Introduction 102
4.2 Plasmonic Mg Nanoparticles 103
  4.2.1 Proposed Mg–Perovskite Hybrid Structure with Simulation 105
4.3 Sample Fabrication and Modification 107
  4.3.1 Size-Controlled Faceted Spheroidal Mg Nanoparticles . 107
  4.3.2 Modification on $CsPbBr_3$ NWs via Electric Field 110
  4.3.3 Hybrid Mg–Perovskite Nanostructures 114
4.4 Setup 115
4.5 μPL Characterization on Hybrid Mg–$CsPbBr_3$ Nanostructures 116
  4.5.1 μPL Characterization at RT for Uncoated Mg NPs . . . 116
  4.5.2 μPL Characterization at 4 K for Uncoated Mg NPs . . . 119
4.6 Plamonic Core-Shell Mg NPs Enhanced Perovskite NW PL at RT 123
  4.6.1 Motivation for spacer design 123
  4.6.2 Comparison with Ag NPs Based Plasmonic Enhancement 126
  4.6.3 Determining the Enhancement factor 127
4.7 Conclusion and Discussion 128

4.1 Chapter Introduction

As a continuation of the study on Ag-enhanced NW emission, this chapter explores Mg as an alternative plasmonic material coupled with NWs to achieve PL enhancement. Section 4.2 provides a review of plasmonic Mg NPs, highlighting their advantages, limitations, and recent developments. Section 4.3 details the synthesis procedures for the designed samples, including improvements in the NWs. Sections 4.5 and 4.6 present a comprehensive investigation of the PL properties of the hybrid structures, first with bare Mg NPs and subsequently with an additional dielectric coating. Finally, the chapter concludes with an analysis of the plasmonic coupling mechanisms in these hybrids, including a comparison with conventional Ag NPs.

4.2 Plasmonic Mg Nanoparticles

Noble metals have been widely employed as plasmonic materials due to their mature synthesizing methods and high Q factor in the visible range. Recently alternative materials have been investigated including metal nitrides [208], graphene [209, 210], superconductors [211], together with metals such as Cu [212, 213], Al [214, 215] and Mg [216, 217]. It is reported that in the visible wavelength range, metals are still regarded as the most compelling way to generate LSPR [218]. However, noble metals such as Au and Ag suffer from their high material cost, while Ag is prone to oxidation, imposing stricter requirements on its practical implementation. Cu and Al exhibit higher optical losses due to their large imaginary dielectric components and are also susceptible to oxidation, which renders their plasmonic resonances less effective [135].

The rise of Mg as an alternative plasmonic material stems primarily from its significant advantages over traditional noble metals. First, Mg is an extremely abundant element on earth and its acquisition cost is much lower than that of Au and Ag. This makes Mg-based plasmonic devices significantly more economically advantageous for future large-scale production and commercial applications [217]. Mg also has low density and good bio-compatibility, which gives it excellent potential for applications in the biomedical field. Moreover, Mg offers unique advantages in its optical properties, in that its plasmonic response extends into the UV region, enabling LSPR modes that span from the UV to the IR. This additional spectral degree of freedom renders Mg highly promising for next-generation nanophotonic devices [216, 219].

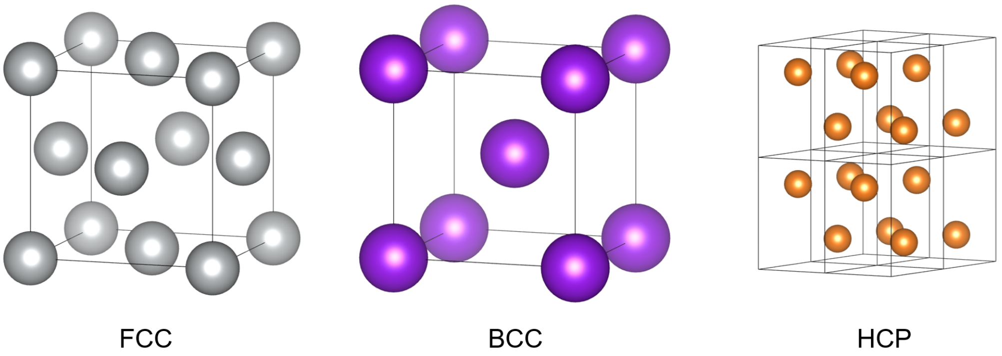

Figure 4.1: Crystal structures of HCP, BCC, and FCC lattices. Schematic representations of the conventional unit cells of hexagonal close-packed HCP, body-centered cubic BCC, and face-centered cubic FCC structures. The line frames represent unit cells. The lattice parameters are taken from Mg (HCP), K (BCC), and Au (FCC), respectively.

Unlike conventional plasmonic metals such as Au, Ag, Cu, and Al, which crystallize in a face-centred cubic (FCC) lattice structure, Mg adopts a hexagonal close-packed (HCP) structure. Shape plays a decisive role in LSPR when the particle size approaches the excitation wavelength, and tailoring particle morphology is widely recognized as one of the most effective strategies to manipulate plasmon resonances, as also discussed in the previous chapter [82]. The exploration of plasmonic Mg therefore opens an extended library of particle geometries, offering diverse field distributions and optical responses [92].

The synthesis of Mg NPs has been achieved through several complementary routes. Physical methods such as inert-gas condensation produce Mg@MgO core–shell particles with controlled diameters of approximately 35 nm [220]; pulsed laser ablation in liquids generates ligand-free Mg colloids by irradiating bulk Mg targets in organic or inert solvents [221]. Nevertheless, colloidal approaches remain the most widely adopted route, where the particle size can be tuned by varying the reducing agent concentration, precursor ratio, solvent polarity, and temperature [222, 223]. Such control has enabled the synthesis of single-crystalline hexagonal platelets and twinned rods with sizes ranging from 80 to 1300 nm [224]. More recently, Ten et al. reported a one-pot colloidal synthesis strategy that selectively smooths the corners and edges of faceted Mg NPs, yielding monodisperse quasi-spherical particles while retaining strong plasmonic responses [225]. This shape-control methodology opens new opportunities for Mg-based LSPR systems with uniform optical properties.

To the best of our knowledge, no detailed experimental or theoretical studies have yet reported the coupling of plasmonic Mg NPs with $CsPbBr_3$ NWs for the enhancement of PL. However, recent work has begun to reveal the unique properties and enhancement effects of Mg plasmonic nanostructures. For instance, Ten *et al.* [226] demonstrated the application of Mg NPs in surface-enhanced Raman scattering (SERS) and light-driven catalysis, reporting enhancement factors of approximately 10^2 for bare Mg NPs and 10^3 when decorated with Pd. Although these values remain significantly lower than those of conventional Au NPs, which typically exceed 10^6, the observed enhancement highlights the potential of Mg as a viable plasmonic material for future applications.

In this context, our work provides the first systematic investigation of plasmonic Mg NPs coupled with $CsPbBr_3$ NWs to enhance their PL emission. By combining the advantages of Mg as an earth-abundant, stable plasmonic material with the superior optical properties of perovskite NWs, this study establishes a new platform for plasmon–semiconductor hybrid structures. The results not only fill an existing gap but also demonstrate the potential of Mg-based nanostructures for next-generation, cost-effective nanophotonic devices.

4.2.1 Proposed Mg–Perovskite Hybrid Structure with Simulation

Similar to Figure 3.1, finite-element simulations were performed to investigate the plasmonic enhancement in the Mg–NW hybrid structure. In the model, the hybrid system consists of Mg NPs (with a self-limiting MgO coating) and a $CsPbBr_3$ NW with a SiO_2 buffer layer. Figure 4.2 shows the resulting field enhancement. The role of the MgO layer will be discussed in Section 4.3, while the use of SiO_2 as the dielectric spacer follows the same rationale as in the Ag-based design, namely to minimize nonradiative losses.

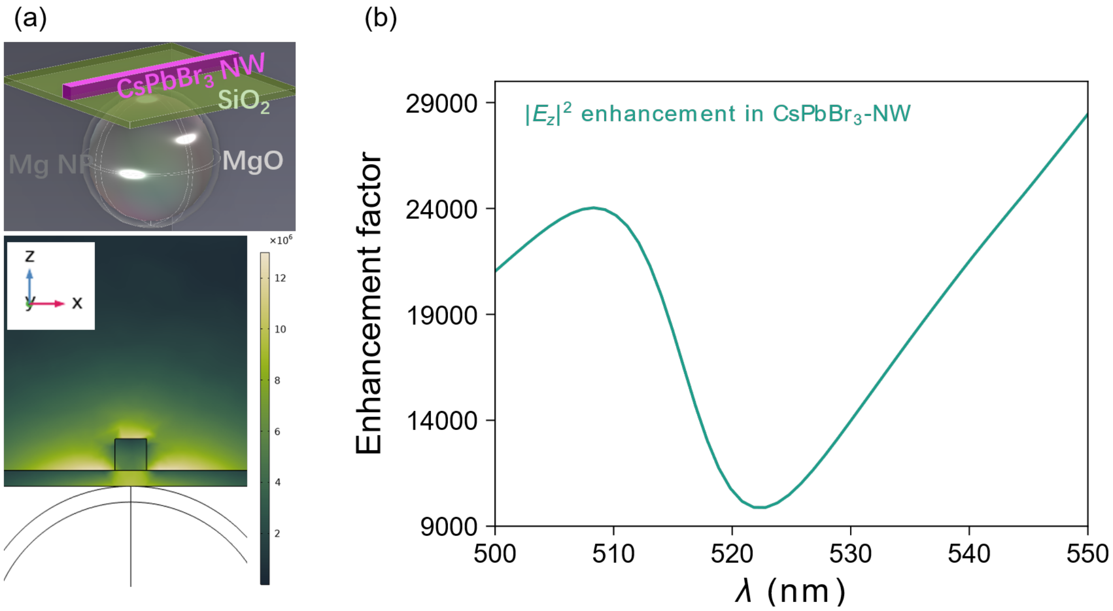

Figure 4.2: Finite-element simulations of plasmonic enhancement in a Mg–$CsPbBr_3$ NW hybrid structure. (a) Schematic and cross-sectional field distribution showing strong localized field distribution at the NW–NP interface. (b) Wavelength-dependent enhancement factor of $|E_z|^2$. The simulations were conducted by Dr. Xavier Romain.

Figure 4.2(a) presents a schematic of the hybrid structure together with the cross-sectional distribution of the electric field intensity, $|E_z|^2$. Panel (b) displays the wavelength-dependent enhancement factor of the perpendicular electric field component, $|E_z|^2$, within the $CsPbBr_3$ NW. A pronounced local field enhancement is observed at the NW–NP interface, indicating that Mg NPs can effectively tailor the electromagnetic environment of the NW. The corresponding simulation parameters are: Mg NP diameter of 90 nm, MgO shell thickness of 5 nm, and SiO_2 spacer thickness of 5 nm. It should be noted that, due to the approximations and boundary conditions inherent in the finite-element method, the simulated values are intended as qualitative illustrations rather than quantitative measures of the actual enhancement factor.

4.3 Sample Fabrication and Modification

4.3.1 Size-Controlled Faceted Spheroidal Mg Nanoparticles

The synthesis of the size-controlled Mg NP via a colloidal process was conducted by our collaborators at the University of Cambridge, and more information is included in their publications [225]. In this method, an organometallic magnesium precursor (di-n-butylmagnesium) is reduced by lithium naphthalenide, an aromatic electron carrier anion, in coordinating ether solvents under an inert atmosphere. The reduction produces colloidal Mg particles that are stabilized by a thin self-limiting MgO shell, which forms upon exposure to air and provides passivation of the metallic core.

The particle size is primarily tuned by controlling the reaction time, precursor concentration, and solvent coordination strength. Shorter reaction times and strongly coordinating solvents yield smaller NPs, while longer times and higher precursor concentration favour the growth of larger particles. In addition, additives such as transition-metal salts can bias nucleation and growth, further refining the particle size distribution [224]. In this way, samples with mean diameters ranging from about 60 nm to over 230 nm were prepared, corresponding to the series used in this thesis, as illustrated in Figure 4.3(a–e). The oxide shell that naturally forms on the particle surface features a thickness of $\sim 10\,\mathrm{nm}$ and protects the metallic Mg core, and ensures that the colloids remain stable under ambient conditions or even after etching [224, 225]. The self-limiting oxide shell also provides a different dielectric layer that tunes the LSPR spectra in general.

All samples thus share the same synthetic origin and morphological characteristics, namely faceted spheroidal Mg NPs with a protective oxide shell, differing only in their mean size. A near-spherical morphology was intentionally targeted to minimize plasmonic losses induced by nonlocal effects; however, the optimal outcome of the synthesis yields faceted spheroidal NPs at the designed sizes. Such near-spherical NPs also help to avoid shape-induced anisotropy and enable a clearer interpretation of LSPR behaviour. These well-defined and stable dispersions provided a consistent platform for the optical studies described in the following sections.

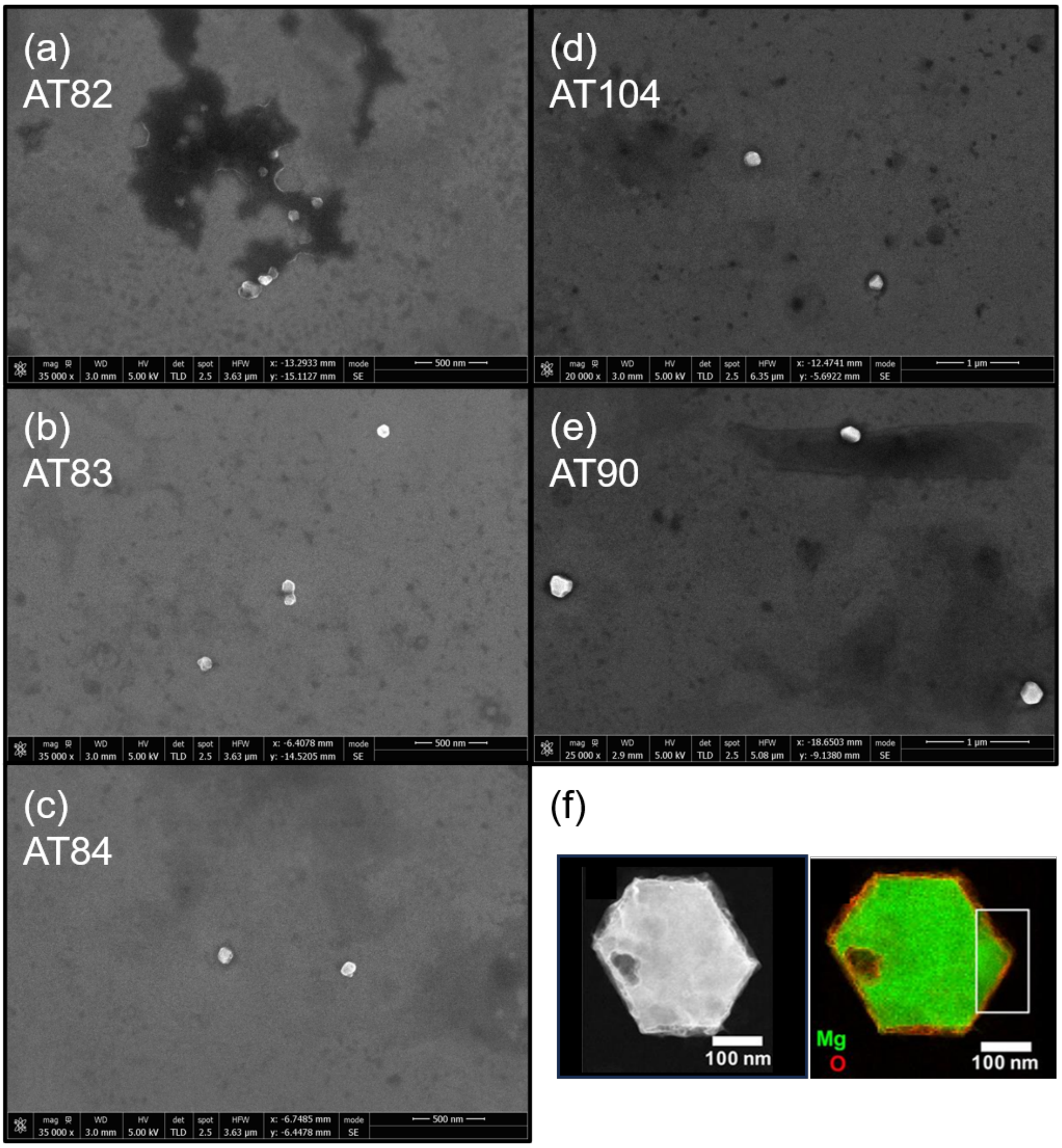

Figure 4.3: Colloidal Mg NPs synthesized in different sizes. (a–e) SEM images demonstrating progressive size increase. (f) STEM image of an individual hexagonal platelet synthesized under similar conditions, exhibiting a ∼10 nm self-limiting oxide shell [224]. The data presented in this figure were collected by Christina Boukouvala from the group of Prof. Emilie Ringe at the University of Cambridge.

Regarding the plasmonic enhancement of the PL emission, the spectral overlap between the plasmonic resonances of the Mg NPs and the emission band of the $CsPbBr_3$ NWs is critical for achieving an effective LSPR enhancement. Figure 4.4 presents the UV-Vis spectra of all Mg NPs used in this study with different sizes. In the spectral region of 500–600 nm, which corresponds to the PL emission of the perovskite NWs, the AT81 sample shows only a limited overlap compared to other NP sizes. This limited coupling suggests a weaker enhancement efficiency for AT81, whereas larger NPs (e.g., AT83 and AT84, ∼90–100 nm) provide stronger spectral overlap and thus more efficient plasmonic coupling.

In addition to the spectral overlap, the plasmonic response modes of Mg NPs evolve with size. For smaller NPs, the extinction spectrum is dominated by the dipolar LSPR mode, which typically produces a single broad absorption band, such as in the case of AT81-84. As the particle size increases, higher-order plasmonic modes beyond the fundamental dipole resonance become significant. For example, quadrupolar modes, where half of the electron cloud moves parallel to the applied field and half moves antiparallel, contributions emerge, leading to the appearance of additional absorption features and spectral broadening [82]. These higher-order resonances can further influence the coupling with excitonic emission, providing additional enhancement pathways depending on their spectral alignment with the perovskite PL band.

Additionally, Mg NPs and Ag NPs coated with SiO_2 core–shell NPs employed in this study were also provided by the group of Prof. Emilie Ringe at the University of Cambridge. While the detailed synthesis protocols are not disclosed here, both types of NPs were prepared via colloidal routes and subsequently encapsulated with a thin amorphous silica shell of 5–10 nm. In the case of Ag@SiO_2, silver NPs are commonly synthesized by chemical reduction and coated with SiO_2 using a modified Stöber method, which yields uniform and controllable shell thicknesses [227, 228]. For Mg@SiO_2, a similar coating approach is adopted in order to further tune the properties of the dielectric spacer, while the silica shell simultaneously acts as an effective barrier against oxidation and maintains optical transparency.

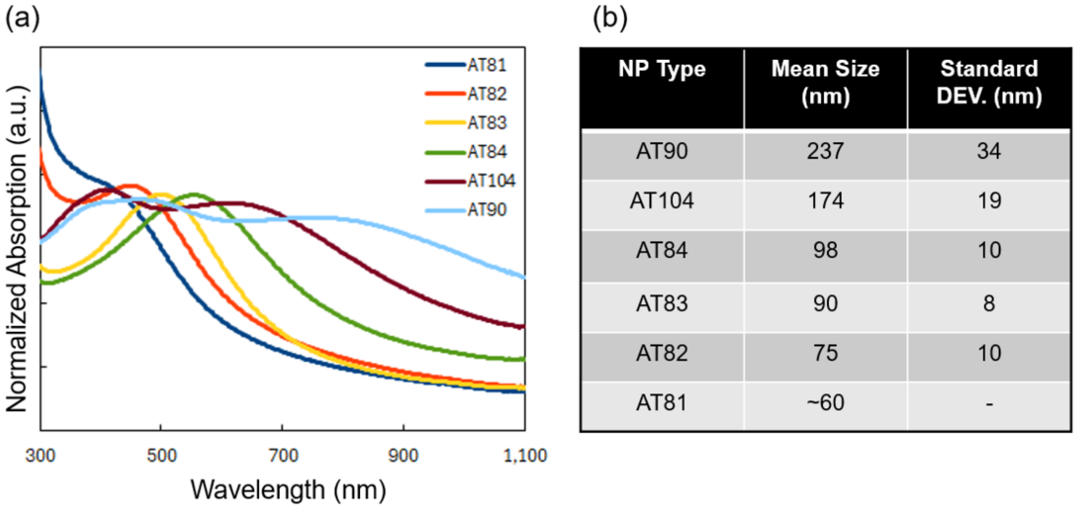

NP Type	Mean Size (nm)	Standard DEV. (nm)
AT90	237	34
AT104	174	19
AT84	98	10
AT83	90	8
AT82	75	10
AT81	~60	-

Figure 4.4: Size-dependent optical absorption of colloidal Mg NPs. (a) Normalized UV-vis absorption spectra of the series used in the chapter. (b) Corresponding mean diameters and size distributions. The data presented in this figure were collected by Christina Boukouvala from the group of Prof. Emilie Ringe at the University of Cambridge.

These core–shell structures combine chemical stability with a tunable dielectric environment, making them suitable for the plasmon–exciton coupling studies described in this thesis.

In the experiments, all Mg NP samples were initially characterized under identical measurement conditions. However, due to fabrication constraints, not all samples were available for further investigation, particularly after the introduction of a newly designed dielectric layer. Nevertheless, the overall size variation among the different batches was relatively modest. The non-ideal surface morphology of the NPs (i.e., their deviation from perfectly smooth spheres) further restricted the manifestation of distinct LSPR features. As a result, even with limited options from samples, we were still able to obtain a fair and representative plasmonic enhancement, which will be further elaborated in the subsequent results section.

4.3.2 Modification on $CsPbBr_3$ NWs via Electric Field

The $CsPbBr_3$ perovskite NWs were synthesized at Leicester University using a colloidal solution-phase approach with the same chemical recipe and reaction conditions (time and temperature) as previously stated. However, as illustrated in the last chapter, the carrier dynamics were highly influenced and dominated by traps in the NW crystal, which are strongly controlled by the NW morphology and assembling and thus by the spot position; this raised concerns about achieving a representative evaluation of the enhancement effect. To lessen the influence of such factors, an improved method for NW fabrication was introduced.

The light-induced assembly of halide perovskite NCs has been reported to partially desorb surface ligands and promote oriented attachment, leading to the formation of 1D $CsPbBr_3$ NWs [229]. Therefore, we hypothesize that an externally applied alternating electric field can play an analogous guiding role during the solution growth window. Prior studies have shown that alternating current (AC) fields can strongly couple to perovskite NWs in a contactless geometry [230], and extensive dielectrophoresis literature demonstrates robust NW alignment from solution under MHz fields [231, 232]. By combining these principles with the light-driven ligand dynamics [229], our method aims to steer NW formation toward higher aspect ratio and smoother morphology using an externally programmed field while preserving the chemical environment of the growth process. This rationale motivates the field parameters and sample choices adopted in the following experiments.

In practice, we adopt a contactless AC configuration capable of coupling the field through the vessel wall, thereby avoiding electrochemical side reactions and operating within a defined frequency–voltage window. Two parallel-plate electrodes are driven by a source with independently tunable amplitude and frequency, while an oscilloscope monitors the waveform in real time. The applied potential establishes a controlled electric field between the plates.

To investigate the influence of the introduced electric field, a comparison of the PL intensity and lifetime at RT was carried out. For PL measurements, the excitation power was fixed at 2 µW, following the conditions used in previous NW experiments to suppress higher-order carrier dynamics and to avoid saturation. TRPL measurements were performed on the same spot with two different excitation powers of 2 µW and 500 nW at a repetition rate of 1.52 MHz, corresponding to fluences of approximately 335 and 84 µJ/cm². These two excitation regimes were chosen to reveal any potential high-power-induced state filling or other nonlinear effects.

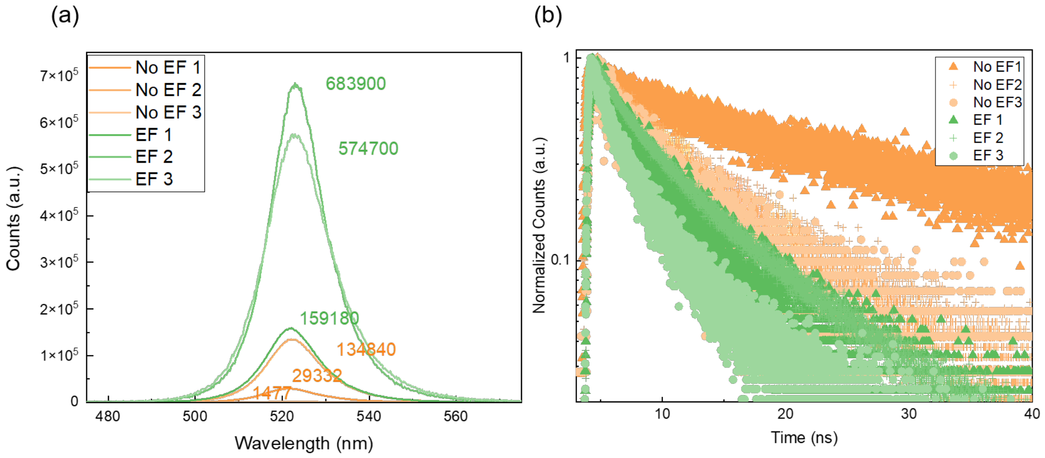

Figure 4.5: Comparison of emission from NWs grown with and without AC electric field. (a) μPL spectra on both samples (w and w/o electric field) with three different positions at the same excitation condition, corresponding peak intensity in counts labelled. (b) Corresponding TRPL of the PL peaks in the low excitation regime.

Figure 4.5(a) shows the PL emission from three different spots on both samples. A ∼5-fold stronger PL emission was observed for the sample grown with AC electric field (labelled as EF in the figure) compared to the reference NWs (labelled as no EF). The absence of spectral shifts indicates that the $CsPbBr_3$ NWs possess similar structural features and confinement dimensions in both cases. The enhanced PL intensity may originate either from increased radiative efficiency due to reduced surface recombination or from NW aggregation on the substrate.

TRPL reveals distinct differences in the recombination dynamics. Bi-exponential fitting to extract the initial decay and long tail lifetimes to evaluate the dynamics was conducted with proper IRF deconvolution, and the corresponding lifetimes are shown in Table 4.1.

In perovskite systems, trap states are broadly distributed in both the bulk and at the surface. For NWs, the large surface-to-volume ratio results in a particularly high density of surface traps. Compared to bulk traps, which primarily affect carrier transport and lifetime, surface traps can rapidly capture photoexcited carriers or excitons and introduce nonradiative recombination channels, thereby directly reducing the PL efficiency [233].

At low fluence, the EF NW exhibits a fast decay component of ∼3 ns and a slow decay component of ∼9 ns, which can be attributed to free-exciton-like radiative emission and trap-assisted emission, respectively. At high fluence, the filling of the limited trap states leads to suppression of the long-lived tail, and consequently a clearly reduced lifetime is observed. In comparison, the reference sample shows τ_1 values ranging from 2–5 ns and τ_2 extending up to 26 ns under low fluence, indicating that the recombination dynamics are significantly modified in the EF NWs. It is worth noting that at position 1 of the reference sample, the fitting reveals a strong contribution from trap-assisted recombination, particularly under low fluence, which is also consistent with the observations of Ag NPs discussed in Section 3.5. Additionally, due to the strong emission of the EF samples, the measurement at position 3 under high fluence is affected by a pile-up effect, where early-arriving photons are oversampled and the subsequent photons are underestimated. This artifact results in an apparently faster decay that does not reflect the real recombination dynamics [234].

In the reference sample, a pronounced long-lived tail indicates that trap-mediated channels significantly contribute to the decay. In contrast, the EF sample exhibits a clear suppression of this component, evidencing reduced trap involvement. As a result, the relative contribution of the fast radiative pathway increases, leading to a shorter amplitude-weighted lifetime despite the enhanced PL intensity. This behaviour suggests that the system is strongly trap-limited in the baseline condition, whereas an extended lifetime, indicative of improved crystal quality enabling long-range exciton diffusion in ideal free-exciton-dominated emissions, has been reported previously [229].

In conclusion, the introduction of the AC electric field enhanced the PL emission by suppressing nonradiative trap states. To minimize the unavoidable influence of NW aggregation on the substrate, 2D PL mappings were performed for both samples, with sonication applied prior to spin coating to redisperse the $CsPbBr_3$

Table 4.1: TRPL lifetime fitting of reference and EF samples

Sample	Position	Low fluence τ_1	Low fluence τ_2	High fluence τ_1	High fluence τ_2
No EF	1	5.27	24.61*	4.63	16.48
No EF	2	4.54	11.49	2.35	7.75
No EF	3	5.29	26.14	/	/
EF	1	3.54	8.27	1.75	5.89
EF	2	3.25	10.12	1.67	5.72
EF	3	2.37	8.03	0.59**	2.78**

Lifetimes were obtained from bi-exponential fits. τ_1 corresponds to the fast decay component, while τ_2 corresponds to the slow decay component.

* For the No EF sample at position 1 under low fluence, the slow decay component with $\tau_2 = 24.61\,\text{ns}$ has a larger amplitude than τ_1; in all other cases, τ_1 contributes more to the overall decay.

** An abnormally small τ_1 component was fitted due to pile-up effects from the high signal level. This artificial fast component does not represent the true decay dynamics and should be excluded.

NWs. This treatment further reduced the tendency for self-attraction arising from long-range dipole–dipole interactions and short-range van der Waals forces [235, 236]. Figure 4.6 presents representative mappings of the EF and reference samples, while multiple scans consistently revealed an average 2.5-fold increase in PL intensity, further confirming the improved PL efficiency.

4.3.3 Hybrid Mg–Perovskite Nanostructures

The fabrication of the hybrid Mg–NW structures was performed immediately prior to characterization to ensure sample freshness. The NW solution was thoroughly dissolved and sonicated before each use in order to minimize aggregation. The Mg NPs, prepared as a stable dispersion in water, were also sonicated to ensure uniformity, and then spin-coated onto Si substrates at 3000 rpm for 60 s to achieve an even distribution. Subsequently, the NWs were spin-coated on top. After solvent evaporation, all samples were loaded into a cryostat and pumped down to vacuum to maintain quality. For experiments requiring higher Mg NP density, Mg NPs were alternatively deposited by dropcasting onto the Si substrates.

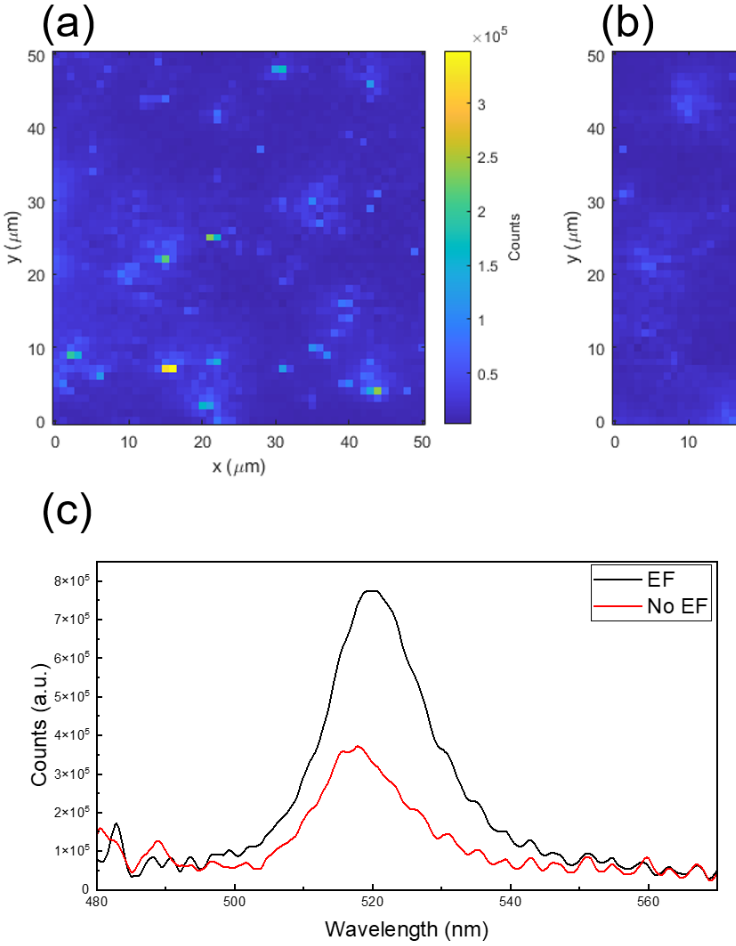

Figure 4.6: 2D mapping of the EF and reference samples. (a–b) 2D PL mappings over a 50 × 50 μm^2 area of (a) the EF sample and (b) the reference sample. The colour scale represents the integrated PL intensity in the range of 500–550 nm. (c) Integrated PL intensity over the entire mapped area. The repetitive fluctuations originate from the relatively low signal-to-noise ratio of this setup. All mappings were performed using a 450 nm CW diode laser with a power density of 1.27 W/cm^2.

4.4 Setup

In this chapter, both pulsed and CW laser excitations were employed. For time-resolved measurements, a 400 nm Ti:sapphire fs laser operating at 7.6 MHz was primarily used, providing a measurable decay window of up to 130 ns. For 2D mapping, in addition to the 405 nm pulsed laser source, a 450 nm CW diode laser was used to acquire steady-state PL mapping images. Low-temperature measurements at 4 K were carried out using a cryostat cooled by liquid He. The TRPL signals were detected by an APD coupled to a TCSPC module with a resolution of 4 ps per bin.

4.5 μPL Characterization on Hybrid Mg–$CsPbBr_3$ Nanostructures

4.5.1 μPL Characterization at RT for Uncoated Mg NPs

RT μPL investigations were first conducted on Mg NPs with different sizes, prepared by directly dropcasting the NPs followed by spin-coated NWs without any spacer material. TRPL decays were recorded at the same positions in order to monitor possible variations in the recombination dynamics. The excitation power was set to $6.7\,\mu\mathrm{J/cm^2}$, a regime in which no saturation, minimal multiexciton processes, negligible state filling, and no sample damage induced by the incident field was expected.

For all measurements, we ensured a comparable number of NWs within the laser spot for comparison by adjusting the excitation positions on the surface. Comparisons were then made only between regions with a similar number of emitters, in order to account for the collective contribution of each NW. Figure 4.7 summarizes the results obtained from this series of experiments.

With regard to the PL intensity, a moderate enhancement is observed in sample AT81–83 within the smaller NP size range. The strongest PL emission with a 4-fold enhancement was observed on AT81 (mean diameter 60 nm), followed by approximately 2× enhancement on AT82–83 (mean diameter 75 nm and 90 nm) compared to the NW only sample, indicating clearly LSPR coupling. In contrast, no significant change is found for AT84, which corresponds to mean NP sizes of approximately 100 nm. This might be due to the limited coupling to the LSPR mode with respect to the smaller overlap of between the PL emission centred at 525 nm and the LSPR spectra indicated in Figure 4.4 (a). The fact that small-sized Mg NPs induce such behaviour can be ascribed, on the one hand, to their favourable spectral overlap with the LSPR, and on the other hand, to the larger effective contact area provided.

Interestingly, PL quenching occurs in sample AT104 with a mean NP size of ~170 nm, while a similar PL intensity was again observed with an increased size

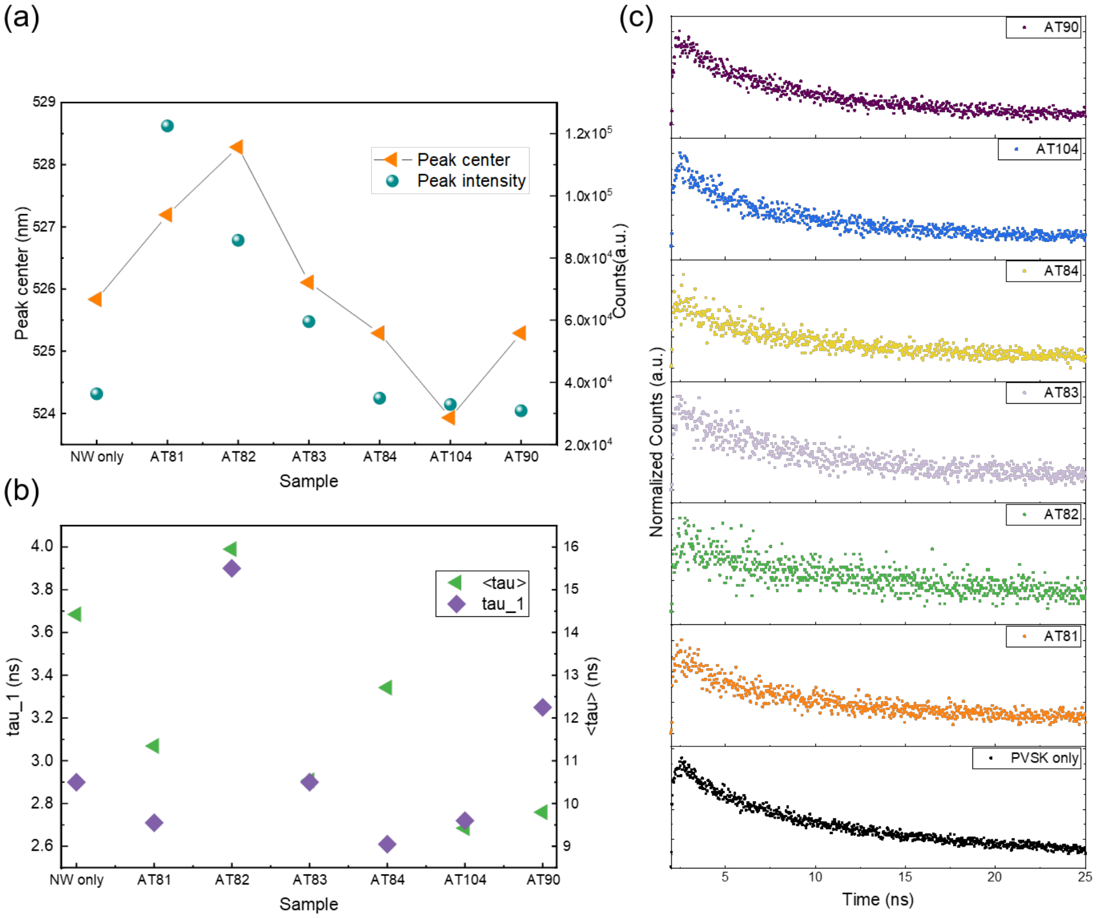

Figure 4.7: RT measurements of the Mg–NW hybrid structure with Mg NPs AT81–104. (a) μPL investigation on the hybrid structure. Blue dots: PL peak intensities as a function of Mg NP size; red dots: spectral peak centres for varying NP size. Both PL enhancement and peak shift are simultaneously observed in sample AT81–83. (b) PL lifetimes of the corresponding samples obtained from bi-exponential fitting. Green triangles: weighted average lifetime [234]; purple diamonds: fast-component lifetime. (c) TRPL decay curves for all seven samples, including the NW-only reference sample.

(~200 nm) of Mg on AT90, suggesting a transition from enhancement to suppression and, a non-monotonic increase in coupling as the NP size increases. According to Figure 4.4 (a), although the dipole modes of these two large NPs have limited overlap at the NW PL emission, the coupling of the quadrupole mode would be promising on AT90 given the size-tuned blue-shift. In general, the dipole plasmon mode is regarded as the dominant resonance in small metallic NPs, strongly coupling to both the far-field and the local near-field. Higher-order modes, such as the quadrupole resonance, typically emerge as the particle size increases, with weaker radiative coupling but more confined near-field distributions [82]. However, in the case of Mg NPs, the intrinsic plasmon quality factor is significantly lower than that of noble metals such as Au or Ag, due to stronger damping. As a result, the dipole mode is inherently weakened. The higher-order coupling becomes relevant especially in the case of ∼10 nm spacing.

It is worth noting that no improvement of the PL intensity does not necessarily mean no LSPR coupling, considering the multiple energy dissipation channels induced by the condition of nearly contacting.

In addition to the PL counts, peak shifts were also observed in the presence of Mg NPs. A blue shift would be expected normally from the mode coupling by comparing the LSPR modes [216]. However, a clear red shift of the peak centre was observed for AT81–83, which have mean diameters smaller than 100 nm and also exhibit prominent PL enhancement. A red shift in the emission of perovskites coupled to plasmonics can originate from several mechanisms, such as energy level hybridization, dielectric screening or plasmon-induced local heating. However, the hybridization of the energy level and the consequent Rabi splitting occur in a strong coupling regime [89, 237], which is unlikely to arise from Mg NPs whose Q factor is much lower than noble metal NPs [92]. Double-peak behaviour is also absent from the PL measurements. Dielectric screening can be excluded in the present case, since the observed shift, unlike the systematic behaviour found with the introduction of PMMA, is not a general feature across all Mg hybrid structures and should therefore not be overemphasized [199, 201, 238, 239]. As for heating, we also rule it out as the main cause because the excitation fluence in our measurements was deliberately kept at a very low level. Secondly, if heating were dominant, one would expect (i) concomitant linewidth broadening due to enhanced exciton–phonon interactions, and, in the presence of defect-mediated pathways, (ii) TRPL signatures of thermally activated nonradiative recombination manifested as accelerated PL decay—none of which were observed in our system.

The spectral shift is correlated with the PL enhancement observed in AT81–83 which is attributed to a Stark-shift-like effect[240–242]. A Stark shift effect typically arises when a quantum-confined system is exposed to an electric field along the confinement axis [240]. In the case of the NWs, which exhibit confinement along two axes, this phenomenon can readily occur. We propose the following mechanism: under strong LSPR, the local electric field is enhanced, resulting in an increased excitation cross-section and the generation of more free carriers. These carriers are trapped at surface defects of the NWs, producing quasi-static local fields. Those local fields thus engineer the optical modes and band structure, which further induce a red shift in emission energy. The fields induced Stark-type shift of the emission accounts for a fairly small red shift of about 20 meV in our case.

Figure 4.7(b) and (c) present the TRPL results. The overall recombination dynamics remain comparable to those of the NW-only sample discussed in Section 4.3. In the hybrid structures without deliberate optimization, neither the fast component τ_1 nor the amplitude-weighted average lifetime $< \tau >= \frac{A_1\tau_1+A_2\tau_2}{A_1+A_2}$ exhibits a systematic correlation with the degree of PL enhancement. This indicates that Purcell-type LDOS enhancement does not play a dominant role in the present configuration.

Taken together, these results suggest that the enhancement of the RT μPL emission originates primarily from confined local fields rather than from lifetime modification. The enhancement factor is dictated by the spectral overlap with the LSPR and by the near-field distribution of the localized fields, both of which are strongly dependent on the Mg NP size distribution.

4.5.2 μPL Characterization at 4 K for Uncoated Mg NPs

Continuing with the μPL investigation, measurements were performed at 4 K under the same excitation conditions and on the same sample. At 4 K, the PL spectra exhibited a variety of shapes in contrast to the Gaussian-like peak observed at RT. This difference is attributed to the higher spectral resolution at cryogenic temperatures and the suppression of phonon scattering, which together allow the intrinsic mechanisms to be more clearly resolved.

We observed more distinct spectral features, including higher emission intensity, sharper emission lines, and pronounced inhomogeneities among different excitation spots, consistent with the comprehensive study in Chapter 3. Notably, most of the 4 K spectra exhibit a characteristic two-peak behaviour, which can be attributed to the typical splitting between free-exciton emission and the broader trapped-exciton emission in low-dimensional perovskite NCs [192]. With increasing temperature, the two peaks gradually merge and undergo a blue shift. This provides further evidence, complementing the results in Fig. 3.7, that the modified NWs exhibit improved luminescence, as reflected by the free-excitonic emission generated at low fluence under cryogenic conditions.

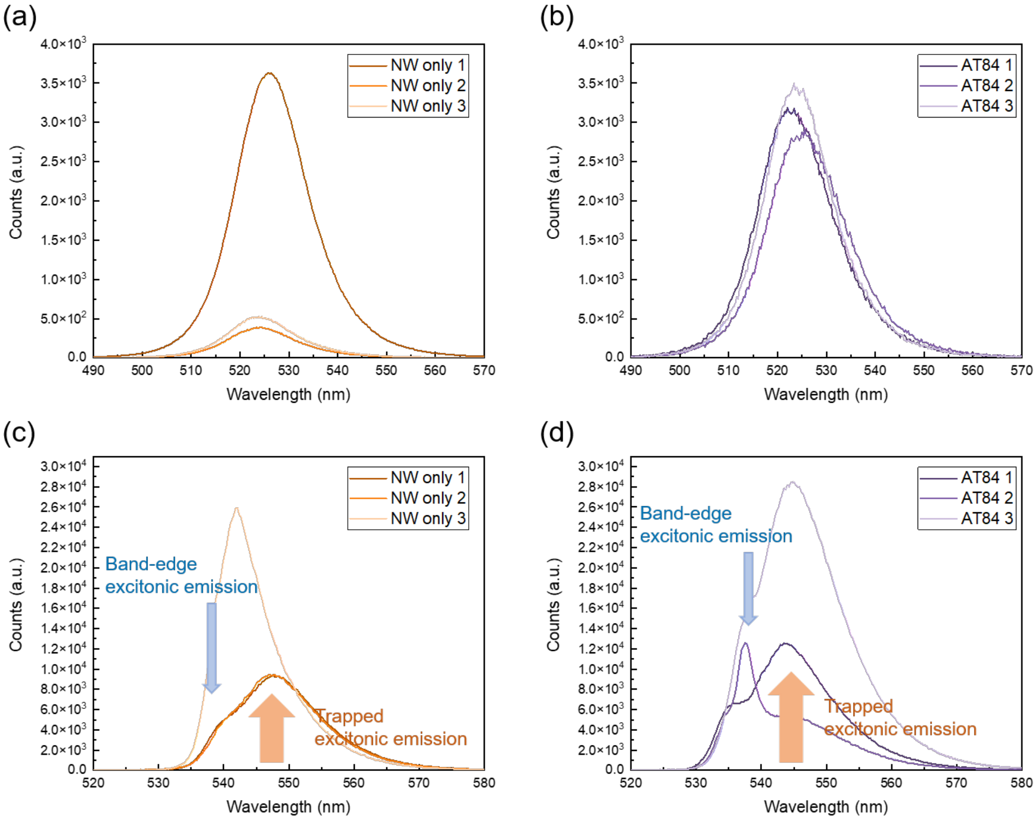

Figure 4.8: Comparison of spectral profiles at RT and 4 K, with and without Mg NPs. (a–b) RT PL spectra of (a) the bare NW sample and the (b) Mg–NW hybrid structure, shown here for AT84 Mg NPs with a mean diameter of 98 nm as an example. (c–d) 4 K PL spectra of the corresponding samples. Note that the labels '1, 2, 3' mark different excitation spots within the same panel; thus, AT84 1 at RT and at 4 K do not necessarily represent the identical spatial position.

By presenting the peak position together with the peak intensity, a clear red shift of the emission relative to the RT case was generally observed in Figure 4.9. This behaviour arises from the absence of exciton activation at cryogenic temperature, where the dominant species are localized excitons, consistent with the extensively studied 4 K PL emission in Chapter 3. Given that the emission channels are highly localized, the variation in the peak centre, particularly in AT82, NPs of diameter 75 nm, can be interpreted as follows: excitation above shallow states redistributes the relative weight of the free-exciton-like emission. In cases of strong coupling, additional emission features may arise on the blue side of the spectrum and even dominate, thereby shifting the overall PL peak toward higher energies.

At 4 K, the enhancement of the PL intensity shows a trend similar to that observed at RT. Stronger enhancement occurs with Mg NPs of sizes smaller than 100 nm due to favourable LSPR coupling, whereas for AT90, NPs of diameter 237 nm, the coupling is limited and energy dissipation dominates, leading to reduced enhancement. In AT104, NPs of diameter 174 nm, an increase in PL intensity is also observed, which can be associated with the transition of the plasmonic coupling mechanism from dipolar to quadrupolar modes.

The TRPL spectra at 4 K all feature an elongated lifetime with significant contribution from the trap-assisted recombinations. Within the initial ∼1–5 ns, all samples display a prompt excitonic decay, followed by a pronounced long-tail component extending from tens–hundreds of ns. The prompt part reflects band-edge excitonic recombination, whereas the long tail is attributed to trapped-excitonic (trap-mediated) emission that becomes prominent when non-radiative channels are suppressed at cryogenic temperatures. The Mg NP-coupled samples exhibit a larger late-time fraction than the NW-only reference, indicating stronger contributions from localized states and interfacial environments introduced by the NPs, except for AT83, NPs of diameter 90 nm, whose behaviour is similar to that of the NW references and is also observed at RT. Clearly, although the PL mechanism at 4 K differs from that at RT, plasmonic coupling still serves to increase the excitation cross section.

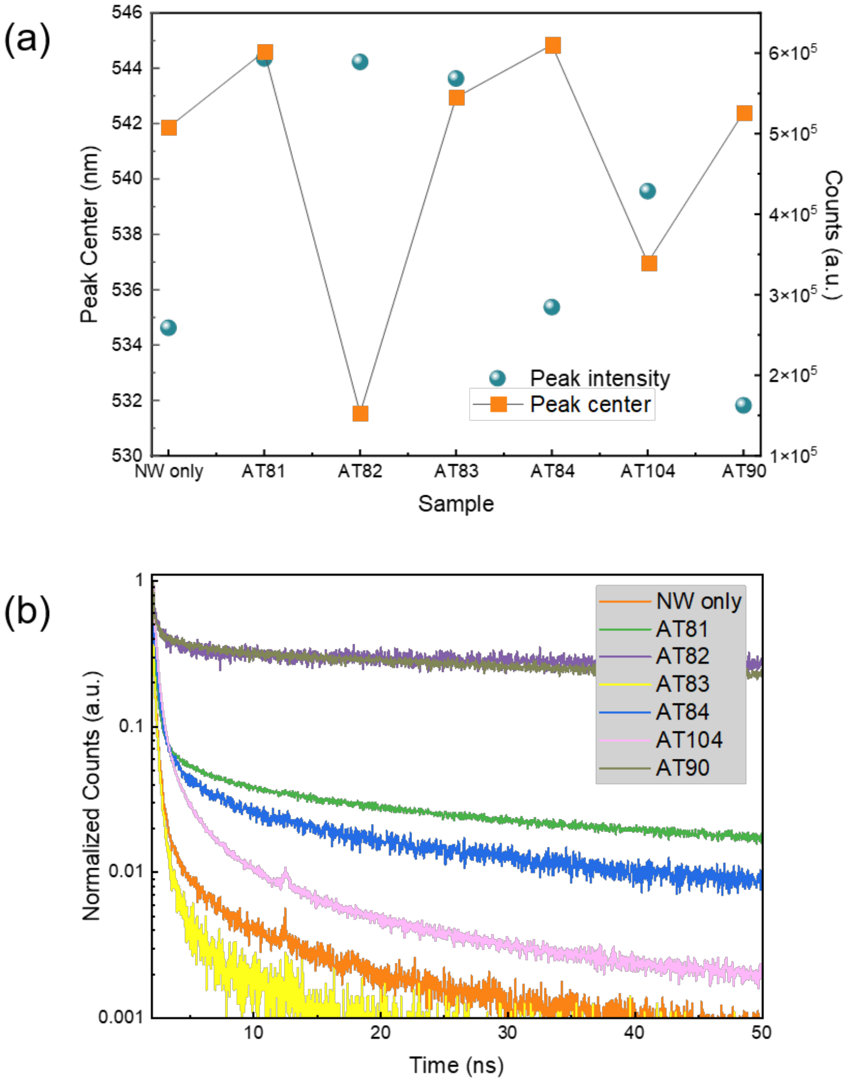

Figure 4.9: 4 K measurements of the Mg–NW hybrid structure with Mg NPs AT81–104. (a) μPL results on the hybrid structure. Blue dots: PL peak intensities as a function of Mg NP size; red dots: spectral peak shifts with varying NP size. An overall red-shifting compared to RT emissions was observed, indicating the transition in PL mechanism. (b) TRPL decay curves at 4 K for all seven samples, including the NW-only reference sample. The long lifetime component is significantly stronger at 4 K

However, due to the limited contribution and resolution of the initial fast decay component, the role of Purcell-enhanced radiative recombination in such hybrid structures remains ambiguous.

In summary, Mg NPs with sizes below 100 nm are favourable for generating plasmonic coupling, primarily through confined local electric fields arising from both the better-matched LSPR modes and the size-dependent near-field distribution. A maximum enhancement of 4-fold was observed at RT and 2.4-fold at 4 K, corresponding to PL processes dominated by free-exciton recombination and by trapped-exciton contributions, respectively. Mg NPs are promising plasmonic materials owing to their stability under ambient conditions at RT and in air. Although phonon interactions affect the emission at RT, the hybrid structures remain effective and are expected to enhance the optical efficiency via plasmonic coupling.

4.6 Plamonic Core-Shell Mg NPs Enhanced Perovskite NW PL at RT

4.6.1 Motivation for spacer design

Following the discussion in Chapter 3, the optimal plasmonic enhancement requires a balance between LSPR coupling and the energy dissipation or quenching associated with morphology. Although the self-limiting MgO shell prevents damping related to direct metal–semiconductor contact, the shell itself is ionic in nature and prone to the formation of surface defects or charged states, which can introduce additional nonradiative recombination pathways. Moreover, as shown both in the previous chapter and in literature [243, 244], the localized field is highly confined in a dielectric spacer, and as the NP size increases, the distance dependence becomes insensitive [244].Therefore, to enable controlled optical interactions and tunable separation, a SiO_2 coating with a thickness below 10 nm was applied.

Figure 4.10 shows the improved RT PL with the presence of coated Mg NPs AT83 (mean diameter 90 nm) and AT84 (mean diameter 98 nm), whose resonance overlaps effectively with the NW emission. Under the same low-fluence excitation conditions,

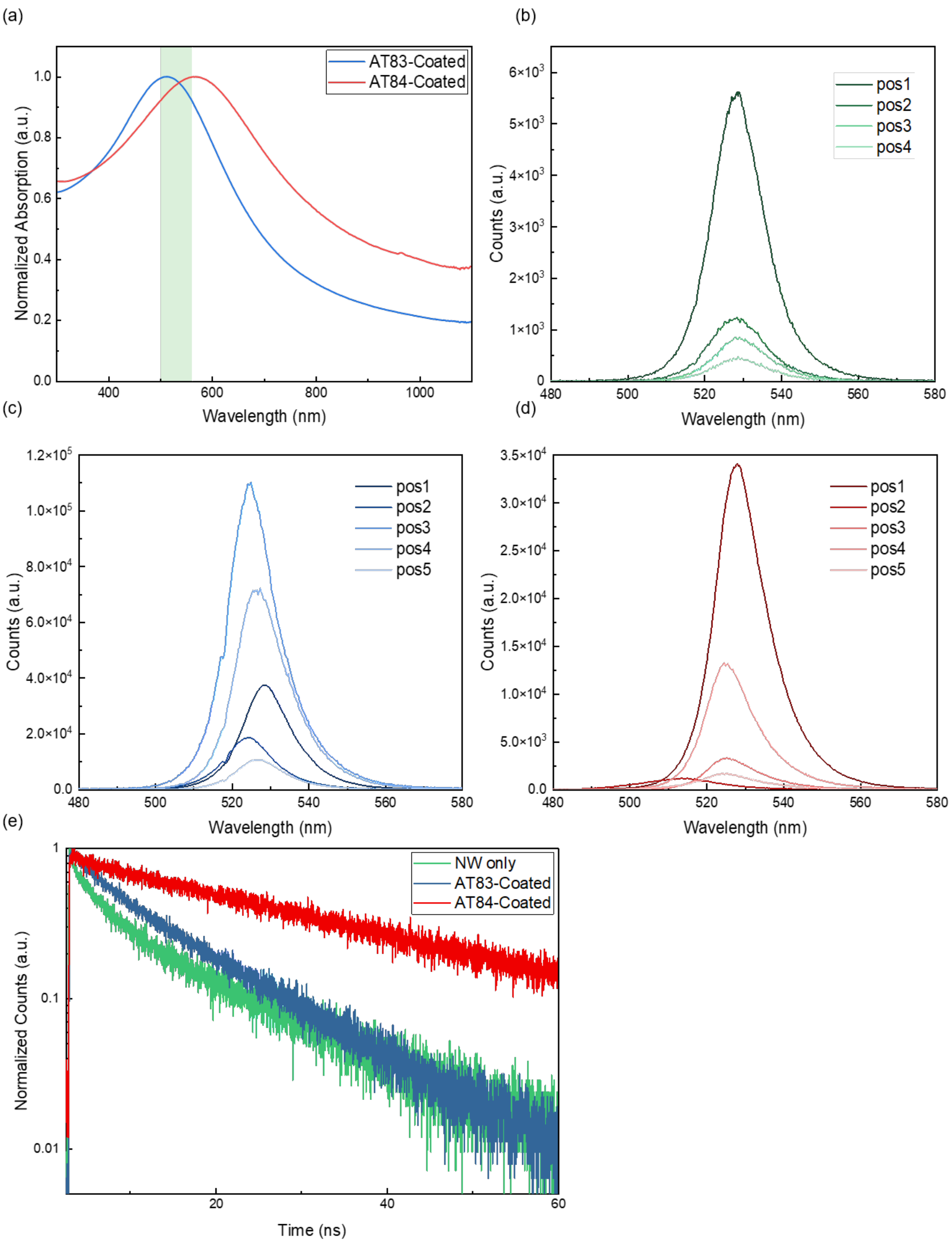

Figure 4.10: PL measurements on SiO_2 coated Mg NPs at RT. (a) UV-Vis absorption spectra of SiO_2 coated AT83 (mean diameter 90 nm) and AT84 (mean diameter 98 nm) Mg NPs. The green shade area indicates the emission from NWs. (b–d) μPL spectra at RT from (b) the reference and (c–d) coated Mg NPs AT83 (blue) and AT84 (red), respectively. Different color brightness in each plot represent different positions. (e) TRPL at RT. The excitation was 7.6 MHz, with a fluence of 16.8 $\mu J/cm^2$.

both the AT83-coated and AT84-coated samples exhibited a significant enhancement in PL intensity. The enhancement was more pronounced for AT83, which features a smaller NP size and consequently better spectral overlap with the LSPR, as expected. The brightest peak in each figure, rather than a better PLQY, is more likely due to the collective contributions from more NWs (reference) or NWs aligned to more Mg NPs (hybrid structure). The detailed minor peak features on the blue-tail region of the PL spectra from the hybrid structures indicate contributions from multiple NWs. A minor blue shift observed for most cases with hybrid structures could be due to suppression of trap state recombinations and higher carrier density induced state filling, while occasional red shifts are attributed to local field tuning of the optical mode and possibly band structure, as discussed above.

The TRPL decay curves again did not exhibit any significant lifetime shortening as would be expected from a classical Purcell effect. On the contrary, an extended lifetime was observed. We attribute this to the reduced energy loss through defect states or other nonradiative pathways upon the introduction of coated Mg NPs. As shown in Figure 4.10(e), the samples with coated Mg NPs (blue and red) display a more mono-exponential decay, whereas the reference sample shows an initial mono-exponential component for the first few ns, which we assign to free excitons, followed by a longer tail consistent with a bi-exponential behaviour that we previously attributed to trapped excitons. The fitted τ for the reference sample, coated AT83 (mean diameter 90 nm) and AT84 (mean diameter 98 nm) are 14.6 ns, 14.6 ns and 20.6 ns respectively.

This can be interpreted as follows: under strong LSPR, not only is the excitation cross section broadened, but the increased LDOS associated with the Purcell effect enhances the probability of radiative recombination by amplifying existing optical modes, thereby providing more available recombination pathways. Once excitons are generated, they are more efficiently exposed to emissive channels, and the decay dynamics reveals emission channels that were previously obscured by trap-mediated processes. A similar situation was observed with Ag NPs at 4 K in Figure 3.17. Thus, the longer and more stable exciton decay, although counter-intuitive in the context of plasmonic enhancement, indicates that plasmonic coupling not only modifies radiative recombination but also suppresses trap-related processes, leading to an apparently extended lifetime.

Compared to the case of uncoated Mg NPs, the application of a thin SiO_2 layer further strengthens the coupling by providing an optimized spacing, such that both mechanisms–enhanced radiative recombination and reduced nonradiative loss–act cooperatively to improve the PL emission.

4.6.2 Comparison with Ag NPs Based Plasmonic Enhancement

Mg NPs are often considered to suffer from higher Ohmic losses and therefore are regarded as less favourable than the widely employed Ag and Au nanostructures for plasmonic applications. To directly evaluate their relative performance, we carried out a comparison between coated Mg NPs and Ag NPs of comparable size (80 nm), both encapsulated with the same thickness of SiO_2.

Figure 4.11 shows the comparison between Ag and Mg as plasmonic NPs enhancing the NW PL. The spectral overlap of Ag is much more limited than that of Mg NPs, and therefore a less enhanced PL intensity was observed. However, a decrease in the PL counts does not necessarily mean a weaker coupling, considering the energy loss of Mg NPs and the collective contribution of an unknown number of NWs. In Figure 4.11(c) one can clearly note that the decay for all three hybrid structures features more mono-exponential shape while the lifetime with Ag is dramatically shortened due to strong LSPR that the radiative recombination rate in this case is further enhanced.

Figure 4.11 compares the plasmonic effects of Ag and Mg NPs on the NW emission. The spectral overlap of Ag is more limited than that of Mg, along with a lower PL enhancement. Nevertheless, a decrease in PL intensity does not necessarily imply weaker coupling, since energy dissipation in Mg and the collective contribution from an unknown number of NWs must also be considered. As shown in Fig. 4.11(c), the decay dynamics of all three hybrid structures display

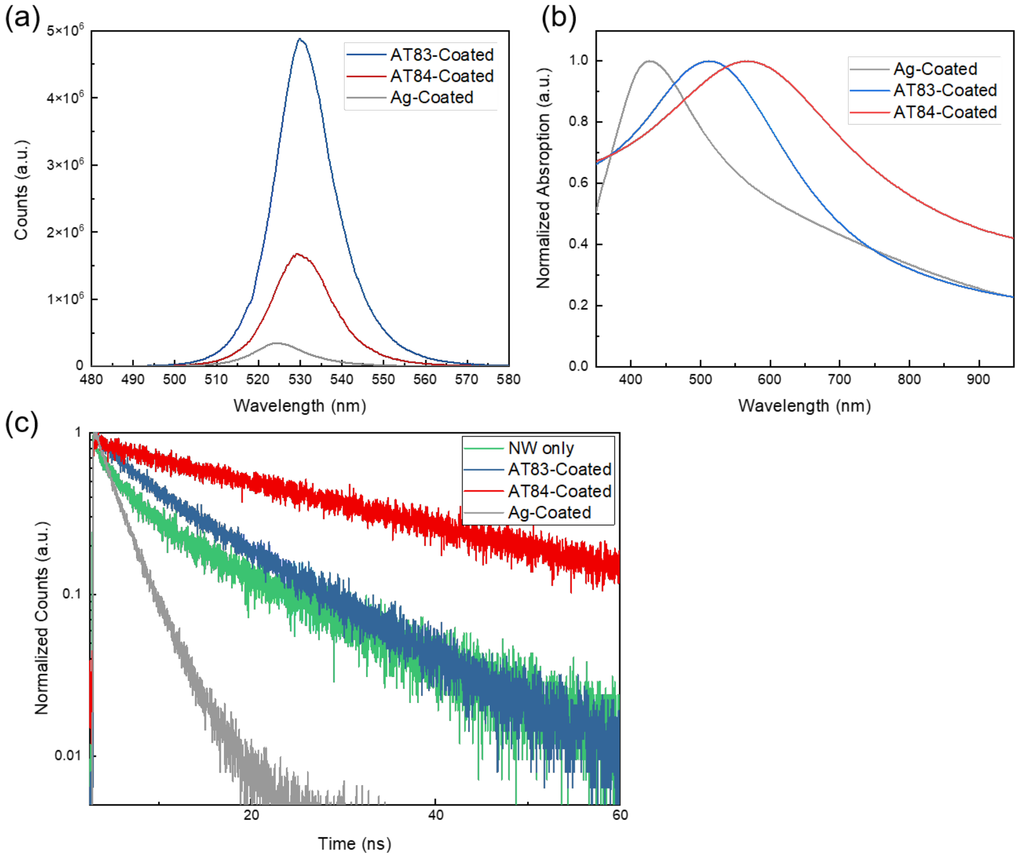

Figure 4.11: Comparison of PL enhancement by SiO_2-coated Mg and Ag NPs. (a) PL spectra of hybrid structures with SiO_2-coated Mg NPs AT83 (90 nm) and AT84 (98 nm), and Ag NPs (80 nm). (b) UV–Vis absorption spectra of the corresponding metal NPs. (c) TRPL decay curves at RT. The excitation repetition rate was 7.6 MHz with a fluence of 16.8 μJ/cm^2.

a more mono-exponential profile, while the lifetime in the Ag case is markedly shortened. This reflects the stronger LSPR coupling in Ag, where the radiative recombination rate is further enhanced.

Overall, these results suggest that Mg, at the cost of higher losses, provides broader spectral overlap with more stable enhancement, whereas Ag enables stronger field enhancement and Purcell effect.

4.6.3 Determining the Enhancement factor

The enhancement factor was determined by 2D mapping using a 405 nm pulsed laser source at 5 μW, scanning an area of 50 μm × 50 μm with a step size of 1 μm in both directions. The mapping was repeated multiple times for each sample, with one representative example shown in Figure 4.12.

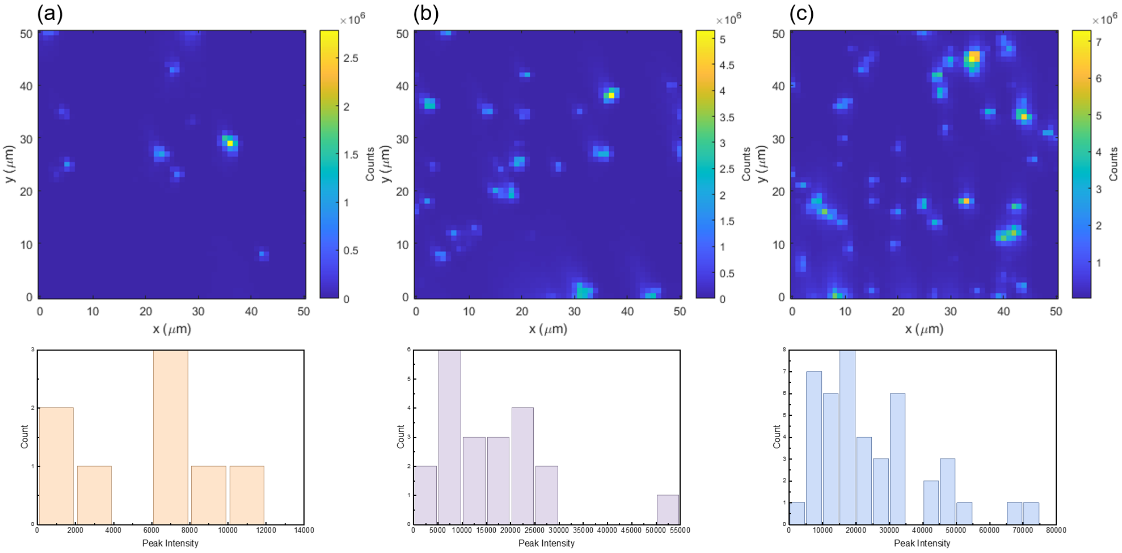

Figure 4.12: 2D mapping of hybrid structures with statistical analysis. Spatial PL mapping and the corresponding histograms of extracted bright pixels with peak intensity for (a) NW-only, (b) NW with SiO_2-coated AT83 (mean diameter 90 nm) Mg NP, and (c) NW with SiO_2-coated AT84 (mean diameter 98 nm) Mg NP samples.

To minimize the influence of NW clustering, we extracted the bright pixels corresponding to positions with NW emission and plotted histograms of the PL peak intensities. Spots with peak intensities lying outside the mean $\pm 3\sigma$ range were excluded (for example, in AT83 the highest-intensity spot shown in Figure 4.12(b)). By collecting all spots that presumably correspond to comparable contributions from individual NWs in each sample, the average peak intensities were obtained. The results show a 1.7-fold enhancement for SiO_2-coated AT83 (diameter 90 nm) and a 4.1-fold enhancement for SiO_2-coated AT84 (diameter 98 nm) Mg NPs.

4.7 Conclusion and Discussion

In this chapter, we have presented an innovative study on facet–spheroid Mg NPs as plasmonic enhancers of PL in a practical configuration. A comprehensive demonstration of plasmon-enhanced emission from core–shell Mg NP–$CsPbBr_3$ NW hybrid structures at RT was conducted. For Mg NPs smaller than 100 nm, strong coupling between their dipolar modes and the emission of improved lead halide perovskite NWs was observed, yielding enhancement factors of 1.7-fold and 4.1-fold for SiO_2-coated Mg NPs with diameters of 90 nm and 98 nm, respectively, based on statistical analysis. The enhancement originates from both the strong local fields and the modulation of recombination pathways, leading to brighter and more efficient excitonic emission at RT.

The mature synthesis techniques of plasmonic Mg NPs with tunable size control further enable the feasibility of LSPR applications ranging from the UV to the near-IR, encompassing both dipolar and higher-order modes. Moreover, the self-limiting oxide shell of Mg provides protection against energy dissipation and ensures the stability of hybrid structures under ambient RT conditions.

In comparison with Ag NPs of similar core–shell configurations, the plasmonic enhancement of Mg is limited by its intrinsically higher Ohmic losses and geometric constraints, which restrict the plasmonic effectiveness. As the present study only explored the effect of varying the spacer without further optimization, the maximal enhancement has not yet been fully realized. Systematic studies on the contribution and modulation of different recombination channels remain an important direction for future work. Additionally, for potential on-chip nanophotonic applications, precise geometrical design and controlled positioning of Mg NPs are also crucial aspects for advancing device performance.

Overall, Mg has emerged as a promising plasmonic material at RT, offering an attractive alternative to the conventional noble metals such as Ag. In addition to its competitive plasmonic performance [214], Mg is earth-abundant and cost-effective, making it particularly appealing for scalable and sustainable optoelectronic technologies. These advantages, combined with its intrinsic stability provided by the native oxide shell, highlight Mg as a practical and versatile platform for plasmonic enhancement, opening pathways toward advanced and low-cost nanophotonic devices.

5

PL of Perovskite Nanoplatelets Integrated with Optical Nanocavity

Contents

5.1 Chapter Introduction 130
5.2 Optical Cavity Coupled PL 131
5.3 Samples 132
  5.3.1 $CsPbI_3$ Nanoplatelets 132
  5.3.2 Optical Nanocavity 137
5.4 μPL Investigation on Nanoplatelets with Different Layer Numbers 139
5.5 μPL Investigation on Nanoplatelets Coupled to Optical Nanocavities 144
5.6 Conclusion and Discussion 148

5.1 Chapter Introduction

This chapter discusses an alternative method to confine the optical modes and modulate the recombination dynamics – optical nanocavities coupling to the perovskite NPLs. Section 5.2 provides a general review of the nanocavity-mediated light–matter interactions with emphasis on perovskite NPLs and competing emitters for such applications. Section 5.3 details the synthesis and characterization of NPLs with controlled layer numbers and the cavity designs employed. Sections 5.4 and 5.5

report the μPL properties of uncoupled NPLs and of NPLs coupled to nanocavities, respectively. The chapter concludes with the observed spectral modification and outlines avenues for optimization toward applications such as single-photon sources, where ultra-narrow emissions are preferred.

5.2 Optical Cavity Coupled PL

Optical nanocavities offer an unparalleled platform for manipulating light–matter interactions at the nanoscale, profoundly influencing the PL properties of quantum emitters. Structures engineered to confine electromagnetic fields within subwavelength volumes provide powerful platforms for the precise control of light–matter interactions. While the foundational principles of cavity quantum electrodynamics, such as the Purcell effect, provide the theoretical framework for understanding these interactions, the contemporary landscape of research is increasingly focused on the practical realization of these effects through sophisticated nanocavity designs and their integration with diverse quantum emitters. From high-quality factor (Q-factor) dielectric photonic crystal nanocavities that enable strong coupling with single QDs [245–247], to plasmonic nanocavities that achieve extreme sub-wavelength confinement and RT strong coupling with quantum emitters [248–250], the engineering of the photonic environment has become a highly sophisticated endeavour.

Currently, the palette of quantum emitters has expanded significantly beyond traditional semiconductor QDs, now encompassing 2D materials like transition metal dichalcogenides (TMDs) and hexagonal boron nitride (hBN) with their unique excitonic and spin properties [250–253], as well as the rapidly developing class of lead halide perovskite NCs, renowned for their high PLQYs and tunable emission [34, 254, 255]. The work by Igarashi et al. investigated the correlation between single-photon emission and the size of caesium lead bromide perovskite NCs, finding that perovskite NPs smaller than approximately 10 nm exhibited high-probability single-photon emissions, which decreased linearly as volume increases [256]. The size-dependent quantum confinement effects relevant for single-photon sources are therefore highlighted, motivating the use of thin NPLs where strong confinement is expected. Integrating such size-controlled perovskite NCs into nanocavities could further optimize their single-photon emission properties, similar to how QDs are used in photonic crystal cavities [246]. Previous work also investigated superlattices formed by $CsPbBr_3$ and $CsPbBrI_2$ NCs [255]. μ-PL spectra and transients revealed lifetimes as short as 160 ps in $CsPbBr_3$ superlattices, 10 times lower than in thin films, attributed to domains of near-identical NCs (1000 to 40,000 NCs) coupled by dipole-dipole interaction. While this work focuses on self-assembled superlattices rather than engineered nanocavities, it demonstrates the potential for collective radiative enhancement in perovskite systems.

Motivated by these advances, our motivation is to establish a RT, lithographic platform that couples layer-controlled $CsPbI_3$ NPLs to dielectric nanocavities. We aim to determine how spectral alignment, quality factor, mode volume, dipole orientation, and loading uniformity govern the observable emitter response. A further goal is to derive simple design rules that translate across materials and processes, enabling compact and scalable sources for integrated photonics and single-photon technologies.

5.3 Samples

5.3.1 $CsPbI_3$ Nanoplatelets

Synthesis

The materials used are as follows: Lead (II) Iodide (PbI_2, 99%, Sigma Aldrich), Oleylamine ($C_{18}H_{37}N$, 70%, Sigma Aldrich), Oleic Acid ($C_{18}H_{34}O_2$, 90%, Sigma Aldrich), caesium acetate (CH_3COOCs, $\geq$99.99%, Sigma Aldrich), Toluene ($C_6H_5CH_3$, 99.8%, Sigma Aldrich), Hexane (C_6H_{14}, $\geq$95%, Sigma Aldrich).

The synthesis of $CsPbI_3$ NPLs was carried out following a colloidal route with separate preparation of precursor solutions.

Regarding the precursor solutions, PbI_2 precursor was prepared by dissolving 46.1 mg of PbI_2 in 10 mL of toluene together with 100 μL of oleylamine (OAm) and 100 μL of OA. The mixture was stirred and heated to 60 °C until completely dissolved. In parallel, a Cs(oleate) stock solution was obtained by dissolving 38.9 mg of caesium acetate in 4 mL of OA under the same conditions.

For the NPL synthesis, 2 mL of the PbI_2 precursor solution was preheated at the desired reaction temperature for 10 min under continuous stirring. A defined volume of Cs(oleate) was then injected and allowed to react for the specified period. The reaction mixture was purified by sequential centrifugation: first at 3000 rpm for 3 min to collect the supernatant, followed by centrifugation at 12000 rpm for 5 min. The final precipitate was redispersed in 1 mL of hexane and filtered through a polytetrafluoroethylene (PTFE) (0.2 μm) filter.

All NPL samples were fabricated by Prof. Robert Hoye's group in the Department of Chemistry, University of Oxford.

Determine the layer number

PL investigation was first conducted on determining the NPL species accessible under the synthesizing conditions. The relationship between the PL peak centre and the corresponding number of monolayers (MLs) is inferred from the work of Tong et al. [257]. The summarized PL peak ranges associated with different ML numbers are presented in Figure 5.1.

Number of MLs	**3**	**4**	**5**	**6**
PL peak range (nm)	600	623-633	647-655	680-685

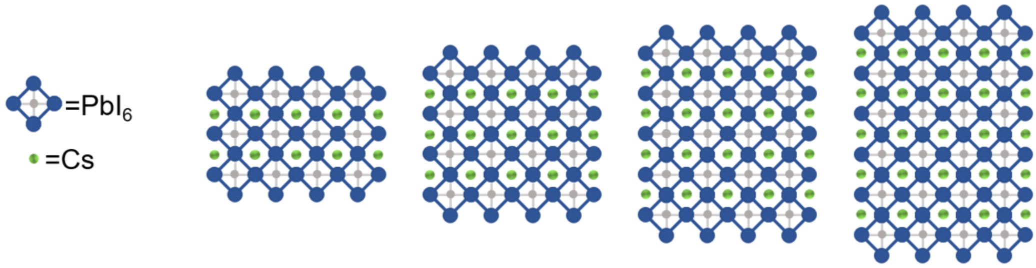

Figure 5.1: Summary of PL peak ranges for $CsPbI_3$ NPLs with n = 3–6 MLs. PL peak positions are inferred from Ref. [257]. A schematic illustration of NPLs with different number of MLs is shown below.

The recipe for the synthesis of NPL with different number of MLs by first tuning the reaction temperature and the injected Cs(oleate) volume, after which the PL for each mixture was directly measured without any purification. In that case, a broader PL peak profile indicates a greater polydispersity of the NPLs. The temperatures and Cs(oleate) volumes selected with the corresponding PL spectra are presented in Figure 5.2. At 0 °C and 30 °C, the operable Cs(oleate) volume window was limited to $\leq 140\,\mu$L and $\leq 120\,\mu$L, respectively, because the photoactive α-phase could not be sustained at larger volumes. This behaviour can be attributed to the limited capacity of the ligands to stabilize the high yield of different NPL populations formed at these temperatures.

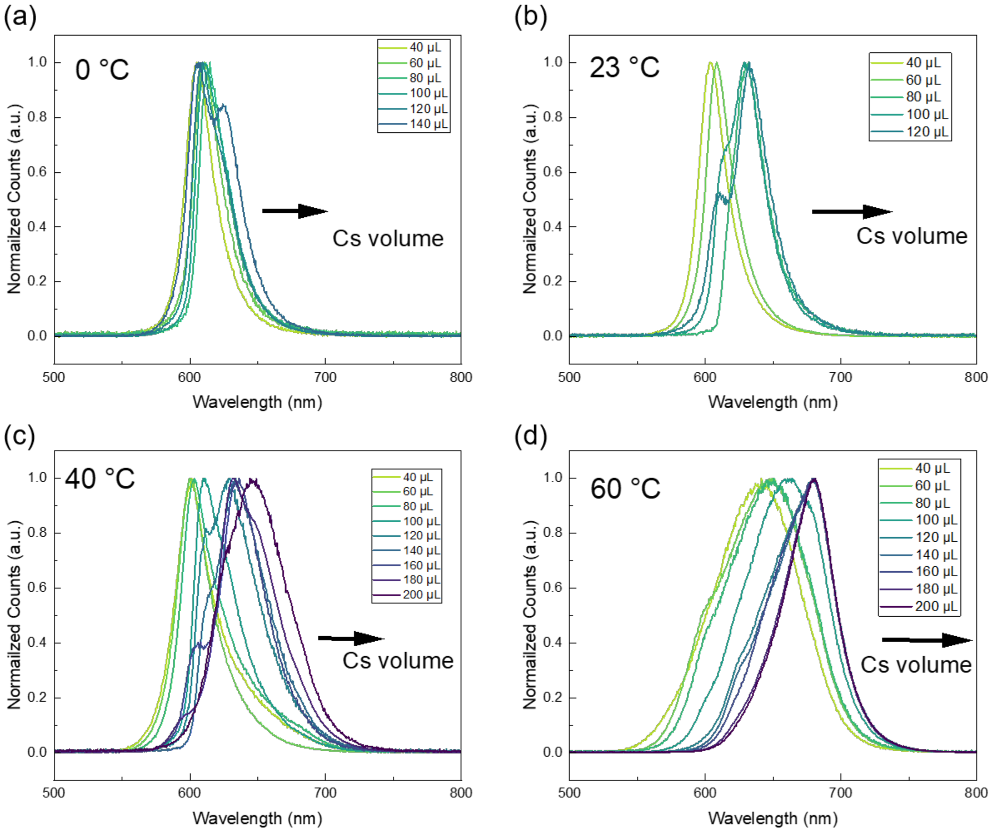

Figure 5.2: Normalized PL spectra of $CsPbI_3$ NPLs synthesized at (a) 0 °C, (b) 23 °C, (c) 40 °C, and (d) 60 °C, with the corresponding Cs(oleate) injection volumes indicated.

In Figure 5.2, it is evident that higher synthesis temperatures and larger

Cs(oleate) volumes lead to broader FWHM values, reflecting the presence of a richer distribution of NPL species. Distinct populations can subsequently be isolated through the purification procedure described above. Whilst a modest linewidth broadening is expected from temperature-induced effects within individual NPL ensembles, the substantially broadened PL spectra observed at elevated temperatures signify the coexistence of multiple PL components originating from NPLs of different thicknesses. Moreover, a pronounced spectral shift is detected at 80 μL of Cs(oleate) at 23 °C, suggesting the formation of quasi-square NPLs. This blue shift can be attributed to reduced quantum confinement together with an increased volume-to-surface ratio in these structures [258]. Although this effect is most clearly resolved at 23 °C, a similar feature is also present at 0 °C, whereas abrupt peak shifts are absent at higher synthesis temperatures, indicating that the emergence of such NPL morphologies requires specific precursor volumes under restricted conditions.

Table 5.1: Synthesis conditions for $CsPbI_3$ NPLs with different monolayer (ML) numbers.

ML number	Cs(oleate) volume / μL	Temperature /°C	Reaction time / s
$n = 3$	30	0	120
$n = 4$	85	23	180
$n = 5$	200	48	20
$n = 6$	240	60	10

It is generally expected that a larger Cs(oleate) volume promotes the formation of thicker NPLs with higher ML numbers. At the lowest synthesis temperature, attempts with smaller Cs(oleate) volumes resulted in negligible NPL yield after centrifugation, indicating that ultrathin NPLs are unstable under these conditions. At 0 °C, the smallest Cs(oleate) volume produced a PL peak centred around 600 nm, corresponding to the thinnest accessible NPLs with $n = 3$ MLs [257]. With increasing temperature, the PL peak progressively red-shifts, reaching a limit at 60 °C that corresponds to $n = 6$ NPLs. Further increases in temperature could not be sustained in solution; thus, dispersions containing NPLs with $n = 3$–6 MLs were accessible. Monodisperse samples of each component were subsequently obtained by carefully tuning the reaction conditions and applying sequential centrifugation. The synthesis conditions corresponding to each ML thickness are summarized in Table 5.1.

Sample characterization

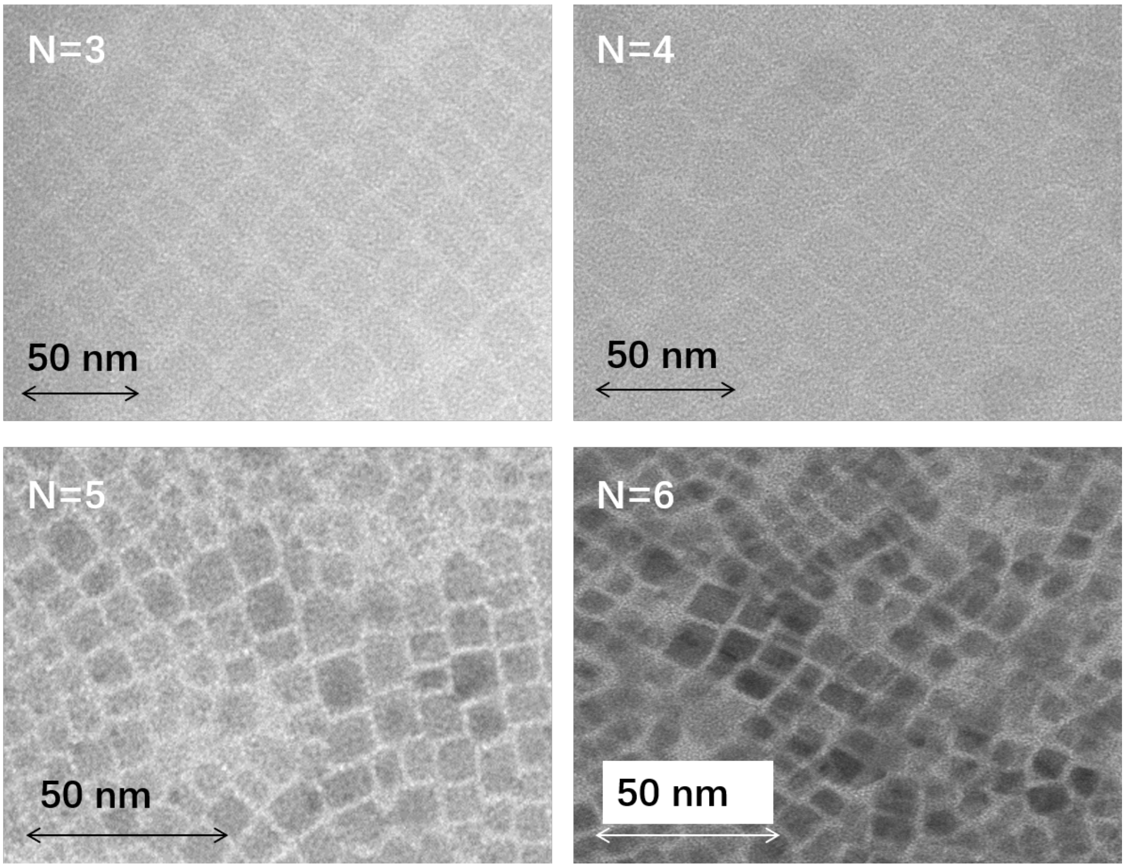

Figure 5.3: TEM images of NPL with different layer numbers. The images were collected by the group of Prof. Robert Hoye at the University of Oxford.

TEM images (Figure 5.3) confirm the successful synthesis of $CsPbI_3$ NPLs with controlled thickness from 3 to 6 MLs. For thinner samples ($n = 3$ and $n = 4$), the NPLs exhibit relatively low image contrast due to their reduced thickness, while the edges remain difficult to resolve. $n = 5$ and $n = 6$ NPLs show more distinct square-like shapes and higher contrast, consistent with increased thickness. These observations corroborate previous PL results, indicating the success in producing the expected NPLs, where different distinct n values are associated with different synthesizing conditions listed above. During the following discussion, an $n = 2$ NPL sample was also mentioned, particularly in Section 5.4, for comparison of the

UV–vis spectra. This sample was synthesized by a similar process as described above with modified parameters.

5.3.2 Optical Nanocavity

The design and fabrication of the nanocavity

Figure 5.4 presents the illustration of the nanocavities used in this work. The cavity structures were defined as square regions of $30 \times 30\,\mu\mathrm{m}^2$, patterned with periodically arranged Si nanopillars using electron-beam lithography. Each pattern was directly fabricated on the Si substrate, ensuring that the resonators and the underlying base are composed of the same material. The nanopillars had a thickness of approximately 100 nm and a period of 415 nm, introducing a lateral refractive index modulation through the etched air sidewalls, which enables diffractive coupling to guided-mode resonances.

Arrays with different pillar diameters were designed, denoted as A1–5 (170 nm), B1–5 (180 nm), and C1–5 (190 nm). This all-Si configuration functions as a weakly modulated 2D grating, where the interplay between nanopillar scattering and the array periodicity supports narrow-band resonances near the $CsPbI_3$ NPL emission window, which has been reported in the literature to lie approximately between 600 and 700 nm [257]. Simulations predict the nanocavity resonance to be centred within 600–700 nm, the same range as emission from NPLs, as will be presented in the following sections. Experimental reflection spectra were also measured, and the corresponding results are provided in Appendix B.1 for completeness. The fabrication of the optical nanocavities and the simulations were carried out by Dr. Mengyun Wang from the Department of Materials, University of Oxford.

After the optical nanocavities were fabricated, the NPL samples were diluted to an appropriate concentration and dropcast onto the cavity surface. Although variations in sample distribution may influence the overall PL intensity, the PL peak profile (i.e., spectral shape) is not significantly affected, as each set of measurements employed NPLs with the same layer number. Attempts to spin-coat the NPLs onto the nanocavities resulted in insufficient material being retained within the

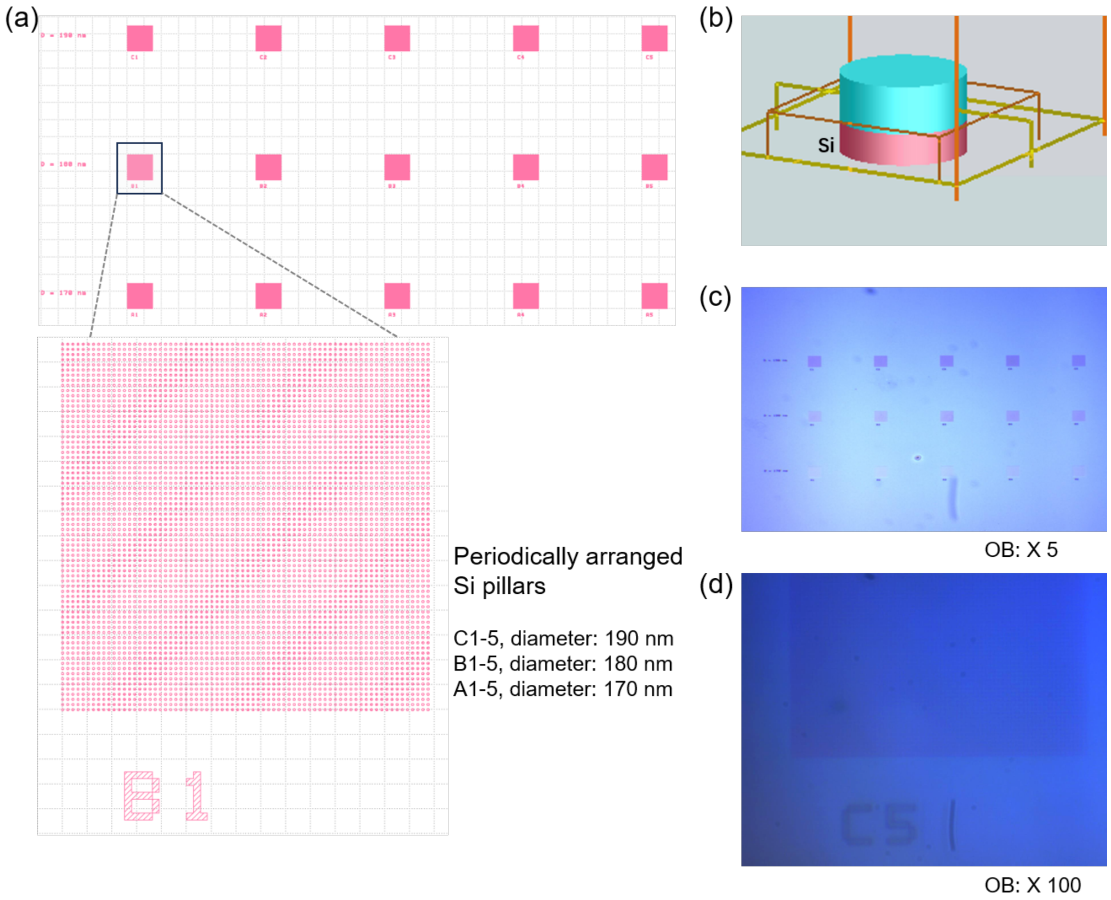

Figure 5.4: Design and fabrication of periodically arranged Si pillar nanocavities. (a) Layout of the nanocavity array, with each block consisting of a periodic arrangement of Si pillars. The inset shows an enlarged view of block B1. The three sets of arrays are defined as C1–5, B1–5, and A1–5, corresponding to pillar diameters of 190 nm, 180 nm, and 170 nm, respectively. (b) Schematic illustration of a single Si pillar nanocavity. (c) Optical microscope image of the patterned arrays at 5× magnification. (d) Optical microscope image at 100× magnification, resolving the periodic pillar arrangement within an individual block (C5).

cavity regions, leading to very weak or even absent PL signals. This is illustrated in Figure 5.5, where the dark circular area (expected to contain NPLs) exhibits no detectable PL emission, in contrast to the bright PL observed from regions outside the cavities. The weak signal near $\sim 500\,\mathrm{nm}$ is attributed to scattered light, as no appreciable difference is observed between the two spectra at this wavelength.

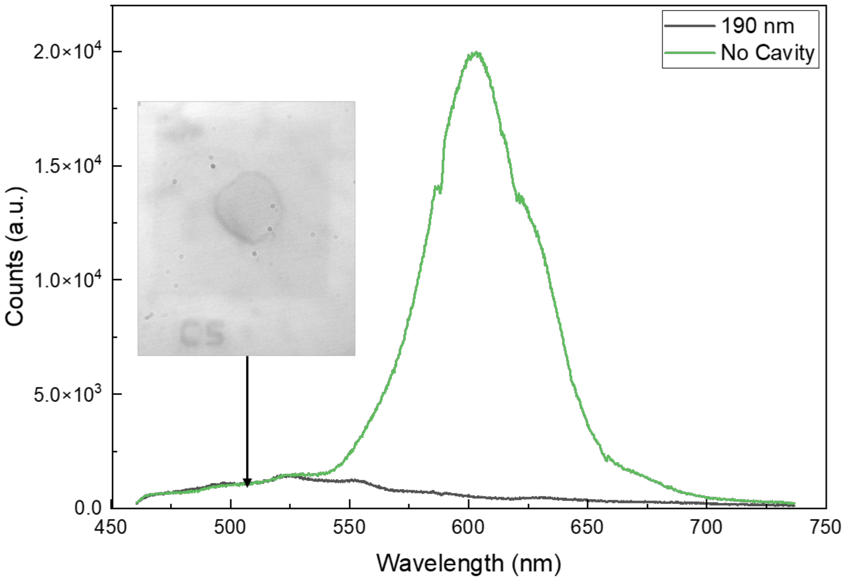

Figure 5.5: Spin-coated NPLs on nanocavity arrays for μPL measurements. Inset: white-light microscope image from the μPL setup, showing the measurement region (C5) with nanopillars of 190 nm diameter.

5.4 μPL Investigation on Nanoplatelets with Different Layer Numbers

The setup in the context of this chapter was the 400 Ti:Sapphire laser operating at 7.6 MHz. For all the TRPL measurements an APD detector with 4 ps bins for the TCSPC card was used. RT μPL investigations were first performed on the NPL samples with different layers to precisely describe the emission properties of NPLs without any coupling to optical nanocavities.

Figure 5.6 shows the normalized PL spectra for n =3–6 NPL samples at the same measurement conditions. The peak centres from Gaussian fitting are 602 nm (n = 3), 630 nm (n = 4), 652 nm (n = 5), 685 nm (n = 6), and the FWHM 24 nm, 28 nm, 46 nm and 37 nm, respectively. The narrow peaks for n = 3 and n = 4 samples indicate the size distribution to be narrow, while the broad peaks for thicker NPLs fabricated under higher temperatures indicate more impurities. Specifically, the n = 4 sample shows the largest broadening, showing most the defects and mixture of different NPL species.

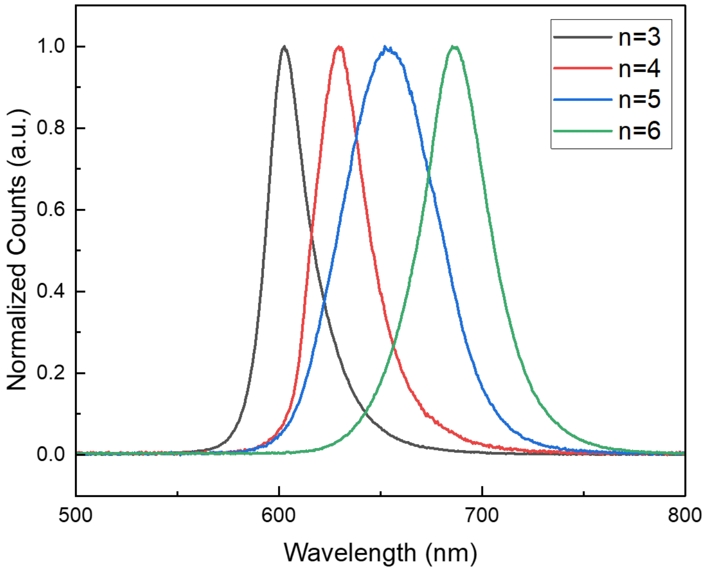

Figure 5.6: Normalized PL spectra of $CsPbI_3$ NPLs. The μPL measurements were performed under 400 nm excitation at a fluence of $0.17\,\mathrm{mJ\,cm^{-2}}$.

The tuning of the emission wavelength by varying the NPL thickness is in good agreement with previously reported PL results [257]. The systematic shift of the peak centre reflects the variation in the 1s excitonic energy, which is further broadened by thermal effects, or equivalently, the change in exciton binding energy. This behaviour can be interpreted as a manifestation of the quantum confinement strength along the out-of-plane direction. In thinner NPLs, the stronger confinement enhances the Coulomb interaction between electrons and holes, leading to larger exciton binding energies and a blue-shift of the emission. In contrast, as the NPL thickness increases, the reduced confinement weakens the binding energy, resulting in a red shift of the excitonic transition.

The gradual change of binding energy could be further visualized by UV–Vis absorption spectra, as in Figure 5.7. The normalized absorption spectra of $CsPbI_3$ NPLs with different thicknesses are shown in Figure 5.7. For thin NPLs (e.g., $n = 2$ and $n = 3$), pronounced excitonic absorption peaks are clearly observed. As the thickness increases (e.g., $n = 4$), the excitonic feature becomes broader and gradually shifts to lower energy, consistent with a reduction in the confinement strength. In the thickest sample ($n = 6$), the distinct excitonic peak is less resolved and the spectrum approaches that of a bulk-like perovskite, in which case only a smooth absorption edge remains.

The excitonic transition energies can be estimated directly from the peak positions of the absorption spectra. These show a systematic red-shift from approximately 2.25 eV at $n = 2$ to below 1.90 eV at $n = 6$, highlighting the crossover from strong excitonic confinement in few-monolayer NPLs to the weakly confined regime in thicker samples.

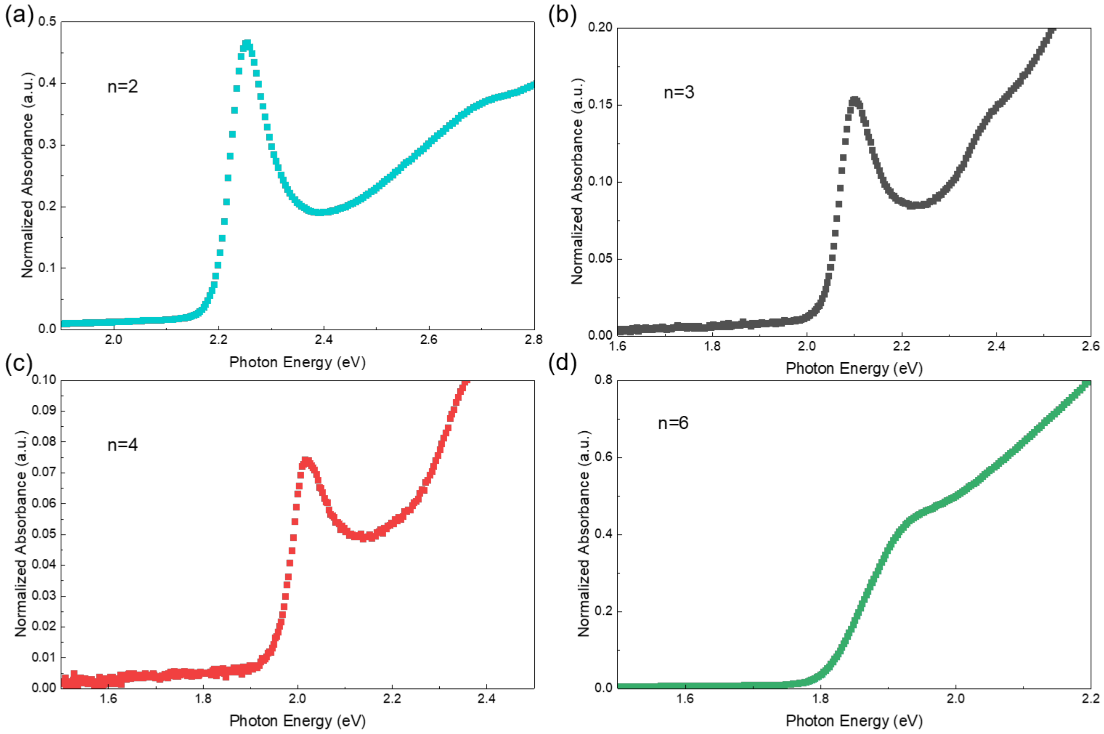

Figure 5.7: Normalized UV–Vis absorption spectra of $CsPbI_3$ NPLs with different thicknesses. (a) $n = 2$, (b) $n = 3$, (c) $n = 4$, and (d) $n = 6$. Pronounced excitonic absorption peaks are observed for thin NPLs, which gradually weaken and broaden with increasing thickness. The $n = 5$ data are missing, due to the high level of impurities in the corresponding NPLs.

X-ray diffraction (XRD) patterns of the NPLs with $n = 3$–6 are shown in Figure 5.8, further support the claims above. All samples exhibit two dominant reflections at $\sim 14°$ and $\sim 28°$, which can be indexed to the (100) and (200) planes of the black-phase $CsPbI_3$ perovskite lattice. For $n = 3$ and $n = 4$, multiple sharp diffraction peaks are observed, consistent with the perovskite crystal structure and indicating good crystallinity. However, extra features are observed at 11.5°, 13.5°, and 27.1°, suggesting the presence of minor secondary phases, potentially related to δ-phase $CsPbI_3$. Also, multilayer diffraction arising from relatively low stacking disorder, as well as partial degradation products, can give rise to additional scattering features, which are more pronounced in NPLs with smaller ML numbers. The $n = 5$ sample exhibits poor diffraction contrast with strong background noise, reflecting the high level of impurities and reduced crystalline quality, in agreement with the absence of clear optical features in its absorption spectrum and the broad PL emission. For $n = 6$, the diffraction pattern is dominated by intense reflections around $2\theta \approx 14°$ and 28°, characteristic of $CsPbI_3$ NCs, where minor splitting at $2\theta \approx 14$ is due to random fluctuations of the thickness.

Power-dependent TRPL were measured at 4 different excitation powers to account for relatively low and high excitation regimes. Figure 5.9 presents the normalized TRPL results.

The decay curves generally exhibited a trend of shorter lifetimes with increasing excitation power. In addition, an increase in the number of layers leads to weaker confinement and a smaller recombination rate, and thus is expected to extend the excitonic lifetime [259]. As shown in Figure 5.9, this tendency is approximately followed, as the $n = 4$ NPL exhibits a longer lifetime than $n = 3$, and $n = 6$ is longer than $n = 5$. However, the lifetimes do not strictly increase with layer number (i.e., $\tau_{n=3} < \tau_{n=4} < \tau_{n=5} < \tau_{n=6}$), which can be attributed to the presence of defects and impurities in thicker NPLs synthesized at higher temperatures. Moreover, multicomponent decay behaviour is evident in all four panels. To analyse this further, a tri-exponential decay fitting was applied to both the lowest fluence ($0.17\,\mathrm{mJ/cm^2}$) and the highest fluence ($1.68\,\mathrm{mJ/cm^2}$) TRPL data. The extracted lifetimes fall into three characteristic timescales: a fast component in the picosecond range, an intermediate component of 1–10 ns, and a slow component above 10 ns. The intermediate lifetimes are typically associated with excitonic recombination [260]. Specifically, at low fluence, the intermediate lifetimes are 3.49, 6.07, 3.26, and 5.38 ns for $n = 3$–6, respectively. Increasing the fluence to $1.68\,\mathrm{mJ/cm^2}$ results in a

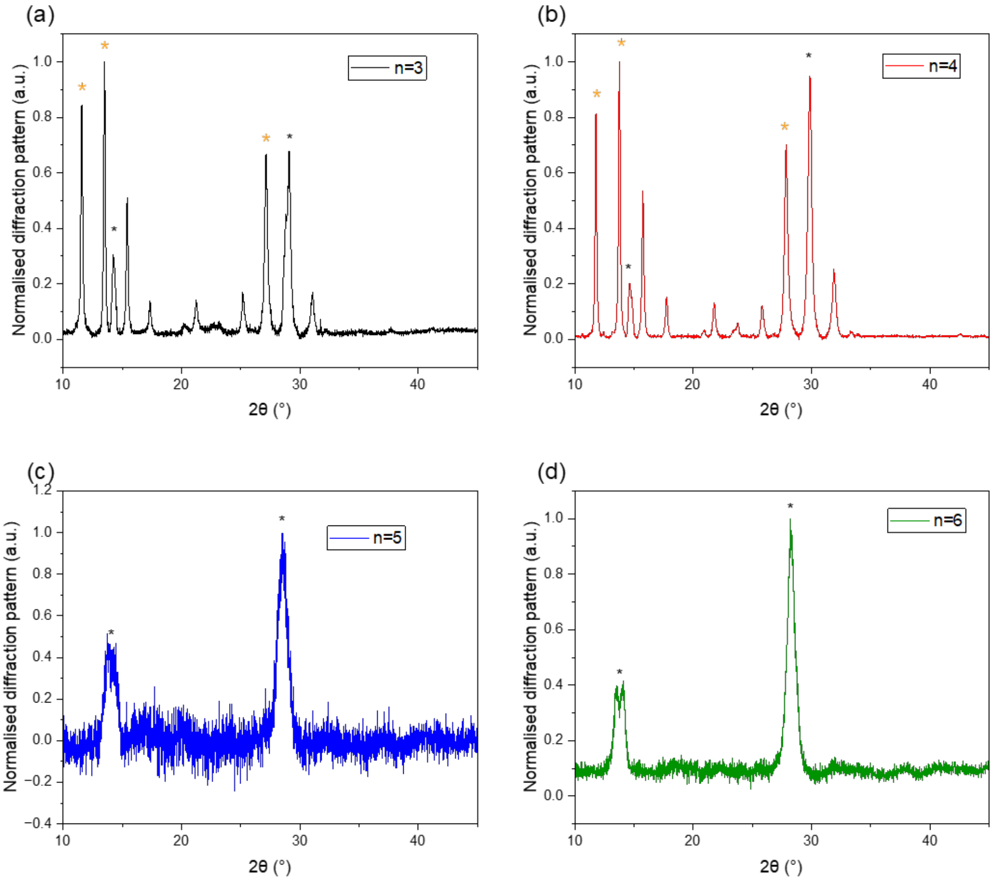

Figure 5.8: XRD patterns of $CsPbI_3$ NPLs with different thicknesses. (a–d) XRD patterns of n =3, 4, 5, and 6, respectively. The reflections marked with black * correspond to the black-phase perovskite peaks at 14.1° ((100) plane) and 28.2° ((200) plane). Additional features marked with orange * in panels (a) and (b) suggest the presence of a secondary phase. The XRD data were collected by Charlie Nicholls from the group of Prof. Robert Hoye at the University of Oxford.

reduction of these values to 1.89, 1.71, and 1.91 ns for $n = 3$, 4, and 6, indicating the involvement of higher-order recombination processes in addition to first-order channels. In contrast, the $n = 5$ sample exhibits a counterintuitive increase in lifetime from 3.26 to 3.96 ns, which we attribute to a higher defect density; this interpretation is consistent with its inferior structural and optical quality. Overall, the observed lifetimes fall within the typical RT regime reported for perovskite NPLs, with both NPL thickness and sample purity playing important roles in determining the decay dynamics.

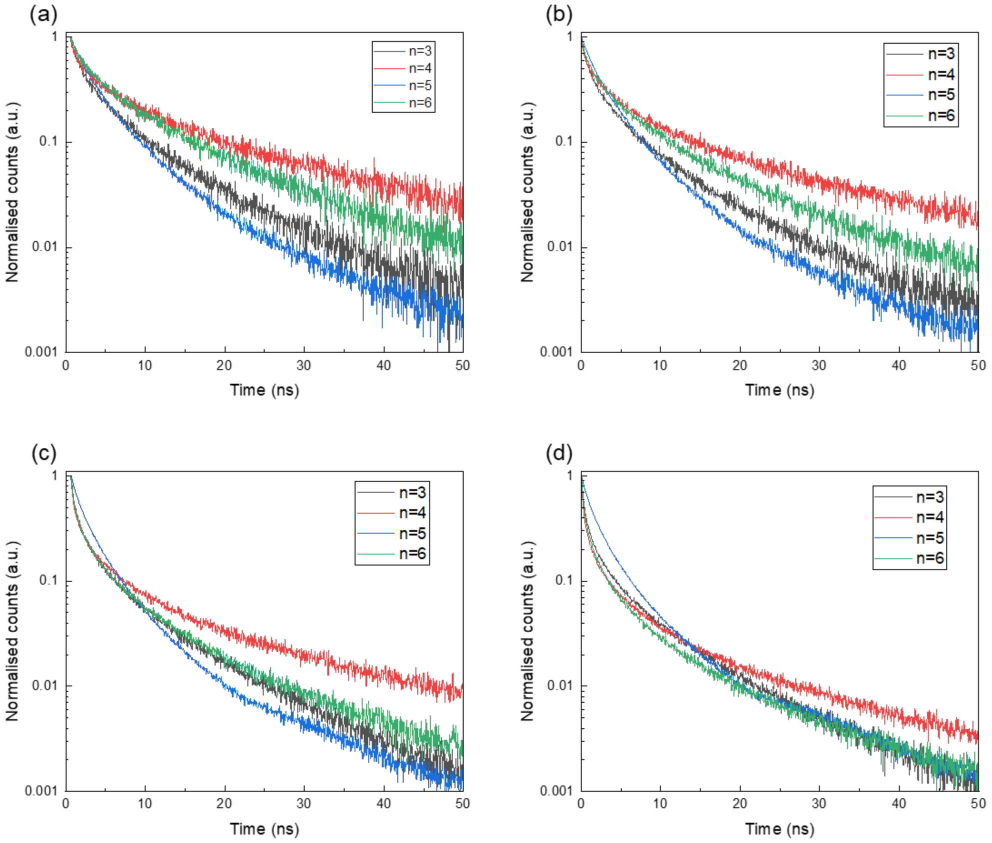

Figure 5.9: TRPL decays of $CsPbI_3$ NPLs with different thicknesses. (a–d) TRPL traces of $n = 3$–6 NPLs measured under excitation fluences of 0.17, 0.34, 0.67, and 1.68 mJ/cm^2, respectively.

5.5 μPL Investigation on Nanoplatelets Coupled to Optical Nanocavities

Rather than relying on cavity-design optimizations, we first selected 3ML NPLs for coupling to the nanocavities, as their excitons are the most robust at RT owing to strong quantum confinement. Starting with 3ML samples therefore provides the cleanest platform for observing intrinsic cavity coupling. RT μPL measures were conducted at dropcasted $n = 3$ NPL onto the whole nanovacity areas, the excitation power was controlled under 0.34 mJ/cm^2 to maintain dominant single-exciton mechanism on the PL emission. To obtain an uncoupled reference, PL spectra were recorded at positions outside the patterned nanocavity area (see

Figure 5.4(a)). On- and off-cavity measurements were performed on the same chip under identical alignment, excitation, and acquisition settings, so that any differences can be attributed to cavity coupling rather than fabrication variability. A direct comparison is shown in Figure 5.10.

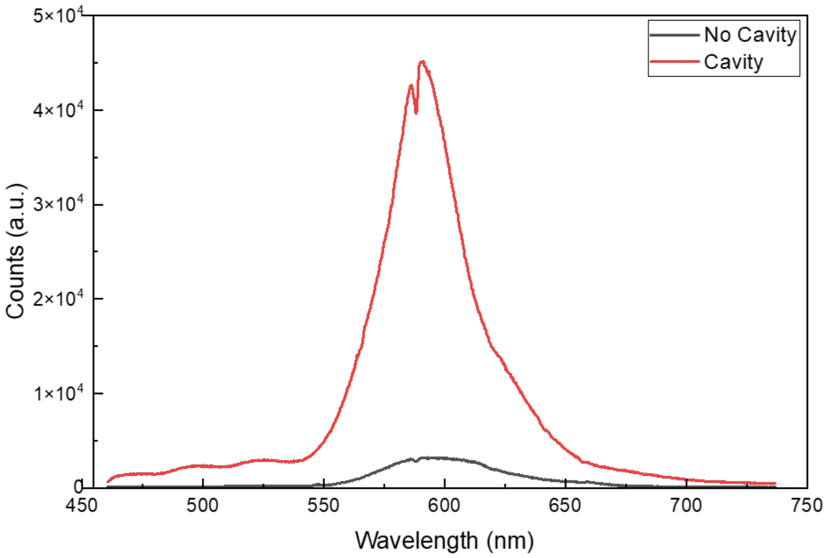

Figure 5.10: PL spectra of $CsPbI_3$ NPLs with and without the nanocavity.

Comparing the PL spectra with and without the nanocavity clearly demonstrates cavity-induced emission enhancement. While the emission peaks for both samples are around 600 nm, the integrated PL intensity of the cavity-coupled nanocavity is enhanced by more than an order of magnitude. The lack of significant spectral shifts indicates that the cavity does not alter intrinsic exciton transitions, but rather enhances radiative recombination efficiency by modifying the local photon environment. A minor dip was observed in the peak profile at ∼580 nm. Careful repeating of the PL showed that it is common to all PL peaks in this series and remains unchanged when the excitation spot is moved. We therefore attribute it to a spectrometer artifact rather than an intrinsic physical effect. However, the apparent intensity enhancement could simply arise from aggregation of the sample on the cavity surface. To address this issue, we repeated the measurement under identical conditions. In the presence of the nanocavity, a more symmetric spectral lineshape was observed, consistent with mode coupling, as evidenced by the normalized PL spectra in Figure 5.11.

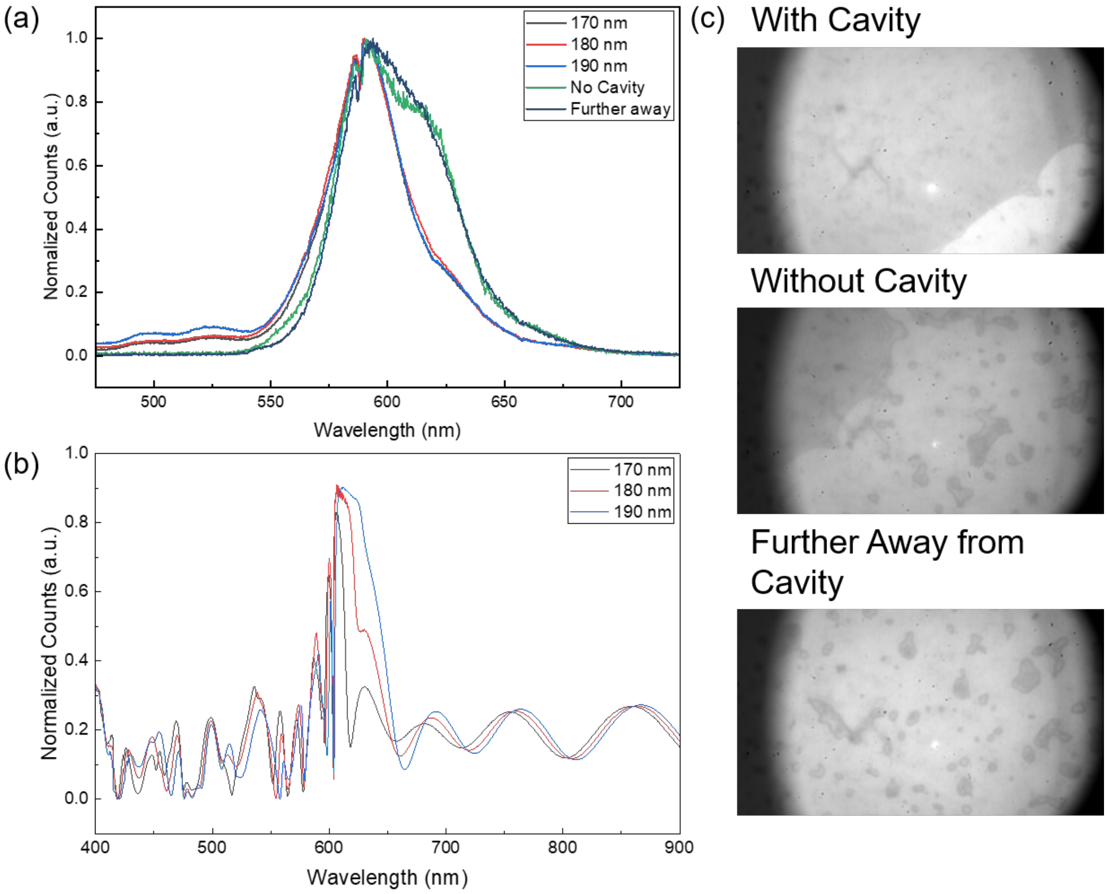

Figure 5.11: Cavity-induced PL spectral shaping and spatial loading of $CsPbI_3$ NPL. (a) Normalized PL of $CsPbI_3$ NPLs measured on nanocavity regions of different pillar diameters and on reference regions. (b) Simulated optical response of nanocavities with varying pillar diameters. (c) Optical microscope images of on-cavity and off-cavity regions; the excitation (laser) spot is indicated. The simulations shown in panel (b) were conducted by Dr. Mengyun Wang

To emphasize spectral-shape modifications independent of intensity, the PL spectra in Figure 5.11(a) are normalized to the peak. Upon coupling to the nanopillar cavity, the emission peak becomes noticeably narrower and more symmetric, and a distinct dip emerges at ∼620 nm. Quantitatively, the FWHM is reduced from ∼ 54 to ∼ 36 nm (a ∼ 33% narrowing), supporting spectrally selective outcoupling by the cavity modes. In addition, several reproducible fine features appear on the short-wavelength tail. These modulations exhibit clear correspondence with the simulated optical response in Figure 5.11(b), indicating cavity-mode filtering rather than numerical artifacts. Consistent with this picture, optical-camera images in Figure 5.11(c) reveal a darker shade on the cavity regions, suggesting stronger NPL loading/aggregation, which is likely due to the resonator topography promoting trapping during drying. This non-uniform coverage cautions against using raw photon counts to define a universal enhancement factor. To further evaluate the Purcell-like enhancement, TRPL measurements were conducted and the results are presented in Figure 5.12.

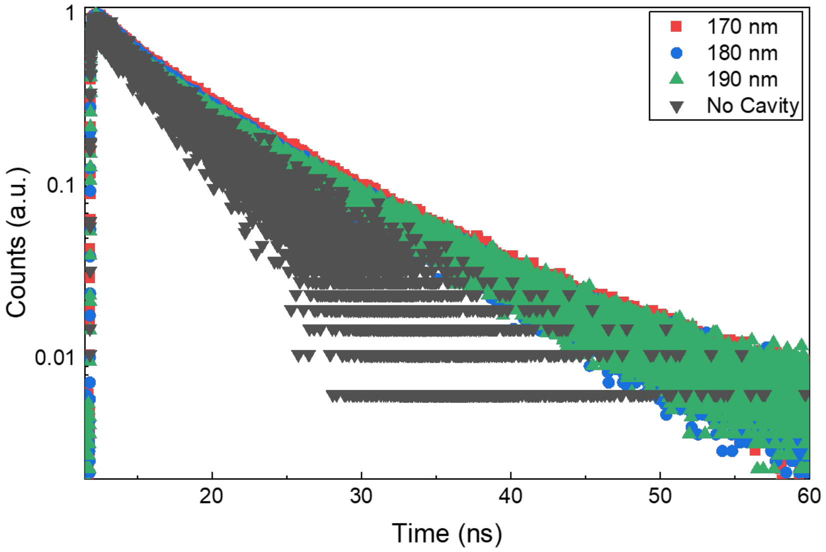

Figure 5.12: TRPL of CsPbI$_3$ NPLs on- and off-cavity. Excitation at 400 nm with a fluence of 0.34 mJ/cm^2.

Under our excitation conditions the TRPL traces are well described by a mono-exponential decay, indicating that first-order recombination dominates. The effective lifetimes obtained for the mono-exponential region are $\tau_{\text{no cav}} = 2.91\,\text{ns}$ and $\tau_{\text{cav}} = 3.12\,\text{ns}$, with no significant shortening observed. The absence of a lifetime reduction suggests that the cavity-induced PL increase arises primarily from improved excitation/collection efficiency and spectral filtering rather than a pronounced Purcell acceleration of the radiative rate. We also note that the cavity regions with darker sample patterns in Figure 5.11 indicate higher NPL loading, which can introduce re-absorption and photon recycling and slightly lengthen the apparent decay. The cavity mainly reshapes the spectrum, while the intrinsic recombination dynamics remain largely unchanged within experimental uncertainty. Further experiments are required to unambiguously reveal cavity-driven modulation of the recombination kinetics; this will likely require optimized cavity designs with higher quality factors and smaller mode volumes, improved spectral alignment and detuning control, and refined fabrication to suppress aggregation and reduce spatially inhomogeneous loading and reabsorption.

5.6 Conclusion and Discussion

We demonstrated the synthesis of NPLs with precise control over the layer number. μPL measurements reveal clear quantum-confinement effects, manifested as tunable excitonic energies and layer-dependent recombination dynamics. We demonstrated cavity-assisted spectral reshaping of $CsPbI_3$ NPL emission and established a on- and off-cavity comparison. Numerical simulations confirm spectral overlap between the designed cavity mode and the PL band of the $CsPbI_3$ NPLs, indicating that the structure is appropriately tuned for coupling. Consistent with these findings, TRPL shows mono-exponential decays with no significant lifetime shortening, while the PL peak shape becomes more symmetric and the collected intensity increases on the cavity. The data support a picture where excitation and collection efficiency and spectral filtering dominate, and where Purcell acceleration of the radiative rate is weak under the present design and loading conditions.

Future optimization should target higher Q and smaller mode volume, better spectral alignment, and more uniform loading. Practical routes include increasing array size to reduce edge leakage, engineering bound states, and tuning period and pillar diameter to align the resonance with the emitter peak. Using a low-concentration, filtered NPL dispersion, tuning the cavity surface wettability, and depositing in multiple passes to form a uniform film could suppress aggregation, reduce uneven loading, and limit reabsorption while preserving effective coupling. Simulations of the LDOS and TRPL versus controlled detuning would further clarify the role of the cavity in recombination dynamics. Hybrid dielectric–plasmonic cavities could combine the spectral selectivity of dielectric resonators with the deep sub-wavelength confinement. By coupling a metal nanostructure to a dielectric mode, the effective mode volume can be reduced while maintaining a quality factor that typically exceeds that of purely plasmonic resonators, thereby enhancing the radiative recombination rate of NPL excitons.

The precise control over light-matter interactions at the nanoscale is a cornerstone for advancing quantum technologies, high-efficiency optoelectronics, and ultrasensitive sensing. Prior work has shown that $CsPbI_3$ integrated with optical microcavities can exhibit $\sim$1 nm linewidths at RT to support single-photon emission [261]. Motivated by this progress, we seek to couple layer-controlled $CsPbI_3$ NPLs to dielectric nanocavities in order to enhance emission, control directionality, and narrow the spectrum toward quantum-light generation, while further optimizing the system parameters.

6

Conclusion and Outlook

The improvement of PL performance is of vital importance to optoelectronic devices, bioimaging, lasers, and quantum optics. In recent years, perovskite nanomaterials, especially $CsPbX_3$ low-dimensional nanomaterials, have attracted widespread attention due to their excellent optical properties. This thesis explored the interplay between metal NPs, nanocavities and lead halide perovskite nanostructures with the aim of manipulating and enhancing their PL properties. Specifically, I investigated the plasmonic enhancement effects induced by Ag (Chapter 3) and Mg NPs (Chapter 4) on $CsPbBr_3$ NWs, and further examined nanocavity–exciton coupling in $CsPbI_3$ NPLs (Chapter 5). These studies collectively provide new insights into the fundamental mechanisms of light–matter interaction in perovskite hybrid systems, as well as their potential for photonic and optoelectronic applications.

Chapter 3 demonstrated how Ag NPs, as a typical novel metal as plasmonic materials, owing to their strong LSPR, can efficiently enhance the PL intensity of $CsPbBr_3$ NWs. The enhanced near-field environment and weakened interface energy dissipation provided by Ag NPs and a PMMA buffer layer resulted in an 8.5-fold stronger emission and modified carrier recombination dynamics at 4 K, highlighting the importance of metal–semiconductor hybridization for perovskite photonics. In contrast, in Chapter 4, Mg NPs showed distinctly different plasmonic characteristics. Mg has a lower Q factor in the visible range, its less favourable overlap with the $CsPbBr_3$ emission spectrum led to weaker enhancement compared to Ag; thus, a 4.1-fold enhancement was observed with SiO_2-coated Mg NPs. This comparative study underlines the critical role of material selection in plasmonic design and offers guidelines for optimizing metal–perovskite interfaces.

Chapter 5 focused on nanocavity-coupled PL emission from $CsPbI_3$ NPLs. By integrating the NPLs with optical cavities, modifications in emission spectra were observed, such as enhanced PL intensity and narrowing of linewidths. These results confirm the feasibility of controlling perovskite emission not only through external plasmonic fields but also via photonic environment engineering. The findings suggest that perovskite nanostructures are highly versatile platforms for achieving tailored light emission, particularly when combined with resonant cavities that enable stronger light–matter coupling.

These results together contribute to a deeper understanding of how plasmonic and cavity effects can be harnessed to manipulate the optical properties of perovskite nanostructures. From a fundamental perspective, it is established that metal NPs and nanocavities can serve as effective external knobs for tuning perovskite PL. Such hybrid systems are promising for the development of efficient nanoscale light emitters with pronounced intensity enhancement, single-photon sources with narrowed linewidths, and low-threshold nanolasers with the potential for directional emission and improved coherence control. The work therefore bridges material design and optical physics, opening pathways toward advanced nanophotonic devices.

Nevertheless, several limitations remain. First, the $CsPbBr_3$ NWs employed in this work are not perfectly uniform in morphology and exhibit relatively high surface-to-volume ratios. As a result, a significant density of surface and internal defect states is present, which contributes notably to the PL dynamics. These states reduce the overall emission efficiency and obscure the underlying recombination mechanisms, making it challenging to achieve precise control over plasmonic enhancement. Regarding the plasmonic materials, Ag NPs provide strong enhancement owing to their favourable resonance characteristics, but they suffer from poor stability under ambient conditions. In contrast, Mg NPs are more stable at RT, yet their higher intrinsic losses limit the achievable enhancement. Achieving optimal coupling between NWs and plasmonic NPs therefore requires further optimization of the hybrid structure's geometric configuration, which in turn demands more precise sample fabrication. In particular, for Mg NPs, it is critical to not only stabilize the plasmonic response but also effectively enhance the radiative recombination rate, which could be directly verified by TRPL measurements. At the same time, the reproducibility of cavity–exciton coupling effects requires more systematic studies. Strong coupling critically depends on the precise control of cavity geometry and NPL placement, which remain experimentally challenging.

Importantly, translating these findings into device-level demonstrations such as perovskite NW/NPL-based LEDs and nanolasers would mark a critical step toward real-world applications. Advances in surface passivation, encapsulation, and composition engineering will be essential to improve the stability and durability of these hybrid systems. Beyond materials selection, the geometry of plasmonic NPs such as their shape, size, and crystallographic order strongly influences the LSPR, motivating focused studies enabled by improved synthesis and precise structural control. Furthermore, stronger exciton confinement and enhanced stability may be achieved by reducing the dimensionality of the perovskite system, such as QDs with smaller spatial sizes and enhanced confinement along all three dimensions, which could provide sharper emission features and more robust excitonic behaviours.

In summary, this thesis systematically explores plasmonic enhancement and nanocavity coupling as two effective routes to improve the PL of low-dimensional perovskite nanostructures. The findings advance the fundamental understanding of perovskite–plasmon–photon interactions and establish a framework for designing cost-effective and scalable nanophotonic and optoelectronic devices.

Appendices

A

Derivation of LSPR resonance conditions

The dielectric function of metals can be described by the Drude model [84]:

$$\varepsilon(\omega) = 1 - \frac{\omega_p^2}{\omega^2 + i\gamma\omega}, \tag{A.1}$$

where ω_p is the plasma frequency given by $\omega_p^2 = \frac{Ne^2}{\epsilon_0 m}$, γ the damping constant with respect to the equation of motion for a damped oscillator with effective mass m and effective charge e as

$$m\ddot{r} = -m\gamma\dot{r} - eE, \tag{A.2}$$

where E is the external electric field.

For NPs much smaller than the incident wavelength, the quasi-static approximation applies. The NP behaves effectively as a dipole with polarizability [84]

$$\alpha(\omega) = 4\pi\varepsilon_m R^3 \frac{\varepsilon(\omega) - \varepsilon_m}{\varepsilon(\omega) + 2\varepsilon_m}, \tag{A.3}$$

where R is the radius and ε_m is the dielectric constant of the surrounding medium. The extinction cross-section is then

$$C_{\text{ext}} \propto \frac{\varepsilon_i}{(\varepsilon_r + 2\varepsilon_m)^2 + \varepsilon_i^2}, \tag{A.4}$$

with ε_r and ε_i referring to the real and imaginary parts of $\varepsilon(\omega)$. Maximization of C_{ext} hence yields the resonance condition

$$\text{Re}\{\varepsilon(\omega)\} = -2\varepsilon_m, \tag{A.5}$$

which defines the LSPR in spherical NPs. Expressed in wavelength units, this condition gives

$$\lambda_{\max} = \frac{\lambda_p}{\sqrt{2n_m^2 + 1}}, \tag{A.6}$$

where λ_p is the plasma wavelength of the bulk metal and n_m the refractive index of the environment, as stated in Chapter 1

The Gans-Mie theory extended the formula from spherical to spheroidal [85]. The polarizability along axis i of an ellipsoid with semi-axes a, b, c is

$$\alpha_i = \frac{4\pi}{3} abc \frac{\varepsilon - \varepsilon_d}{\varepsilon_d + (\varepsilon - \varepsilon_d) P_i}, \tag{A.7}$$

where ε_d is the dielectric constant of the surrounding medium and P_i is the depolarization factor, depending only on the aspect ratio. For example, in prolate spheroids,

$$P_a = \frac{1 - e^2}{e^2} \left[\frac{1}{2e} \ln \left(\frac{1 + e}{1 - e} \right) - 1 \right], \qquad e = \sqrt{1 - \frac{b^2}{a^2}}, \tag{A.8}$$

$$P_b = P_c = \frac{1 - P_a}{2}, \tag{A.9}$$

where $P_a + P_b + P_c = 1$. The longitudinal depolarization factor P_a decreases with increasing aspect ratio, shifting the longitudinal resonance to longer wavelengths. This indicates the tunability of LSPR peaks in anisotropic NPs.

B

Reflection of Nanocavities

To verify the optical response of the fabricated nanocavity arrays, reflectance measurements were also performed on samples with different nanopillar diameters. Figure B.1 shows the experimental reflection spectra in comparison with the bare Si substrate, a platinum-coated reference (Pt_ref), and the dark background signal. Pronounced oscillatory features are observed in the 450–650 nm spectral range for the patterned arrays, in contrast to the broad reflection from the bare substrate and Pt_ref.

While the simulated spectra in Chapter 5 predict sharper and higher reflection peaks close the PL emission from the NPLs, the experimental results display broader and less intense features. This discrepancy arises primarily from the idealized assumptions in the simulations, while in practice, the fabricated arrays with finite lateral dimensions are subject to fabrication imperfections and material losses, which together broaden the resonances and reduce their amplitude.

Nevertheless, both experiment and simulation consistently indicate the presence of resonant features over 600 nm, overlapping with the $CsPbI_3$ NPL emission band, thereby validating the nanocavity design.

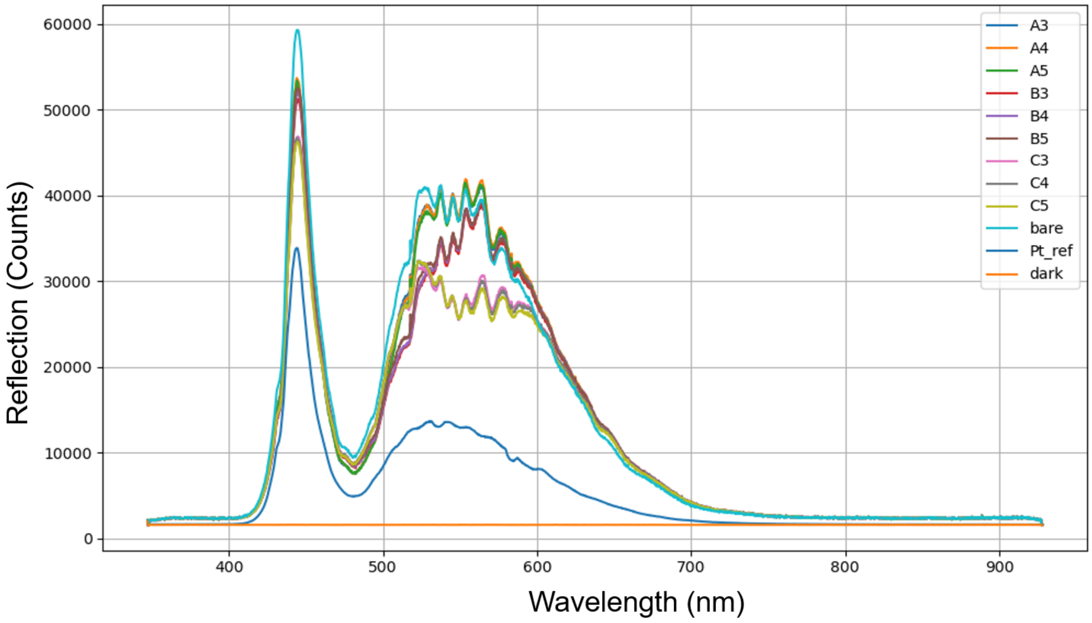

Figure B.1: Reflection spectra of Si pillar nanocavities. Arrays with different pillar diameters are shown for the A, B, and C series (A3–5: 170 nm; B3–5: 180 nm; C3–5: 190 nm), in comparison with a bare Si substrate, a platinum-coated reference (Pt_ref), and the dark background signal. These modulations arise from guided-mode resonances induced by the lateral index modulation, and spectrally overlap with the emission band of $CsPbI_3$ NPLs, confirming that the designed nanocavity arrays can provide optical feedback near the perovskite PL wavelength. The data presented in this figure were collected by Dr. Mengyun Wang

References

[1] Loredana Protesescu et al. “Nanocrystals of cesium lead halide perovskites (CsPbX3, X= Cl, Br, and I): novel optoelectronic materials showing bright emission with wide color gamut”. *Nano letters* 15.6 (2015), pp. 3692–3696.

[2] He Huang et al. “Lead halide perovskite nanocrystals in the research spotlight: stability and defect tolerance”. *ACS energy letters* 2.9 (2017), pp. 2071–2083.

[3] Jun Kang and Lin-Wang Wang. “High defect tolerance in lead halide perovskite CsPbBr3”. *The journal of physical chemistry letters* 8.2 (2017), pp. 489–493.

[4] Jarvist Moore Frost. “Calculating polaron mobility in halide perovskites”. *Physical Review B* 96.19 (2017), p. 195202.

[5] Chang Woo Myung et al. “A New Perspective on the Role of A-Site Cations in Perovskite Solar Cells”. *Advanced Energy Materials* 8.14 (2018), p. 1702898.

[6] Haiming Zhu et al. “Organic cations might not be essential to the remarkable properties of band edge carriers in lead halide perovskites”. *Advanced Materials* 29.1 (2016).

[7] Makhsud I Saidaminov et al. “Inorganic lead halide perovskite single crystals: phase-selective low-temperature growth, carrier transport properties, and self-powered photodetection”. *Advanced Optical Materials* 5.2 (2017), p. 1600704.

[8] Song Wei et al. “Room-temperature and gram-scale synthesis of CsPbX 3 (X= Cl, Br, I) perovskite nanocrystals with 50–85% photoluminescence quantum yields”. *Chemical Communications* 52.45 (2016), pp. 7265–7268.

[9] Abhishek Swarnkar et al. “Colloidal CsPbBr3 perovskite nanocrystals: luminescence beyond traditional quantum dots”. *Angewandte Chemie* 127.51 (2015), pp. 15644–15648.

[10] Michael A Becker et al. “Bright triplet excitons in caesium lead halide perovskites”. *Nature* 553.7687 (2018), pp. 189–193.

[11] Jongseob Kim et al. “The role of intrinsic defects in methylammonium lead iodide perovskite”. *The journal of physical chemistry letters* 5.8 (2014), pp. 1312–1317.

[12] Feng Gao et al. “Recent progresses on defect passivation toward efficient perovskite solar cells”. *Advanced Energy Materials* 10.13 (2020), p. 1902650.

[13] Michael L Agiorgousis et al. “Strong covalency-induced recombination centers in perovskite solar cell material CH3NH3PbI3”. *Journal of the American Chemical Society* 136.41 (2014), pp. 14570–14575.

[14] Aron Walsh. “Principles of chemical bonding and band gap engineering in hybrid organic–inorganic halide perovskites”. *The Journal of Physical Chemistry C* 119.11 (2015), pp. 5755–5760.

[15] Marina R Filip et al. “Steric engineering of metal-halide perovskites with tunable optical band gaps”. *Nature communications* 5.1 (2014), p. 5757.

[16] Matthew P Hautzinger, Willa Mihalyi-Koch, and Song Jin. “A-site cation chemistry in halide perovskites”. *Chemistry of Materials* 36.21 (2024), pp. 10408–10420.

[17] Victor Moritz Goldschmidt. “Die gesetze der krystallochemie”. *Naturwissenschaften* 14.21 (1926), pp. 477–485.

[18] Chonghea Li et al. “Formability of abx3 (x= f, cl, br, i) halide perovskites”. *Structural Science* 64.6 (2008), pp. 702–707.

[19] Gregor Kieslich, Shijing Sun, and Anthony K Cheetham. “Solid-state principles applied to organic–inorganic perovskites: new tricks for an old dog”. *Chemical Science* 5.12 (2014), pp. 4712–4715.

[20] Will Travis et al. “On the application of the tolerance factor to inorganic and hybrid halide perovskites: a revised system”. *Chemical science* 7.7 (2016), pp. 4548–4556.

[21] Matthew R Linaburg et al. “Cs1–x Rb x PbCl3 and Cs1–x Rb x PbBr3 solid solutions: understanding octahedral tilting in lead halide perovskites”. *Chemistry of Materials* 29.8 (2017), pp. 3507–3514.

[22] Zhen Li et al. “Stabilizing perovskite structures by tuning tolerance factor: formation of formamidinium and cesium lead iodide solid-state alloys”. *Chemistry of Materials* 28.1 (2016), pp. 284–292.

[23] Akihiro Kojima et al. “Organometal halide perovskites as visible-light sensitizers for photovoltaic cells”. *Journal of the american chemical society* 131.17 (2009), pp. 6050–6051.

[24] Constantinos C Stoumpos and Mercouri G Kanatzidis. “The renaissance of halide perovskites and their evolution as emerging semiconductors”. *Accounts of chemical research* 48.10 (2015), pp. 2791–2802.

[25] Michael Saliba et al. “Incorporation of rubidium cations into perovskite solar cells improves photovoltaic performance”. *Science* 354.6309 (2016), pp. 206–209.

[26] Jae Keun Nam et al. “Potassium incorporation for enhanced performance and stability of fully inorganic cesium lead halide perovskite solar cells”. *Nano letters* 17.3 (2017), pp. 2028–2033.

[27] Zhengwei Xu et al. “Phase diagram and stability of mixed-cation lead iodide perovskites: A theory and experiment combined study”. *Physical Review Materials* 4.9 (2020), p. 095401.

[28] Constantinos C Stoumpos et al. “Ruddlesden–Popper hybrid lead iodide perovskite 2D homologous semiconductors”. *Chemistry of Materials* 28.8 (2016), pp. 2852–2867.

[29] Ian C Smith et al. “A layered hybrid perovskite solar-cell absorber with enhanced moisture stability”. *Angewandte Chemie International Edition* 53.42 (2014), pp. 11232–11235.

[30] SN Ruddlesden and PJAC Popper. “New compounds of the K2NiF4 type”. *Acta Crystallographica* 10.8 (1957), pp. 538–539.

[31] SN Ruddlesden and Paul Popper. “The compound Sr3Ti2O7 and its structure”. *Acta Crystallographica* 11.1 (1958), pp. 54–55.

[32] Vikash Kumar Ravi, Ganesh B Markad, and Angshuman Nag. “Band edge energies and excitonic transition probabilities of colloidal CsPbX3 (X= Cl, Br, I) perovskite nanocrystals”. *ACS Energy Letters* 1.4 (2016), pp. 665–671.

[33] Federico Brivio, Alison B Walker, and Aron Walsh. “Structural and electronic properties of hybrid perovskites for high-efficiency thin-film photovoltaics from first-principles”. *Apl Materials* 1.4 (2013).

[34] Ling-yi Huang and Walter RL Lambrecht. “Electronic band structure trends of perovskite halides: Beyond Pb and Sn to Ge and Si”. *Physical Review B* 93.19 (2016), p. 195211.

[35] Arthur Marronnier et al. “Influence of disorder and anharmonic fluctuations on the dynamical Rashba effect in purely inorganic lead-halide perovskites”. *The Journal of Physical Chemistry C* 123.1 (2018), pp. 291–298.

[36] Evan Lafalce et al. “Rashba splitting in organic–inorganic lead–halide perovskites revealed through two-photon absorption spectroscopy”. *Nature Communications* 13.1 (2022), p. 483.

[37] Kang Wang et al. “All-inorganic cesium lead iodide perovskite solar cells with stabilized efficiency beyond 15%”. *Nature communications* 9.1 (2018), p. 4544.

[38] Arthur Marronnier et al. “Anharmonicity and disorder in the black phases of cesium lead iodide used for stable inorganic perovskite solar cells”. *ACS nano* 12.4 (2018), pp. 3477–3486.

[39] Constantinos C Stoumpos et al. “Crystal growth of the perovskite semiconductor CsPbBr3: a new material for high-energy radiation detection”. *Crystal growth & design* 13.7 (2013), pp. 2722–2727.

[40] Waqar Ahmad et al. “Inorganic CsPbI3 perovskite-based solar cells: A choice for a tandem device”. *Solar Rrl* 1.7 (2017), p. 1700048.

[41] Bo Li et al. “Surface passivation engineering strategy to fully-inorganic cubic CsPbI3 perovskites for high-performance solar cells”. *Nature communications* 9.1 (2018), p. 1076.

[42] Feng Yang et al. “Surface stabilized cubic phase of CsPbI3 and CsPbBr3 at room temperature”. *Chinese Physics B* 28.5 (2019), p. 056402.

[43] Giovanni Mannino et al. “Temperature-dependent optical band gap in CsPbBr3, MAPbBr3, and FAPbBr3 single crystals”. *The journal of physical chemistry letters* 11.7 (2020), pp. 2490–2496.

[44] Ke Wei et al. “Temperature-dependent excitonic photoluminescence excited by two-photon absorption in perovskite CsPbBr3 quantum dots”. *Optics letters* 41.16 (2016), pp. 3821–3824.

[45] Gabriele Rainò et al. “Superfluorescence from lead halide perovskite quantum dot superlattices”. *Nature* 563.7733 (2018), pp. 671–675.

[46] Muhammad Imran et al. “Colloidal synthesis of strongly fluorescent CsPbBr3 nanowires with width tunable down to the quantum confinement regime”. *Chemistry of Materials* 28.18 (2016), pp. 6450–6454.

[47] Dandan Zhang et al. “Synthesis of composition tunable and highly luminescent cesium lead halide nanowires through anion-exchange reactions”. *Journal of the American Chemical Society* 138.23 (2016), pp. 7236–7239.

[48] Vladimir S Chirvony et al. “Inhomogeneous broadening of photoluminescence spectra and kinetics of nanometer-thick (phenethylammonium) 2PbI4 perovskite thin films: implications for optoelectronics”. *ACS Applied Nano Materials* 4.6 (2021), pp. 6170–6177.

[49] Dmitriy Afanasyev, Niyazbek Ibrayev, and Nurxat Nuraje. “Effect of plasmonic nanostructures on the optical properties of CH3NH3PbI perovskite films”. *Frontiers in Materials* 7 (2021), p. 600424.

[50] Samuel W Eaton et al. “Lasing in robust cesium lead halide perovskite nanowires”. *Proceedings of the National Academy of Sciences* 113.8 (2016), pp. 1993–1998.

[51] Jianmei Huang et al. “Rich chemistry in inorganic halide perovskite nanostructures”. *Advanced Materials* 30.48 (2018), p. 1802856.

[52] Zhao Yuan et al. “One-dimensional organic lead halide perovskites with efficient bluish white-light emission”. *Nature communications* 8.1 (2017), p. 14051.

[53] Rui Su et al. “Perovskite semiconductors for room-temperature exciton-polaritonics”. *Nature Materials* 20.10 (2021), pp. 1315–1324.

[54] Hartmut Haug and Stephan W Koch. *Quantum theory of the optical and electronic properties of semiconductors.* world scientific, 2009.

[55] B Zh Poghosyan and GH Demirjian. “Binding energy of hydrogenic impurities in quantum well wires of InSb/GaAs”. *Physica B: Condensed Matter* 338.1-4 (2003), pp. 357–360.

[56] Louis Brus. “Electronic wave functions in semiconductor clusters: experiment and theory”. *The Journal of Physical Chemistry* 90.12 (1986), pp. 2555–2560.

[57] Kaibo Zheng et al. “Exciton binding energy and the nature of emissive states in organometal halide perovskites”. *The journal of physical chemistry letters* 6.15 (2015), pp. 2969–2975.

[58] Limeng Ni et al. “Real-time observation of exciton–phonon coupling dynamics in self-assembled hybrid perovskite quantum wells”. *ACS nano* 11.11 (2017), pp. 10834–10843.

[59] Hamid Pashaei Adl et al. “Homogeneous and inhomogeneous broadening in single perovskite nanocrystals investigated by micro-photoluminescence”. *Journal of Luminescence* 240 (2021), p. 118453.

[60] Gregory D Scholes and Garry Rumbles. “Excitons in nanoscale systems”. *Nature materials* 5.9 (2006), pp. 683–696.

[61] Daniel Rossi et al. “Light-induced activation of forbidden exciton transition in strongly confined perovskite quantum dots”. *ACS nano* 12.12 (2018), pp. 12436–12443.

[62] Shuli Wang et al. “Thickness-dependent dark-bright exciton splitting and phonon bottleneck in CsPbBr3-based nanoplatelets revealed via magneto-optical spectroscopy”. *Nano Letters* 22.17 (2022), pp. 7011–7019.

[63] Damien Canneson et al. “Negatively charged and dark excitons in CsPbBr3 perovskite nanocrystals revealed by high magnetic fields”. *Nano letters* 17.10 (2017), pp. 6177–6183.

[64] Adam D Wright et al. “Electron–phonon coupling in hybrid lead halide perovskites”. *Nature communications* 7.1 (2016), p. 11755.

[65] Claudiu M Iaru et al. “Strong carrier–phonon coupling in lead halide perovskite nanocrystals”. *ACS nano* 11.11 (2017), pp. 11024–11030.

[66] Samuel Brem et al. “Phonon-assisted photoluminescence from indirect excitons in monolayers of transition-metal dichalcogenides”. *Nano letters* 20.4 (2020), pp. 2849–2856.

[67] Keisei Shibata et al. “Exciton localization and enhancement of the exciton–LO phonon interaction in a CsPbBr3 single crystal”. *The Journal of Physical Chemistry C* 124.33 (2020), pp. 18257–18263.

[68] M Sebastian et al. “Excitonic emissions and above-band-gap luminescence in the single-crystal perovskite semiconductors CsPbB r 3 and CsPbC l 3”. *Physical Review B* 92.23 (2015), p. 235210.

[69] Xiangzhou Lao et al. “Photoluminescence signatures of thermal expansion, electron–phonon coupling and phase transitions in cesium lead bromide perovskite nanosheets”. *Nanoscale* 12.13 (2020), pp. 7315–7320.

[70] Xiaoming Wang et al. “Atomistic mechanism of broadband emission in metal halide perovskites”. *The Journal of Physical Chemistry Letters* 10.3 (2019), pp. 501–506.

[71] Bogdan M Benin et al. “Highly emissive self-trapped excitons in fully inorganic zero-dimensional tin halides”. *Angewandte Chemie International Edition* 57.35 (2018), pp. 11329–11333.

[72] WTRW Shockley and WT Read Jr. “Statistics of the recombinations of holes and electrons”. *Physical review* 87.5 (1952), p. 835.

[73] Re N Hall. “Electron-hole recombination in germanium”. *Physical review* 87.2 (1952), p. 387.

[74] Matthew N Ashner et al. “Size-dependent biexciton spectrum in CsPbBr3 perovskite nanocrystals”. *ACS Energy Letters* 4.11 (2019), pp. 2639–2645.

[75] Juan A Castañeda et al. “Efficient biexciton interaction in perovskite quantum dots under weak and strong confinement”. *ACS nano* 10.9 (2016), pp. 8603–8609.

[76] Bin Li et al. “Excitons and biexciton dynamics in single CsPbBr3 perovskite quantum dots”. *The Journal of Physical Chemistry Letters* 9.24 (2018), pp. 6934–6940.

[77] Carolina Villamil Franco et al. “Auger recombination and multiple exciton generation in colloidal two-dimensional perovskite nanoplatelets: implications for light-emitting devices”. *ACS Applied Nano Materials* 4.1 (2020), pp. 558–567.

[78] Yuanzhi Jiang et al. “Reducing the impact of Auger recombination in quasi-2D perovskite light-emitting diodes”. *Nature communications* 12.1 (2021), p. 336.

[79] YC Shen et al. “Auger recombination in InGaN measured by photoluminescence”. *Applied Physics Letters* 91.14 (2007).

[80] Alexander Kiligaridis et al. “Are Shockley-Read-Hall and ABC models valid for lead halide perovskites?” *Nature communications* 12.1 (2021), p. 3329.

[81] Margherita Taddei et al. “Interpreting halide perovskite semiconductor photoluminescence kinetics”. *ACS Energy Letters* 9.6 (2024), pp. 2508–2516.

[82] K Lance Kelly et al. *The optical properties of metal nanoparticles: the influence of size, shape, and dielectric environment.* 2003.

[83] Kathryn M Mayer and Jason H Hafner. “Localized surface plasmon resonance sensors”. *Chemical reviews* 111.6 (2011), pp. 3828–3857.

[84] Craig F Bohren and Donald R Huffman. *Absorption and scattering of light by small particles.* John Wiley & Sons, 2008.

[85] Richard Gans. “Über die form ultramikroskopischer goldteilchen”. *Annalen der Physik* 342.5 (1912), pp. 881–900.

[86] Lukas Novotny and Bert Hecht. *Principles of nano-optics.* Cambridge university press, 2012.

[87] James T Hugall, Anshuman Singh, and Niek F van Hulst. “Plasmonic cavity coupling”. *Acs Photonics* 5.1 (2018), pp. 43–53.

[88] Ora Bitton, Satyendra Nath Gupta, and Gilad Haran. “Quantum dot plasmonics: from weak to strong coupling”. *Nanophotonics* 8.4 (2019), pp. 559–575.

[89] Xiaobo Han et al. “Rabi splitting in a plasmonic nanocavity coupled to a WS2 monolayer at room temperature”. *ACS Photonics* 5.10 (2018), pp. 3970–3976.

[90] Stefan A Maier et al. *Plasmonics: fundamentals and applications.* Vol. 1. Springer, 2007.

[91] Feng Wang and Y Ron Shen. “General properties of local plasmons in metal nanostructures”. *Physical review letters* 97.20 (2006), p. 206806.

[92] Elizabeth R Hopper et al. “Opportunities and challenges for alternative nanoplasmonic metals: Magnesium and beyond”. *The Journal of Physical Chemistry C* 126.26 (2022), pp. 10630–10643.

[93] Cristian Ciracì et al. “Probing the Ultimate Limits of Plasmonic Enhancement”. *Science* 337.6098 (2012), pp. 1072–1074.

[94] Nicolas Fontaine et al. “Thinking outside the shell: novel sensors designed from plasmon-enhanced fluorescent concentric nanoparticles”. *Analyst* 145.18 (2020), pp. 5965–5980.

[95] Pengju Shi et al. “Micro-homogeneity of lateral energy landscapes governs the performance in perovskite solar cells”. *Nature Communications* 15.1 (2024), p. 9703.

[96] Christiane Becker et al. “Nanophotonic-enhanced two-photon-excited photoluminescence of perovskite quantum dots”. *ACS Photonics* 5.11 (2018), pp. 4668–4676.

[97] Coherent Inc. *Verdi V-Series Data Sheet.* Accessed: 2025-07-17. 2023. URL: `https://www.coherent.com/lasers/cw-solid-state/verdi`.

[98] Ursula Keller. “Recent developments in compact ultrafast lasers”. *nature* 424.6950 (2003), pp. 831–838.

[99] Shai Yefet and Avi Pe'er. "A review of cavity design for Kerr lens mode-locked solid-state lasers". *Applied Sciences* 3.4 (2013), pp. 694–724.

[100] PL Kelley. "Self-focusing of optical beams". *Physical Review Letters* 15.26 (1965), p. 1005.

[101] RH Stolen and A Ashkin. "Optical Kerr effect in glass waveguide". *Applied Physics Letters* 22.6 (1973), pp. 294–296.

[102] Arkady Major et al. "Dispersion of the nonlinear refractive index in sapphire". *Optics letters* 29.6 (2004), pp. 602–604.

[103] Coherent, Inc. *Mira Optima 900-F Femtosecond Laser System Datasheet.* `https://tzin.bgu.ac.il/~glevi/website/datasheets/Mira900Brochure.pdf`. Accessed: 2025-07-17. 2020.

[104] Coherent, Inc. *Mira 900 and 900-D Laser Systems Datasheet.* `https://www.coherent.com/resources/datasheet/lasers/COHR_Mira900_DS_0318_2.pdf`. Accessed: 2025-07-17. 2020.

[105] Robert W Boyd, Alexander L Gaeta, and Enno Giese. "Nonlinear optics". In: *Springer Handbook of Atomic, Molecular, and Optical Physics.* Springer, 2008, pp. 1097–1110.

[106] PicoQuant GmbH. *LDH Series: Picosecond Pulsed Diode Lasers.* `https://www.picoquant.com/products/category/picosecond-pulsed-diode-lasers/ldh-series`. Accessed: 2025-07-17. 2024.

[107] PicoQuant GmbH. *PDL 800-B Picosecond Pulsed Laser Driver.* `https://www.picoquant.com/products/detail/pdl-800-b`. Accessed: 2025-07-17. 2024.

[108] Victor Ivanovich Klimov et al. "Optical gain and stimulated emission in nanocrystal quantum dots". *science* 290.5490 (2000), pp. 314–317.

[109] Tanja Ivanovska et al. "Long-lived photoinduced polarons in organohalide perovskites". *The Journal of Physical Chemistry Letters* 8.13 (2017), pp. 3081–3086.

[110] Eugene Hecht. *Optics.* eng. 5th ed. Boston, Mass: Pearson, 2017.

[111] Max Born, Emil. Wolf, and A. B. Bhatia. *Principles of optics : electromagnetic theory of propagation, interference and diffraction of light.* eng. 7th (expanded) ed., repr. with corr. Cambridge: Cambridge University Press, 2002.

[112] Jakob J. Stamnes. "Focusing of a perfect wave and the airy pattern formula". *Optics Communications* 37.5 (1981), pp. 311–314.

[113] Sheng He et al. "Electron trapping prolongs the lifetime of charge-separated states in 2D perovskite nanoplatelet-hole acceptor complexes". *The Journal of Physical Chemistry Letters* 14.9 (2023), pp. 2241–2250.

[114] Bahaa Saleh, Malvin Teich, and Barry Masters. "Fundamentals of Photonics, Second Edition". *Journal of biomedical optics* 13 (July 2008), p. 049901.

[115] Patrick C Lee and DJTJOPC Meisel. "Adsorption and surface-enhanced Raman of dyes on silver and gold sols". *The Journal of Physical Chemistry* 86.17 (1982), pp. 3391–3395.

[116] Yugang Sun and Younan Xia. “Shape-controlled synthesis of gold and silver nanoparticles”. *science* 298.5601 (2002), pp. 2176–2179.

[117] Nadeem Baig, Irshad Kammakakam, and Wail Falath. “Nanomaterials: A review of synthesis methods, properties, recent progress, and challenges”. *Materials advances* 2.6 (2021), pp. 1821–1871.

[118] Panagiotis Grammatikopoulos, Theodoros Bouloumis, and Stephan Steinhauer. “Gas-phase synthesis of nanoparticles: current application challenges and instrumentation development responses”. *Physical Chemistry Chemical Physics* 25.2 (2023), pp. 897–912.

[119] Shengfu Yang et al. “Growing metal nanoparticles in superfluid helium”. *Nanoscale* 5.23 (2013), pp. 11545–11553.

[120] Asim Ali Yaqoob, Khalid Umar, and Mohamad Nasir Mohamad Ibrahim. “Silver nanoparticles: various methods of synthesis, size affecting factors and their potential applications–a review”. *Applied Nanoscience* 10.5 (2020), pp. 1369–1378.

[121] Li Song et al. “Investigation on stability of silver nanoparticles with different ligands”. *Journal of Nanoparticle Research* 25.12 (2023), p. 255.

[122] Evgeny Loginov, Luis F Gomez, and Andrey F Vilesov. “Surface deposition and imaging of large Ag clusters formed in He droplets”. *The Journal of Physical Chemistry A* 115.25 (2011), pp. 7199–7204.

[123] Ruoxue Yan, Daniel Gargas, and Peidong Yang. “Nanowire photonics”. *Nature photonics* 3.10 (2009), pp. 569–576.

[124] Arianna Cretı et al. “Enhanced optical absorption of GaAs near-band-edge transitions in GaAs/AlGaAs core–shell nanowires: implications for nanowire solar cells”. *ACS Applied Nano Materials* 5.12 (2022), pp. 18149–18158.

[125] Hyun Chul Park et al. “How Effective is Plasmonic Enhancement of Colloidal Quantum Dots for Color-Conversion Light-Emitting Devices?” *Small* 13.48 (2017), p. 1701805.

[126] Mark S Gudiksen et al. “Growth of nanowire superlattice structures for nanoscale photonics and electronics”. *nature* 415.6872 (2002), pp. 617–620.

[127] Samuel W Eaton et al. “Semiconductor nanowire lasers”. *Nature reviews materials* 1.6 (2016), pp. 1–11.

[128] Fernando Patolsky et al. “Detection, stimulation, and inhibition of neuronal signals with high-density nanowire transistor arrays”. *Science* 313.5790 (2006), pp. 1100–1104.

[129] Ai Ling Feng et al. “Distance-dependent plasmon-enhanced fluorescence of upconversion nanoparticles using polyelectrolyte multilayers as tunable spacers”. *Scientific reports* 5.1 (2015), p. 7779.

[130] Dandan Zhang et al. “Solution-phase synthesis of cesium lead halide perovskite nanowires”. *Journal of the American Chemical Society* 137.29 (2015), pp. 9230–9233.

[131] Yonghua Chen et al. “Plasmon-enhanced blue photoluminescence efficiency from CsPb (Br/Cl) 3 perovskite nanocrystals by silver nanoparticles”. *The Journal of Physical Chemistry C* 125.19 (2021), pp. 10631–10638.

[132] William L Barnes, Alain Dereux, and Thomas W Ebbesen. “Surface plasmon subwavelength optics”. *nature* 424.6950 (2003), pp. 824–830.

[133] GH Ma et al. “Observation of resonant energy transfer in Au: CdS nanocomposite”. *Applied physics letters* 84.23 (2004), pp. 4684–4686.

[134] Qingzhang You et al. “Resonance photoluminescence enhancement of monolayer MoS2 via a plasmonic nanowire dimer optical antenna”. *ACS Applied Materials & Interfaces* 14.20 (2022), pp. 23756–23764.

[135] Peter B Johnson and R-WJPrB Christy. “Optical constants of the noble metals”. *Physical review B* 6.12 (1972), p. 4370.

[136] HY Lin et al. “Carrier transfer induced photoluminescence change in metal-semiconductor core-shell nanostructures”. *Applied physics letters* 88.16 (2006).

[137] Koichi Okamoto, Saurabh Vyawahare, and Axel Scherer. “Surface-plasmon enhanced bright emission from CdSe quantum-dot nanocrystals”. *Journal of the Optical Society of America B* 23.8 (2006), pp. 1674–1678.

[138] Assegid Mengistu Flatae et al. “Plasmon-assisted suppression of surface trap states and enhanced band-edge emission in a bare CdTe quantum dot”. *The journal of physical chemistry letters* 10.11 (2019), pp. 2874–2878.

[139] AV Maslov and Cun-Zheng Ning. “Size reduction of a semiconductor nanowire laser by using metal coating”. In: *Physics and simulation of optoelectronic devices XV*. Vol. 6468. SPIE. 2007, pp. 138–144.

[140] Ronald Fuchs and Francisco Claro. “Multipolar response of small metallic spheres: Nonlocal theory”. *Physical Review B* 35.8 (1987), p. 3722.

[141] BNJ Persson and ND Lang. “Electron-hole-pair quenching of excited states near a metal”. *Physical Review B* 26.10 (1982), p. 5409.

[142] Ming Li et al. “Size-dependent energy transfer between CdSe/ZnS quantum dots and gold nanoparticles”. *The Journal of Physical Chemistry Letters* 2.17 (2011), pp. 2125–2129.

[143] CS Yun et al. “Nanometal surface energy transfer in optical rulers, breaking the FRET barrier”. *Journal of the American Chemical Society* 127.9 (2005), pp. 3115–3119.

[144] Mani Prabha Singh and Geoffrey F Strouse. “Involvement of the LSPR spectral overlap for energy transfer between a dye and Au nanoparticle”. *Journal of the American Chemical Society* 132.27 (2010), pp. 9383–9391.

[145] Jacob B Khurgin. “Hot carriers generated by plasmons: where are they generated and where do they go from there?” *Faraday discussions* 214 (2019), pp. 35–58.

[146] Xinyu Huang et al. “Efficient plasmon-hot electron conversion in Ag–CsPbBr3 hybrid nanocrystals”. *Nature communications* 10.1 (2019), p. 1163.

[147] Stephen A Lee and Stephan Link. “Chemical interface damping of surface plasmon resonances”. *Accounts of chemical research* 54.8 (2021), pp. 1950–1960.

[148] S. M. Sze and Kwok Kwok Ng. *Physics of semiconductor devices.* eng. Third edition. Hoboken, N.J: Wiley-Interscience, 2007.

[149] Junyang Huang et al. “Plasmon-induced trap state emission from single quantum dots”. *Physical Review Letters* 126.4 (2021), p. 047402.

[150] Quan Sun et al. “Direct imaging of the near field and dynamics of surface plasmon resonance on gold nanostructures using photoemission electron microscopy”. *Light: science & applications* 2.12 (2013), e118–e118.

[151] Pablo Albella et al. “Electric and magnetic field enhancement with ultralow heat radiation dielectric nanoantennas: considerations for surface-enhanced spectroscopies”. *Acs Photonics* 1.6 (2014), pp. 524–529.

[152] Tintu Kuriakose et al. “Plasmon-Enhanced Photo-Luminescence Emission in Hybrid Metal–Perovskite Nanowires”. *Nanomaterials* 15.8 (2025), p. 608.

[153] Ratan Das et al. “Synthesis of silver nanoparticles and their optical properties”. *Journal of Experimental Nanoscience* 5.4 (2010), pp. 357–362.

[154] Yajie Bian et al. “Distance-Dependent plasmon-enhanced fluorescence of submonolayer rhodamine 6G by gold nanoparticles”. *Nanoscale Research Letters* 16.1 (2021), p. 90.

[155] Mark K Kinnan et al. “Plasmon coupling in two-dimensional arrays of silver nanoparticles: I. Effect of the dielectric medium”. *The Journal of Physical Chemistry C* 113.17 (2009), pp. 7079–7084.

[156] Guangda Niu, Xudong Guo, and Liduo Wang. “Review of recent progress in chemical stability of perovskite solar cells”. *Journal of Materials Chemistry A* 3.17 (2015), pp. 8970–8980.

[157] Jinli Yang et al. “Origin of the thermal instability in CH3NH3PbI3 thin films deposited on ZnO”. *Chemistry of Materials* 27.12 (2015), pp. 4229–4236.

[158] IP Pashuk, NS Pidzyrailo, and MG Matsko. “Exciton absorption, luminescence, and resonance Raman scattering of light in CsPbCl3 and CsPbBr3 crystals at low temperature”. *Sov. Phys. Solid State* 23.7 (1981), p. 1263.

[159] Gabriele Rainò et al. “Single cesium lead halide perovskite nanocrystals at low temperature: fast single-photon emission, reduced blinking, and exciton fine structure”. *ACS nano* 10.2 (2016), pp. 2485–2490.

[160] Qiuyu Shang et al. “Surface plasmon enhanced strong exciton–photon coupling in hybrid inorganic–organic perovskite nanowires”. *Nano letters* 18.6 (2018), pp. 3335–3343.

[161] Felix Deschler et al. “High photoluminescence efficiency and optically pumped lasing in solution-processed mixed halide perovskite semiconductors”. *The journal of physical chemistry letters* 5.8 (2014), pp. 1421–1426.

[162] Yiping Wang et al. “Photon transport in one-dimensional incommensurately epitaxial CsPbX3 arrays”. *Nano letters* 16.12 (2016), pp. 7974–7981.

[163] Haiping He et al. “Exciton localization in solution-processed organolead trihalide perovskites”. *Nature communications* 7.1 (2016), p. 10896.

[164] Pengfei Qi et al. “Phonon scattering and exciton localization: molding exciton flux in two dimensional disorder energy landscape”. *elight* 1.1 (2021), p. 6.

[165] Alan Baldwin et al. “Local energy landscape drives long-range exciton diffusion in two-dimensional halide perovskite semiconductors”. *The Journal of Physical Chemistry Letters* 12.16 (2021), pp. 4003–4011.

[166] Christian Wehrenfennig et al. “Homogeneous emission line broadening in the organo lead halide perovskite ch3nh3pbi3–x cl x”. *The journal of physical chemistry letters* 5.8 (2014), pp. 1300–1306.

[167] Chunyang Yin et al. “Bright-exciton fine-structure splittings in single perovskite nanocrystals”. *Physical review letters* 119.2 (2017), p. 026401.

[168] Peter C Sercel et al. “Exciton fine structure in perovskite nanocrystals”. *Nano letters* 19.6 (2019), pp. 4068–4077.

[169] Lei Hou, Philippe Tamarat, and Brahim Lounis. “Revealing the exciton fine structure in lead halide perovskite nanocrystals”. *Nanomaterials* 11.4 (2021), p. 1058.

[170] Ariadni Boziki et al. “Molecular origin of the asymmetric photoluminescence spectra of CsPbBr3 at low temperature”. *The journal of physical chemistry letters* 12.10 (2021), pp. 2699–2704.

[171] Ivan Pelant and Jan Valenta. *Luminescence Spectroscopy of Semiconductors.* Oxford University Press, Feb. 2012.

[172] Zhen-Yu Zhang et al. “The role of trap-assisted recombination in luminescent properties of organometal halide CH3NH3PbBr3 perovskite films and quantum dots”. *Scientific reports* 6.1 (2016), p. 27286.

[173] Georgian Nedelcu et al. “Fast anion-exchange in highly luminescent nanocrystals of cesium lead halide perovskites (CsPbX3, X= Cl, Br, I)”. *Nano letters* 15.8 (2015), pp. 5635–5640.

[174] Jonathan Vandenwijngaerden et al. “NIR Luminescence from Deep-Level Traps in CsPbBr3 Microcrystals”. *The Journal of Physical Chemistry Letters* 16.14 (2025), pp. 3491–3500.

[175] Yang Li et al. “Exciton versus free carrier emission: Implications for photoluminescence efficiency and amplified spontaneous emission thresholds in quasi-2D and 3D perovskites”. *Materials Today* 49 (2021), pp. 35–47.

[176] Hong-Hua Fang et al. “Long-lived hot-carrier light emission and large blue shift in formamidinium tin triiodide perovskites”. *Nature communications* 9.1 (2018), p. 243.

[177] TLKZ Schmidt, K Lischka, and W Zulehner. “Excitation-power dependence of the near-band-edge photoluminescence of semiconductors”. *Physical Review B* 45.16 (1992), p. 8989.

[178] Zhaojun Zhang et al. “Vertically aligned CsPbBr3 nanowire arrays with template-induced crystal phase transition and stability”. *The Journal of Physical Chemistry C* 125.8 (2021), pp. 4860–4868.

[179] D Bimberg, M Sondergeld, and E Grobe. “Thermal dissociation of excitons bounds to neutral acceptors in high-purity GaAs”. *Physical Review B* 4.10 (1971), p. 3451.

[180] Xinyue Huang et al. “Intrinsic Localized Excitons in MoSe2/CrSBr Heterostructure”. *Advanced Materials* 37.6 (2025), p. 2413438.

[181] Hajime Shibata et al. "Excitation-power dependence of free exciton photoluminescence of semiconductors". *Japanese journal of applied physics* 44.8R (2005), p. 6113.

[182] Petr Klenovskỳ, Petr Steindl, and Dominique Geffroy. "Excitonic structure and pumping power dependent emission blue-shift of type-II quantum dots". *Scientific Reports* 7.1 (2017), p. 45568.

[183] S Wachter et al. "Excitation induced shift and broadening of the exciton resonance". *Physica B: Condensed Matter* 314.1-4 (2002), pp. 309–313.

[184] Handong Jin et al. "It's a trap! On the nature of localised states and charge trapping in lead halide perovskites". *Materials Horizons* 7.2 (2020), pp. 397–410.

[185] Xinyu Shen et al. "Passivation strategies for mitigating defect challenges in halide perovskite light-emitting diodes". *Joule* 7.2 (2023), pp. 272–308.

[186] Thomas P Darlington et al. "Imaging strain-localized excitons in nanoscale bubbles of monolayer WSe2 at room temperature". *Nature Nanotechnology* 15.10 (2020), pp. 854–860.

[187] Michael Seitz et al. "Exciton diffusion in two-dimensional metal-halide perovskites". *Nature communications* 11.1 (2020), p. 2035.

[188] Indy du Fossé et al. "Limits of defect tolerance in perovskite nanocrystals: effect of local electrostatic potential on trap states". *Journal of the American Chemical Society* 144.25 (2022), pp. 11059–11063.

[189] Fang Pan et al. "Free and self-trapped exciton emission in perovskite CsPbBr 3 microcrystals". *RSC advances* 12.2 (2022), pp. 1035–1042.

[190] Wenqiang Liu et al. "Localized exciton emission in CsPbBr 3 nanocrystals synthesized with excess bromide ions". *Journal of Materials Chemistry C* 7.35 (2019), pp. 10783–10788.

[191] J. A. Peters et al. "Excitons in CsPbBr3 Halide Perovskites". In: *Metal-Halide Perovskite Semiconductors: From Physical Properties to Opto-electronic Devices and X-ray Sensors*. Ed. by Wanyi Nie and Krzysztof (Kris) Iniewski. Cham: Springer International Publishing, 2023, pp. 73–88. URL: `https://doi.org/10.1007/978-3-031-26892-2_5`.

[192] Xiangzhou Lao et al. "Luminescence and thermal behaviors of free and trapped excitons in cesium lead halide perovskite nanosheets". *Nanoscale* 10.21 (2018), pp. 9949–9956.

[193] Biswajit Dey et al. "Temperature-induced localized exciton dynamics in inorganic CsPbX3 (X= I, Br, Cl) perovskite nanocrystals". *Journal of Luminescence* 281 (2025), p. 121199.

[194] Andrew P Schlaus et al. "How lasing happens in CsPbBr3 perovskite nanowires". *Nature communications* 10.1 (2019), p. 265.

[195] Tania Palmieri et al. "Mahan excitons in room-temperature methylammonium lead bromide perovskites". *Nature communications* 11.1 (2020), p. 850.

[196] A. F. van Driel et al. "Statistical analysis of time-resolved emission from ensembles of semiconductor quantum dots: Interpretation of exponential decay models". *Phys. Rev. B* 75 (3 2007), p. 035329.

[197] MR Wagner et al. “Bound excitons in ZnO: Structural defect complexes versus shallow impurity centers”. *Physical Review B—Condensed Matter and Materials Physics* 84.3 (2011), p. 035313.

[198] Oliver Brandt et al. “Temperature dependence of the radiative lifetime in GaN”. *Physical Review B* 58.24 (1998), R15977.

[199] Sabrine Ayari et al. “Radiative lifetime of localized excitons in transition-metal dichalcogenides”. *Physical Review B* 98.20 (2018), p. 205430.

[200] Haining Wang et al. “Radiative lifetimes of excitons and trions in monolayers of the metal dichalcogenide MoS 2”. *Physical Review B* 93.4 (2016), p. 045407.

[201] Linyou Cao. “Two-dimensional transition-metal dichalcogenide materials: Toward an age of atomic-scale photonics”. *Mrs Bulletin* 40.7 (2015), pp. 592–599.

[202] Tintu Kuriakose et al. “Nonlinear self-confined plasmonic beams: experimental proof”. *ACS photonics* 7.9 (2020), pp. 2562–2570.

[203] Maria Chiara Sportelli et al. “The pros and cons of the use of laser ablation synthesis for the production of silver nano-antimicrobials”. *Antibiotics* 7.3 (2018), p. 67.

[204] M Boutinguiza et al. “Production of silver nanoparticles by laser ablation in open air”. *Applied Surface Science* 336 (2015), pp. 108–111.

[205] Tânia Ribeiro, Carlos Baleizão, and José Paulo S Farinha. “Artefact-free evaluation of metal enhanced fluorescence in silica coated gold nanoparticles”. *Scientific reports* 7.1 (2017), p. 2440.

[206] Kai Yao et al. “Plasmon-induced trap filling at grain boundaries in perovskite solar cells”. *Light: Science & Applications* 10.1 (2021), p. 219.

[207] A Femius Koenderink. “On the use of Purcell factors for plasmon antennas”. *Optics letters* 35.24 (2010), pp. 4208–4210.

[208] Urcan Guler, Vladimir M Shalaev, and Alexandra Boltasseva. “Nanoparticle plasmonics: going practical with transition metal nitrides”. *Materials Today* 18.4 (2015), pp. 227–237.

[209] Alexander N Grigorenko, Marco Polini, and Kostya S Novoselov. “Graphene plasmonics”. *Nature photonics* 6.11 (2012), pp. 749–758.

[210] Youngsin Park et al. “Surface plasmon-mediated photoluminescence boost in graphene-covered CsPbBr3 quantum dots”. *Applied Surface Science* 681 (2025), p. 161601.

[211] A Tsiatmas et al. “Superconducting plasmonics and extraordinary transmission”. *Applied Physics Letters* 97.11 (2010).

[212] Vahagn Mkhitaryan et al. “Can copper nanostructures sustain high-quality plasmons?” *Nano Letters* 21.6 (2021), pp. 2444–2452.

[213] Soojin Jeong et al. “Heterometallic seed-mediated growth of monodisperse colloidal copper nanorods with widely tunable plasmonic resonances”. *Nano Letters* 20.10 (2020), pp. 7263–7271.

[214] Mark W Knight et al. “Aluminum for plasmonics”. *ACS nano* 8.1 (2014), pp. 834–840.

[215] Dayne F Swearer et al. “Heterometallic antenna- reactor complexes for photocatalysis”. *Proceedings of the National Academy of Sciences* 113.32 (2016), pp. 8916–8920.

[216] Emilie Ringe. “Shapes, plasmonic properties, and reactivity of magnesium nanoparticles”. *The Journal of Physical Chemistry C* 124.29 (2020), pp. 15665–15679.

[217] Alemayehu Nana Koya et al. “Nanoporous metals: From plasmonic properties to applications in enhanced spectroscopy and photocatalysis”. *ACS nano* 15.4 (2021), pp. 6038–6060.

[218] Philippe Tassin et al. “A comparison of graphene, superconductors and metals as conductors for metamaterials and plasmonics”. *Nature Photonics* 6.4 (2012), pp. 259–264.

[219] Yael Gutierrez et al. “How an oxide shell affects the ultraviolet plasmonic behavior of Ga, Mg, and Al nanostructures”. *Optics express* 24.18 (2016), pp. 20621–20631.

[220] Luca Pasquini et al. “Metal-hydride transformation kinetics in Mg nanoparticles”. *Applied Physics Letters* 94.4 (2009).

[221] Mohamed M ElFaham, M Okil, and Ayman M Mostafa. “Fabrication of magnesium metallic nanoparticles by liquid-assisted laser ablation”. *Journal of the Optical Society of America B* 37.9 (2020), pp. 2620–2625.

[222] Andrea R Tao, Susan Habas, and Peidong Yang. “Shape control of colloidal metal nanocrystals”. *small* 4.3 (2008), pp. 310–325.

[223] Maria Wuithschick et al. “Size-controlled synthesis of colloidal silver nanoparticles based on mechanistic understanding”. *Chemistry of Materials* 25.23 (2013), pp. 4679–4689.

[224] Elizabeth R Hopper et al. “Size control in the colloidal synthesis of plasmonic magnesium nanoparticles”. *The Journal of Physical Chemistry C* 126.1 (2021), pp. 563–577.

[225] Andrey Ten et al. “Colloidal synthesis and etching yield monodisperse plasmonic quasi-spherical Mg nanoparticles”. *Nanoscale Horizons* (2025).

[226] Andrey Ten et al. “Magnesium nanoparticles for surface-enhanced Raman scattering and plasmon-driven catalysis”. *Acs Nano* 18.28 (2024), pp. 18785–18799.

[227] Christina Graf et al. “A general method to coat colloidal particles with silica”. *Langmuir* 19.17 (2003), pp. 6693–6700.

[228] Luis M Liz-Marzán, Michael Giersig, and Paul Mulvaney. “Synthesis of nanosized gold- silica core- shell particles”. *Langmuir* 12.18 (1996), pp. 4329–4335.

[229] Jiakai Liu et al. “Light-induced self-assembly of cubic CsPbBr3 perovskite nanocrystals into nanowires”. *Chemistry of Materials* 31.17 (2019), pp. 6642–6649.

[230] Ella Sanders et al. “Remanent polarization and strong photoluminescence modulation by an external electric field in epitaxial CsPbBr3 nanowires”. *ACS nano* 15.10 (2021), pp. 16130–16138.

[231] Sourobh Raychaudhuri et al. “Precise semiconductor nanowire placement through dielectrophoresis”. *Nano letters* 9.6 (2009), pp. 2260–2266.

[232] Mingwei Li et al. "Bottom-up assembly of large-area nanowire resonator arrays". *Nature nanotechnology* 3.2 (2008), pp. 88–92.

[233] Chen-Xu Chen et al. "Distinctive bulk-and surface-specific photoluminescence and photocarrier dynamics in CH3NH3PbI3 perovskite". *Crystal Growth & Design* 21.1 (2020), pp. 45–51.

[234] Joseph R Lakowicz. *Principles of fluorescence spectroscopy.* Springer, 2006.

[235] Ihor Cherniukh et al. "Shape-directed co-assembly of lead halide perovskite nanocubes with dielectric nanodisks into binary nanocrystal superlattices". *Acs Nano* 15.10 (2021), pp. 16488–16500.

[236] Jiakai Liu et al. "Self-assembly and regrowth of metal halide perovskite nanocrystals for optoelectronic applications". *Accounts of Chemical Research* 55.3 (2022), pp. 262–274.

[237] Ning Zhou et al. "Silver nanoshell plasmonically controlled emission of semiconductor quantum dots in the strong coupling regime". *ACS nano* 10.4 (2016), pp. 4154–4163.

[238] Sk Shamim Hasan Abir et al. "Tunable CsPb (Br/Cl) 3 perovskite nanocrystals and further advancement in designing light emitting fiber membranes". *Materials Advances* 2.8 (2021), pp. 2700–2710.

[239] Niko Hildebrandt et al. "Plasmonic quenching and enhancement: metal–quantum dot nanohybrids for fluorescence biosensing". *Chemical Communications* 59.17 (2023), pp. 2352–2380.

[240] G Walters et al. "The quantum-confined Stark effect in layered hybrid perovskites mediated by orientational polarizability of confined dipoles". *Nature communications* 9.1 (2018), p. 4214.

[241] Frieder Conradt et al. "Electric-Field Fluctuations as the Cause of Spectral Instabilities in Colloidal Quantum Dots". *Nano Letters* 23.21 (2023), pp. 9753–9759.

[242] Nathan D Cottam et al. "Light-Induced Stark Effect and Reversible Photoluminescence Quenching in Inorganic Perovskite Nanocrystals". *Advanced Optical Materials* 9.13 (2021), p. 2100104.

[243] Wenwen Yin et al. "Nanoparticle core size and spacer coating thickness-dependence on metal-enhanced luminescence in optical oxygen sensors". *Talanta* 259 (2023), p. 123690.

[244] Feifei Liu, Xinping Zhang, and Xiaohui Fang. "Plasmonic plano-semi-cylindrical nanocavities with high-efficiency local-field confinement". *Scientific Reports* 7.1 (2017), p. 40071.

[245] Constantin Dory et al. "Complete coherent control of a quantum dot strongly coupled to a nanocavity". *Scientific reports* 6.1 (2016), p. 25172.

[246] Kevin Hennessy et al. "Quantum nature of a strongly coupled single quantum dot–cavity system". *Nature* 445.7130 (2007), pp. 896–899.

[247] K Kuruma et al. "Time-resolved vacuum Rabi oscillations in a quantum-dot–nanocavity system". *Physical Review B* 97.23 (2018), p. 235448.

[248] Satyendra Nath Gupta et al. "Complex plasmon-exciton dynamics revealed through quantum dot light emission in a nanocavity". *Nature Communications* 12.1 (2021), p. 1310.

[249] Shu Hu et al. "Robust consistent single quantum dot strong coupling in plasmonic nanocavities". *Nature Communications* 15.1 (2024), p. 6835.

[250] Chenyang Li et al. "Giant photoluminescence enhancement of monolayer WSe2 using a plasmonic nanocavity with on-demand resonance". *Nano Letters* 24.19 (2024), pp. 5879–5885.

[251] Yuan Luo et al. "Strong light-matter coupling in van der Waals materials". *Light: Science & Applications* 13.1 (2024), p. 203.

[252] Luca Sortino et al. "Optically addressable spin defects coupled to bound states in the continuum metasurfaces". *Nature communications* 15.1 (2024), p. 2008.

[253] Longlong Yang et al. "Revealing broken valley symmetry of quantum emitters in WSe2 with chiral nanocavities". *Nature Communications* 14.1 (2023), p. 4265.

[254] Matthias Ginterseder et al. "Lead halide perovskite nanocrystals with low inhomogeneous broadening and high coherent fraction through dicationic ligand engineering". *Nano Letters* 23.4 (2023), pp. 1128–1134.

[255] Hamid Pashaei Adl et al. "Superradiance emission and its thermal decoherence in lead halide perovskites superlattices". *Advanced Optical Materials* 11.15 (2023), p. 2202497.

[256] Hina Igarashi, Mitsuaki Yamauchi, and Sadahiro Masuo. "Correlation between single-photon emission and size of cesium lead bromide perovskite nanocrystals". *The Journal of Physical Chemistry Letters* 14.9 (2023), pp. 2441–2447.

[257] Yu Tong et al. "Highly luminescent cesium lead halide perovskite nanocrystals with tunable composition and thickness by ultrasonication". *Angewandte Chemie International Edition* 55.44 (2016), pp. 13887–13892.

[258] Mengyun Chen et al. "Kinetically Controlled Synthesis of Quasi-Square CsPbI3 Nanoplatelets with Excellent Stability". *Small* 20.15 (2024), p. 2306360.

[259] Johannes Heitmann et al. "Excitons in Si nanocrystals: confinement and migration effects". *Physical Review B* 69.19 (2004), p. 195309.

[260] Quinten A Akkerman et al. "Solution synthesis approach to colloidal cesium lead halide perovskite nanoplatelets with monolayer-level thickness control". *Journal of the American Chemical Society* 138.3 (2016), pp. 1010–1016.

[261] Tristan Farrow et al. "Ultranarrow line width room-temperature single-photon source from perovskite quantum dot embedded in optical microcavity". *Nano Letters* 23.23 (2023), pp. 10667–10673.